UNIVERSITY OF SOUTHAMPTON

FACULTY OF SOCIAL SCIENCES

School of Mathematical Sciences

Gravitational waves from magnetically induced thermal neutron star mountains

by

Emma Osborne

Thesis for the degree of Doctor of Philosophy

September 2019

UNIVERSITY OF SOUTHAMPTON

ABSTRACT

FACULTY OF SOCIAL SCIENCES

School of Mathematical Sciences

Thesis for the degree of Doctor of Philosophy

GRAVITATIONAL WAVES FROM MAGNETICALLY INDUCED THERMAL NEUTRON STAR MOUNTAINS

by Emma Osborne

With the detection of GW150914, the era of gravitational wave astronomy has commenced. One possible source of gravitational waves is accreting neutron stars. Many low mass X-ray binary neutron stars are spinning at frequencies considerably lower than the neutron star break-up frequency. Gravitational wave emission might account for this observed maximum spin cap. For an isolated neutron star to emit gravitational waves, it must deform from its axial symmetry to produce a time-varying gravitational field. One way this can occur is through the development of a misaligned quadrupole moment. A quadrupole moment or 'mountain' can develop if temperature asymmetries exist in a neutron star crust.

In this thesis, we investigate whether temperature asymmetries can develop in an accreted neutron star crust. We construct a self-consistent model of a spherically symmetric background thermal profile of an accreted crust. A temperature perturbation is then induced by inserting a magnetic field. The presence of a magnetic field causes anisotropies in the thermal conductivity to develop, due to electrons interacting with the field. We explore the parameter space of accretion rate, impurity parameter and magnetic field strength. We then investigate the influence of shallow crustal heating on our model. Later, we consider the effects of existing temperature asymmetries on the surface of the crust, which can arise from non-spherical accretion. We find these perturbation mechanisms are unlikely to induce temperature asymmetries that can produce a sufficiently large mass quadrupole moment which generates energy losses via gravitational wave emission to balance the spin-up torque from accretion.

Table of Contents

List of Figures

UNIVERSITY OF Southampton

Academic Thesis: Declaration Of Authorship

I, ... [please print name]

declare that this thesis and the work presented in it are my own and has been generated by me as the result of my own original research.

[title of thesis] .....

.....

I confirm that:

1. This work was done wholly or mainly while in candidature for a research degree at this University;
2. Where any part of this thesis has previously been submitted for a degree or any other qualification at this University or any other institution, this has been clearly stated;
3. Where I have consulted the published work of others, this is always clearly attributed;
4. Where I have quoted from the work of others, the source is always given. With the exception of such quotations, this thesis is entirely my own work;
5. I have acknowledged all main sources of help;
6. Where the thesis is based on work done by myself jointly with others, I have made clear exactly what was done by others and what I have contributed myself;
7. Either none of this work has been published before submission, or parts of this work have been published as: [please list references below]:

Signed: .....

Date: .....

Acknowledgements

I would like to say a very big thank you to my supervisor Ian Jones, for his guidance, patience, and support throughout my PhD journey. The combination of his friendly, welcoming approach and enthusiasm for the subject enabled me to achieve this challenging pursuit. Thank you to my 2nd supervisor Ian Hawke, for his valuable help and incredible ability to read my disfunctional code.

I would also like to thank Nils Andersson, for always supporting and encouraging my public engagement endeavours, providing me with invaluable experience in a field I am now building a career in. These collaborations, along with his open-office, offering a 'shoulder to swear on', enriched my PhD experience.

I am grateful to all the friends I have made during my time at Southampton, making it an enjoyable place to live and work. To my friends in office 2019, Garvin, Alex, Olly and Patrick, thank you for our science chats, office banter and impromptu visits to the pub. To Marcella Wijngaarden, thank you for being you and the friendship we have formed on this journey together. I wish you all the best of luck for your future endeavours.

I would like to say a heartfelt thank you to my husband, Oliver Dean, for his endless support, incredible artistic skills and belief in me; to my late Nan, Eileen Osborne, for her enthusiasm and unphased desire to understand gravitational waves; and finally to my Dad, Philip Osborne, for teaching me to aim high and instilling the confidence in me to pursue my dreams, without him, none of this would have been possible.

CHAPTER 1

Introduction

1.1 Introduction to gravitational waves

In 1916, Albert Einstein published his general theory of relativity (Einstein, 1916). In this theory, Einstein proposed gravity as a geometric property of spacetime. Curvature in spacetime arises from the presence of mass and energy. A consequence of this theory is the existence of gravitational waves. Gravitational waves are generated when a body's mass quadrupole, or higher order mass multipole, changes in time. A quadrupole moment is the lowest order moment that generates gravitational waves, as the conservation of mass does not allow monopole radiation and the conservation of momentum doesn't allow dipole radiation (Saulson, 1994). The measure of the distortion of spacetime caused by gravitational waves is known as strain.

Gravitational wave detectors, such as LIGO, measure gravitational wave strain using laser interferometry. As a gravitational wave passes through the detector, two arms, which are orthogonal to each other, measure the relative change in length induced by the gravitational wave, as one arm is squeezed and the other is stretched.

In 2015, LIGO detected a gravitational wave signal for the first time (Abbott et al., 2016b). The signal came from two coalescing black holes of mass $\sim 30\mathrm{M}_{\odot}$. The signal lasted for ~ 0.2s, showing an increase in frequency consistent with an inspiral, merger and ringdown, producing a final single black hole. The gravitational wave strain measured

from this event was 1×10^{-21}. Since this initial detection, there have been eight further confirmed detections of binary black hole mergers (GW151226 (Abbott et al., 2016a), GW170104 (Abbott et al., 2017b), GW170814 (Abbott et al., 2017d), GW170608 (Abbott et al., 2017c), GW170729, GW170809, GW170818 and GW170823 (Abbott et al., 2018b)).

In 2017, LIGO detected the first gravitational wave signal from a pair of inspiralling neutron stars, with a strain amplitude of order 10^{-22} (Abbott et al., 2017e). A γ-ray burst, GRB 170817A, was detected 1.7s after the binary neutron star merger (GW170817), which originated from the same region of the sky as GW170817 (Abbott et al., 2017f). The coincidence of these signals sparks the dawn of a new era of multi-messenger astronomy. This combination of gravitational wave and electromagnetic signals enables new insights to be made into gravitation, astrophysics and cosmology (Abbott et al., 2017h). From this detection alone, constraints were placed on the measurement of the Hubble constant (Abbott et al., 2017a), binary neutron star mergers were found to be sources of heavy elements in the universe (Kasen et al., 2017), gravitational waves were confirmed to travel at (or close to) the speed of light (Abbott et al., 2017g) and constraints were also placed on the neutron star radii and equation of state (Abbott et al., 2018a).

As the era of gravitational wave astronomy is well and truly upon us, gravitational waves are proving to be an effective new tool for probing the universe, enabling us to gain a deeper insight into the laws of physics. Neutron stars are particularly interesting objects to use to study fundamental physics, due to their extreme compactness which gives rise to the existence of matter at the highest known pressures in the universe. The incredibly strong gravitational fields of neutron stars makes them excellent subjects for gravitational wave astronomy. The combination of these properties make neutron stars fantastic laboratories for testing the laws of physics in extreme environments.

1.2 Neutron stars as sources of continuous gravitational waves

The gravitational wave signals that have been detected so far have come from coalescing compact binaries. Another type of gravitational wave signal that is expected to be detected in the near future is continuous waves. The most likely source of continuous gravitational waves are spinning neutron stars. For a neutron star to produce gravitational waves, it must develop a deformation from its axial symmetry. There are three key mechanisms in which an isolated neutron star may produce continuous gravitational waves: precession, non-axisymmetric instabilities and non-axisymmetric deformations.

1.2.1 Gravitational waves from freely precessing neutron stars

Free precession of a neutron star occurs when the star develops a deformation that is misaligned from its axis of rotation. The deformation may be supported by either crustal deformations or an internal magnetic field. The precession could be excited by a physical mechanism such as accretion torques, electromagnetic torques, glitches and stellar encounters (Jones and Andersson, 2001). A neutron star is most likely to develop an oblate deformation, arising in the solid neutron star crust.

Once the star is in free precession, damping effects will take place. Kinetic energy from the star's 'wobble' is dissipated into the star as thermal energy. Gravitational waves will also radiate energy away. Jones and Andersson (2001) finds the precession of stars with an oblate deformation are quickly damped. Stars that develop deformations through astrophysical processes, produce gravitational wave signals that may well be too weak to detect by LIGO.

1.2.2 Gravitational waves from neutron star instabilities

Neutron stars can develop unstable modes of oscillation. If these oscillations are non-axisymmetric, the star will generate gravitational waves. Neutron stars can support a large number of different pulsation modes, the most important modes that lead to gravitational wave emission are the so-called f-modes and r-modes.

The f-mode is the fundamental mode, which is restored predominantly by pressure forces. The f-mode is most likely to develop during violent processes, such as neutron star mergers or neutron star formation by supernova core collapse (Glampedakis and Gualtieri, 2018). The f-mode generates gravitational radiation readily, although this also acts as a rapid damping mechanism.

R-modes in rotating stars, are caused by the Coriolis force, which acts as a restoring force (Andersson, 2003). The r-mode satisfies the requirements for the the Chandrasekhar-Friedman-Schutz (CFS) instability (Chandrasekhar, 1970; Friedman and Schutz, 1978), which demonstrates the star is able to find lower energy and angular momentum configurations, allowing the mode amplitude to grow. The r-mode is consequently unstable to gravitational wave emission (Andersson, 1998). Viscosity of the neutron star interior provides damping to the system. The r-mode instability grows as long as the timescale required to damp the system by viscosity is longer than than the gravitational wave driving timescale.

1.2.3 Gravitational waves from neutron star mountains

Steadily spinning neutron stars can also develop non-axisymmetric deformations by growing mountains. Mountains can arise when the star is distorted by the presence of a magnetic field or when the solid crust is strained. In accreting systems, the transfer of matter through accretion can incite crustal mountains through the development of temperature asymmetries and magnetically confined mountains. It is these types of mountains we will examine in this thesis.

1.2.3.1 Magnetic mountains

The magnetic field of a neutron star can induce quadrupolar deformations. The poloidal component of the magnetic field tends to deform the star to an oblate shape, and the toroidal field tends to generate a prolate deformation (Glampedakis and Gualtieri, 2018). If these deformations are misaligned to the axis of rotation, the neutron star will generate gravitational radiation as it spins.

Another type of magnetically induced deformation that may occur in accreting neutron stars is that of magnetically confined mountains. As material is accreted onto the neutron star, the accreted matter accumulates in a column at the polar caps, creating a small distortion in the magnetic field. At the bottom of the accreted column, a horizontal pressure gradient develops, causing the magnetic field to deform at the poles. As the accreted material spreads towards the equator, the frozen-in magnetic flux is dragged and compressed into a belt at the magnetic equator. This magnetic belt restricts the accreted matter to the magnetic poles, causing mountains to form. The magnetic poles are usually misaligned from the axis of rotation, resulting in the emission of gravitational waves as the neutron star spins (Payne and Melatos, 2004; Melatos and Payne, 2005; Vigelius and Melatos, 2009).

1.2.3.2 Thermal Mountains

Many low mass X-ray binary neutron stars have been observed to be rotating within the narrow spin frequency range 250-750Hz (Patruno et al., 2017). As these are accreting systems, a broad range of rotational frequencies, up to the break up frequency of ~ 1500 Hz, would be expected, due to the transfer of angular momentum. The spin-up torque from accretion could be reduced by the interaction of the accretion disk with the magnetosphere of the neutron star, as discussed by White and Zhang (1997). This mechanism requires a link between the accretion rate and magnetic field strength of LMXBs, although it is unclear as to why this should exist. An alternative explanation for this observation, comes from the possibility that these neutron stars are developing some form of asymmetry through accretion, causing them to lose energy by radiating

gravitational waves.

As accreted material falls onto the neutron star surface, it begins to undergo compression. As the matter is compressed, pressure sensitive electron capture reactions begin to occur, resulting in the formation of higher density matter. The temperature of an accreted crust is hot enough for the electron capture reactions to also be temperature sensitive. If temperature asymmetries exist in the crust, lateral density variations develop, as hotter regions capture electrons at lower pressures. If a temperature asymmetries exist in the accreted crust, a mass quadrupole moment can develop. If the mountain is misaligned from the star's axis of rotation, gravitational wave radiation is emitted as the star rotates (Bildsten, 1998) (Ushomirsky et al., 2000).

1.3 Searching for continuous gravitational waves

Advanced LIGO targets astrophysical sources that emit gravitational waves within the frequency range 10-10^4Hz (Martynov et al., 2016). Neutron stars with mountain deformations emit gravitational waves at frequencies double their spin frequency. Stars with rotational frequencies in the range 250-750Hz produce continuous gravitational wave signals that lie well within the detectable bounds of LIGO. Although the signals produced by these deformed spinning neutron stars are potentially detectable with LIGO, there are many constraints hindering detection.

The gravitational wave strain amplitude of continuous sources in the Milky Way galaxy is expected to be many orders of magnitude smaller than those detected from compact binary mergers (Glampedakis and Gualtieri, 2018). In order to detect these weak signals, data must be integrated over long time periods (Riles, 2017). This becomes very computationally expensive in the case of all-sky searches, due to the Doppler modulation of the signal caused by the Earth's rotation (Sathyaprakash and Schutz, 2009). Constraining the parameter space, such as sky-location, enables less computationally costly targeted sky searches to be conducted.

To extract such a weak signal, a large sample of data ($\sim$ years) is required. One of the biggest drawbacks of this, is the targeted source must sustain a non-axisymmetric deformation for the duration of the data set, to ensure gravitational waves are being continually emitted. For this reason, accreting neutron stars are of particular interest. The accretion spin-up torque in accreting neutron stars may be halted by energy losses due to gravitational wave emission. This mechanism was first discussed in the context of gravitational wave emission from f-mode instabilities by Papaloizou and Pringle (1978) and Wagoner (1984), and for gravitational waves generated by r-mode instabilities by Andersson et al. (1999). Sufficiently large neutron star mountains may also generate an-

gular momentum losses via gravitational wave emission as considered by Bildsten (1998), Ushomirsky et al. (2000), Haskell et al. (2006), Johnson-McDaniel and Owen (2013), Cutler (2002), Haskell et al. (2008), Payne and Melatos (2004), Melatos and Payne (2005) and Vigelius and Melatos (2009).

The LMXBs Scorpius X-1 and XTE J1751-305 have been targeted as continuous gravitational wave sources, as they are expected to emit signals that are detectable by LIGO. Although no detections have been claimed to date, upper limits have been placed on the gravitational wave strain of these sources of 1.8×10^{-24} (Meadors et al., 2017).

Understanding the physics of neutron stars from a theoretical perspective, along with electromagnetic observations, will help to guide targeted continuous gravitational wave searches, with the hope of detecting these elusive signals in the near future.

1.4 Thesis outline

In this thesis, the work of Bildsten (1998) and Ushomirsky et al. (2000) is built upon by developing a self-consistent model of an accreted neutron star crust, to investigate if temperature asymmetries can develop in the presence of a magnetic field. Bildsten (1998) and Ushomirsky et al. (2000) assumed the existence of temperature asymmetries in an accreted neutron star crust. We intend to close the loop on this work by quantifying the temperature perturbation that can develop in an accreted neutron star crust. We explore the parameter space of accretion rate and crustal impurity parameter, to determine if these temperature asymmetries are sufficiently large to produce a mass quadrupole moment, that is misaligned from the axis of rotation, that can generate energy losses via gravitational radiation which balances the spin-up torque from accretion.

Chapter 2 reviews some of theory behind gravitational wave emission and takes an in-depth look at how thermal mountains can develop in an accreted crust, along with the maximum mountain the crust can sustain before cracking, by reviewing the work of Bildsten (1998) and Ushomirsky et al. (2000). The possibility of thermal instabilities, arising from the magnetic field in the crust, following the work of Price et al. (2012), is also discussed.

In chapter 3, we begin our original work by constructing a toy model of a constant density neutron star crust. A magnetic field is then inserted into a spherically symmetric background model of the thermal profile of an accreted crust, to incite a temperature perturbation.

Later in chapter 4, we build upon the toy model that was developed in chapter 3, by using

a realistic equation of state. A neutron star core is constructed using relativistic gravity and an accreted crust placed on top, constructed in Newtonian gravity. The background thermal profile of a spherically symmetric crust is then modelled for a normal core and a superfluid core. We then incite a temperature perturbation by inserting a magnetic field and determine a value of $\delta T/T$ for both stars from this self-contained model. Recent observations have shown a shallow crustal heating mechanism may exist in some LMXBs. We explore this possibility by studying the effects shallow crustal heating has on our model and ultimately on the value of $\delta T/T$.

In chapter 5, we build on our model from chapter 4 by introducing non-spherical accretion. This modification implements a temperature asymmetry onto the surface of the neutron star crust. The effects this temperature perturbation has on the thermal profile for a realistic neutron star is modelled independently and then compared to the temperature perturbation induced by the presence of the magnetic field. Finally, we conclude in chapter 6.

CHAPTER 2

Neutron star mountains

Neutron stars are incredibly dense objects. They have a central density of the order $\rho_c \approx 10^{15}$ g cm^{-3} and magnetic field strength of up to $B \approx 10^{15}$ Gauss. This high density creates a strong gravitational environment, making neutron stars excellent laboratories for testing the laws of physics in extreme conditions. These properties also make neutron stars excellent gravitational wave source candidates (Shapiro and Teukolsky, 1983, p.2).

For an isolated neutron star to emit gravitational waves, it must deform from its spherical symmetry to produce a time-varying gravitational field. One way this can occur is through the development of a misaligned quadrupole moment. A quadrupole moment or 'mountain' can develop if temperature asymmetries exist in a neutron star crust (Bildsten, 1998).

In this chapter, a literature review of the theory behind gravitational wave emission is considered. The structure of a neutron star and the composition is then discussed. The work of Bildsten (1998) and Ushomirsky et al. (2000) on the possible sources of temperature and compositional asymmetries is reviewed, and calculations to quantify the magnitude of such asymmetries are then performed. Lastly, how the magnetic field influences the temperature evolution within the neutron star crust is investigated.

2.1 Gravitational waves

Gravitational radiation arises when a source produces a time-varying gravitational field. Gravitational waves travel at the speed of light and send ripples through spacetime. For a rotating neutron star to emit gravitational waves it must deform from its axial symmetry. The development of a mass quadrupole moment is investigated, as this is the lowest order non-conserved mass multipole of a system. In this section the Greek alphabet is used to for spacetime components, and Latin alphabet is used for spatial components only.

2.1.1 Propagation of gravitational waves

A description of the propagation of gravitational waves is obtained from the linearised Einstein equations (Misner et al., 1973). In geometrised units (G=c=1), the Einstein field equations can be written as

$$G_{\mu\nu} = 8\pi T_{\mu\nu}, \tag{2.1.1}$$

where $G_{\mu\nu}$ is the Einstein tensor and $T_{\mu\nu}$ is the stress-energy tensor.

The Einstein equation can be linearised by being placed in the weak field limit as

$$g_{\mu\nu} = \eta_{\mu\nu} + h_{\mu\nu}, \qquad |h_{\mu\nu}| \ll 1, \tag{2.1.2}$$

where $g_{\mu\nu}$ is the metric tensor, $\eta_{\mu\nu}$ is the Minkowski metric and $h_{\mu\nu}$ is the metric perturbation. This approximation corresponds to a perturbation on a flat spacetime background. In this limit the linearised Einstein field equation becomes

$$-\bar{h}^{\alpha}_{\mu\nu,\alpha} - \eta_{\mu\nu}\bar{h}^{\alpha\beta}_{\alpha\beta,} + \bar{h}^{\alpha}_{\mu\alpha,\nu} + \bar{h}^{\alpha}_{\nu\alpha,\mu} = 16\pi T_{\mu\nu}, \tag{2.1.3}$$

where $\bar{h}_{\mu\nu}$ is the trace reversed metric perturbation tensor and is defined as

$$\bar{h}_{\mu\nu} = h_{\mu\nu} - \frac{1}{2}\eta_{\mu\nu}h. \tag{2.1.4}$$

The linearised field equation can be simplified further by introducing the gauge condition

$$\bar{h}^{\mu\alpha}{}_{,\alpha} = 0. \tag{2.1.5}$$

By applying this gauge condition and placing the linearised field equation in a vacuum, the wave equation is retrieved:

$$\Box\bar{h}_{\mu\nu} \equiv \bar{h}^{\alpha}_{\mu\nu,\alpha} = 0. \tag{2.1.6}$$

The gravitational wave can be transformed into the transverse-traceless gauge $h^{\mathrm{TT}}_{\mu\nu}$ in

which only the spatial components are non-zero (Misner et al., 1973, p.947). This is written as a function of the polarisation tensors

$$h_{jk}^{\mathrm{TT}} = h_{+}e_{jk}^{+} + h_{\times}e_{jk}^{\times}, \tag{2.1.7}$$

where e_{jk}^{+} and $e_{jk}^{\times}$ are the plus and cross polarisation tensors respectively (Misner et al., 1973, p.953) and can be written as

$$e_{jk}^{+} = \begin{pmatrix} 0 & 0 & 0 & 0 \\ 0 & 1 & 0 & 0 \\ 0 & 0 & -1 & 0 \\ 0 & 0 & 0 & 0 \end{pmatrix} \quad e_{jk}^{\times} = \begin{pmatrix} 0 & 0 & 0 & 0 \\ 0 & 0 & 1 & 0 \\ 0 & 1 & 0 & 0 \\ 0 & 0 & 0 & 0 \end{pmatrix}. \tag{2.1.8}$$

These polarisations arise as they are the only non-vanishing components of h_{jk}^{TT} and correspond to the relative acceleration experienced by particles transverse to the direction of propagation of the gravitational wave.

2.1.2 Mass quadrupole moment

The mass quadrupole moment of a neutron star can be calculated, to a good approximation, in the Newtonian limit. To determine if a Newtonian approximation is suitable, a measure of the compactness of a neutron star is required. The compactness parameter is a dimensionless number obtained from the ratio of mass M and radius R of an object. This presents a measure of the importance of general relativity in the system. The compactness of a neutron star is

$$\frac{M}{R} = 0.21 \left(\frac{M}{1.4M_{\odot}}\right)\left(\frac{10\,\mathrm{km}}{R}\right), \tag{2.1.9}$$

where $M_{\odot}$ is the mass of the sun. The measure of compactness given in equation (2.1.9) is sufficiently small such that the gravitational wave emission from a neutron star can be treated as a weak-field correction to Newtonian gravity. A more in-depth treatment of a neutron star in general relativity and Newtonian gravity is conducted in chapter 4 of this thesis.

The trace-free mass quadrupole moment in the Newtonian limit is mathematically defined in Cartesian coordinates as (Misner et al., 1973)

$$I_{jk} \equiv \int \rho \left[x_j x_k - \frac{1}{3}\delta_{jk}(x)^2\right] dV, \tag{2.1.10}$$

and in the transverse-traceless gauge Ŧ_{jk} becomes

$$\text{Ŧ}^{TT}_{jk} \equiv P_{jl}P_{km}\text{Ŧ}_{lm} - \frac{1}{2}P_{jk}\left(P_{lm}\text{Ŧ}_{lm}\right), \tag{2.1.11}$$

where m_A is the mass of the Ath particle, x^A_j are the spatial coordinates of the Ath particle, δ_{jk} is the Kronecker delta and P_{jk} is the projection tensor where

$$P_{jk} = \delta_{jk} - n_j n_k, \tag{2.1.12}$$

and n_i is the unit vector in the direction of the propagation. The mass quadrupole is related to the observable quantity luminosity $L_{\rm GW}$ by the following relationship

$$L_{\rm GW} \equiv \frac{dE}{dt} = -\frac{1}{5}\frac{G}{c^5}\langle \dddot{\text{Ŧ}}_{jk}\dddot{\text{Ŧ}}^{jk}\rangle, \tag{2.1.13}$$

where dot indicates the derivative with respect to time and $\langle ...\rangle$ means 'time averaged over one period'.

The gravitational wave luminosity equation can be modified further to the more specific case of a rigid neutron star crust supporting a mountain. For an object with moments of inertia I_1, I_2 and I_3 that is non-axisymmetric ($I_1 \neq I_2$) rotating about the principle axis $\boldsymbol{e}_3$ the gravitational luminosity is

$$\frac{dE}{dt} = -\frac{32}{5}\frac{G}{c^5}\left(I_1 - I_2\right)^2\Omega^6, \tag{2.1.14}$$

where $\Omega = 2\pi\nu_s$ and ν_s is the neutron star spin frequency (Shapiro and Teukolsky, 1983, p.471).

2.2 Neutron star structure

To understand how mountains form in a neutron star, the composition and structure must first be understood. Neutron stars are composed primarily of neutrons. As the density increases, from the neutron stars surface towards the core, the composition also varies, creating layers of structure. A neutron star is comprised of a liquid ocean, solid crust and superfluid core as depicted in Fig. 2.2.1.

From the surface, going deeper into the star, ocean material increases in density and begins to crystallise to form a crust. The crust is made up of two sub-layers: an outer and inner crust. The outer crust consists of nuclei in a lattice, on a background of relativistic degenerate electrons. In addition to this, the inner crust has free neutrons and lies on a superfluid core (Shapiro and Teukolsky, 1983, p.251).

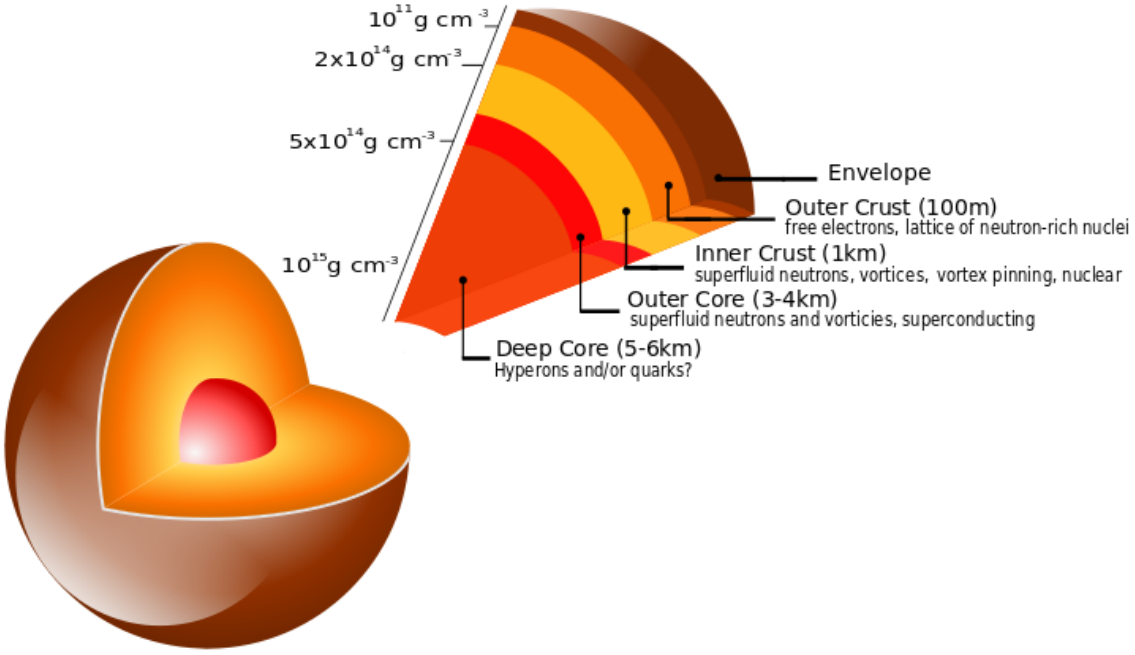

Figure 2.2.1: Cartoon of the internal structure and composition of a neutron star.

In accreting neutron star systems, matter that falls onto the surface of the star is buried under newly accreted material. As this matter is buried, it undergoes a series of nuclear reactions, including electron capture. These processes are density sensitive and create layers of elements of different compositions.

At sufficiently high temperatures, such as an accreted neutron star crust where $T \approx 10^8$ K, these reactions become more sensitive to temperature. Bildsten (1998) suggests that if temperature asymmetries exist in the crust, electron captures that usually occur deeper in the crust, will begin to take place closer to the neutron stars surface, where the crust is hotter. If the temperature gradients exist, density variations will develop correspondingly.

If these density fluctuations are sufficiently large, a quadrupole moment can develop, which if misaligned from the axis of rotation, will generate gravitational waves that produce a spin-down torque which may balance with the angular momentum spin-up torque from accretion, preventing the stars spin frequency from increasing. A representation of this effect is shown in Fig. 2.2.2.

2.2.1 Neutron star crust composition

The composition of an accreted neutron star crust is complex. The crust is composed of transition layers where electron capture processes occur. This section details the equation of state of an accreted neutron star crust as calculated by Haensel and Zdunik

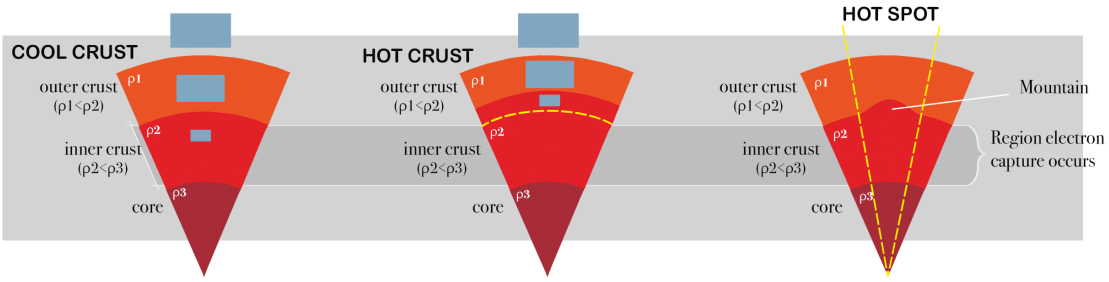

Figure 2.2.2: A cartoon depiction of how accreted matter undergoes compression and density changes as it moves deeper inside the crust. In the cool crust, matter undergoes compression and electron capture reactions begin to occur forming regions of denser matter. When the crust is hot, the electron capture reactions begin to occur at lower densities, forming regions of denser matter closer to the neutron star surface. If temperature asymmetries exist, variations in the lateral density distributions arise. These density asymmetries can lead to a mass quadrupole moment forming in the radial direction, perpendicular to the axis of rotation, coming out of the page (Ushomirsky et al., 2000).

(1990a) and Haensel and Zdunik (1990b).

This is a simplified model which assumes an initial composition of ^{56}Fe, the presence of a single species at any given depth, along with $\beta-$ and neutron equilibrium. This results in a stepwise reduction in Z for nuclei via electron capture reactions, as density increases. More complex models exist that allow for the presence of multiple species (Gupta et al., 2007), (Gupta et al., 2008), and a full reaction network (Schatz et al., 2014). These more complex models find the neutron reactions reduce to lower Z via electron capture cascades or nuclear Urca cycles, instead of the stepwise process of this simpler model of Haensel and Zdunik (1990b) and Haensel and Zdunik (1990a). We selected to use this model for our calculations to enable a comparison of results of our work with that of Ushomirsky et al. (2000) as shown in later chapters.

Haensel and Zdunik (1990b) follow the evolution of accreted matter as it undergoes compression due to increasing pressure. As the pressure increases, electron capture reactions begin to occur, resulting in a systematic decrease in proton number Z. As Z decreases, the Coulomb barrier is lowered and the separation between nuclei decreases, enabling pycnonuclear reactions to begin to occur. Haensel and Zdunik (1990b) produced a table detailing the non-equilibrium processes that occur in both the inner and outer crust, which is reproduced in figure 2.2.3. On average, 1 MeV of the total energy from accretion is deposited into the matter, the rest is radiated away by neutrinos.

Haensel and Zdunik (1990b) expand the equation of state data shown in figure 2.2.3 in Haensel and Zdunik (1990a). The equation of state given in Haensel and Zdunik (1990a) is for the density interval $\sim 10^8$ g cm^{-3} $< \rho <\sim 10^{13}$ g cm^{-3}. The lower limit of this density range arises from the minimum density of the processed accreted matter, just below the bottom of the helium layer. The upper limit arises as the equation of state becomes very similar to that of a cold catalysed crust, also the validity of the model used

Table 1. Non-equilibrium processes in the outer crust

P (dyn cm^{-2})	ρ (g cm^{-3})	Reaction	$\Delta\rho/\rho$	total heat (MeV/nucleon)	deposited heat (MeV/nucleon)
$7.235\ 10^{26}$	$1.494\ 10^{9}$	$^{56}\mathrm{Fe} \rightarrow {}^{56}\mathrm{Cr} - 2e^- + 2\nu_e$	0.08	0.04	0.01
$9.569\ 10^{27}$	$1.114\ 10^{10}$	$^{56}\mathrm{Cr} \rightarrow {}^{56}\mathrm{Ti} - 2e^- + 2\nu_e$	0.09	0.04	0.01
$1.152\ 10^{29}$	$7.848\ 10^{10}$	$^{56}\mathrm{Ti} \rightarrow {}^{56}\mathrm{Ca} - 2e^- + 2\nu_e$	0.10	0.05	0.01
$4.747\ 10^{29}$	$2.496\ 10^{11}$	$^{56}\mathrm{Ca} \rightarrow {}^{56}\mathrm{Ar} - 2e^- + 2\nu_e$	0.11	0.05	0.01
$1.361\ 10^{30}$	$6.110\ 10^{11}$	$^{56}\mathrm{Ar} \rightarrow {}^{52}\mathrm{S} + 4n - 2e^- + 2\nu_e$	0.12	0.06	0.05

Table 2. Non-equilibrium processes in the inner crust

P (dyn cm^{-2})	ρ (g cm^{-3})	reactions	X_n	$\Delta\rho/\rho$	deposited heat (MeV/nucleon)
$1.980\ 10^{30}$	$9.075\ 10^{11}$	$^{52}\mathrm{S} \rightarrow {}^{46}\mathrm{Si} + 6n - 2e^- + 2\nu_e$	0.07	0.13	0.09
$2.253\ 10^{30}$	$1.131\ 10^{12}$	$^{46}\mathrm{Si} \rightarrow {}^{40}\mathrm{Mg} + 6n - 2e^- + 2\nu_e$	0.18	0.14	0.10
$2.637\ 10^{30}$	$1.455\ 10^{12}$	$^{40}\mathrm{Mg} \rightarrow {}^{34}\mathrm{Ne} + 6n - 2e^- + 2\nu_e$ $^{34}\mathrm{Ne} + {}^{34}\mathrm{Ne} \rightarrow {}^{68}\mathrm{Ca}$	0.29	0.17	0.47
$2.771\ 10^{30}$	$1.766\ 10^{12}$	$^{68}\mathrm{Ca} \rightarrow {}^{62}\mathrm{Ar} + 6n - 2e^- + 2\nu_e$	0.39	0.08	0.05
$3.216\ 10^{30}$	$2.134\ 10^{12}$	$^{62}\mathrm{Ar} \rightarrow {}^{56}\mathrm{S} + 6n - 2e^- + 2\nu_e$	0.45	0.09	0.05
$3.825\ 10^{30}$	$2.634\ 10^{12}$	$^{56}\mathrm{S} \rightarrow {}^{50}\mathrm{Si} + 6n - 2e^- + 2\nu_e$	0.50	0.09	0.06
$4.699\ 10^{30}$	$3.338\ 10^{12}$	$^{50}\mathrm{Si} \rightarrow {}^{44}\mathrm{Mg} + 6n - 2e^- + 2\nu_e$	0.55	0.09	0.07
$6.043\ 10^{30}$	$4.379\ 10^{12}$	$^{44}\mathrm{Mg} \rightarrow {}^{36}\mathrm{Ne} + 8n - 2e^- + 2\nu_e$ $^{36}\mathrm{Ne} + {}^{36}\mathrm{Ne} \rightarrow {}^{72}\mathrm{Ca}$ $^{72}\mathrm{Ca} \rightarrow {}^{66}\mathrm{Ar} + 6n - 2e^- + 2\nu_e$	0.61	0.14	0.28
$7.233\ 10^{30}$	$5.839\ 10^{12}$	$^{66}\mathrm{Ar} \rightarrow {}^{60}\mathrm{S} + 6n - 2e^- + 2\nu_e$	0.70	0.04	0.02
$9.238\ 10^{30}$	$7.041\ 10^{12}$	$^{60}\mathrm{S} \rightarrow {}^{54}\mathrm{Si} + 6n - 2e^- + 2\nu_e$	0.73	0.04	0.02
$1.228\ 10^{31}$	$8.980\ 10^{12}$	$^{54}\mathrm{Si} \rightarrow {}^{48}\mathrm{Mg} + 6n - 2e^- + 2\nu_e$	0.76	0.04	0.03

Figure 2.2.3: Table of equation of state data for an accreted neutron star crust reproduced from Haensel and Zdunik (1990b).

by Haensel and Zdunik (1990a) becomes questionable at high densities $\sim 10^{14}$ g cm^{-3}. This equation of state data is shown in table 2.2.4, which includes a list of the nuclides present in the crust of an accreting neutron star. In the third, fourth and fifth columns of table 2.2.4 the maximum pressure $P_{\rm max}$, mass density $\rho_{\rm max}$ and baryon density $n_{\rm b,max}$, are given for which the nuclide is present.

Table 2. Composition of the crust of an accreting neutron star

Z	A	P_{max} (dyn cm^{-2})	ρ_{max} (g cm^{-3})	$n_{b,max}$ (cm^{-3})	μ_e MeV	X_n	$\Delta\rho/\rho$ (%)
26	56	$7.235\ 10^{26}$	$1.494\ 10^{9}$	$8.994\ 10^{32}$	4.59	0.00	8.2
24	56	$9.569\ 10^{27}$	$1.1145\ 10^{10}$	$6.701\ 10^{33}$	8.69	0.00	8.9
22	56	$1.152\ 10^{29}$	$7.848\ 10^{10}$	$4.708\ 10^{34}$	16.15	0.00	9.8
20	56	$4.747\ 10^{29}$	$2.496\ 10^{11}$	$1.494\ 10^{35}$	22.99	0.00	10.9
18	56	$1.361\ 10^{30}$	$6.110\ 10^{11}$	$3.651\ 10^{35}$	29.89	0.00	12.1
16	52	$1.980\ 10^{30}$	$9.075\ 10^{11}$	$5.418\ 10^{35}$	32.78	0.07	13.1
14	46	$2.253\ 10^{30}$	$1.131\ 10^{12}$	$6.748\ 10^{35}$	33.73	0.18	14.4
12	40	$2.637\ 10^{30}$	$1.455\ 10^{12}$	$8.682\ 10^{35}$	34.85	0.29	16.0
20	68	$2.771\ 10^{30}$	$1.766\ 10^{12}$	$1.054\ 10^{36}$	34.98	0.39	8.3
18	62	$3.216\ 10^{30}$	$2.134\ 10^{12}$	$1.273\ 10^{36}$	35.98	0.45	8.6
16	56	$3.825\ 10^{30}$	$2.634\ 10^{12}$	$1.571\ 10^{36}$	37.10	0.50	9.0
14	50	$4.699\ 10^{30}$	$3.338\ 10^{12}$	$1.990\ 10^{36}$	38.40	0.55	9.3
12	44	$6.044\ 10^{30}$	$4.379\ 10^{12}$	$2.610\ 10^{36}$	39.92	0.61	13.8
18	66	$7.233\ 10^{30}$	$5.665\ 10^{12}$	$3.377\ 10^{36}$	39.52	0.70	4.4
16	60	$9.2385\ 10^{30}$	$7.041\ 10^{12}$	$4.196\ 10^{36}$	40.85	0.73	4.3
14	54	$1.228\ 10^{31}$	$8.980\ 10^{12}$	$5.349\ 10^{36}$	42.37	0.76	4.0
12	48	$1.602\ 10^{31}$	$1.127\ 10^{13}$	$6.712\ 10^{36}$	43.41	0.79	3.5
24	96	$1.613\ 10^{31}$	$1.137\ 10^{13}$	$6.769\ 10^{36}$	43.55	0.79	1.5
22	88	$1.816\ 10^{31}$	$1.253\ 10^{13}$	$7.464\ 10^{36}$	43.69	0.80	....

Figure 2.2.4: Composition of the crust of an accreting neutron star reproduced from Haensel and Zdunik (1990a).

Understanding the composition of an accreted neutron star crust enables a realistic model of the thermal profile of the crust to be constructed. The data from tables 2.2.3 and 2.2.4 will be used for a crust of varying density. In the simple case of a constant density star, the average energy generation rate from electron capture in the crust is calculated from the total energy released per unit time $\epsilon_{\rm total}$ as

$$\epsilon_{\rm total} = \frac{\dot{M} E_{\rm nuc}}{m_{\rm b}}, \tag{2.2.1}$$

where $\dot{M}$ is the total accretion rate per unit time, $m_{\rm b}$ is the mass of a baryon, $\dot{M}/m_{\rm b}$ is the number of accreted nucleons per unit time and $E_{\rm nuc}$ is the total heat energy deposited per nucleon. From table 2.2.4, the total heat energy deposited into the accreted crust is 1.33 MeV.

2.3 Temperature asymmetries in accreting neutron stars

In 1998, Bildsten proposed that accreting neutron stars could grow mountains if temperature asymmetries developed in the crust. In this section, we summarise the original back-of-the-envelope argument by Bildsten (1998) that demonstrated the viability of this mechanism. The mass quadrupole moment produced by a single electron capture layer is calculated. A back-of-the-envelope estimate of whether this mass asymmetry is sufficiently large to produce gravitational waves that balance the spin-up torque from accretion, is then conducted following the analysis of Bildsten (1998).

2.3.1 Quadrupole moment generated by electron captures

The crust undergoes compression as matter is accreted onto the neutron star. This compression process continually increases the electron Fermi energy $E_{\rm F}$, until the energy requirement for electron capture to occur is exceeded, initiating electron capture reactions. From the Fermi energy distribution, the pressure in the outer crust created by relativistic degenerate electrons was calculated by Bildsten (1998) to be

$$p(E_{\rm F}) = 1.42 \times 10^{30}\,{\rm erg\,cm^{-3}} \left(\frac{E_{\rm F}}{30\,{\rm MeV}}\right)^4. \tag{2.3.1}$$

Hydrostatic equilibrium is written as $p = -gm$ where m is the mass per unit area above the point considered and g is the local acceleration due to gravity. Using only electron degeneracy pressure (as neutron degeneracy pressure is negligible at low densities), the mass above a given spherical surface of the crust as a function of the Fermi energy $M_{\rm cr}$ is determined from hydrostatic equilibrium and equation (2.3.1) as

$$\begin{aligned} M_{\rm cr}(E_{\rm F}) &= \frac{4\pi R^2 p}{g}, \\ &\approx 5 \times 10^{-5}\,{\rm M_\odot} \frac{R_6^4}{M_{1.4}} \left(\frac{E_{\rm F}}{30\,{\rm MeV}}\right)^4, \end{aligned} \tag{2.3.2}$$

where R is the neutron star radius, using the thin crust approximation $g = GM/R^2$, R_6 is the radius in units of 1×10^6 cm, $M_{1.4} = 1.4\,{\rm M_\odot}$, G is the gravitational constant and M is the mass of the neutron star.

The electron capture process causes denser layers to form. These reactions also have a temperature dependence. In the regions where the crust is hotter, regions of higher density form closer to the surface, creating transverse pressure gradients. This would lead to flow if the matter below these dense regions was liquid. For $T_8 < 10$, where T_8 is temperature in units of 1×10^8 K, the matter is solid at these depths, as would be calculated by the well known formula for the crystallisation of ionic lattices (Shapiro and

Teukolsky, 1983, p.87). These pressure gradients are balanced by a small shear stress with modulus, $\mu \approx 10^{-2}p$. Perturbing the Fermi energy in equation (2.3.2) and introducing a non-zero temperature to effectively allow electrons with a lower Fermi energy $\Delta E_{\rm F} \approx 10k_{\rm B}\Delta T$ to be captured gives

$$\triangle M \approx 5.8 \times 10^{-7}\,{\rm M}_{\odot}\triangle T_8 \frac{R_6^4}{M_{1.4}}\left(\frac{E_{\rm F}}{30\,{\rm MeV}}\right)^3. \tag{2.3.3}$$

The value 5.8×10^{-7} calculated in equation 2.3.3 is an order of magnitude smaller than the value shown in Bildsten (1998). This seems to be a typo in Bildsten's paper.

The quadrupole moment required to prevent a neutron star from spinning up, due to the increase in angular momentum from accreted matter, is calculated for a neutron star radiating gravitational wave energy at a rate of

$$\frac{dE}{dt} = \frac{32GQ^2\Omega^6}{5c^5}, \tag{2.3.4}$$

where Q is the misaligned quadrupole moment (Shapiro and Teukolsky, 1983, p.488). The angular moment loss rate $J_{\rm gw}$ is equal to the gravitational wave luminosity divided by the neutron stars angular frequency as

$$J_{\rm gw} = \frac{1}{\Omega}\frac{dE}{dt}. \tag{2.3.5}$$

The angular momentum transferred to the neutron star through accretion $J_{\rm a}$ is calculated from the specific angular momentum of particles in a Keplerian orbit, in this case the accretion rate $\dot{M}$ is

$$J_{\rm a} \approx \dot{M}(GMR)^{\frac{1}{2}}, \tag{2.3.6}$$

where M is the mass of the neutron star and R is the radius of the star. The quadrupole moment required for a critical frequency of 300Hz is calculated by equating equations (2.3.5) and (2.3.6) in equilibrium to give

$$Q \approx 4.5 \times 10^{37}\,{\rm g\,cm^2}\left(\frac{\dot{M}}{10^{-9}{\rm M}_{\odot}{\rm yr}^{-1}}\right)^{\frac{1}{2}}\left(\frac{300\,{\rm Hz}}{\nu_{\rm s}}\right)^{\frac{5}{2}}. \tag{2.3.7}$$

The idealised moment of inertia I of a spherically symmetric, constant density, neutron star is

$$I = \frac{2}{5}MR^2. \tag{2.3.8}$$

For a neutron star with $M = 1.4\,{\rm M}_{\odot}$ and $R = 10$km, the moment of inertia is calculated to be $I \approx 10^{45}$g cm^2. By dividing the quadrupole moment by the moment of inertia, an

approximation of the mass asymmetry generated by electron captures is made as

$$\frac{\Delta M}{M} \approx \frac{Q}{I} \approx \frac{10^{37}}{10^{45}} \approx 10^{-8}. \tag{2.3.9}$$

The result computed in equation (2.3.9) is the about an order of magnitude smaller than the value calculated by Bildsten as shown in equation (2.3.3). This suggests that the gravitational waves created by the asymmetric quadrupole moment, sufficient to counteract the spin-up torque from accretion, if a large enough temperature asymmetry exists.

2.3.2 Thermal timescales

Bildsten (1998) estimated how long it would take for heat to be conducted around the accreted neutron star crust, to give an indication of the thermal timescales that temperature asymmetries can exist for in the crust.

From the heat conduction equation, the time taken for heat to be conducted through a distance H can be calculated. The heat conduction equation is

$$\frac{\partial T}{\partial t} = \frac{K}{C_{\mathrm{p}}\rho}\frac{\partial^2 T}{\partial x^2}, \tag{2.3.10}$$

where C_{p} is the specific heat capacity per unit mass. The thermal conductivity K is written as

$$K = \frac{\pi^2 k_{\mathrm{B}}^2 T n_{\mathrm{e}} c^2}{3 E_{\mathrm{F}} \nu_{\mathrm{ep}}}, \tag{2.3.11}$$

where k_{B} is the Boltzmann constant, n_{e} is electron number density and ν_{ep} is the electron-phonon scattering frequency. Using the approximations

$$t_{\mathrm{th}} \approx \frac{T}{\dot{T}}, \tag{2.3.12}$$

$$\frac{\partial^2 T}{\partial x^2} \approx \frac{T}{H^2}, \tag{2.3.13}$$

the thermal timescale t_{th} is determined to be

$$t_{\mathrm{th}} \approx \frac{\rho C_p H^2}{K}. \tag{2.3.14}$$

The distance H can be defined as the scale height. This is the distance through which the pressure-density gradient changes by a factor of 2. Similarly, the time to transport heat around the star at the same depth is

$$t_{\mathrm{th,R}} \approx \frac{\rho C_p R^2}{K}. \tag{2.3.15}$$

Comparing the thermal timescales shown in equations (2.3.14) and (2.3.15), for a neutron star with a radius of 10km and a crust 1km thick, $H^2/R^2 \sim 0.01$. These timescales show the time taken to transport heat around the crust is greater than the time taken to locally heat it. This suggest that large temperature asymmetries exist as long as the neutron star is actively accreting in an asymmetric way.

2.4 Composition and temperature asymmetries in accreting neutron stars

Ushomirsky et al. (2000) built upon the work by Bildsten (1998) by calculating the temperature asymmetries in an accreting neutron star crust, assuming some asymmetry in either the nuclear heating rate or the composition of the crust. They investigated how long these asymmetries would be maintained for by thermal flow throughout the crust and core. They also investigated how large a mass quadrupole the crust could elastically sustain.

Composition asymmetries exist due to non-axisymmetric nuclear burning in X-ray bursts. Different elements have different charge to mass ratios giving rise to different thermal conductivities. This variation in thermal conductivity can lead to temperature asymmetries. Temperature asymmetries can also arise from variations in nuclear heating. In the deep crust nuclear reactions release heat energy. The amount of energy released depends on the elements present. In this section the treatment of Ushomirsky et al. (2000) is adopted.

Composition variations in the crust create local fluctuations in the amount of energy released due to nuclear reactions. This asymmetry in nuclear energy release is given as

$$f_{\rm nuc} = \frac{\delta\epsilon_{\rm nuc}}{\epsilon_{\rm nuc}}, \tag{2.4.1}$$

where $\epsilon_{\rm nuc}$ is the local energy deposited by nuclear reactions and an asymmetry is present when $f_{\rm nuc} \neq 0$.

The burning of different atomic masses from different points on the star creates charge-to-mass ratio (Z^2/A) variations. This affects both the thermal conductivity K and neutrino emissivity ϵ_ν of the crust and are functions of Z^2/A as follows: $K \propto (Z^2/A)^{-1}\rho T^{n_{\rm k}}$ (Schatz et al., 1999) and $\epsilon_\nu \propto (Z^2/A)\rho T^{n_{\rm e}}$ (Haensel et al., 1996) where $n_{\rm k}$ and $n_{\rm e}$ are the temperature sensitivity coefficients of conduction and neutrino emission respectively. The asymmetry in conductivity due to the composition asymmetries is written as

$$f_{\rm comp} = \frac{\delta(Z^2/A)}{(Z^2/A)}. \tag{2.4.2}$$

Regions where $f_{\rm comp} > 0$ radiate neutrinos more efficiently and the thermal conductivity decreases.

The lateral temperature variation δT can be calculated from both $f_{\rm nuc}$ and $f_{\rm comp}$. On a spherically symmetric background, the core is approximated to an isothermal perfect conductor. This assumption is valid as the thermal conductivity of the core is significantly higher than the crust, and consequently $\delta T_{\rm core} << \delta T_{\rm crust}$. The conductivity perturbation and the neutrino emissivity perturbation equations are

$$\frac{\delta K}{K} = -f_{\rm comp} + n_k \frac{\delta T}{T} \qquad \text{and} \qquad \frac{\delta \epsilon_\nu}{\epsilon_\nu} = f_{\rm comp} + n_e \frac{\delta T}{T}. \tag{2.4.3}$$

when $\delta \rho = 0$.

Local changes in ϵ_ν occur on scales smaller than the complete capture layer shifts. This does not affect the total energy released in a capture layer, as this is dependent solely on the local accretion rate and the total energy released per nucleon $E_{\rm nuc}$ of the element.

The charge to mass ratio varies with density in the neutron star crust. Capture layers where $f_{\rm comp} > 0$ will have larger temperature asymmetries because the thermal conductivity decreases, enabling temperature gradients to exist on longer timescales. This suggests that regions in the crust where $f_{\rm comp}$ is at a maximum will produce the largest mass quadrupole moments through electron capture.

Ushomirsky et al. (2000) incite asymmetries into the accreted neutron star crust through asymmetric nuclear heating $f_{\rm nuc}$ and composition $f_{\rm comp}$. There is no obvious way of deciding what composition asymmetries might exist in the crust. One could try modelling an asymmetric process, following the asymmetric motion of fluid elements through the crust. But this is a difficult calculation. We therefore decided to look at a simpler source of asymmetry, the anisotropy in thermal conductivity due to a magnetic field, where the necessary formalism already exists.

2.5 Elastic crust

The elasticity of the crust must be understood in order to calculate how large a mountain the crust can support without cracking. In this section we summarise the treatment of (Ushomirsky et al., 2000). This model is for a non-rotating neutron star. For gravitational waves to be produced it is a requirement that the neutron star is rotating, inclusion of the rotational effects would modify the solution of order $(\nu_{\rm s}/\nu_{\rm b})^2 \sim 4\%$ where $\nu_{\rm s} \approx 300$Hz is the neutron star spin frequency and $\nu_{\rm b} \gtrsim 1$ kHz is the break up frequency of the neutron star (Paul D. Lasky, 2015).

The crust is modelled as an elastic solid with shear modulus μ and an equation of state that is purely a function of density ρ and the electron mean molecular weight $\mu_{\rm e}$ where $p = p(\rho, \mu_{\rm e})$. The perturbed electron mean molecular weight only has non-zero values inside the capture layers. As the capture layers move around, due to the perturbing temperature source, the value of $\mu_{\rm e}$ is altered. It is this temperature dependence of $\mu_{\rm e}$ that influences the equation state.

2.5.1 The perturbed crust

The pressure created by the downward flow of accreted matter is neglected as this is negligible when compared to the gravitational and shear forces. The crustal displacement vector is defined in terms of spherical harmonics and its radial ξ_r and perpendicular $\xi_\perp$ components as

$$\xi^a \equiv \xi_r(r) Y_{lm} \hat{r}^a + \xi_\perp \beta^{-1} r \nabla^a Y_{lm}, \tag{2.5.1}$$

where $\hat{r}^a$ is the radial unit vector and $\beta \equiv \sqrt{l(l+1)}$.

The stress tensor of the crust in the Newtonian limit is given by Landau et al. (1986) as

$$\boldsymbol{\tau}_{ab} = -p(\rho, \mu_e)\boldsymbol{g}_{ab} + \mu(\nabla_a \xi_b + \nabla_b \xi_a - \frac{2}{3}\boldsymbol{g}_{ab}\nabla^c \xi_c), \tag{2.5.2}$$

where $\boldsymbol{g}_{ab}$ is the flat 3-metric, ∇_a is the associated derivative operator and μ is the shear modulus.

The stress tensor is perturbed to first order on a spherically symmetric background. Eulerian perturbations are denoted with δ and Lagrangian are represented with Δ. The Eulerian and Lagrangian perturbations relate to the scalar quantity Λ as

$$\Delta\Lambda = \delta\Lambda + \xi^a \nabla_a \Lambda. \tag{2.5.3}$$

The perturbing source terms arises from either the composition perturbation $\Delta\mu_{\rm e}/\mu_{\rm e}$ or temperature asymmetries δT as detailed in section 2.4. The Lagrangian pressure perturbations that emerge as a result of these variations are defined as: for a smooth composition gradient

$$\Delta p = \left.\frac{\partial p}{\partial \rho}\right|_{\mu_{\rm e}} \Delta\rho + \left.\frac{\partial p}{\partial \mu_{\rm e}}\right|_{\rho} \Delta\mu_{\rm e}, \tag{2.5.4}$$

for a temperature perturbation

$$\Delta p = \left.\frac{\partial p}{\partial \rho}\right|_T \Delta\rho + \left.\frac{\partial p}{\partial T}\right|_\rho \Delta T,$$
$$\Delta p = \left.\frac{\partial p}{\partial \rho}\right|_T \Delta\rho + \left.\frac{\partial p}{\partial T}\right|_\rho \left(\delta T + \xi_r \frac{dT}{dr}\right). \tag{2.5.5}$$

The scalar Eulerian and Lagrangian perturbations are proportional to the spherical harmonics Y_{lm}, due to the spherically symmetric background. The source terms can be represented in terms of their spherical harmonics as

$$\Delta\mu_e = \Delta\mu_e(r) Y_{lm}(\theta,\ \phi), \tag{2.5.6a}$$
$$\delta T = \delta T(r) Y_{lm}(\theta,\ \phi). \tag{2.5.6b}$$

The stress tensor is perturbed to give

$$\delta\tau_{ab} = \boldsymbol{g}_{ab} Y_{lm} \delta\tau_{rr} + \boldsymbol{e}_{ab} Y_{lm} [2\mu(\xi_r/r - \partial_r \xi_r)] + \boldsymbol{f}_{ab} \delta\tau_{r\perp} + \Lambda_{ab} 2\mu\beta\xi_\perp/r, \tag{2.5.7}$$

where

$$\delta\tau_{rr} = -\delta p + \mu\left(\frac{4}{3}\delta_r\xi_r - \frac{4}{3}\xi_r/r + \frac{2}{3}\beta\xi_\perp/r\right), \tag{2.5.8a}$$
$$\delta\tau_{r\perp} = \mu(r\delta_r(\xi_\perp/r) + \beta\xi_r/r), \tag{2.5.8b}$$

and

$$\boldsymbol{e}_{ab} \equiv \boldsymbol{g}_{ab} - \hat{r}_a \hat{r}_b, \tag{2.5.9a}$$
$$\boldsymbol{f}_{ab} \equiv \beta^{-1} r(\hat{r}_a \nabla_b Y_{lm} + \hat{r}_b \nabla_a Y_{lm}), \tag{2.5.9b}$$
$$\Lambda_{ab} \equiv \beta^{-2} r^2 \nabla_a \nabla_b Y_{lm} + \beta^{-1} \boldsymbol{f}_{ab}. \tag{2.5.9c}$$

The density perturbation in the crust is derived from the momentum equation as follows

$$\rho \frac{dv_a}{dt} = \nabla^b \tau_{ab} - \rho \nabla_a \Phi. \tag{2.5.10}$$

Setting the acceleration term to zero in the momentum equation

$$\nabla^a \tau_{ab} = \rho \nabla_b \Phi. \tag{2.5.11}$$

Perturbing the stress-energy tensor, using the Cowling approximation ($\rho\nabla^b\delta\Phi = 0$) and equating the remaining terms gives

$$\nabla^a \delta\tau_{ab} = \delta\rho \nabla_b \Phi = \delta\rho g \hat{r}_b, \tag{2.5.12}$$

where $g(r) \equiv GM_r/r^2$ is the local gravitational acceleration of the background model and $\delta\rho$ is the Eulerian density perturbation calculated from the continuity equation as

$$\delta\rho = -\nabla^a(\rho\xi_a) = -\left[\frac{1}{r^2}\frac{\partial}{\partial r}(r^2\rho\xi_r) - \rho\beta\frac{\xi_\perp}{r}\right]Y_{lm}. \tag{2.5.13}$$

The Eulerian pressure perturbation $\delta p = \Delta p + \rho g\xi_r$ as shown in equation (2.5.8a) is derived from equation (2.5.4) or (2.5.5) depending on the perturbing source term. Equation (2.5.13) describes the density perturbation the elastic crust can sustain on a spherically symmetric background. From this Ushomirsky et al. (2000) found a neutron star with $M = 1.4\mathrm{M}_\odot$, $R = 10$km could sustain a maximum quadrupole moment of $Q_{22} \approx 10^{38}$ g cm^2, for a breaking strain of 10^{-2}, in the crust. The quadrupole moment required to balance the spin up torque from accretion for such a star was calculated in Bildsten (1998) to be $Q_{22} \approx 4.5 \times 10^{37}\,\mathrm{g\,cm^2}$. This result confirms the initial back of the envelope calculation shown in equation (2.3.7) that the crust is able to elastically sustain a quadrupole moment sufficiently large to halt accretion spin-up, by radiating gravitational wave energy, without cracking. A calculation of how large a compositional asymmetry, or temperature asymmetry, can develop is clearly required. In later chapters, we will compute how large a temperature asymmetry is obtained if an internal magnetic field makes the thermal conductivity anisotropic.

Ushomirsky et al. (2000) find a temperature perturbation ratio $\delta T/T \sim 1\%$ would generate a sufficiently large quadrupole moment of $Q_{22} \sim 2 \times 10^{-37}$ per capture layer. Approximating this value over several capture layers and dividing by the moment of inertia, a parametrised formula of the ellipticity ϵ of the neutron star crust can written as

$$\epsilon = \frac{Q_{22}}{I} \approx 5 \times 10^{-8}\left(\frac{\delta T/T}{1\%}\right). \tag{2.5.14}$$

In later chapters, we will use this formula to provide an estimate of the mountain size produced by the temperature asymmetries calculated from our original work. The value of $\delta T/T$ will be taken at $\rho = 1 \times 10^{12}$ g cm^{-3}, as Ushomirsky et al. (2000) find the higher density inner crust is the part that contributes the most to the quadrupole moment, with the temperature perturbation peaking at approximately this density.

2.6 Thermoresistive instabilities

An alternative method of how temperature asymmetries may arise in a neutron star's crust is through thermoresistive instabilities. This idea is completely different to the work of Bildsten (1998), and although we have chosen not to go down this path, it is included here as an illustration of a completely different way of potentially generating neutron star mountains.

Thermoresistive instabilities is an effect that arises due to the magnetic field of a neutron star. Unlike the previous considerations, for these instabilities to arise the neutron star itself does not need to be in an accreting system. The information in this section has been taken from Price et al. (2012) where magnetars are discussed.

Magnetars are highly magnetic neutron stars ($B \approx 10^{15}\mathrm{G}$) (Duncan and Thompson, 1992). Their magnetic fields are constantly evolving due to Ohmic heating, ambipolar diffusion and Hall drift effects. Ohmic heating is the loss of electrical energy as heat due to resistance. Ambipolar diffusion arises due to the motion of electrons and the magnetic field relative to the ions present in the crust. The Hall effect is a consequence of the magnetic field displacing electrons such that an electric field develops perpendicular to the direction of current flow.

The magnetic fields in magnetars have both toroidal and poloidal components. High currents in the outer crust generate the toroidal element of the magnetic field which leads to Ohmic heating. As the current decays, a heating layer forms, giving rise to high surface temperatures. This process accounts for the observed trend of increasing surface temperature with increasing magnetic field strength in neutron stars with $B \approx 10^{13}\mathrm{G}$ (Pons and Geppert, 2007). The current decay process is determined by the electron-phonon interactions in the outer crust at temperatures below the crustal melting temperature. The magnetic diffusivity varies with temperature. A small increase in temperature leads to an increase in Ohmic heating, which in turn leads to an increase in resistivity. If the thermal conductivity is low, a temperature runaway effect may occur.

2.6.1 Magnetic field evolution

From magnetohydrodynamics the ohmic decay timescale can be deduced. The magnetohydrodynamic equation is

$$\rho \frac{d\boldsymbol{v}}{dt} = -\nabla p - \rho \nabla \Phi + \frac{1}{c}\boldsymbol{J} \times \boldsymbol{B}, \tag{2.6.1}$$

where ρ is the density, $\boldsymbol{v}$ is the velocity, p is the pressure, Φ is the gravitational potential, c is the speed of light, $\boldsymbol{J}$ is the current density and $\boldsymbol{B}$ is the magnetic field. From Maxwell's equations and Ohm's law, the magnetic field evolution can be described by the Ohmic decay, ambipolar diffusion and Hall effect contributions as

$$\frac{\partial \boldsymbol{B}}{\partial t} = -c\boldsymbol{\nabla} \times \left(\frac{\boldsymbol{J}}{\sigma} - \frac{\boldsymbol{v}}{c} \times \boldsymbol{B} + \frac{1}{cn_{\mathrm{e}}e}\boldsymbol{J} \times \boldsymbol{B} \right), \tag{2.6.2}$$

where σ is the electrical conductivity, n_{e} is electron number density and e is the charge of an electron. The first term on the right hand side in equation (2.6.2) describes the Ohmic decay in the magnetic field evolution. Using this Ohmic decay term, along with

the timescale approximation $\tau \approx \frac{\boldsymbol{B}}{\partial \boldsymbol{B}/\partial t}$, the Ohmic timescale at $T \approx 10^8$K is

$$\tau_{\rm ohm} = L^2 \eta^{-1}, \tag{2.6.3}$$

$$= 3 \times 10^5 \left(\frac{L}{1\,{\rm km}}\right)^2 \left(\frac{\eta}{10^{-3}\,{\rm cm}^2\,{\rm s}^{-1}}\right)^{-1} {\rm yr}, \tag{2.6.4}$$

where L is the typical magnetic field length-scale and $\eta = c^2/(4\pi\sigma)$ is the magnetic diffusivity Price et al. (2012).

The neutron star crust is modelled as an infinite slab, with x pointing into the star as shown in Fig. 2.6.1.

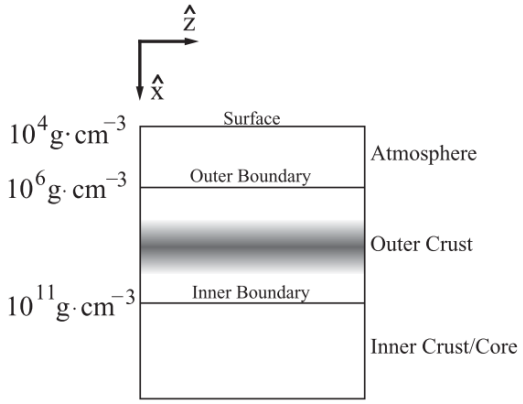

Figure 2.6.1: Schematic diagram of the neutron star model where the shaded area represents the region undergoing Ohmic heating reproduced from Price et al. (2012).

The thermal evolution of the outer crust is described as

$$c_\nu(\rho,T)\frac{\partial T(x)}{\partial t} = \frac{4\pi\eta(\rho,T)}{c^2}J^2 + \nabla\cdot[K(\rho,T)\nabla T(x)] - Q_\nu(\rho,T), \tag{2.6.5}$$

where ρ is the density, c_ν is the specific heat capacity, Q_ν is the neutrino emissivity and K is the thermal conductivity. The first term on the right hand side of equation (2.6.5) is the heat contribution from Ohmic heating. More specifically, the square of the electrical current J arises from the relationship between current and electric field along with Joule heating per unit volume as

$$\boldsymbol{J}(x) = \sigma \boldsymbol{E}, \tag{2.6.6}$$

$$\boldsymbol{J}\cdot\boldsymbol{E} = \frac{J^2}{\sigma}. \tag{2.6.7}$$

The magnetic field evolution as computed from the induction equation and Ohm's law is

$$\frac{\partial \boldsymbol{B}(x)}{\partial t} = -\nabla\times[\eta(\rho,T)\nabla\times\boldsymbol{B}(x)], \tag{2.6.8}$$

where the magnetic field is related to the current by

$$\boldsymbol{J}(\boldsymbol{x}) = \frac{c}{4\pi}\nabla \times \boldsymbol{B}(x). \tag{2.6.9}$$

2.6.2 Thermal instability

Price et al. (2012) analysed the stability of the system by adding a temperature perturbation

$$T(t) = T_0 + \delta T e^{\gamma t}, \tag{2.6.10}$$

to the heat diffusion equation (2.6.5), where δT is the perturbation and γ is the growth decay rate. The heat diffusion equation becomes

$$\frac{\partial^2 \delta T}{\partial x^2} = \frac{1}{K}\left[c_\nu \gamma - \frac{4\pi}{c^2}\eta' J_0^2 - \frac{\partial K'}{\partial x}\frac{\partial T_0}{\partial x} - K'\frac{\partial^2 T_0}{\partial x^2}\right]\delta T - \frac{1}{K}\left[\frac{\partial K_0}{\partial x} + K'\frac{\partial T_0}{\partial x}\right]\frac{\partial \delta T}{\partial x}, \tag{2.6.11}$$

where prime indicates differentiation with respect to T at fixed x.

The perturbed boundary conditions were found by Price et al. (2012) by integrating through the atmosphere for several values of the unperturbed stellar surface temperature. There is no Ohmic heating in the atmosphere and no explicit allowances for the heat blanket. This creates uniquely defined values for a given surface temperature at the outer boundary as $T_{\rm ob}$ and the temperature gradient as $dT_{\rm ob}/dx$. The temperature gradient is a function of the outer boundary temperature as

$$\frac{dT_{\rm ob}}{dx} = f(T_{\rm ob}). \tag{2.6.12}$$

By differentiating this equation with respect to $T_{\rm ob}$, the outer boundary condition is

$$f'(T_{\rm ob}) = \frac{d}{dT_{\rm ob}}\left(\frac{dT_{\rm ob}}{dx}\right). \tag{2.6.13}$$

The boundary at the crust-core interface $T_{\rm ib}$ is assumed to be an infinite heat reservoir where $\delta T_{\rm ib} = 0$ (Price et al., 2012).

By numerical experiment, an instability was found. To see how γ scales with the parameters of the problem Price et al. (2012) computed an approximate analytical expression. The dominant terms in the perturbed heat equation (2.6.11) was found to be

$$\frac{\partial^2 \delta T}{\partial x^2} = \frac{1}{K}\left[c_\nu \gamma - \frac{4\pi}{c^2}\eta' J_0^2\right]\delta T. \tag{2.6.14}$$

Using a plane wave to describe the heat flow, $\delta T = A \exp i(kx - \omega t)$, and setting $K = \frac{1}{L}$

an approximate expression for the instability growth rate evaluated at the heating peak was established by (Price et al., 2012) as

$$\gamma \approx \frac{1}{c_\nu}\left[\frac{4\pi}{c^2}\eta'_{\rm p}J^2_{\rm p} - \frac{K_{\rm p}}{L^2}\right], \tag{2.6.15}$$

where the index 'p' indicates parameters evaluated at heating peak.

Price et al. (2012) found that the instability growth rate was affected by a change in surface temperature, as this alters the heating location. If the crust temperature exceeds the melting point the system begins to stabilise as the magnetic diffusivity becomes negligible and heating feedback is lost. For a fixed current density, larger values of L correspond to larger magnetic fields. The instability growth rate is highly dependent on the heating location due to the spatial variation of the thermal conductivity and magnetic diffusivity. Instabilities are most likely to develop in regions of low thermal conductivity, as the heat is not easily dissipated. The minimum magnetic field required to destabilise the crust is $3 \times 10^{15}\mathrm{G}$. The instabilities arise closer to the neutron star's surface.

An investigation into whether a similar mechanism arises in low mass X-ray binaries would provide an alternative strategy to grow mountains. Thermoresistive instabilities could provide the temperature asymmetry required to generate a mass quadrupole moment sufficiently large to prevent a neutron star's spin frequency from increasing. Although the high magnetic field strength required for such an effect, as found by Price et al. (2012) is discouraging.

CHAPTER 3

Modelling the thermal profile of a uniform density neutron star crust

From Bildsten's initial back of the envelope calculations, a more in depth analysis was performed by Ushomirsky et al. (2000). In the paper Ushomirsky et al. (2000) investigated how large a quadrupole moment the crust could elastically sustain. The authors found the crust could maintain a mass quadrupole moment of $Q_{22} \approx 1.2 \times 10^{38}$ g cm^2 before cracking. Bildsten calculated the mass quadrupole moment required, to generate gravitational waves with enough angular momentum to balance the spin-up torque from accretion, to be $Q_{22} \approx 4.5 \times 10^{37}$g cm^2. Bildsten's mass quadrupole estimate lies well within the bounds of the maximum quadrupole moment that can be sustained by an accreted neutron star crust. This result suggests a deeper investigation into how large a mass quadrupole moment can develop in a neutron star crust is required.

The work in this chapter builds on that done by Bildsten (1998) and Ushomirsky et al. (2000). Bildsten (1998) assumed the existence of a temperature asymmetry in an accreted neutron star crust. In this work, we will calculate the temperature asymmetry induced by the presence of a magnetic field for neutron star undergoing spherical accretion. A model of the thermal profile of a neutron star crust is developed in stages. A background model of the temperature distribution in a spherically symmetric neutron star is developed, which is then perturbed by the addition of a magnetic field.

In an accreted neutron star crust, there are many different microphysical processes at play. To build confidence in this model and to ensure it works accurately, a toy model is

initially constructed. The problem is simplified to an accreted neutron star crust of uniform density. Removing the density dependence of the variable parameters, will make the results easier to predict and determine if the model is producing reliable results.

In the first part of this chapter, a background model of a spherically symmetric, constant density, accreted neutron star crust is created. Accretion provides a heat source which deposits energy into the crust via nuclear reactions. Heat sinks arise from neutrino radiation and heat being conducted into and out of the crust. Using these inputs, an ordinary differential equation (ODE) is derived from the heat equation describing how the temperature varies within a spherically symmetric neutron star crust.

Later in the chapter, a magnetic field is inserted into the neutron star crust. The addition of a magnetic field may enable temperature asymmetries to develop. From the literature, Yakovlev and Urpin (1980), Geppert et al. (2004), Pons and Geppert (2007), Page et al. (2007) and Aguilera et al. (2008) show the temperature distribution in a magnetised neutron star crust is anisotropic. This anisotropy arises from the interaction of electrons with the magnetic field. Electrons are the predominant heat carriers in a neutron star crust. The thermal conductivity perpendicular to the direction of the magnetic field lines is reduced as shown in equation 3.4.5 (Aguilera et al., 2008). The significance of the effect the magnetic field has on the thermal conductivity of an accreted neutron star crust is investigated in this chapter, to see how the magnetic field perturbs the temperature distribution in an accreting neutron star crust.

The work in this chapter is for the simplified case of a uniform density crust. We select density parameters as: density $\rho = 1 \times 10^{12}$, proton number $Z = 16$, mass number $A = 56$, mass fraction of free neutrons $X = 0$, and the electron chemical potential $\mu_{\rm e} = 33.73$MeV. These density dependent values were obtained from Haensel and Zdunik (1990a). The outer and inner boundary of the crust are set for radii $r_{\rm OB} = 10$km and $r_{\rm IB} = 9$km respectively. This model was constructed in preparation for a non-uniform realistic equation of state calculation, which is detailed in chapter 4.

3.1 Heat flux distribution in an accreted neutron star crust

To investigate the temperature distribution in a neutron star crust a background profile of the radial heat flux must first be developed. The thermal profile of a spherically symmetric neutron star crust, with heat input from electron captures arising from accreted material, is modelled from the heat equation. The heat equation is

$$\rho C_p \frac{\partial T}{\partial t} = -\boldsymbol{\nabla} \cdot \boldsymbol{F} + \dot{Q}, \tag{3.1.1}$$

where ρ is the mass density, C_p is the specific heat capacity at constant pressure, T is temperature, F is the heat flux and $\dot{Q}$ is the net rate of production of heat per unit time. The heat equation can be simplified by considering the static solution in terms of the heat flux. From Fourier's law

$$\boldsymbol{F} = -K\boldsymbol{\nabla}T, \tag{3.1.2}$$

where K is the thermal conductivity. The divergence of the flux is computed as

$$\boldsymbol{\nabla}\cdot\boldsymbol{F} = -\boldsymbol{\nabla}K\cdot\boldsymbol{\nabla}T - K\nabla^2 T. \tag{3.1.3}$$

How the heat varies with radius within the crust is described by exploiting the spherical symmetry of the divergence of the flux (equation (3.1.3)), this can be expressed in spherical polar coordinates as

$$\boldsymbol{\nabla}\cdot\boldsymbol{F} = -\frac{dK}{dr}\frac{dT}{dr} - K\frac{1}{r^2}\frac{d}{dr}\left(r^2\frac{dT}{dr}\right), \tag{3.1.4}$$

where r is the spatial coordinate in the radial direction. From equation (3.1.2), Ushomirsky et al. (2000) write the time-independent divergence of the flux as

$$\begin{aligned}\boldsymbol{\nabla}\cdot\boldsymbol{F} &= \dot{Q}\\ &= \rho\left(\epsilon_{\mathrm{nuc}} - \epsilon_\nu\right),\end{aligned} \tag{3.1.5}$$

where ρ is the density, ϵ_{nuc} is the local energy deposited per unit mass per unit time by nuclear reactions and ϵ_ν is the neutrino energy production per unit mass per unit time.

Combining equations (3.1.4) and (3.1.5), an expression for the heat distribution in the crust, including the heat source and sink terms, can be written as

$$\rho\left(\epsilon_{\mathrm{nuc}} - \epsilon_\nu\right) = -\frac{dK}{dr}\frac{dT}{dr} - K\frac{1}{r^2}\frac{d}{dr}\left(r^2\frac{dT}{dr}\right). \tag{3.1.6}$$

Integrating equation (3.1.6) will produce a description of how the temperature within the crust varies with radius.

3.1.1 Thermal conductivity

The thermal conductivity is a temperature dependent quantity that is governed by the heat transport mechanisms present in the neutron star crust: electrons K_{e}, neutrons K_{n}, protons K_{p} and phonons K_{ph} (Aguilera et al., 2008). The scalar thermal conductivity can be written as a linear combination of these heat transport processes as

$$K = K_{\mathrm{e}} + K_{\mathrm{n}} + K_{\mathrm{p}} + K_{\mathrm{ph}}. \tag{3.1.7}$$

In the crust, electrons are the dominant heat transport mechanism (Aguilera et al., 2008) and the only contribution that will be considered from now on, such that $K = K_{\rm e}$.

From Yakovlev and Urpin (1980) the thermal conductivity is a function of temperature and can be written as

$$K = \frac{\pi^2 k_{\rm B}^2 T n_{\rm e}}{3 m_{\rm e}^*} \tau(T), \tag{3.1.8}$$

where $k_{\rm B}$ is the Boltzmann constant, $\tau(T) = \frac{1}{\nu}$ is the relaxation time and ν is the scattering frequency arising from interactions between electrons and other particles or excitations. $n_{\rm e}$ is the electron number density, defined as the number of electrons per unit volume and is written as

$$n_e = n_b \frac{Z}{A}(1 - X_n), \tag{3.1.9}$$

where Z is the proton number, A is the mass number and X_n is the fraction of free neutrons. The electron effective mass $m_{\rm e}^*$ is derived from the mass-energy equivalence principle to accommodate the degenerate, relativistic nature of the electrons in the crust such that

$$m_{\rm e}^* = \left(m^2 + \frac{p_{\rm F}^2}{c^2} \right)^{\frac{1}{2}}, \tag{3.1.10}$$

where m is the electron rest mass, c is the speed of light and $p_{\rm F}$ is the Fermi momentum. For a degenerate electron gas, the Fermi momentum is given by

$$p_{\rm F} = \hbar (3\pi^2 n_{\rm e})^{\frac{1}{3}}, \tag{3.1.11}$$

where $\hbar$ is the reduced Planck constant (Yakovlev and Urpin, 1980). The Fermi momentum can be written in terms of density using the electron mean molecular weight $\mu_{\rm e} = A/Z$. The Fermi momentum written as a function of ρ is

$$p_{\rm F} = \hbar \left(\frac{3\pi^2 \rho}{\mu_{\rm e} m_{\rm b}} \right)^{\frac{1}{3}}, \tag{3.1.12}$$

where $m_{\rm b}$ is the baryon mass. Combining equations (3.1.10) and (3.1.12) gives the electron effective mass as

$$\begin{aligned} m_{\rm e}^* &= \left(m^2 + \frac{\hbar}{c^2} \left(\frac{3\pi^2 \rho}{\mu_{\rm e} m_{\rm b}} \right)^{\frac{2}{3}} \right)^{\frac{1}{2}}, \\ m_{\rm e}^* &\approx 9.16 \times 10^{-26} \left(\frac{\rho_{12} Z}{A} \right)^{\frac{1}{3}}, \\ \frac{m_{\rm e}^*}{m_{\rm e}} &\approx 100 \left(\frac{\rho_{12} Z}{A} \right)^{\frac{1}{3}}, \end{aligned} \tag{3.1.13}$$

where

$$m^2 \ll \frac{\hbar}{c^2}\left(\frac{3\pi^2\rho}{\mu_{\rm e} m_{\rm b}}\right)^{\frac{2}{3}}. \tag{3.1.14}$$

The ratio $\frac{m_{\rm e}^*}{m_{\rm e}}$ shows how much larger $m_{\rm e}^*$ is than $m_{\rm e}$ due to relativistic effects.

3.1.2 Electron scattering frequency and relaxation time

The thermal conductivity of a neutron star crust is a function of relaxation time $\tau(T) = \frac{1}{\nu}$, arising from the interactions of electrons with other particles or excitations. In the literature, there does not appear to be standard agreement on the dominant scattering processes that occur in an accreted neutron star crust. This gives rise to a range of relaxation timescales in the thermal conductivity. Bildsten (1998) uses electron-phonon interaction as the dominant scattering frequency. Ushomirsky et al. (2000) use a linear combination of the electron-ion and electron-electron contributions for the scattering frequency. More recent publications including: Geppert et al. (2004), Page et al. (2007), Aguilera et al. (2008) and Brown and Cumming (2009) use a formalism from Yakovlev and Urpin (1980) that characterises the solid outer crust as being dominated by electron-phonon scattering and the inner crust as having electron-impurity scattering as the dominant mechanisms. The formalism used here is that given by Yakovlev and Urpin (1980), as this is the most commonly used formalism in the literature.

Following the formalism from Yakovlev and Urpin (1980) and Brown and Cumming (2009) the scattering frequency ν in the neutron star crust will be written as

$$\nu = \nu_{\rm ep} + \nu_{\rm eQ}, \tag{3.1.15}$$

where $\nu_{\rm ep}$ and $\nu_{\rm eQ}$ are the electron-phonon and electron-impurity scattering frequencies respectively. Electron-phonon scattering is temperature dependent as

$$\begin{aligned}\nu_{\rm ep} &= \frac{13 e^2 k_{\rm B} T}{\hbar^2 c}, \\ &\approx 1.25 \times 10^{18} T_8 \text{ Hz}.\end{aligned} \tag{3.1.16}$$

Going deeper into the crust, as the density increases, electron-impurity scattering becomes more important in mediating the thermal transport. Electron-impurity scattering is a function of impurity parameter, a dimensionless number that indicates how crystalline $Q_{imp} \ll 1$ or disordered $Q_{imp} \gg 1$ the neutron star crust is (Pons et al., 2013). The impurity parameter measures the distribution of nuclide charge numbers for i species and is defined as

$$Q_{\rm imp} \equiv n_{\rm ion}^{-1} \sum_i n_{\rm i}(Z_{\rm i} - \langle Z \rangle)^2, \tag{3.1.17}$$

where $n_{\rm ion}$ is the ion number density summed over all species. The electron-impurity scattering is written as

$$\nu_{\rm eQ} = \frac{4\pi Q_{\rm imp} e^4 n_{\rm ion}}{p_{\rm F}^2 v_{\rm F}} \Lambda_{\rm imp}. \tag{3.1.18}$$

where $\Lambda_{\rm imp} \sim 1$ is the coulomb logarithm (Brown and Cumming, 2009), and $v_{\rm F}$ is the Fermi velocity. Using the expression for the Fermi momentum as shown in equation in (3.1.12) and the relation

$$n_{\rm ion} = \frac{n_{\rm e}}{Z} = \frac{\rho}{\mu_{\rm e} m_{\rm b} Z}, \tag{3.1.19}$$

the electron-impurity scattering can be written as

$$\nu_{\rm eQ} = 1.77 \times 10^{18} \frac{Q_{\rm imp}}{Z} \left(\frac{\rho_{12}}{\mu_{\rm e}}\right)^{\frac{1}{3}} \text{Hz}, \tag{3.1.20}$$

From equation (3.1.15) the relationship between scattering frequency and relaxation time is given by Page et al. (2007) as

$$\tau(T) = \frac{1}{(\nu_{\rm ep} + \nu_{\rm eQ})}. \tag{3.1.21}$$

Figure 3.1.1 is a phase-space plot of the scattering frequency. This graph shows which scattering frequency regime dominates for different temperatures and impurity parameters, inside the accreted neutron star crust. For low temperatures and an impure crust (high $Q_{\rm imp}$) impurity scattering processes dominate. At high temperatures for a pure crust, electron-phonon scattering processes dominate. By setting the electron-phonon and electron-impurity scattering frequencies equal to one another, along with equations (3.1.16) and (3.1.20) a parametrised formula of the temperature as a function of impurity parameter can be written as

$$T = 1.42 \times 10^{8} \frac{Q_{\rm imp}}{Z} \left(\frac{\rho_{12}}{\mu_{\rm e}}\right)^{\frac{1}{3}} \text{K}. \tag{3.1.22}$$

To generate figure 3.1.1 the density dependent values were selected from Haensel and Zdunik (1990a) for $\rho = 1 \times 10^{12}$g cm^{-3} as $Z = 14$ and $\mu_{\rm e} = 33.73$ MeV. In this background model, both scattering regimes will be included, as it is unclear which scattering mechanism will dominate.

3.1.3 Heat source and sink terms

Heat is deposited into a neutron star crust via accretion. Some of this heat is conducted through the crust and into the core, and some heat is radiated away by neutrinos. The heat source and sink terms in the heat equation (3.1.6), are computed from the microphysical processes that take place in the crust. In this section, the energy deposited into

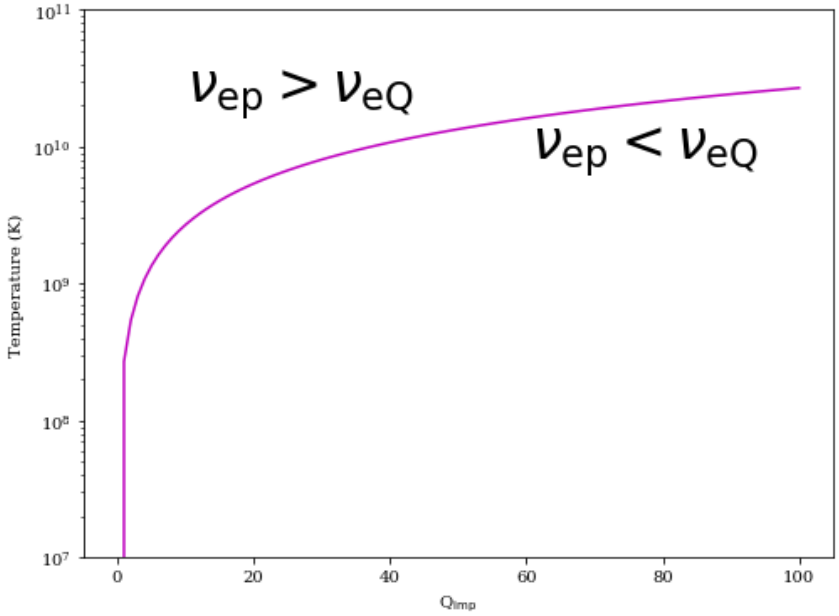

Figure 3.1.1: A phase-space plot to show which scattering frequency regimes dominate for different temperatures and impurity parameters for $\rho = 1 \times 10^{12}\mathrm{g\,cm^{-3}}$, $Z = 14$ and $\mu_\mathrm{e} = 33.73$ MeV. Electron-phonon scattering ν_ep dominates for high temperatures and low impurity parameter. Electron-impurity scattering ν_eQ dominates at low temperatures and high impurity parameter.

the crust by nuclear reactions along with the energy radiated out of the crust from neutrino production is computed.

The energy from accretion will be deposited only at transition layers. In this chapter, as we are considering a uniform density crust, the energy deposited will be smoothed over the whole crust, neglecting the transition layers. Later in chapter 4, the transition layers will be reinstated. The local energy generation rate, averaged over the crust, is calculated by dividing equation (2.2.1) by the volume of the crust. The energy released per unit volume per unit time in the crust is

$$\rho\epsilon_\mathrm{nuc} = \frac{3\dot{M}E_\mathrm{nuc}}{m_\mathrm{b}4\pi(R^3_\mathrm{outer} - R^3_\mathrm{inner})}, \tag{3.1.23}$$

where R_outer and R_inner are the outer and inner radii of the crust respectively and E_nuc is the total energy deposited per accreted nucleon.

The neutrino energy production rate by Haensel et al. (1996) is derived from electron $\nu\bar{\nu}$ bremsstrahlung and has value

$$\begin{aligned}\rho\epsilon_\nu &= \frac{8\pi G_\mathrm{F}^2 Z^2 e^4 C_+^2}{567\hbar^9 c^8}\left(k_\mathrm{B}T\right)^6 n_\mathrm{i} L, \\ &= 3.229 \times 10^{17}\rho_{12}T_9^6\frac{Z^2}{A}X_\mathrm{A}\ \mathrm{erg\,s^{-1}\,cm^{-3}},\end{aligned} \tag{3.1.24}$$

where $G_{\rm F} = 1.436 \times 10^{-49}\,{\rm erg\,cm^3}$ is the Fermi weak coupling constant, Z is the atomic charge, e is the charge of an electron, $C_+^2 \approx 1.675$ takes into account the generation of electron, mu and tau neutrinos, $n_{\rm i}$ is the number density of nuclei (ions), the dimensionless parameter $L \sim 1$ is a slowly varying function of density, temperature and nucleus parameters, $\hbar$ is the reduced Planck constant, c is the speed of light, A is the atomic mass and $X_{\rm A}$ is the mass fraction of nuclei with atomic mass A (Haensel et al., 1996).

Choosing parameter values for a typical point in a neutron star crust, equation (3.1.24) can be simplified further. For A=46, Z=14 (Haensel and Zdunik, 1990a), in the middle of the capture layer where $\rho_{12} = 1$ and the neutrino cooling rate is $\rho\epsilon_\nu = 1.93 \times 10^{18}\,{\rm T_9^6\,erg\,s^{-1}\,cm^{-3}}$. When considering a uniform star this expression for $\rho\epsilon_\nu$ can be re-written as a factor of temperature multiplied by a constant by employing these approximations as

$$\rho\epsilon_\nu = CT_9^6, \tag{3.1.25}$$

where $C = 3.229 \times 10^{17}\rho_{12}\frac{Z^2}{A}X_{\rm A}\ {\rm erg\,s^{-1}\,cm^{-3}}$ which is set to $C = 1.93 \times 10^{18}$ erg s^{-1} cm^{-3} for a uniform density neutron star crust.

3.1.4 Boundary conditions

The neutron star crust has an outer boundary where the crust meets the infalling accreted material and an inner boundary at the crust-core interface. The boundary conditions used follows those given by Ushomirsky et al. (2000). The outer boundary condition, at the surface of the crust, is set to the steady burning temperature of the hydrogen/helium layer on the surface of the star and the accretion rate as

$$T_{\rm burn} \approx 5.3 \times 10^8\,{\rm K}\left(\frac{\dot{m}}{\dot{m}_{\rm Edd}}\right)^{2/7}, \tag{3.1.26}$$

where $\dot{m}$ is the local accretion rate per unit time, $\dot{m}_{\rm Edd} \equiv 3.029 \times 10^{-9}{\rm M_\odot\ yr^{-1}}$ is the local Eddington accretion rate (Schatz et al., 1999).

To compute a value for the inner boundary (the crust-core interface) condition Ushomirsky et al. (2000) approximate a neutron star's core to be a perfect conductor, where all of the heat flux conducted into the core is radiated away as neutrinos. The neutrino luminosity of the core is then calculated from the modified Urca formula (Shapiro and Teukolsky, 1983, p.321). The luminosity of the core is written as

$$\begin{aligned} -F_{\rm inner}4\pi R_{\rm inner}^2 &= L_{\rm core} \\ &= 5.3 \times 10^{39}\,{\rm erg\,s^{-1}}\left(\frac{M}{\rm M_\odot}\right)\left(\frac{\rho_{\rm nuc}}{\rho}\right)^{1/3} T_9^8 \exp\left(-\frac{\Delta}{k_{\rm B}T}\right), \end{aligned} \tag{3.1.27}$$

where $F_{\rm inner}$ is the flux at the crust/core interface, $\rho_{\rm nuc}$ is the nuclear density, ρ is the uniform density of the star and Δ is the superfluid gap energy that is initially set to zero corresponding to a neutron star with a non-superfluid core.

Using equation (3.1.2) with (3.1.27) the temperature gradient at the crust-core boundary can be written as

$$\frac{dT}{dr} = \frac{L_{\rm core}}{4\pi K R_{\rm inner}^2}. \tag{3.1.28}$$

To build a thermal profile of the neutron star crust, using the outer and inner boundary conditions detailed in equations (3.1.26) and (3.1.28) respectively, the heat equation, along with the boundary conditions, must be solved by numerical integration.

3.1.5 Temperature distribution model

The thermal profile of a spherically symmetric, constant density, neutron star crust is constructed from the heat equation. Heat is deposited by nuclear reactions from accretion and radiated away via neutrino emission processes.

From equation (3.1.6), a second order ODE describing how the temperature varies with radius in an accreted neutron star crust is constructed as

$$\frac{d^2T}{dr^2} = -\frac{1}{K}\frac{dK}{dr}\frac{dT}{dr} - \frac{2}{r}\frac{dT}{dr} - \frac{\dot{Q}}{K}, \tag{3.1.29}$$

where $\dot{Q} = \rho\epsilon_{\rm nuc} - \rho\epsilon_{\nu}$.

The thermal conductivity from equation (3.1.8) can be re-written to show the temperature dependence more explicitly by using equation (3.1.15) as

$$K = C_{\rm K} T \frac{1}{C_{\rm ep}T + \nu_{\rm eQ}}, \tag{3.1.30}$$

where

$$C_{\rm K} = \frac{\pi^2 k_{\rm B}^2 n_{\rm e}}{3m_{\rm e}^*}, \tag{3.1.31}$$

and

$$C_{\rm ep} = \frac{13e^2 k_{\rm B}}{\hbar^2 c}. \tag{3.1.32}$$

From this expression for the thermal conductivity, the first order derivative of the thermal conductivity with respect to radius, for a constant density crust, can be written as

$$\frac{dK}{dr} = C_{\rm K}\left[\frac{1}{C_{\rm ep}T + \nu_{\rm eQ}}\frac{dT}{dr} - \frac{C_{\rm ep}T}{(C_{\rm ep}T + \nu_{\rm eQ})^2}\frac{dT}{dr}\right]. \tag{3.1.33}$$

The second order ODE shown in equation (3.1.29) becomes

$$\frac{d^2T}{dr^2} = -\frac{dT}{dr}\left[\frac{1}{T}\frac{dT}{dr} - \frac{1}{C_{\rm ep}T + \nu_{\rm eQ}}\left(C_{\rm ep}\frac{dT}{dr}\right)\right] - \frac{2}{r}\frac{dT}{dr} - \frac{\dot{Q}}{K}. \tag{3.1.34}$$

A static solution of the thermal profile of a spherically symmetric, uniform density neutron star crust will be computed by numerically solving the equation (3.1.34) for the outer and inner boundary conditions, detailed in equations (3.1.26) and (3.1.28) respectively, using the shooting method.

3.2 Numerical methods

The ODE shown in equation (3.1.29) is a boundary valued problem with the outer and inner boundary conditions set as defined in equations (3.1.26) and (3.1.28) respectively. Equation (3.1.34) is solved numerically using the shooting method. The shooting method reduces a boundary value problem to an initial value problem by 'shooting' trajectories until one is found that satisfies the appropriate boundary condition.

The shooting method was selected to solve the ODE as it is quick and adaptive. To test the accuracy of the results obtained using the shooting method, the ODE results will be checked using finite difference methods and convergence testing.

The function that solves the initial value problem requires the outer boundary values of both temperature $T_{\rm OB}$ and the first order temperature derivative with respect to radius $(\frac{dT}{dr})_{\rm OB}$. The temperature at the outer boundary is set to a known function of accretion rate as detailed in equation (3.1.26). The temperature derivative at the outer boundary is not predefined. A value of $(\frac{dT}{dr})_{\rm OB}$ is obtained using the shooting method.

The SciPy python function `scipy.optimize.brentq` is used to seek the root value of the shooting function. The trial root value is set as the outer boundary value of $(\frac{dT}{dr})_{\rm OB}$. With both the values of $T_{\rm OB}$ and $(\frac{dT}{dr})_{\rm OB}$ specified, the python function scipy.integrate.odeint is used to integrate the initial value function, which contains the second order ODE as shown in equation 3.1.34, to determine the successive values of T and $\frac{dT}{dr}$ into an array for decreasing r values from $R_{\rm outer}$ to $R_{\rm inner}$, moving from the crust to the core, the inner boundary. The value of T at the inner boundary from this array is then compared to the set boundary condition at the crust/core interface as shown in equation (3.1.28). If the values match then the computation is complete.

3.2.1 Non-dimensionalisation

The differential equation given in equation (3.1.29) will be solved using the shooting method written in Python. To enable the computation to be accurate and effective, the heat equation must be non-dimensionalised.

A simple method of non-dimensionalisation is to divide t, T and R in equation 3.1.29 by a typical timescale temperature and radius respectively to produce the following relations:

$$\begin{aligned} \hat{T} &= T/T_{\rm typ}, \\ \hat{t} &= t/t_{\rm typ}, \\ \hat{r} &= r/R_{\rm typ}, \end{aligned} \tag{3.2.1}$$

where '$\hat{}$' indicates the non-dimensionalised parameter. Time has been included in this calculation as it may be required in the future.

A common value of radius was selected to be the outer radius of a neutron star crust where $R_{\rm typ} = R_{\rm outer}$ such that $0.9 \leqslant \hat{r} \leqslant 1$.

A typical thermal timescale $t_{\rm typ}$ is determined by using equation (3.1.1), the approximations $\nabla^2 T \approx \frac{T}{R^2}$ and $\frac{T}{\dot{T}} \approx t_{\rm typ}$ to give

$$t_{\rm typ} \sim \frac{\rho C_{\rm p} R^2}{K}. \tag{3.2.2}$$

To determine a value for $T_{\rm typ}$ there are two different approaches that can be made. The first is to equate the nuclear heating and the neutrino cooling terms in the heat source as follows

$$\rho\epsilon_{\rm nuc} = \rho\epsilon_{\nu}, \tag{3.2.3}$$

using equation (3.2.3) and the the definitions for $\rho\epsilon_{\rm nuc}$ and $\rho\epsilon_{\nu}$ given in equations (3.1.23) and (3.1.24) respectively, a typical temperature value is calculated to be

$$T_{\rm typ1} = 1 \times 10^9 {\rm K} \left(\frac{\rho\epsilon_{\rm nuc}}{C}\right)^{\frac{1}{6}}, \tag{3.2.4}$$

where C is the factor multiplying T_9^6 in equation 3.1.25. A value for $T_{\rm typ1}$ can be calculated by setting $\rho\epsilon_{\rm nuc} = 35.3 \times 10^{16}$ cgs (for an accretion rate of $\dot{M} = 1 \times 10^{-9} {\rm M}_\odot$ yr^{-1}), $\rho = 1 \times 10^{12}$g cm^{-3}, $Z = 16$, $A = 56$ and $X_{\rm A} = 1$ and inserting these values into equation (3.2.4) as

$$T_{\rm typ1} = 5.48 \times 10^8 {\rm K}. \tag{3.2.5}$$

The second method equates the thermal conduction into the core with nuclear heating as follows

$$\rho\epsilon_{\rm nuc} = \frac{dK}{dr}\frac{dT}{dr} + K\left[\frac{2}{r}\frac{\partial T}{\partial r} + \frac{\partial^2 T}{\partial r^2}\right], \tag{3.2.6}$$

$$\approx \frac{KT}{R^2}, \tag{3.2.7}$$

rearranging to give

$$T_{\rm typ2} = \frac{\rho\epsilon_{\rm nuc}R^2}{K}. \tag{3.2.8}$$

For $\dot{M} = 1\times10^{-9}\mathrm{M}_\odot$ yr^{-1}, $T = 1\times10^8$ K and $R = 1\times10^6$ cm, typical values of the thermal conductivity and energy released in the crust per unit time were calculated to be $K = 2.5\times10^{19}$ erg s^{-1} cm^{-1} K^{-1} and $\rho\epsilon_{\rm nuc} = 5.34\times10^{16}$ cgs, respectively. Substituting these values into equation (3.2.8) gives

$$T_{\rm typ2} = 2.13\times10^9 \text{ K}. \tag{3.2.9}$$

$T_{\rm typ2}$ is one order of magnitude larger than $T_{\rm typ1}$. Initially is was unclear as to which $T_{\rm typ}$ would be the better choice. After testing the code for different outer boundary temperatures and accretion rates $T_{\rm typ2}$ was slightly better suited to numerical calculations as the dimensionless values were an order of magnitude smaller, but either choice would give sensible results.

Using the relations shown in equations (3.2.2) and (3.2.8), the heat equation given in equation (3.1.29) is non-dimensionalised and written as

$$\frac{\partial\hat{T}}{\partial\hat{t}} = \frac{1}{K}\frac{dK}{d\hat{r}}\frac{d\hat{T}}{d\hat{r}} + \frac{2}{\hat{r}}\frac{\partial\hat{T}}{\partial\hat{r}} + \frac{\partial^2\hat{T}}{\partial\hat{r}^2} + \frac{\dot{Q}R^2}{KT_{typ}}. \tag{3.2.10}$$

The thermal profile of a neutron star crust will be computed by solving the following dimensionless ODE

$$\frac{d^2\hat{T}}{d\hat{r}^2} = -\frac{1}{K}\frac{dK}{d\hat{r}}\frac{d\hat{T}}{d\hat{r}} - \frac{2}{\hat{r}}\frac{d\hat{T}}{d\hat{r}} - \frac{\dot{Q}R^2}{KT_{\rm typ}}, \tag{3.2.11}$$

where

$$T_{\rm typ} = \frac{\rho\epsilon_{\rm nuc}R^2}{K}, \tag{3.2.12}$$

$$\hat{R}_{\rm outer} = 1,$$

$$\hat{R}_{\rm inner} = 0.9.$$

using the shooting method. Using equations (3.1.30) and (3.1.33) the full non-dimensionalised

form of equation (3.1.34) is written as

$$\frac{d^2\hat{T}}{d\hat{r}^2} = -\frac{d\hat{T}}{d\hat{r}}\left[\frac{1}{T}\frac{dT}{d\hat{r}} - \frac{1}{C_{\rm ep}T + \nu_{\rm eQ}}\left(C_{\rm ep}\frac{dT}{d\hat{r}}\right)\right] - \frac{2}{\hat{r}}\frac{d\hat{T}}{d\hat{r}} - \frac{\dot{Q}R^2}{KT_{\rm typ}}. \tag{3.2.13}$$

The boundary conditions in dimensionless form are

$$\begin{aligned} \hat{T}_{\rm outer} &= 0.25\left(\frac{\dot{M}}{\dot{m}_{\rm Edd}}\right)^{\frac{2}{7}}, \\ \frac{d\hat{T}}{d\hat{r}}\Big|_{\rm inner} &= \frac{L_{\rm core}}{4\pi K\hat{R}^2_{\rm inner}T_{\rm typ}R_{\rm typ}}. \end{aligned} \tag{3.2.14}$$

3.3 Background heat flux model results

Integrating equation (3.2.13) using numerical techniques gives the temperature distribution in an accreted neutron star crust of constant density.

A plot of how temperature varies with radius is shown in figure 3.3.1 for the free parameters: accretion rate and $Q_{\rm imp} = 1$. The temperature decreases with radius when moving from the outer crust boundary to the inner crust/core interface for all three accretion rates. The temperature gradient is steeper for a higher accretion rate when compared to that of lower accretion rates, as more energy is input into the crust via nuclear reactions per unit time.

A plot of how the flux (equation (3.1.2)) varies with radius is shown in figure 3.3.2. The magnitude of the rate of energy flow per unit area is at a maximum at the inner boundary and a minimum at the outer boundary. The negative sign of the flux shows the heat is flowing inwards from both the inner and outer boundaries.

The neutrino emissivity as shown in equation (3.1.24) is a function of temperature to the sixth power. A plot of how the neutrino cooling varies with radius in a neutron star crust is plotted in figure 3.3.3. It can be seen that neutrino cooling is highest at larger radii. This corresponds to the crustal temperature being at a maximum at the outer boundary.

The electron relaxation time in the thermal conductivity comprises of two terms: electron-phonon and electron-impurity scattering frequencies, as shown in equations (3.1.16), (3.1.18) and (3.1.21) . The electron-phonon scattering is temperature dependent and dominant at high temperatures $T > 10^7$K. How the electron-phonon scattering varies with radius is shown in figure 3.3.4. The electron-phonon scattering frequency is approximately one order of magnitude larger than the electron-impurity scattering. This is due to the impurity parameter employed of $Q_{\rm imp} = 1$ (Brown and Cumming, 2009), the high

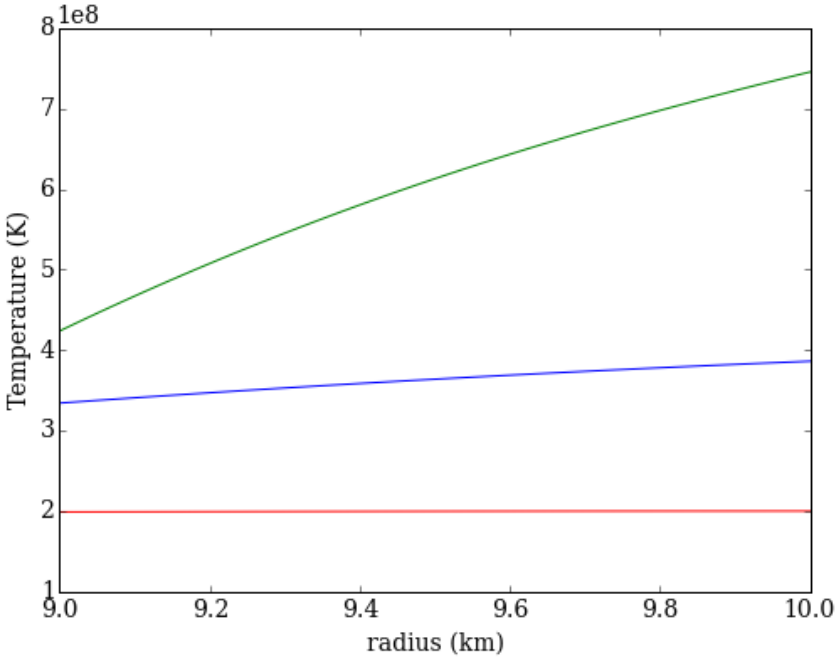

Figure 3.3.1: The temperature as a function of radius, for a uniform density neutron star crust ($\rho = 1\times10^{12}$ g cm^{-3}), was calculated. In this figure, how the temperature varies with radius inside the neutron star crust is shown for different accretion rates for $Q_{\rm imp} = 1$. The green line corresponds to the fastest accretion rate of $\dot{M}_1 = 1\times10^{-8}M_\odot$ yr^{-1}, blue line with an accretion rate of $\dot{M}_1 = 1\times10^{-9}M_\odot$ yr^{-1} and the red line with the slowest accretion rate $\dot{M}_1 = 1\times10^{-10}M_\odot$ yr^{-1}.

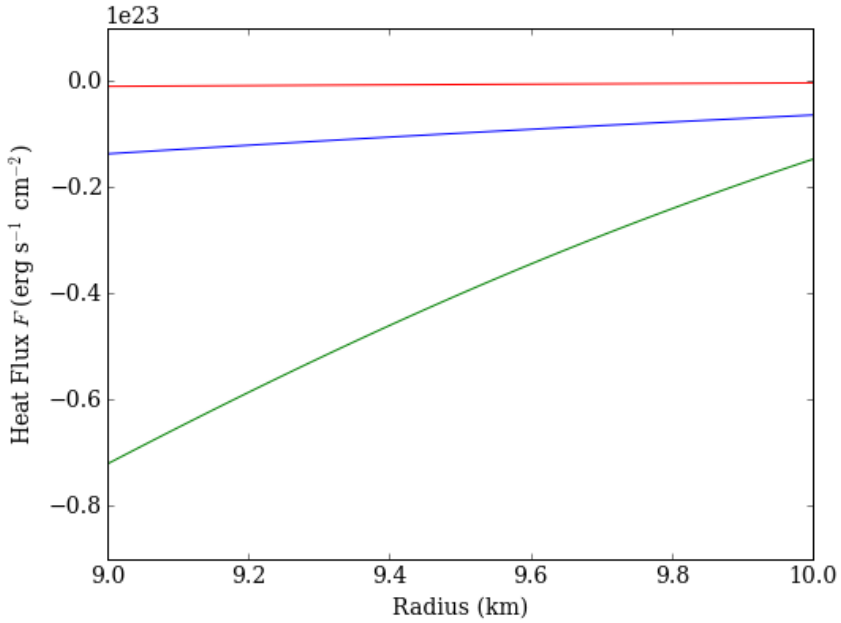

Figure 3.3.2: This figure shows the heat flux distribution inside the crust for different accretions rates.The heat flux is a function of temperature and varies with radius inside an accreted neutron star crust with impurity parameter $Q_{\rm imp} = 1$. The green line corresponds to the fastest accretion rate of $\dot{M}_1 = 1\times10^{-8}M_\odot$ yr^{-1}, blue line with an accretion rate of $\dot{M}_1 = 1\times10^{-9}M_\odot$ yr^{-1} and the red line with the slowest accretion rate $\dot{M}_1 = 1\times10^{-10}M_\odot$ yr^{-1}.

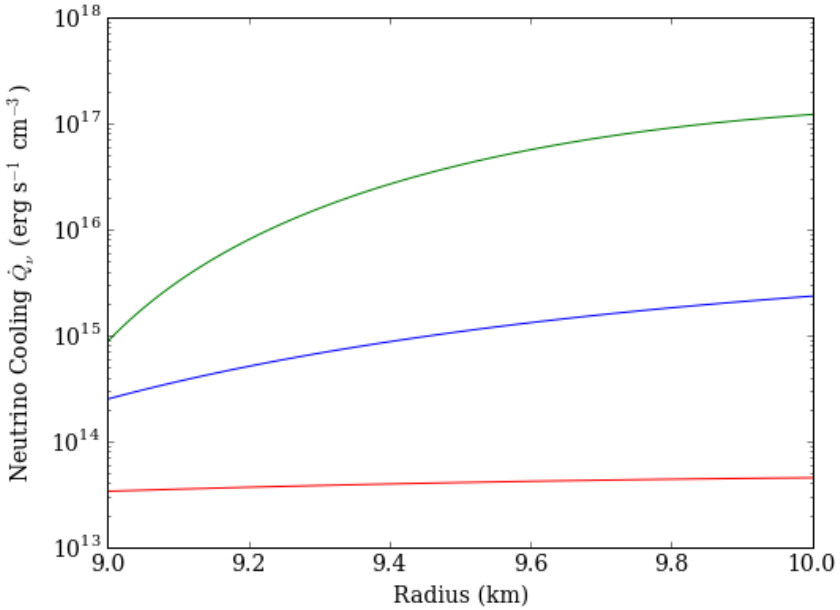

Figure 3.3.3: Neutrino cooling is a function of temperature. This figure shows how the neutrino emissivity varies with radius inside an accreted neutron star crust for different accretions rates with $Q_{\rm imp} = 1$. The neutrino cooling rate is at a maximum at the outer radius of the star and decreases with decreasing radius (towards the centre of the star). The green line corresponds to the fastest accretion rate of $\dot{M}_1 = 1\times10^{-8}M_\odot$ yr^{-1}, blue line with an accretion rate of $\dot{M}_1 = 1\times10^{-9}M_\odot$ yr^{-1} and the red line with the slowest accretion rate $\dot{M}_1 = 1\times10^{-10}M_\odot$ yr^{-1}.

temperature of the neutron star crust $\sim 10^8$K and the temperature dependency of the electron-phonon scattering. This result is consistent with the discussion in section 3.1.2 and figure 3.1.1.

The results in this subsection show how the temperature is distributed in a uniform density accreted neutron star crust. The temperature sensitive neutrino cooling mechanism is represented for different accretion rates. The electron-phonon and electron-impurity scattering frequencies, that affect the thermal conductivity, are also represented. In the next section, the validity of these results will be reviewed using numerical testing techniques.

3.3.1 Numerical Testing

To check the accuracy of the ODE solver implemented and the validity of the results produced, the numerical techniques are tested using a variety of methods. The problem being solved within this body of work is complex. As more variable parameters are introduced, the possibility of errors arising increases. To build confidence in the routine and results, mostly in preparation for the introduction of the density dependent parameters in the next chapter, three different numerical tests were employed.

Initially, the results were checked to see if they converge for increasing resolution. Fol-

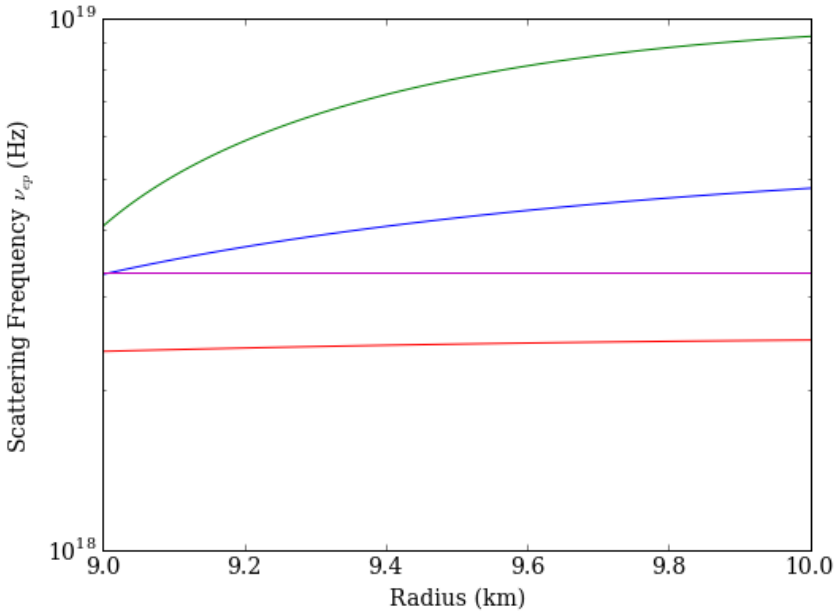

Figure 3.3.4: The electron-phonon scattering frequency varies with radius inside an accreted neutron star crust for different accretions rates. The electron-phonon scattering frequency increases with increasing temperature, and is at a maximum at the outer boundary. The green line corresponds to the fastest accretion rate of $\dot{M}_1 = 1 \times 10^{-8} M_\odot$ yr^{-1}, blue line with an accretion rate of $\dot{M}_1 = 1 \times 10^{-9} M_\odot$ yr^{-1} and the red line with the slowest accretion rate $\dot{M}_1 = 1 \times 10^{-10} M_\odot$ yr^{-1}. The magenta line represents the electron-impurity scattering, which is a function of the impurity parameter where $Q_{\rm imp} = 1$ and is independent of temperature.

lowing this, the self consistency of the model was inspected by confirming that the energy of the system was conserved. Upon passing these tests, a further investigation into the accuracy of the model was carried out by approximating the derivatives using finite differencing techniques. A more detailed description of these tests and the methods employed are detailed in the subsections that follow.

3.3.1.1 Convergence Test

A convergence ratio C_{test} was computed for the temperature values produced by the ODE solver. To test for convergence, equation (3.1.34) was solved numerically for various controlled error parameters in the numerical integrator. More specifically, the rtol parameter in the python function scipy.integrate.odeint was varied for different tolerances. Reducing the rtol value should decrease the error in the calculation which increases the accuracy of the calculation. The numerically computed temperature can be written as a function of the error in the calculation as

$$T = T_{\rm exact} + A\delta^n, \tag{3.3.1}$$

where $T_{\rm exact}$ is the exact temperature value, A is a constant, n is the order of convergence and δ is a measure of the numerical error in the calculation, which in the work

contained within this section corresponds to the rtol value used when solving the ODE. To determine whether the ODE solutions are convergent, a value for n must be determined.

Using equation (3.3.1), the convergence ratio $C_{\rm test}$ was computed at the mid-point of the neutron star crust, using different accuracy parameters corresponding to the rtol values employed, using the relation

$$C_{\rm test} = \frac{T_{\rm high} - T_{\rm low}}{T_{\rm high} - T_{\rm medium}}, \tag{3.3.2}$$

where $T_{\rm low}, T_{\rm medium}$, and $T_{\rm high}$ corresponds to the error control used when calculating the temperature. $T_{\rm low}$ has the largest rtol value and $T_{\rm high}$ the lowest. The relationship between the unknown exact value of temperature $T_{\rm exact}$ at a given radius and the error δ^n in the calculation arising from the rtol value is assumed to be

$$\begin{aligned} T_{\rm low} &= T_{\rm exact} + A\delta^n_{\rm low}, \\ T_{\rm medium} &= T_{\rm exact} + A\delta^n_{\rm medium}, \\ T_{\rm high} &= T_{\rm exact} + A\delta^n_{\rm high}. \end{aligned} \tag{3.3.3}$$

The rtol values were set to: $\delta^n_{\rm low} : 1.5 \times 10^{-8}$, $\delta^n_{\rm medium} : 1.5 \times 10^{-10}$ and $\delta^n_{\rm high} : 1.5 \times 10^{-12}$. The rtol value for $\delta^n_{\rm low}$ was selected as the default value of rtol in the scipy.integrate.odeint function in python. Combining equations (3.3.2) and (3.3.3) a value for n is determined as

$$n = \frac{\log(C_{\rm test} - 1)}{\log_{10}(2)}. \tag{3.3.4}$$

For first order convergence n must be positive. The higher the value of n, the better the convergence. The code computes $n = 1.07$ suggesting the ODE solver is convergent and to slightly better than first order.

3.3.1.2 Energy conservation self-consistency test

Testing the code to check that energy is conserved provides a simple self-consistency check. This is achieved by ensuring the energy radiated out of the core by neutrinos, plus the heat energy lost through the outer and inner boundaries via conduction, is equal to the total heat input by accretion.

The total neutrino radiation energy emitted by $\nu\bar{\nu}$ bremsstrahlung radiation per unit time via the crust is calculated by integrating equation (3.1.24) over the crust as

$$E_\nu = \int_{R_{\rm inner}}^{R_{\rm outer}} \rho\epsilon_\nu 4\pi r^2 dr, \tag{3.3.5}$$

where R_{outer} and R_{inner} are the radii at the outer and inner boundaries respectively. The total heat conducted into the core and out of the crust per unit time is calculated from the flux (equation (3.1.2)) at the crust-core interface as

$$E_{\text{K}} = -K\frac{dT}{dr}4\pi R^2, \tag{3.3.6}$$

where R is set to the inner boundary radius to calculate $E_{\text{K(core)}}$ and $R = R_{\text{outer}}$ for $E_{\text{K(crust)}}$.

The sum of thermal energy conducted out of the crust into the core and out of the surface of the crust, along with the neutrino energy radiated out of the crust as

$$E_{\text{total}} = E_{\nu} - E_{\text{K(core)}} + E_{\text{K(crust)}}. \tag{3.3.7}$$

The total heat energy generated in the crust by accretion per unit time ϵ_{total} is

$$\epsilon_{\text{total}} = \frac{\dot{M}E_{\text{nuc}}}{m_{\text{nuc}}}. \tag{3.3.8}$$

The self-consistency test is passed when $E_{\text{total}} = \epsilon_{\text{total}}$. Equation (3.3.5) is solved by integrating over the volume of the crust. Each term shown in equation (3.3.7) is computed and then summed together to determine E_{total}. The total heat energy input via accretion ϵ_{total} is computed analytically using equation (3.3.8). A summary of these results is shown in table 3.3.5.

Accretion Rate ($M_{\odot}\text{yr}^{-1}$)	$E_{\text{total}}(\text{erg}\,\text{s}^{-1}\,\text{cm}^{-3})$	$\epsilon_{\text{total}}(\text{erg}\,\text{s}^{-1}\,\text{cm}^{-3})$	$\frac{E_{\text{total}}-\epsilon_{\text{total}}}{E_{\text{total}}}$
1×10^{-8}	$6.071\,402\,0 \times 10^{33}$	$6.071\,401\,5 \times 10^{33}$	1.00×10^{-7}
1×10^{-9}	$6.071\,405\,8 \times 10^{34}$	$6.071\,401\,5 \times 10^{34}$	7.57×10^{-7}
1×10^{-10}	$6.071\,413\,7 \times 10^{35}$	$6.071\,401\,5 \times 10^{35}$	1.92×10^{-6}

Table 3.3.5: A table summarising the results of the self-consistency test for the computation of the thermal profile in a constant density, spherically symmetric, accreted neutron star crust. A ratio of the total energy input from accretion and the total heat energy transported out of the crust via heat conduction and neutrino emissivity, is calculated for the accretion rates: $1 \times 10^{-8}M_{\odot}$, $1 \times 10^{-9}M_{\odot}$, $1 \times 10^{-10}M_{\odot}$. This comparison checks that energy is conserved in the system.

In table 3.3.5, the values of the ratio of $E_{\text{total}}/\epsilon_{\text{total}}$ are equal to unity to an accuracy of a least 10^{-6}, beyond this the value begins to diverge from 1. This is expected as the error arises solving the ODE, and also from integrating to obtain E_{ν}. The order of accuracy in these results is sufficient to conclude the energy conservation test of the system is passed.

3.3.1.3 Finite Difference Test

Finite difference methods provide another internal consistency check to test the ODE is being solved correctly by the Python package odeint. From Taylor series expansions an expression for the second derivative of a function $f(x)$ at any point h can be written as

$$f"(x) = \frac{f(x+h) - 2f(x) + f(x-h)}{2h^2}. \tag{3.3.9}$$

Equation (3.3.9) is called the central finite difference stencil. This stencil is used to calculate $\frac{d^2T}{dr^2}$ from the T values computed by the ODE shown in equation (3.1.29). To calculate the second order derivative at the outer $f"(x)_{OB}$ and inner $f"(x)_{IB}$ boundaries, equation (3.3.9) has to be modified to ensure the values of h are consecutive and correspond to decreasing values of r (i.e. from the outer crust to the crust/core interface) (Fornberg, 1988) such that

$$\begin{aligned} f"(x)_{OB} &= \frac{2f(x) - 5f(x+h) - 4f(x+2h) - f(x+3h)}{h^2}, \\ f"(x)_{IB} &= \frac{2f(x) - 5f(x-h) - 4f(x-2h) - f(x-3h)}{h^2}. \end{aligned} \tag{3.3.10}$$

The second order derivative of temperature with respect to radius is computed using finite differencing methods for an accretion rate of $\dot{M}_1 = 0.5 \times 10^{-9} M_\odot$ yr^{-1}. From equations (3.3.9) and (3.3.10) $\frac{d^2T}{dr^2}$ can be written as a function of temperature as

$$\frac{d^2T}{dr^2} = \frac{T(r+1) - 2T(r) + T(r-1)}{(\Delta r)^2}, \tag{3.3.11}$$

$$\frac{d^2T}{dr^2}(r_{\text{outer}}) = \frac{2T(r) - 5T(r+1) + 4T(r+2) - T(r+3)}{(\Delta r)^2}, \tag{3.3.12}$$

$$\frac{d^2T}{dr^2}(r_{\text{inner}}) = \frac{2T(r-1) - 5T(r-2) + 4T(r-3) - T(r-4)}{(\Delta r)^2}, \tag{3.3.13}$$

where r is a radial element. The values calculated from equations (3.3.11) are then compared to the values of $\frac{d^2T}{dr^2}$ as calculated using the ODE shown in equation (3.1.29) for number of radial steps $n = \frac{r_{OB} - r_{IB}}{\Delta r} = 100$. A comparison of these results are shown in figure 3.3.6. In figure 3.3.6 shows the ODE values of $\frac{d^2T}{dr^2}$ correlate with the finite differencing values very well.

A measure of the accuracy of the ODE values of $\frac{d^2T}{dr^2}$ can be investigated further by taking the fractional error between the ODE values and those computed by the finite differencing methods. The fractional error is calculated by dividing the difference of the two results by a typical value of $\frac{d^2T}{dr^2}$ as calculated by the ODE. This is plotted in figure 3.3.7 for $Q_{\text{imp}} = 1$. Figure 3.3.7 shows a divergence from zero at higher radii values and an error of order 10^{-3}. This is sufficiently small to determine that the ODE has computed

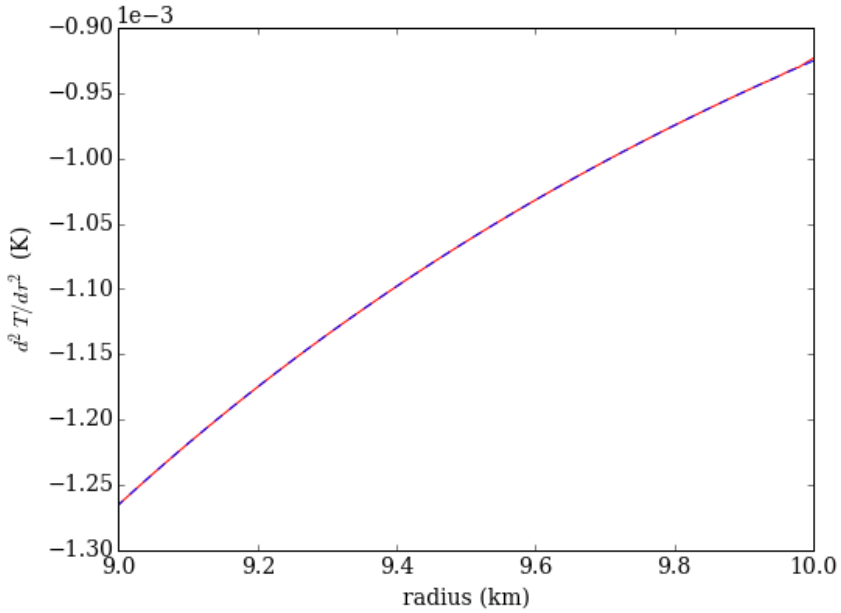

Figure 3.3.6: A test of the accuracy of the ODE solver values, d^2T/dr^2, was calculated using finite differencing. The values from finite differencing were then compared to the ODE solver values. A comparison of these values calculated for an accretion rate of $\dot{M}_1 = 1 \times 10^{-8} M_\odot$ yr^{-1} and $Q_{\rm imp} = 1$ as shown in this figure.

the values of $\frac{d^2T}{dr^2}$ within the required degree of accuracy for this work.

3.4 Thermal conductivity in presence of a magnetic field

The thermal conductivity has so far been considered as a scalar. In reality the situation is far more complex. Electrons are the dominant mediators of heat in an accreted neutron star crust. In the presence of a magnetic field, the thermal conductivity is altered due to the interaction between the electrons and magnetic field. The significance of the effect the magnetic field has on the thermal conductivity is described, with a view to incite a temperature perturbation in the accreted neutron star crust.

3.4.1 Thermal conductivity tensor

In the presence of a magnetic field the thermal conductivity is written as a tensor κ. The heat flux in tensor form is

$$F_\mu = -\kappa_{\mu\nu} \nabla^\nu T. \tag{3.4.1}$$

The heat flux including the magnetic field contributions $\boldsymbol{F}_{\rm B}$ is given by Yakovlev and Urpin (1980) as

$$\boldsymbol{F} = -\kappa_\perp \left[\boldsymbol{\nabla} T + (\omega_{\rm B} \tau(T))^2 \boldsymbol{b} \cdot (\boldsymbol{b} \cdot \boldsymbol{\nabla} T) + \omega_B \tau(T) (\boldsymbol{b} \times \boldsymbol{\nabla} T) \right], \tag{3.4.2}$$

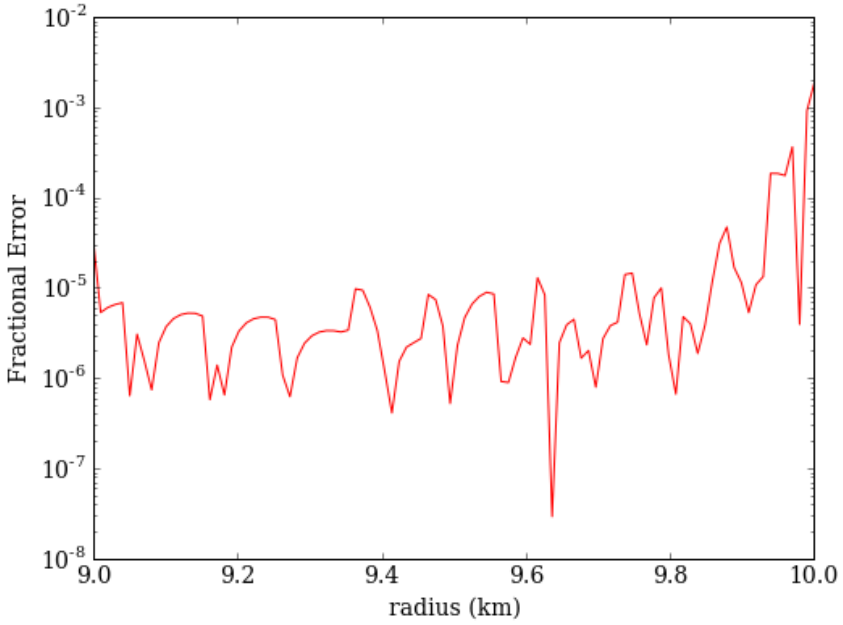

Figure 3.3.7: A plot of the fractional difference between the two curves of 3.3.6.

where $\kappa_\perp$ is the thermal conductivity tensor component perpendicular to the magnetic field, $\boldsymbol{b}$ is the unit vector of the magnetic field and $\omega_{\rm B}\tau(T)$ is the magnetisation parameter. The third term on the right hand side of equation 3.4.2 is from the Hall effect. The classical electron gyrofrequency $\omega_{\rm B}$ arises from the angular frequency of the circular motion of an electron perpendicular to the magnetic field B. The electron gyrofrequency is defined as

$$\omega_{\rm B} = \frac{eB}{m_{\rm e}^* c}, \tag{3.4.3}$$

where e is the charge of an electron and $m_{\rm e}^*$ is the effective electron mass. Following the treatment of Aguilera et al. (2008) the electron contribution of the thermal conductivity tensor in spherical polar coordinates is written as

$$\kappa_{\mu\nu} = \kappa_\perp \left(I_{\mu\nu} + (\omega_{\rm B}\tau(T))^2 \begin{pmatrix} b_{rr} & b_{r\theta} & b_{r\phi} \\ b_{r\theta} & b_{\theta\theta} & b_{\theta\phi} \\ b_{r\phi} & b_{\theta\phi} & b_{\phi\phi} \end{pmatrix} + \omega_{\rm B}\tau(T) \begin{pmatrix} 0 & -b_\phi & b_\theta \\ b_\phi & 0 & -b_r \\ -b_\theta & b_r & 0 \end{pmatrix} \right), \tag{3.4.4}$$

where I is the identity matrix and b_r, b_θ, b_ϕ are the components of the unit vector $\boldsymbol{b}$ in the direction of the magnetic field, and $b_{ij} = b_i b_j$ for $i, j = r, \theta, \phi$. It is worth noting that there appears to be a sign discrepancy in the final term of (3.4.4) in Aguilera et al. (2008).

The thermal conductivity tensor (equation (3.4.4)) can be written in Cartesian coordinates to build intuition by undergoing a change of basis by substituting $r \to x$, $\theta \to y$, and $\phi \to z$. For a magnetic field orientated along the z-axis, such that vectors $b_x = b_y = 0$,

equation (3.4.4) becomes

$$\kappa = \kappa_{\perp} \begin{pmatrix} 1 & \omega_{\mathrm{B}}\tau(T) & 0 \\ -\omega_{\mathrm{B}}\tau(T) & 1 & 0 \\ 0 & 0 & 1+(\omega_{\mathrm{B}}\tau(T))^2 \end{pmatrix}. \tag{3.4.5}$$

The components of the thermal conductivity tensor can be defined in terms of the scalar conductivity and the magnetisation parameter as follows

$$\kappa_{\parallel} = \kappa_0 = \frac{\pi^2 k_{\mathrm{B}}^2 T n_{\mathrm{e}}}{3m_{\mathrm{e}}^*}\tau(T), \tag{3.4.6}$$

$$\kappa_{\perp} = \frac{\kappa_0}{1+(\omega_{\mathrm{B}}\tau(T))^2}, \tag{3.4.7}$$

$$\kappa_{\wedge} = \frac{\kappa_0 \omega_{\mathrm{B}}\tau(T)}{1+(\omega_{\mathrm{B}}\tau(T))^2}. \tag{3.4.8}$$

Employing the definitions from equations (3.4.6), (3.4.7) and (3.4.8) for a magnetic field oriented along the z-axis, the conductivity tensor reduces to the form

$$\kappa = \begin{pmatrix} \kappa_{\perp} & \kappa_{\wedge} & 0 \\ -\kappa_{\wedge} & \kappa_{\perp} & 0 \\ 0 & 0 & \kappa_{\parallel} \end{pmatrix}, \tag{3.4.9}$$

where $\kappa_{\parallel}$ is the thermal conductivity parallel to the magnetic field and $\kappa_{\wedge}$ is the so-called Hall component (Geppert et al., 2004). Equation (3.4.9) corresponds to the thermal conductivity tensor given by Page et al. (2007).

The thermal conductivity is influenced by the magnetic field, as can be seen in equations (3.4.7) and (3.4.8). It would be interesting to investigate the significance of the effect the magnetisation parameter has on the temperature distribution in the crust.

3.5 Influence of magnetic field on the perturbed heat equation

3.5.1 Impurity parameter and the magnetisation parameter

An estimate of the magnitude of the magnetisation parameter was calculated to assess how significantly this parameter affects the thermal conductivity. For a magnetic field $B = 1 \times 10^9$ G and an impurity parameter $Q_{\mathrm{imp}} = 1$, using equations (3.1.16), (3.1.18), (3.1.21), (3.4.3) and the background temperature values, a plot of how the magnetisation parameter varies with radius for our uniform density crust was created and is shown in figure 3.5.1.

The magnetisation parameter is a function of impurity parameter. Using equations (3.4.3),

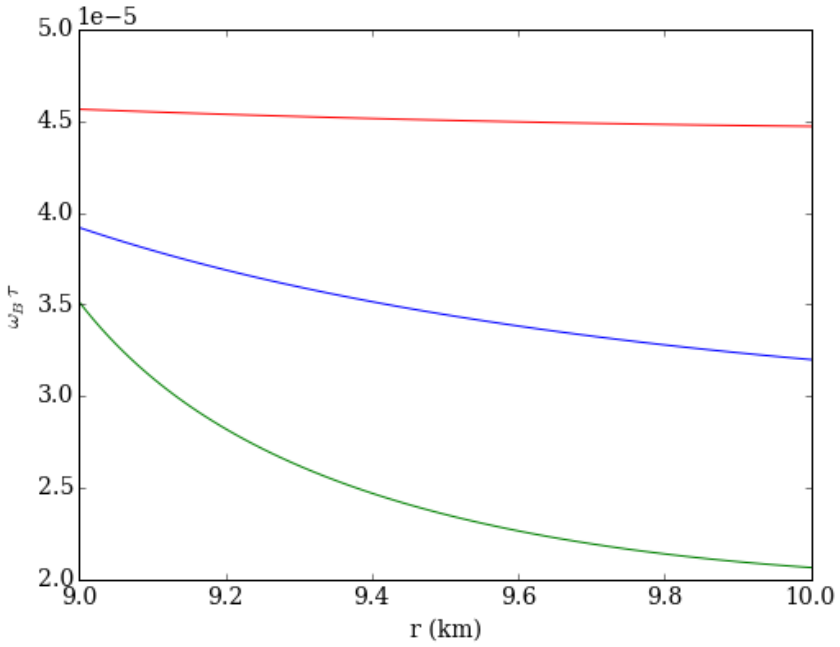

Figure 3.5.1: The magnetisation parameter is a function of temperature due to electron scattering frequency dependence. This figure shows how the magnetisation parameter varies with radius for $B = 10^9$G, $Q_{\rm imp} = 1$ different accretion rates, and is larger at smaller radii, towards the inner crust. The green line corresponds to the fastest accretion rate of $\dot{M}_1 = 1 \times 10^{-8} M_\odot$ yr^{-1}, blue line with an accretion rate of $\dot{M}_1 = 1 \times 10^{-9} M_\odot$ yr^{-1} and the red line with the slowest accretion rate $\dot{M}_1 = 1 \times 10^{-10} M_\odot$ yr^{-1}.

(3.1.16), (3.1.18), and (3.1.21), this can be written explicitly as

$$\omega_{\rm B}\tau(T) = \frac{eB}{m_{\rm e}^* c}\left(\frac{13e^2 k_{\rm B} T}{\hbar^2 c} + \frac{4\pi Q_{\rm imp} e^4 n_{\rm ion}}{p_{\rm F}^2 v_{\rm F}}\right)^{-1}. \tag{3.5.1}$$

For $T = 10^8$ K and $Q_{\rm imp} = 1$, the first term in the parenthesis of equation (3.5.1), the electron-phonon scattering, dominates in this high temperature and low impurity regime.

From figure 3.5.1, $\omega_{\rm B}\tau$ is at a maximum at the crust/core interface and decreases with increasing radii, for all three accretion rates. This pattern arises because the electron relaxation time τ is inversely proportional to temperature, which increases with increasing radii, when electron-phonon scattering dominates. How $\omega_{\rm B}\tau$ varies with radius in a realistic crust would differ as $m_{\rm e}^*$ would also vary with radius.

The magnetisation parameter also decreases as the accretion rate increases. This trend arises because temperature is a function of accretion rate. The temperature of the crust increases with accretion rate. The temperature dependence of the magnetisation parameter arises from the electron-phonon scattering, this is shown explicitly in equation 3.5.1. The temperature as a function of accretion rate is shown in figure 3.3.1.

This suggests the magnetic field may significantly affect the thermal conductivity. A

larger magnetisation parameter implies larger temperature asymmetries may develop in the neutron star crust. To quantify the significance of the magnetic field on the temperature distribution, a more detailed analysis was conducted as described below.

The impurity parameter is a dimensionless number that indicates whether the structure of a neutron star crust is crystalline $Q_{\rm imp} \ll 1$ or disordered $Q_{\rm imp} \gg 1$ (Pons et al., 2013). This parameter varies quite broadly in the literature as a detailed composition of the crust is not well understood. Brown and Cumming (2009) use $Q_{\rm imp} \approx 100$ for an accreted crust whereas Geppert et al. (2004) use $Q_{\rm imp} = 0.1$. A high impurity parameter $Q_{\rm imp} > 10$ corresponds to an amorphous structure and a low $Q_{\rm imp}$, to a crystalline lattice structure. Recent modelling of transiently accreting systems suggest $Q_{\rm imp} \approx 1$ (Page and Reddy, 2013).

The calculations from Ushomirsky et al. (2000) give an insight into the scale of the magnetisation parameter that is required to develop a temperature asymmetry large enough for a mountain to grow that is sufficient to slow the spin up torque from accretion. Ushomirsky et al. (2000) calculated a typical $\delta T/T \sim 10^{-2}$, for an accretion rate $\dot{M} = 0.5\dot{m}_{\rm Edd}$, this corresponds to an ellipticity ϵ of

$$\epsilon \approx \frac{Q}{I} \approx 5 \times 10^{-6} \frac{\delta T}{T}, \tag{3.5.2}$$

where Q is the mass quadrupole moment and I is the moment of inertia. From our initial estimate of the magnetisation parameter shown in equation (3.5.1), and using the approximation $\delta T/T \approx \omega_{\rm B}\tau$, we find

$$\omega_{\rm B}\tau \sim 4 \times 10^{-5} {\rm B}_9, \tag{3.5.3}$$

corresponding to an ellipticity of

$$\epsilon \approx \frac{Q}{I} \approx 2 \times 10^{-10} {\rm B}_9, \tag{3.5.4}$$

for $Q_{\rm imp} = 1$ and $T = 10^8$ K. This suggests a magnetic field of $B \sim 10^{12}$ G is required to build a sufficiently large mountain. Lander (2013) found that a magnetic field of order 10^{12}G can induce magnetic mountains with an ellipticity of $\epsilon_{\rm B}\ 10^{-8}$ for a neutron star with a superconducting core. We will now carry out a detailed numerical calculation, to obtain a more accurate value for the temperature perturbation.

3.5.2 Perturbing the flux by inserting a magnetic field

Starting with the expression for heat flux in the presence of a magnetic field (equation (3.4.2)) from Yakovlev and Urpin (1980) and the relations of the thermal conductivity tensor components given in equation (3.4.7), an expression for the flux in terms of the mag-

netisation parameter can be written as

$$\boldsymbol{F} = -\frac{\kappa_{\parallel}}{1+(\omega_{\mathrm{B}}\tau(T))^2}\left[\boldsymbol{\nabla}T + (\omega_{\mathrm{B}}\tau(T))^2\boldsymbol{b}\cdot(\boldsymbol{b}\cdot\boldsymbol{\nabla}T) + \omega_{\mathrm{B}}\tau(T)(\boldsymbol{b}\times\boldsymbol{\nabla}T)\right]. \tag{3.5.5}$$

The perturbations created by the influence of the magnetic field on the thermal conductivity is calculated by placing the heat flux in the presence of a magnetic field (equation (3.5.5)) on the non-magnetic spherically symmetric background heat flux (equation (3.1.2)). To enable the magnetic field to be treated as a perturbation, we will assume $\omega_{\mathrm{B}}\tau \ll 1$. This assumption is not employed in the work of Pons and Geppert (2007), as they consider high magnetic field strength magnetars. The perturbed flux, temperature and thermal conductivity are

$$\begin{aligned} \boldsymbol{F} &= \boldsymbol{F_0} + \delta\boldsymbol{F}, \\ T &= T_0 + \delta T, \\ \kappa_{\parallel} &= \kappa_0 + \delta\kappa_{\parallel}, \end{aligned} \tag{3.5.6}$$

where $\kappa_{\parallel}$ is a function of temperature and density. The perturbation relations shown in equation (3.5.6) is then used to calculate the anisotropic heat flux distribution as

$$\begin{aligned} \boldsymbol{F_0} + \delta\boldsymbol{F} = &-\frac{(\kappa_0+\delta\kappa_{\parallel})}{1+(\omega_{\mathrm{B}}\tau(T))^2}\{\boldsymbol{\nabla}(T_0+\delta T) + (\omega_{\mathrm{B}}\tau(T))^2\left[\boldsymbol{b}\cdot\boldsymbol{\nabla}(T_0+\delta T)\right]\cdot\boldsymbol{b} \\ &+ \omega_{\mathrm{B}}\tau(T)\left[\boldsymbol{b}\times\boldsymbol{\nabla}(T_0+\delta T)\right]\}. \end{aligned} \tag{3.5.7}$$

When $\omega_{\mathrm{B}}\tau(T)$ is small, the Taylor series approximation $\left[1+(\omega_{\mathrm{B}}\tau(T))^2\right]^{-1} \approx 1-(\omega_{\mathrm{B}}\tau(T))^2$, up to second order in $\omega_{\mathrm{B}}\tau(T)$, can be used. Expanding equation (3.5.7) up to linear order and simplifying, the thermal flux perturbation due to the magnetic field becomes

$$\delta\boldsymbol{F} = -\kappa_0\left[\boldsymbol{\nabla}\delta T + \omega_{\mathrm{B}}\tau(T)(\boldsymbol{b}\times\boldsymbol{\nabla}T_0)\right] - \delta\kappa_{\parallel}\boldsymbol{\nabla}T_0. \tag{3.5.8}$$

We assume $\delta\rho = 0$ and $\delta\epsilon_{\mathrm{nuc}} = 0$, which amounts to assuming that ρ and ϵ_{nuc} are independent of temperature and magnetic field strength. Combining these assumptions with the expression for the divergence of the heat flux, given by Ushomirsky et al. (2000), as shown in equation (3.1.5), an expression for the perturbed heat flux including the magnetic field is found to be

$$\boldsymbol{\nabla}\cdot\delta\boldsymbol{F} = -\rho\delta\epsilon_{\nu}, \tag{3.5.9}$$

Using the relation $\tilde{\omega}_{\mathrm{B}} = \frac{e}{m_e^* c}$ equation (3.5.8) can be written as

$$\delta\boldsymbol{F} = -\kappa_0\left[\boldsymbol{\nabla}\delta T + \tilde{\omega}_{\mathrm{B}}\tau(T)(\boldsymbol{B}\times\boldsymbol{\nabla}T_0)\right] - \delta\kappa_{\parallel}\boldsymbol{\nabla}T_0, \tag{3.5.10}$$

where $\boldsymbol{B}$ is the magnetic field vector. Taking the divergence of equation (3.5.10) and using equation (3.5.9) an expression for the divergence of the perturbed heat flux is written

as

$$-\rho\delta\epsilon_\nu = \boldsymbol{\nabla}\cdot\left(\kappa_0\boldsymbol{\nabla}\delta T + \delta\kappa_\parallel\boldsymbol{\nabla}T_0\right) + \left(\tilde{\omega}_{\rm B}\tau(T)\boldsymbol{\nabla}\kappa_0 + \kappa_0\tilde{\omega}_{\rm B}\boldsymbol{\nabla}\tau(T)\right)\cdot\left(\boldsymbol{B}\times\boldsymbol{\nabla}T_0\right) + \kappa_0\tilde{\omega}_{\rm B}\tau(T)\left[(\boldsymbol{\nabla}\times\boldsymbol{B})\cdot\boldsymbol{\nabla}T_0\right]. \tag{3.5.11}$$

The magnetic field can be decomposed into its poloidal $\boldsymbol{B}_{\rm pol}$ and toroidal $\boldsymbol{B}_{\rm tor}$ components using the Mie representations (Maier, 2005; Pons and Geppert, 2007) as

$$\boldsymbol{B} = \boldsymbol{B}_{\rm pol} + \boldsymbol{B}_{\rm tor}, \tag{3.5.12}$$

$$\boldsymbol{B}_{\rm pol} = -\boldsymbol{\nabla}\times\left(\boldsymbol{r}\times\boldsymbol{\nabla}\Phi\right), \tag{3.5.13}$$

$$\boldsymbol{B}_{\rm tor} = -\boldsymbol{r}\times\boldsymbol{\nabla}\Psi. \tag{3.5.14}$$

Using equations (3.5.12), (3.5.13) and (3.5.14), and cancelling orthogonal terms, equation (3.5.11) becomes

$$-\rho\delta\epsilon_\nu = \boldsymbol{\nabla}\cdot\left(\kappa_0\boldsymbol{\nabla}\delta T + \delta\kappa_\parallel\boldsymbol{\nabla}T_0\right) + \kappa_0\tilde{\omega}_{\rm B}\tau(T)\left[(\boldsymbol{\nabla}\times(-\boldsymbol{\nabla}\times(\boldsymbol{r}\times\boldsymbol{\nabla}\Phi) - \boldsymbol{r}\times\boldsymbol{\nabla}\Psi))\cdot\boldsymbol{\nabla}T_0\right]. \tag{3.5.15}$$

Expanding and simplifying the magnetic field terms in equation (3.5.15) enables the perturbed heat flux to be written as

$$-\rho\delta\epsilon_\nu = \nabla\kappa_0\cdot\nabla\delta T + \kappa_0\nabla^2\delta T + \boldsymbol{\nabla}\delta\kappa_\parallel\cdot\boldsymbol{\nabla}T_0 + \delta\kappa_\parallel\nabla^2T_0 - \kappa_0\tilde{\omega}_{\rm B}\tau(T)\left(\frac{1}{r}\nabla_\perp^2\Psi\boldsymbol{e}_r\cdot\boldsymbol{\nabla}T_0\right), \tag{3.5.16}$$

where

$$\boldsymbol{\nabla}_\perp = \frac{1}{\sin\theta}\frac{\partial}{\partial\theta}\left(\sin\theta\frac{\partial}{\partial\theta}\right) + \frac{1}{\sin^2\theta}\frac{\partial^2}{\partial\phi^2}, \tag{3.5.17}$$

is the angular piece of ∇^2 operator on a unit sphere.

Upon expanding the magnetic field terms in equation (3.5.15) the perturbed poloidal terms of the magnetic field cancelled. This was not an obvious result. Initially, it was thought that the (dipolar) poloidal magnetic field would be most interesting to investigate, as experimentally observed parameters of the poloidal magnetic field exist. The perturbed heat flux equation contains only the perturbed toroidal components of the magnetic field due to the geometry of the magnetic field, although the poloidal components of the magnetic field may appear at order $(\omega_{\rm B}\tau)^2$ and above.

The perturbed heat flux shown in equation (3.5.16) can be written solely as a function of temperature. Using equation (3.1.25), the perturbed heat losses via neutrino emissivity can be written as

$$\rho\delta\epsilon_\nu = 6C_\epsilon T^5\delta T, \tag{3.5.18}$$

where $C_\epsilon = 3.229 \times 10^{-37} \rho_{12} \frac{Z^2}{A} X_A \ \mathrm{erg\,s^{-1}\,cm^{-3}}$.

An expression for the perturbed thermal conductivity component, that is parallel to the magnetic field, is derived from equation 3.4.6 and can be written as a function of δT as

$$\delta\kappa_\parallel = \frac{\kappa_0}{dT}\delta T = \frac{C_\kappa \nu_{\mathrm{eQ}} \delta T}{\nu^2}. \tag{3.5.19}$$

From equation (3.5.19), using $\nu = \nu_{\mathrm{ep}}(T) + \nu_{\mathrm{eQ}}$ where $\nu_{\mathrm{ep}} = C_{\mathrm{ep}} T$, the gradient of the perturbed parallel component of the thermal conductivity tensor is

$$\boldsymbol{\nabla}\delta\kappa_\parallel = \frac{C_\kappa \nu_{\mathrm{eQ}}}{\nu^2}\left(\boldsymbol{\nabla}\delta T - \frac{2C_{\mathrm{ep}}\delta T \boldsymbol{\nabla} T}{\nu}\right), \tag{3.5.20}$$

where the constants from the above equations are defined as

$$\begin{aligned} C_\kappa &= \frac{\pi^2 k_{\mathrm{B}}^2 n_{\mathrm{e}}}{3 m_{\mathrm{e}}^* \nu_{\mathrm{eQ}}}, \\ C_{\mathrm{ep}} &= \frac{13 e^2 k_{\mathrm{B}}}{h^2 c}, \end{aligned} \tag{3.5.21}$$

and $\nu = \nu_{\mathrm{ep}} + \nu_{\mathrm{eQ}}$ and $\nu_{\mathrm{ep}} = C_{\mathrm{ep}} T$. Using equations (3.5.18), (3.5.19) and (3.5.20), the perturbed heat flux equation is written solely as a function of temperature as

$$\begin{aligned} -6C_\epsilon T^5 \delta T =& \nabla\kappa_0 \cdot \nabla\delta T + \kappa_0 \nabla^2 \delta T + \frac{C_\kappa \nu_{\mathrm{eQ}}}{\nu^2}\left(\boldsymbol{\nabla}\delta T \cdot \boldsymbol{\nabla} T_0 - \frac{2\delta T C_{\mathrm{ep}} \boldsymbol{\nabla} T_0 \cdot \boldsymbol{\nabla} T_0}{\nu}\right) \\ &+ \frac{C_\kappa \nu_{\mathrm{eQ}} \delta T}{\nu^2}\nabla^2 T_0 - \kappa_0 \tilde{\omega}_B \tau(T)\left(\frac{1}{r}\nabla_\perp^2 \Psi \boldsymbol{e}_r \cdot \boldsymbol{\nabla} T_0\right). \end{aligned} \tag{3.5.22}$$

From the relation $\frac{\kappa_0}{T_0} = \frac{C_\kappa}{\nu}$ and rearranging to make $\nabla^2\delta T$ the subject, equation (3.5.22) can be re-written as a second order PDE as

$$\begin{aligned} \nabla^2 \delta T =& \frac{6C_\epsilon T^5 \delta T}{\kappa_0} - \frac{2\nu_{\mathrm{eQ}}}{\nu}\frac{\nabla\delta T \nabla T_0}{T_0} + \frac{2\nu_{\mathrm{eQ}}\nu_{ep}}{\nu^2}\frac{\delta T(\boldsymbol{\nabla} T_0)^2}{T_0^2} - \frac{\nu_{\mathrm{eQ}}}{\nu}\frac{\delta T \nabla^2 T_0}{T_0} \\ &+ \tilde{\omega}_{\mathrm{B}} \tau(T)\left(\frac{1}{r}\nabla_\perp^2 \Psi \boldsymbol{e}_r \cdot \boldsymbol{\nabla} T_0\right). \end{aligned} \tag{3.5.23}$$

Equation (3.5.23) can then be decomposed into spherical harmonics using the the expressions

$$\begin{aligned} \delta T &= \mathrm{Re}\left[\delta T_{lm}(r) Y_{lm}(\theta, \phi)\right], \\ \Psi &= \mathrm{Re}\left[\Psi_{lm}(r) Y_{lm}(\theta, \phi)\right], \end{aligned} \tag{3.5.24}$$

as

$$\frac{d^2\delta T_{lm}}{dr^2} = -\frac{2}{r}\frac{d\delta T_{lm}}{dr} + \frac{6C_\epsilon T_0^5 \delta T_{lm}}{\kappa_0} + \frac{l(l+1)}{r^2}\delta T_{lm} - \frac{2\nu_{\rm eQ}}{\nu T_0}\frac{d\delta T_{lm}}{dr}\frac{dT_0}{dr} + \frac{2\nu_{\rm eQ}\nu_{ep}\delta T_{lm}}{\nu^2 T_0^2}\left(\frac{dT_0}{dr}\right)^2 - \frac{\nu_{\rm eQ}\delta T_{lm}}{\nu T_0}\left(\frac{2}{r}\frac{dT_0}{dr} + \frac{d^2T_0}{dr^2}\right) - \tilde{\omega}_{\rm B}\tau(T)\frac{l(l+1)}{r}\Psi_{lm}\frac{dT_0}{dr}. \quad (3.5.25)$$

Equation (3.5.25) shows the anisotropic heat flux distribution due to the magnetisation parameter, arising from the interaction of electrons with the magnetic field, in a neutron star crust. Numerically computing the solution to equation (3.5.25) will quantify the significance of this effect.

An expression for Ψ_{l0} was taken from Pons and Geppert (2007) as

$$\Psi_{l0} = c[(r - R_i)(r - R)]^2, \quad (3.5.26)$$

where $R_{\rm i}$ and R are the inner and outer radii of the crust respectively and c is a constant determined by the maximum value of the toroidal magnetic field. Equation (3.5.26) was modified to include the $m \neq 0$ contributions, with the indices set as $m = l = 2$, for a quadrupole. The magnetic field is set to have a quadrupole moment to ensure any perturbation induced by the field is quadrupolar, and therefore results in gravitational wave emission. Equation (3.5.26) then becomes

$$\Psi_{22}Y_{22} = c\frac{1}{4}\sqrt{\frac{15}{2\pi}}[(r - R_{\rm i})(r - R)]^2 \sin^2\theta e^{2i\phi}. \quad (3.5.27)$$

An expression for equation (3.5.27) with the complex components removed, is written as

$$\Psi(r, \theta, \phi) = c\frac{1}{4}\sqrt{\frac{15}{2\pi}}[(r - R_i)(r - R)]^2 \sin^2\theta\cos 2\phi. \quad (3.5.28)$$

From equations (3.5.14) and (3.5.28) a value for the free parameter c in equation (3.5.27) can be calculated for an $l = m = 2$ toroidal magnetic field. The toroidal magnetic field for $l = m = 2$ is written as

$$\boldsymbol{B}_{\rm tor} = c\frac{1}{4}\sqrt{\frac{15}{2\pi}}\left[(r - R_i)(r - R)\right]^2\left(-\sin\theta\sin 2\phi\,\boldsymbol{e}_\theta + \sin\theta\cos\theta\cos 2\phi\,\boldsymbol{e}_\phi\right). \quad (3.5.29)$$

To obtain a typical value of c, values from the mid-point of the neutron star crust were selected. A toroidal magnetic field strength value of $B = 1 \times 10^{12}$G was chosen for this calculation. Using equation (3.5.28) and setting $\theta = \frac{\pi}{2}$, $\phi = \frac{\pi}{4}$, $r = 9.5 \times 10^5$ cm, $R_{\rm i} = 9 \times 10^5$ cm, $R = 1 \times 10^6$ cm and in equation (3.5.29) and rearranging, the value for the constant c is determined as $c = 6.6 \times 10^{-8}\left(\frac{B_c}{10^{12}\rm G}\right)$ where $B_{\rm c}$ is the value B at the

chosen point in the middle of the crust. The results will scale linearly in B. Equation (3.5.25) can then be written as

$$\frac{d^2\delta T_{lm}}{dr^2} = -\frac{2}{r}\frac{d\delta T_{lm}}{dr} + \frac{6C_\epsilon T_0^5 \delta T_{lm}}{\kappa_0} + \frac{l(l+1)}{r^2}\delta T_{lm} - \frac{2\nu_{\rm eQ}}{\nu T_0}\frac{d\delta T_{lm}}{dr}\frac{dT_0}{dr} + \frac{2\nu_{\rm eQ}\nu_{\rm ep}\delta T_{lm}}{\nu^2 T_0^2}\left(\frac{dT_0}{dr}\right)^2 - \frac{\nu_{\rm eQ}\delta T_{lm}}{\nu T_0}\left(\frac{2}{r}\frac{dT_0}{dr} + \frac{d^2T_0}{dr^2}\right) - \tilde{\omega}_{\rm B}\tau(T)\frac{l(l+1)}{r}c\frac{1}{4}\sqrt{\frac{15}{2\pi}}[(r-R_i)(r-R)]^2\frac{dT_0}{dr}. \tag{3.5.30}$$

3.5.3 Perturbed Boundary Conditions

For the perturbed temperature boundary conditions Ushomirsky et al. (2000) set the temperature perturbation at the top of the crust $\delta T_{\rm top}$ to zero, as the thermal conductivity of the ocean is much higher than that of the crust. It is worth noting that the flux coming out of the crust is not zero and is potentially observable. At the crust/core interface $\delta T_{\rm bot}$ Ushomirsky et al. (2000) assume the core is perfectly conducting, enabling $\delta T_{\rm bot}$ to be equated to zero. The advantage of this condition is that it is approximately true for both a normal and superfluid neutron star core.

These boundary conditions will be used for the numerical integration of the second order differential equation for the perturbed temperature, as shown in equation (3.5.30). Integrating (3.5.30) will show how the presence of a magnetic field in a constant density neutron star crust may induce a temperature perturbation.

3.6 Numerical computation of the perturbed heat flux

In this section, the numerical techniques that are employed to solve the second order ODE of the perturbed heat flux, as shown in equation (3.5.30), are outlined. Solving equation (3.5.30) will determine the temperature perturbation that arises from inserting a magnetic field into a neutron star crust that is undergoing accretion.

Equation (3.5.25) can be written in the non-dimensionalised form using the definitions given in equations (3.2.1) and (3.2.8) as

$$\frac{d^2\delta\hat{T}_{lm}}{d\hat{r}^2} = -\frac{2}{\hat{r}}\frac{d\delta\hat{T}_{lm}}{d\hat{r}} + \frac{6C_\epsilon \hat{T}^5 T_{\rm typ}^5 R_{\rm typ}^2 \delta\hat{T}_{lm}}{\kappa_0} - \frac{2\nu_{\rm eQ}}{\nu}\frac{1}{\hat{T}_0}\frac{d\delta\hat{T}_{lm}}{d\hat{r}}\frac{d\hat{T}_0}{d\hat{r}} + \frac{2\nu_{\rm eQ}\nu_{\rm ep}}{\nu^2}\frac{\delta\hat{T}_{lm}}{\hat{T}_0^2}\left(\frac{d\hat{T}_0}{d\hat{r}}\right)^2 - \frac{\nu_{\rm eQ}}{\nu}\frac{\delta\hat{T}_{lm}}{\hat{T}_0}\left(\frac{2}{\hat{r}}\frac{d\hat{T}_0}{d\hat{r}} + \frac{d^2\hat{T}_0}{d\hat{r}^2}\right) + \frac{l(l+1)}{\hat{r}}\left(\frac{\delta\hat{T}_{lm}}{\hat{r}} - \tilde{\omega}_{\rm B}\tau(T)\frac{d\hat{T}_0}{d\hat{r}}\Psi_{lm}\right), \tag{3.6.1}$$

where $\Psi_{lm} = cR_{\rm typ}^4[(\hat{r}-\hat{R}_{\rm i})(\hat{r}-\hat{R})]^2$.

$\delta\hat{T}$ at both the inner and outer boundaries is set to zero following the formalism given by Ushomirsky et al. (2000).

3.6.1 Perturbed Heat Flux Results

The ODE describing how the perturbed heat flux varies in the crust with radius (equation (3.6.1)) is solved numerically by integration methods as detailed in section 3.2. The results of this computation are given in this section.

The magnitude of the source term from equation (3.5.30) can be quantified at different locations in the crust by plotting this as a function of radius. This provides an interesting insight, as the source term is independent of the perturbed temperature δT. Figure 3.6.1 shows how the source term (the last term in equation (3.5.25)) varies with radius, in the neutron star crust, for different accretion rates, $B = 10^{12}$ G and $Q_{\rm imp} = 1$. The magnitude of the source term is largest towards the centre of the crust. The accretion rate influences the magnitude and sign of the source term, due to the temperature dependence of the relaxation time τ and the explicit occurrence of the dT/dr factor.

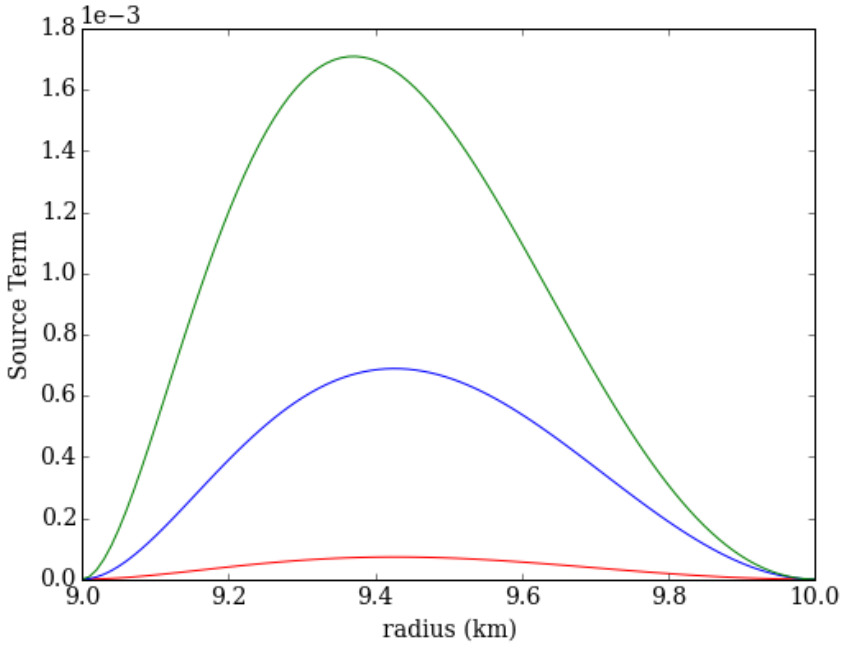

Figure 3.6.1: The source term in the perturbation equation (3.5.30) is plotted as function of radius to quantify the strength of this parameter at different locations in the neutron star crust for a magnetic field strength for $B = 10^{12}$G and $Q_{\rm imp} = 1$. The green line corresponds to the fastest accretion rate of $\dot{M}_1 = 1 \times 10^{-8} M_\odot$ yr^{-1}, blue line with an accretion rate of $\dot{M}_1 = 1 \times 10^{-9} M_\odot$ yr^{-1} and the red line with the slowest accretion rate $\dot{M}_1 = 1 \times 10^{-10} M_\odot$ yr^{-1}. The magnitude of the source term is larger towards the centre of the crust.

A plot of how the perturbed temperature varies with radius for $Q_{\rm imp} = 1$ and magnetic field strength $B = 10^{12}$G, for different accretion rates, is shown in figure 3.6.2. To obtain the actual temperature perturbation, this radial function needs to be multiplied by the

real part of $Y_{22}(\theta, \phi)$. At the crustal boundaries the perturbed temperature is zero. This is due to the boundary conditions as specified in section 3.5.3. In the middle of the crust the perturbed temperature follows from the assumed field and reaches a maximum. It can be seen that the higher accretion rates lead to a larger temperature perturbation. This is an expected result as the higher the accretion rate, the more energy is transferred to the system. This result corresponds well with how the source term varies with radius in the crust as shown in figure 3.6.1.

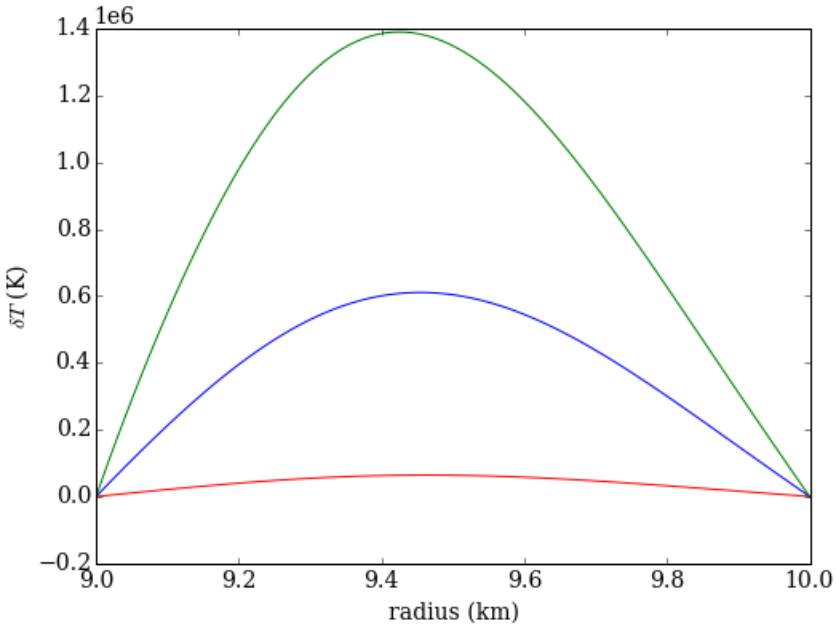

Figure 3.6.2: This figure shows how the perturbed temperature varies with radius for a uniform density accreted neutron star crust for $B = 1 \times 10^{12}$ G and $Q_{\rm imp} = 1$. Multiplication of this radial function by the real part of $Y_{22}(\theta\phi)$ will recover the actual temperature perturbation. The green line corresponds to the fastest accretion rate of $\dot{M}_1 = 1 \times 10^{-8} M_\odot$ yr^{-1}, blue line with an accretion rate of $\dot{M}_1 = 1 \times 10^{-9} M_\odot$ yr^{-1} and the red line with the slowest accretion rate $\dot{M}_1 = 1 \times 10^{-10} M_\odot$ yr^{-1}. The perturbed temperature is at a maximum in the middle of the crust and is larger for faster accretion rates.

To enable a comparison of the ratio of $\delta T/T$ with the magnetisation parameter $\omega_{\rm B}\tau$, the ratio $\delta T/T$ for $B = 10^{12}$G and $Q_{\rm imp} = 1$, is plotted as a function of radius and is shown in figure 3.6.3. Initial estimates of $\omega_{\rm B}\tau$, for the given magnetic field strength as calculated in section 3.5.1 and shown in figure 3.5.1, suggested $\delta T/T \sim \omega_{\rm B}\tau \sim 4 \times 10^{-5}{\rm B}_9$. Figure 3.6.3 shows that the perturbation is approximately one order of magnitude smaller than this.

In figure 3.6.4 the influence of the impurity parameter on the temperature perturbation ratio is shown for accretion rate $\dot{M}_1 = 1 \times 10^{-9} M_\odot$ yr^{-1}. The smaller the impurity parameter, the larger the temperature perturbation ratio. Figure 3.1.1 shows lower temperatures and high impurity parameter values are required for electron-impurity scattering to become the dominant scattering mechanism in the crust. This can be seen in figure 3.6.4 as the lower impurity values $Q_{\rm imp} \sim 0.1 - 1$ do not have a significant effect on the

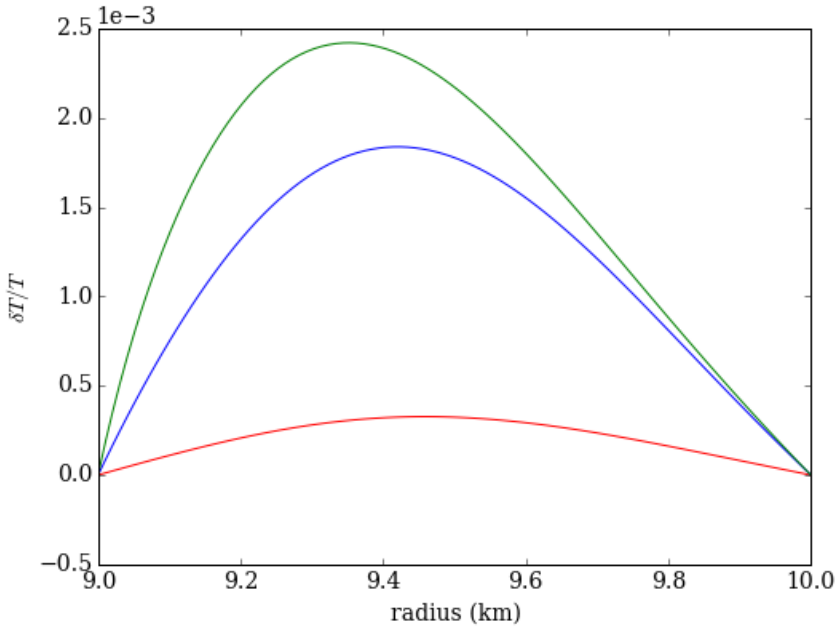

Figure 3.6.3: The magnitude of the temperature perturbation, due to the magnetic field, in a neutron star crust is shown in this figure by plotting how the ratio $\delta T/T$ varies with radius for different accretion rates, magnetic field strength $B = 10^{12}$G and impurity parameter $Q_{\rm imp} = 1$. The green line corresponds to the fastest accretion rate of $\dot{M}_1 = 1 \times 10^{-8} M_\odot$ yr^{-1}, blue line with an accretion rate of $\dot{M}_1 = 1 \times 10^{-9} M_\odot$ yr^{-1} and the red line with the slowest accretion rate $\dot{M}_1 = 1 \times 10^{-10} M_\odot$ yr^{-1}.

$\delta T/T$ when compared to the high values of $Q_{\rm imp}$. The overall trend of $\delta T/T$ decreasing as $Q_{\rm imp}$ increases arises as the relaxation time τ decreases with increasing values of $Q_{\rm imp}$, consequently reducing the value of the magnetisation parameter $\omega_{\rm B}\tau$. The relationship between magnetisation parameter and $Q_{\rm imp}$ is shown explicitly in equation (3.5.1).

For $Q_{\rm imp} \approx 1$ the temperature perturbation ratio, due to a magnetic field strength $B = 10^{12}$G, is of order 10^{-3}. Whilst $\omega_{\rm B}\tau$ is formally the perturbation parameter, the results for $\delta T/T$ only have a precise linear scaling with the magnetic field strength, not impurity parameter. This is because $Q_{\rm imp}$ also affects the background solution to our model. The ellipticity ϵ required for a sufficiently large mass quadrupole moment can be written as a function of the temperature perturbation ratio as

$$\epsilon = \frac{Q}{I} \approx 5 \times 10^{-8} \left(\frac{\delta T/T}{1\%} \right), \tag{3.6.2}$$

where Q is the mass quadrupole moment and I is the moment of inertia. The temperature perturbation induced in the crust by the magnetic field for $\dot{M} = 10^{-9} M_\odot$ yr^{-1} and $Q_{\rm imp} = 1$ is written as

$$\frac{\delta T}{T} = 2 \times 10^{-6} \mathrm{B}_9. \tag{3.6.3}$$

The ellipticity parameter can then be written as a function of magnetic field

$$\epsilon = \frac{Q}{I} \approx 1 \times 10^{-11} \mathrm{B}_9, \tag{3.6.4}$$

In chapter 4, we will use a more realistic equation of state, one of varying density, to gain a deeper insight as to the effect the magnetic field has on the thermal conductivity and consequently the temperature distribution in an accreted neutron star crust.

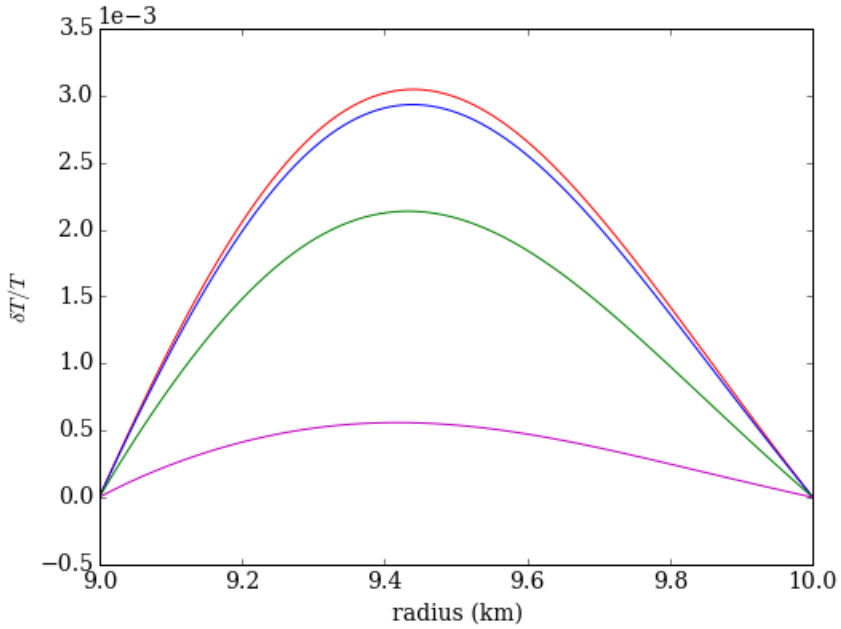

Figure 3.6.4: This figure shows the ratio $\delta T/T$ varies with radius in a neutron star crust for different impurity parameters for a magnetic field strength $B = 10^{12}$G and an accretion rate of $\dot{M}_1 = 1 \times 10^{-9} M_\odot$ yr^{-1}. The magenta line corresponds to $Q_{\mathrm{imp}} = 100$, green line to $Q_{\mathrm{imp}} = 10$, blue line with $Q_{\mathrm{imp}} = 1$ and the red line with the lowest impurity parameter $Q_{\mathrm{imp}} = 0.1$. The influence the impurity parameter has on the perturbation ratio is minimal for $Q_{\mathrm{imp}} < 1$.

3.6.2 Finite difference test

The accuracy of the numerical computation of the second order perturbed temperature equation (equation (3.5.30)) was tested using the finite difference techniques outlined in section 3.3.1.3.

Values for $d^2\delta T_{22}/dr^2$ were obtained using two different methods. The first used the numerical solutions of δT and $d\delta T/dr$ and substituting these back into the original ODE (equation (3.5.30)). The second method obtained solutions by directly differentiating the values of $d\delta T/dr$ from the numerical solutions using a finite difference stencils shown in equations (3.3.9) and (3.3.10). The results from these two different method were then compared as an internal check of the accuracy of the ODE solver. A plot of the finite difference and ODE solutions is shown in figure 3.6.5. From figure 3.6.5 it can be seen that the calculation of the second order derivative of the perturbed temperature by the

ODE solver is in agreement with the values computed using finite difference methods.

To investigate the accuracy further, the fractional error between the $d^2\delta T_{22}/dr^2$ values computed by the ODE solver and finite differencing are shown in figure 3.6.6. In figure 3.6.6 there are small divergences from zero. This arises due to numerical errors in the ODE solver and the order of error in the finite difference calculation. The error is amplified at the boundaries, particularly at the inner boundary. There is a significant increase in the error at the outer boundary. The errors contained within this finite difference test are of order 10^{-4}. This value is sufficiently small to determine that the ODE solver results of $d^2\delta T_{22}/dr^2$ are correct to the degree of accuracy required.

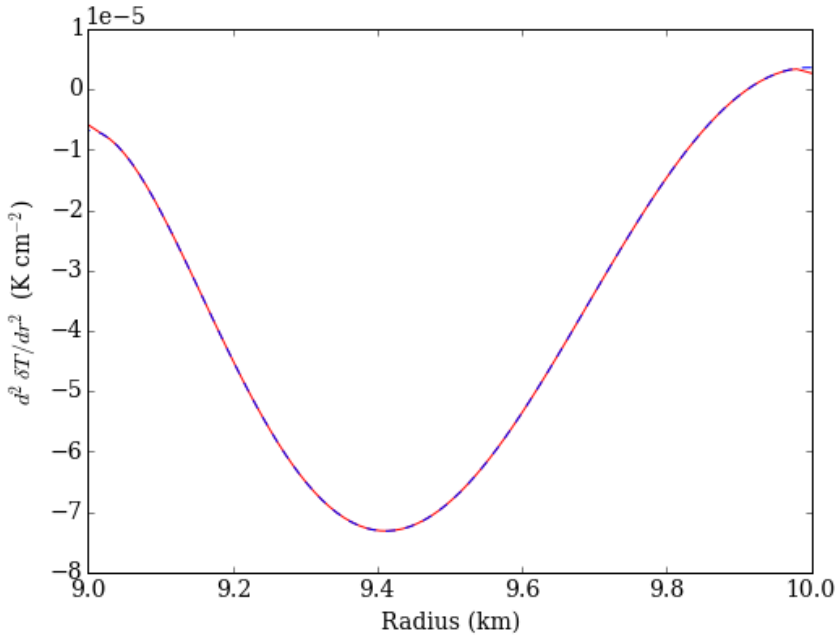

Figure 3.6.5: A test of the accuracy of the ODE solver values, $d^2\delta T_{22}/dr^2$, was calculated using finite differencing. The values from finite differencing were then compared to the ODE solver values. A comparison of these values calculated for an accretion rate of $\dot{M}_1 = 1 \times 10^{-8} M_\odot$ yr^{-1}. The two calculation methods yielded nearly identical results, with small divergences at the boundaries.

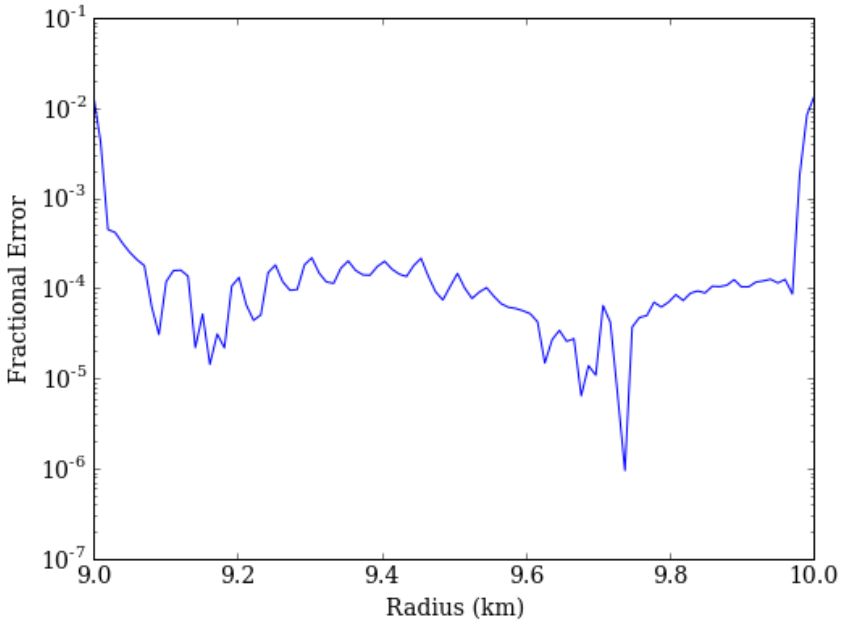

Figure 3.6.6: A plot to determine the accuracy of the ODE solver by comparing $d^2\delta T_{22}/dr^2$ values computed by integration with those calculated using finite difference methods. The values presented here were calculated for an accretion rate of $\dot{M}_1 = 1 \times 10^{-8} M_\odot$ yr^{-1}. In this figure the maximum divergence from zero, which corresponds to the error between the two methods, is $\approx 10^{-2}$. This error is sufficiently small to conclude the ODE solver results are accurate the degree required for these computations.

3.6.3 Summary

The work contained within this chapter has built upon that done by Bildsten (1998) and Ushomirsky et al. (2000), by investigating whether temperature asymmetries can develop in an accreted neutron star crust. This is important as Bildsten (1998) has shown that if temperature asymmetries are present in a neutron star crust, then a mass quadrupole moment could develop. The presence of a mass quadrupole moment, that is misaligned from the axis of rotation of the neutron star, would generate gravitational waves. The loss of angular moment by the production of gravitational waves could explain the observed narrow spin frequencies of low mass X-ray binaries, as this energy loss would balance the spin-up torque transferred by accreted material. In this chapter, a background model of the temperature distribution for a spherically symmetric, constant density, accreted neutron star crust was constructed. A magnetic field was then introduced to generate a temperature perturbation.

In the background model, the magnitude of the heat flux was found to be at a minimum at the outer crust boundary and a maximum at the crust-core interface. This corresponds to heat being deposited into the crust by accretion. In addition to this, heat is radiated out of the crust via neutrino bremsstrahlung radiation. In the crust, it is assumed that the dominant heat transport mechanism is governed by electrons, and the thermal conductivity depends only on the interactions of electrons with phonons and impurities.

On this toy background model, a magnetic field was inserted into the neutron star crust. The addition of a magnetic field induced a temperature perturbation due to the electrons present in the crust, interacting with the magnetic field. Electrons are the dominant heat transport mechanism in the crust. In the presence of a magnetic field, the thermal conductivity is expected to reduce when moving perpendicular to the magnetic field lines. Hall effects would also arise leading to anisotropies in the thermal conductivity. The thermal conductivity parallel to the field lines would be unaffected. This variation in how easily heat is transported through the crust, when a magnetic field is present, may lead to an uneven temperature distribution.

From back of the envelope calculations, the magnetic field was expected to generate a temperature perturbation that is proportional to the magnetisation parameter as $\omega_{\rm B}\tau \sim \frac{\delta T}{T} \sim 4 \times 10^{-5} {\rm B}_9$ for $T = 10^8$ K and $Q_{\rm imp} = 1$. An ellipticity of $\epsilon \sim 10^{-7}$ is expected to be sufficiently large to induce a quadrupole moment that generates enough angular momentum losses, via gravitational wave emission, to balance the spin up torque from accretion. In this toy model, the temperature perturbation induced in the crust by the

magnetic field for $\dot{M} = 10^{-9} M_{\odot}$ yr^{-1} and $Q_{\rm imp} = 1$ was determined as

$$\frac{\delta T}{T} = 2 \times 10^{-6} \mathrm{B}_9. \tag{3.6.5}$$

The ellipticity ϵ required for a sufficiently large mass quadrupole moment is

$$\epsilon = \frac{Q}{I} \approx 5 \times 10^{-8} \left(\frac{\delta T / T}{1\%} \right), \tag{3.6.6}$$

Our results corresponds to an ellipticity of

$$\epsilon = \frac{Q}{I} \approx 1 \times 10^{-11} \mathrm{B}_9, \tag{3.6.7}$$

We also found, that once we linearised in B, only the toroidal components of the magnetic field remained.

Although this value is a couple of orders of magnitude smaller than what is required, it is worthwhile investigating this temperature perturbation method in more detail. The next step would be to upgrade the toy model for a more realistic star that has a variable density. This would enable a clearer depiction to be drawn as to the significance of the effect the magnetic field has the temperature distribution in an accreted neutron star crust.

CHAPTER 4

Thermal profile of neutron star crust for a realistic equation of state

In this chapter, a model of the temperature distribution in a spherically symmetric, accreted neutron star crust for a realistic equation of state of variable density is developed. A magnetic field is then inserted to incite a temperature perturbation in the accreted crust. This work builds on the work from chapter 3 by solving the heat equation for a more realistic star, one of varying density.

In the chapter 3, it was shown that the presence of a magnetic field in a spherically symmetric, constant density, accreted neutron star crust would induce a temperature perturbation $\delta T/T$ of $2 \times 10^{-6}\mathrm{B}_9$ with an impurity parameter $Q_{\mathrm{imp}} = 1$. This perturbation ratio scales linearly with magnetic field strength. For a quadrupole moment to develop in the crust, that is sufficiently large to generate gravitational waves that balance the spin-up angular momentum transfer from accretion, a temperature perturbation of $\delta T/T \sim 1\%$ is required (Ushomirsky et al., 2000). The temperature perturbation calculated in the toy, constant density model is approximately two orders of magnitude smaller than that required to generate a sufficiently large mass quadrupole moment for a 10^{12}G field. As this toy model is a simplified case, it is worth while undertaking a more thorough investigation, for a neutron star with a realistic equation of state, to truly quantify how large temperature asymmetries can develop in the crust of a spherically accreting neutron star.

In this chapter a variable density neutron star with an accreted crust is constructed. Ini-

tially, both the Newtonian and relativistic hydrostatic structure equations are used to determine whether a Newtonian accreted crust is a good approximation. Next, a background thermal profile of the crust is composed, building on the work in the previous chapter by including density dependence, which was previously set as constant. The temperature profile is then perturbed by inserting a magnetic field. An investigation into the significance of this perturbation on the temperature profile of the neutron star crust is conducted.

4.1 Background hydrostatic structure

A neutron star can be constructed numerically from the hydrostatic structure equations. This enables a description of the pressure-density relationship of a spherically symmetric neutron star to be obtained. For simplicity, we will begin by considering Newtonian gravity. The general form of the hydrostatic equilibrium equation is

$$\boldsymbol{\nabla} P = -\rho \boldsymbol{\nabla} \Phi, \tag{4.1.1}$$

where ρ is density, P is pressure and Φ is the gravitational potential. For a spherically symmetric neutron star, the differential hydrostatic equilibrium equation is written as

$$\frac{dP}{dr} = -\frac{Gm(r)\rho}{r^2}, \tag{4.1.2}$$

where $m(r)$ is the mass within radius r, which can be written in the differential form

$$\frac{dm(r)}{dr} = 4\pi r^2 \rho. \tag{4.1.3}$$

An expression for the pressure-density relation can be written as

$$\frac{1}{r^2}\frac{d}{dr}\left(\frac{r^2}{\rho}\frac{dP}{dr}\right) = -4\pi G\rho, \tag{4.1.4}$$

where G is the gravitational constant.

4.1.1 Solving Newtonian hydrostatic structure equations

The pressure-density relation for a neutron star can be computed by solving the Newtonian hydrostatic equilibrium equation shown in equation (4.1.4). The hydrostatic equilibrium equation is a second order differential equation, which is best solved numeri-

cally as a set of two first order differential equations which are

$$\begin{aligned} \frac{dm}{dr} &= 4\pi r^2 \rho(r), \\ \frac{dP}{dr} &= -\frac{Gm(r)\rho(r)}{r^2}. \end{aligned} \tag{4.1.5}$$

The equations in (4.1.5) are solved using input values from a tabulated equation of state. Solving the equations in this way, allows the mass and radius of a neutron star to be calculated for the corresponding equation of state.

Equation (4.1.5) was solved using the python built-in numerical integration function scipy.integrate.ode. This integrator was selected as it allowed the integration step size to change, subject to appropriate conditions being satisfied. The ability to vary the integration step size was important for determining the radius of the star.

The integration routine was set to integrate the hydrostatic structure equations from the centre of the neutron star to the surface, for incrementally increasing values of radial position. To stop the integration from going beyond the surface of the star, a condition was placed to ensure integration could only occur when the pressure of the star was positive. If this condition was met, the integration values calculated were recorded. This process was then repeated for each radial step until the positive pressure condition was no longer satisfied. Initially the radial step size was set to 1 km. To enable the radial surface to be resolved to a higher order of accuracy, an additional routine was employed for when the positive pressure condition was not met.

If the integration stopped, due to the pressure becoming negative, the integration values were reset to the values obtained from the last successful iteration of the integration routine. The radial step size was then reduced by 50%, and the integration routine recommenced. This process then continues until the pressure becomes negative and the desired accuracy has been attained.

4.1.1.1 Newtonian hydrostatic structure results

Initially, the Newtonian hydrostatic structure equations were solved using the SLy equation state, which describes both the solid crust and the liquid core of neutron stars in a physically consistent manner, and the FPS tabulated equation of state data for a cold catalysed neutron star from Haensel and Potekhin (2004a), in preparation for solving the Tolman–Oppenheimer–Volkoff equation. A plot of the equation of state data was created to show the pressure-density relation for each equation of state, this is shown in 4.1.1.

The hydrostatic structure equations shown in equation (4.1.4) were solved to determine

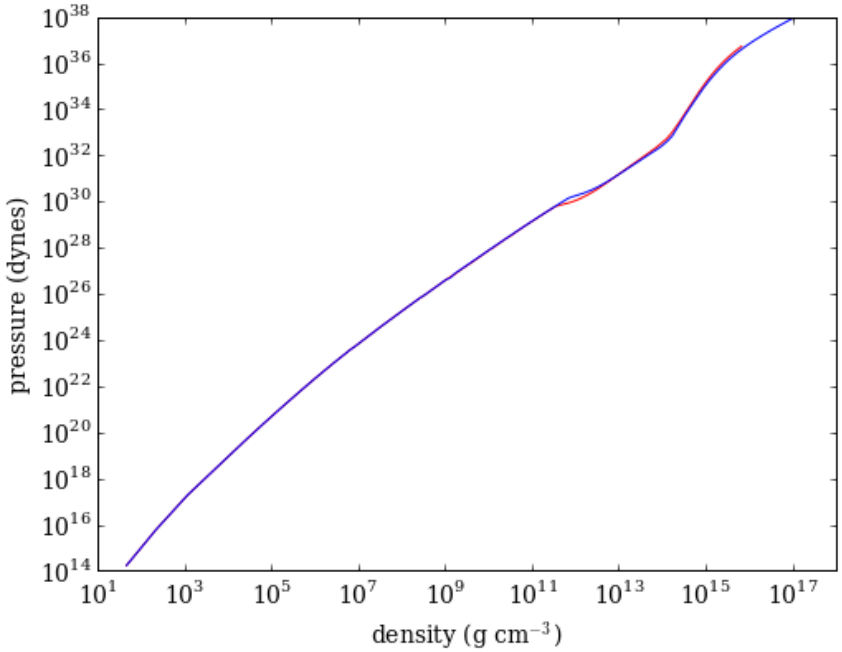

Figure 4.1.1: A plot of pressure versus density for both SLy (red line) and FPS (blue line) equation of state data (Haensel and Potekhin, 2004a). There is a fractional difference between each of the equation of state values of pressure of order $\sim 10^{-1}$.

the final mass and radius of a neutron star with central density $\rho_c = 1.5 \times 10^{15}$g cm^{-3} for both the SLy and FPS tabulated equation of state data. These plots are shown in figure 4.1.2. For both equations of state, the final radius of the star is approximately 18 km. This is much larger than expected, as neutron stars are typically expected to have a radius of the order 10 km. The two equations of state also produced very high mass stars, with total masses of about $4M_\odot$ and $6M_\odot$, much greater than expected.

An exploration of the central density parameter space was undertaken to investigate the influence the initial conditions have on the final solution. Graphical representations of how the radius and mass of a star varies for different initial central density values are shown in figures 4.1.3 and 4.1.4 respectively. From these figures it can be seen that a lower central density generates neutron stars with smaller radii and lower masses when compared to a higher central density value. A sensible initial value of central density $\rho \approx 10^{15}$g cm^{-3}, produces a star with radius $r \approx 15$km and mass $m \approx 2.5M_\odot$.

The values obtained from both equations of state are considerably larger than the expected values of $r \approx 10$ km and $m \approx 1.4$ M$_\odot$. The stars produced are considerably larger in radius resulting in a lower density with a slight increase in central density. This suggests approximating the neutron stars to be in the Newtonian limit is not accurate. An investigation into the suitability of the Newtonian approximation can be conducted by comparing these results to those obtained in the relativistic regime, using the Tolman–Oppenheimer–Volkoff (TOV) hydrostatic structure equations.

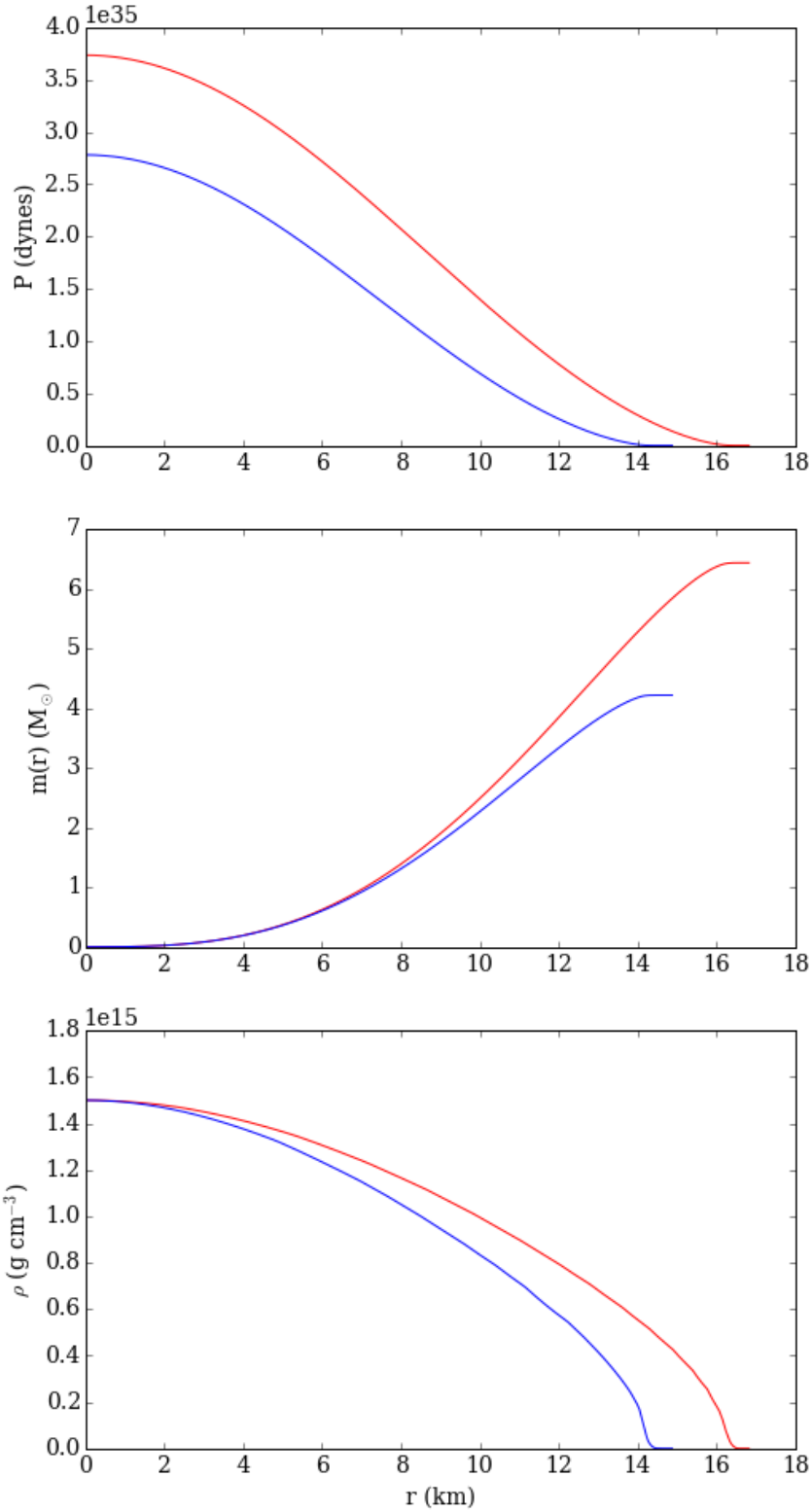

Figure 4.1.2: A plot of $P(r)$, $m(r)$ and $\rho(r)$ as a function of radius for a star with central density $\rho = 1.5 \times 10^{15}$ g cm^{-3} and total mass 4M$_\odot$ and 6M$_\odot$ for the FPS (blue line) and SLy (red line) equations of state data respectively solved in Newtonian gravity (Haensel and Potekhin, 2004a).

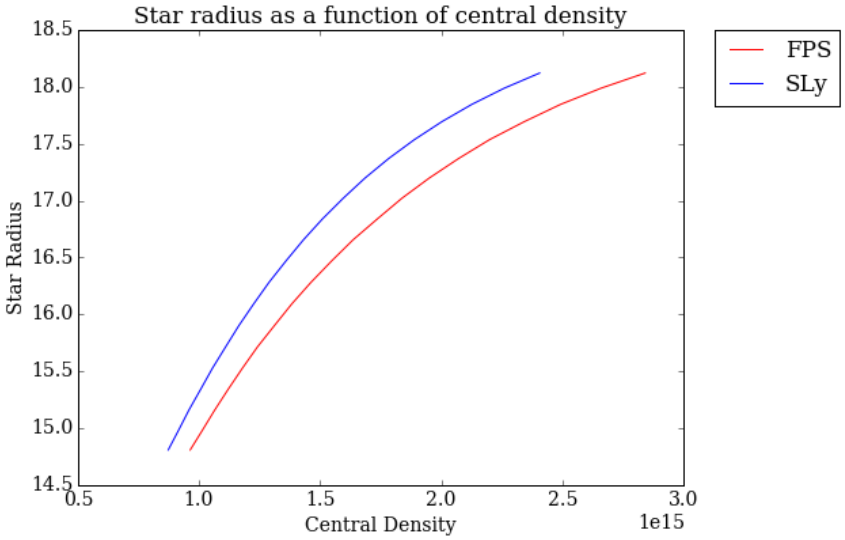

Figure 4.1.3: This figure shows the range of neutron star radii as calculated for different central densities in Newtonian gravity. The FPS equation of state data is represented in blue, SLy data in red.

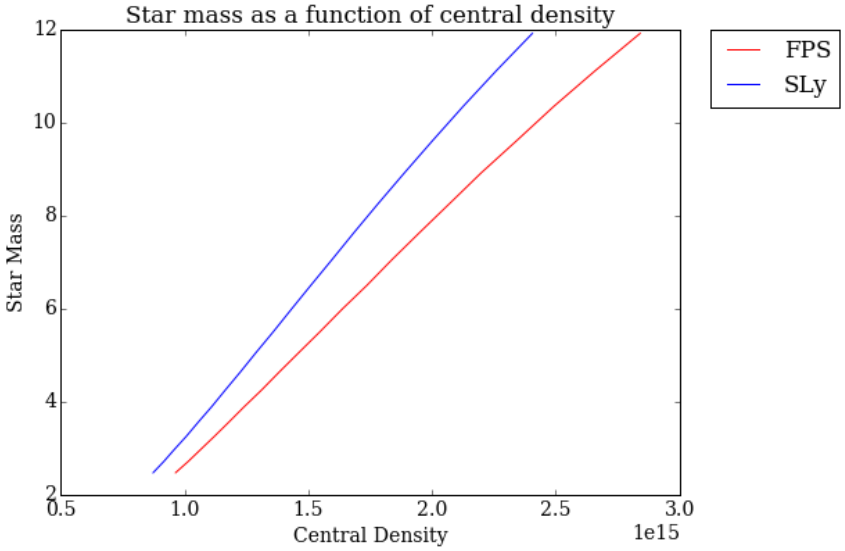

Figure 4.1.4: This figure shows the range of neutron star masses as calculated for different central densities in Newtonian gravity. The FPS equation of state data is represented in blue, SLy data in red.

4.1.2 Solving the relativistic hydrostatic structure equations

A relativistic description of the pressure-density relation for a static spherically symmetric star can be obtained from the Einstein equations.

The metric for a static, spherically symmetric spacetime is

$$ds^2 = -e^{\nu(r)}dt^2 + e^{\lambda(r)}dr^2 + r^2(d\theta^2 + \sin^2\theta\, d\phi^2), \tag{4.1.6}$$

where $\nu(r)$ and $\lambda(r)$ are functions that vary only with r (Hartle, 2003, p. 520). The neutron star is approximated to a perfect fluid with stress-energy tensor

$$T^{\alpha\beta} = (\rho + p)u^\alpha u^\beta + g^{\alpha\beta}p, \tag{4.1.7}$$

where $u^\alpha = (e^{-\nu/2}, 0, 0, 0)$ is the four-velocity. In the static weak field limit $\nu(r) \to 2\Phi(r)/c^2$, where $\Phi(r)$ is the Newtonian gravitational potential inside the star. From the Einstein equations and using the definition

$$e^{-\lambda(r)} \equiv 1 - \frac{2Gm(r)}{rc^2}, \tag{4.1.8}$$

the equations of structure for spherical relativistic stars are

$$\frac{dm(r)}{dr} = 4\pi r^2 \rho(r), \tag{4.1.9a}$$

$$\frac{dp(r)}{dr} = -\left[\rho(r) + p(r)\right]\left(\frac{Gm(r)}{c^2} + \frac{4\pi r^3 G p(r)}{c^4}\right)\left(\frac{r}{r - \frac{2Gm}{c^2}}\right)^{-1}, \tag{4.1.9b}$$

$$\frac{d\nu(r)}{dr} = -\frac{1}{\rho(r) + p(r)}\frac{dp(r)}{dr}, \tag{4.1.9c}$$

where $m(r)$ is the mass inside the circumferential radius r and ϵ is the energy per unit volume. These are known as the Tolman-Oppenheimer-Volkoff (TOV) equations (Oppenheimer and Volkoff, 1939).

The TOV equations were solved using the SLy tabulated equation of state data (Haensel and Potekhin, 2004a) to solve for both the neutron star crust and core. A second hybrid data set was created to produce a neutron star with an SLy core and an accreted crust. The accreted crustal equation of state data was taken from Haensel and Zdunik (1990a). The hybrid data is comprised of SLy data for the density ranges $1.462 \times 10^{13}\,\mathrm{g\,cm^{-3}} < \rho_{\mathrm{core}} < 6.749 \times 10^{15}\,\mathrm{g\,cm^{-3}}$ with accreted data appended onto the SLy core data for the density range $3.207 \times 10^{7}\,\mathrm{g\,cm^{-3}} < \rho_{\mathrm{crust}} < 1.462 \times 10^{13}\,\mathrm{g\,cm^{-3}}$. These density ranges were selected to ensure the full data set of the accreted crust tabulated data from Haensel and Zdunik (1990a) was used. A plot of the pressure-density relation for the hybrid data is shown in figure 4.1.5. The greatest variation in the two models occurs at higher densi-

ties. Figure 4.1.6 highlights these differences by zooming in on the gradient for relevant density range.

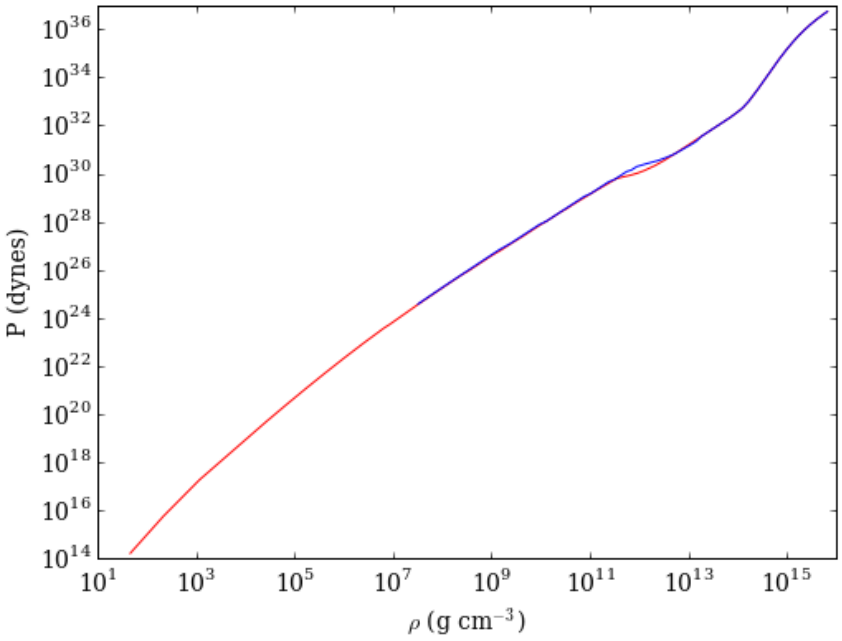

Figure 4.1.5: A graphical representation of the $p(\rho)$, SLy data in red and hybrid data in blue (SLy core with accreted crust) as calculated from the tabulated equation of state data (Haensel and Potekhin, 2004a) (Haensel and Zdunik, 1990a).

The TOV equations were solved using the same numerical integration methods as used to solve the Newtonian hydrostatic structure equations described in section 4.1.1.1. The SLy and hybrid data was solved for three different cases; *i)* SLy data solved using TOV equations, *ii)* Hybrid data solved using TOV equations and *iii)* Hybrid data solved using TOV equations for the core and Newtonian hydrostatic equations for the accreted crust, all for a central density of $\rho = 1.5 \times 10^{15}$g cm^{-3}. These three different methods of solving the equation of state data were employed to enable comparisons to be drawn between: a relativistic star consisting of cold catalysed matter with that of an accreted crust and a neutron star with a relativistic accreted crust with a Newtonian accreted crust. From this comparison, we will be able to determine if solving the accreted crust equation of state data using the Newtonian hydrostatic structure equations is a good approximation to make. We would prefer to use the model for a neutron star with a Newtonian accreted crust, as this is the simpler case, making it easier to incorporate additional physics, specifically a magnetic field later in this chapter. In the future, it would be nice to build on this model to account for relativistic effects, although this is currently beyond the scope of this work.

Figure 4.1.7 shows the $p(r)$, $m(r)$ and $\rho(r)$ relations for each of these three cases. In figure 4.1.7 it is quite difficult to resolve by eye the variation that arises in each case. Figure 4.1.8 shows the data for each of the three cases for the accreted crustal radii only, to show

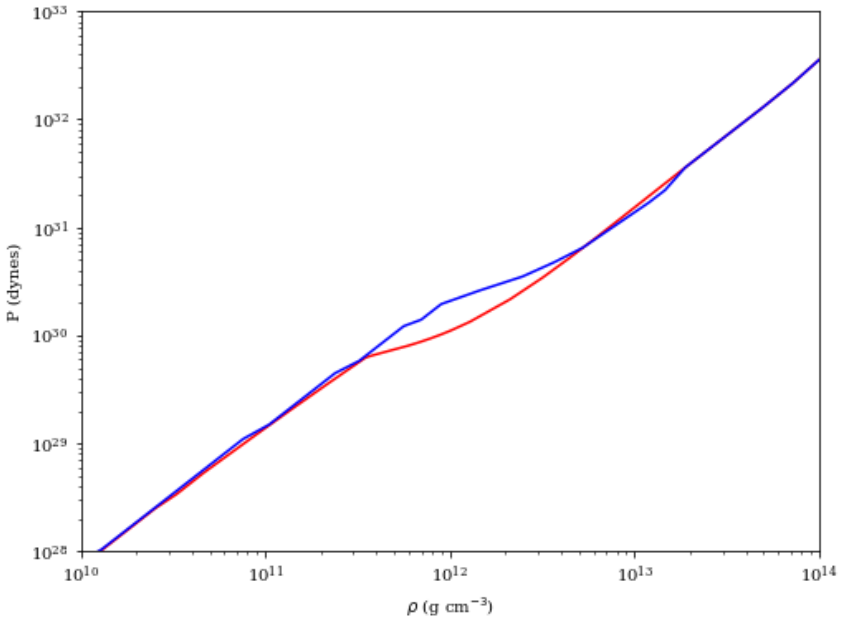

Figure 4.1.6: Same as figure 4.1.5 over a narrower density range to highlight differences in the two models.

more clearly how the data diverges for the different models.

From figure 4.1.8 it can be seen that case *iii)* for an accreted crust solved in Newtonian gravity, shown as the blue curve, yields a neutron star with a larger radius when compared to case *i)* for the non-accreted crust in relativistic gravity. The differences between case *i)* and *ii)*, for an accreted crust solved in relativistic gravity, is small. The cases *i)* and *ii)* produce a neutron star of $\approx 1.847 M_{\odot}$ and a radius of $\approx$ 11.1km, whereas case *iii)* produces a star with radius $\Delta r \approx 300$ m larger.

The Newtonian approximation produces a neutron star with more mass $\Delta M \approx 0.0004$ $M_{\odot}$ and a larger radius $\Delta r \approx 300$ m than when solving in the relativistic limit. These differences are sufficiently small that we will, in the remainder of this thesis, use this star i.e. with relativistic gravity in the core and Newtonian gravity in the accreted crust. This suggests that using the Newtonian hydrostatic equations to solve for the accreted crust on a TOV core is a suitable approximation, whereas using the Newtonian hydrostatic equations to solve for the whole neutron star (core and crust) as shown in section 4.1.1.1, is not a good approximation.

Ushomirsky et al. (2000) compute a crust from the Newtonian hydrostatic structure equations to have a thickness of 1.1 km and a mass of 0.06 $M_{\odot}$. The hybrid equation of state data solved for a TOV core and Newtonian crust yields a crust with thickness 1.45 km and mass 0.09 $M_{\odot}$, for a crust/core boundary density of $\rho = 2 \times 10^{14}$ g cm^{-3}. This result is a little thicker and more massive than that calculated by Ushomirsky et al. (2000).

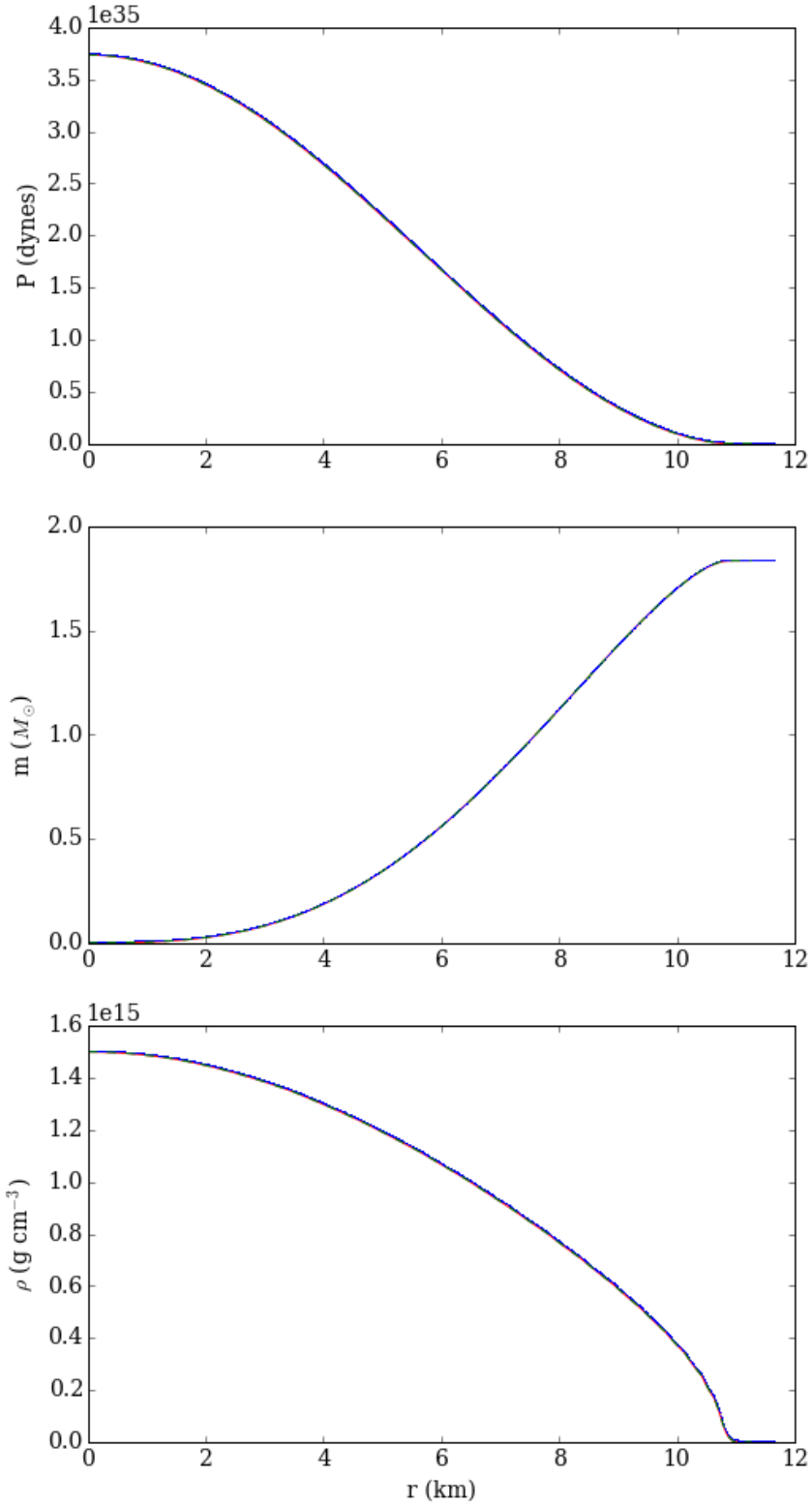

Figure 4.1.7: A graphical representation of the $p(r)$, $m(r)$ and $\rho(r)$ for case *i)* TOV SLy data in red, case *ii)* TOV hybrid data (SLy core with accreted crust) in green and case *iii)* TOV SLy core and Newtonian accreted crust in blue, calculated using the tabulated equation of state data (Haensel and Potekhin, 2004a) (Haensel and Zdunik, 1990a). The results presented here are difficult to distinguish by eye. The results for the crustal densities only are presented in figure 4.1.8, where a more meaningful comparison can be made.

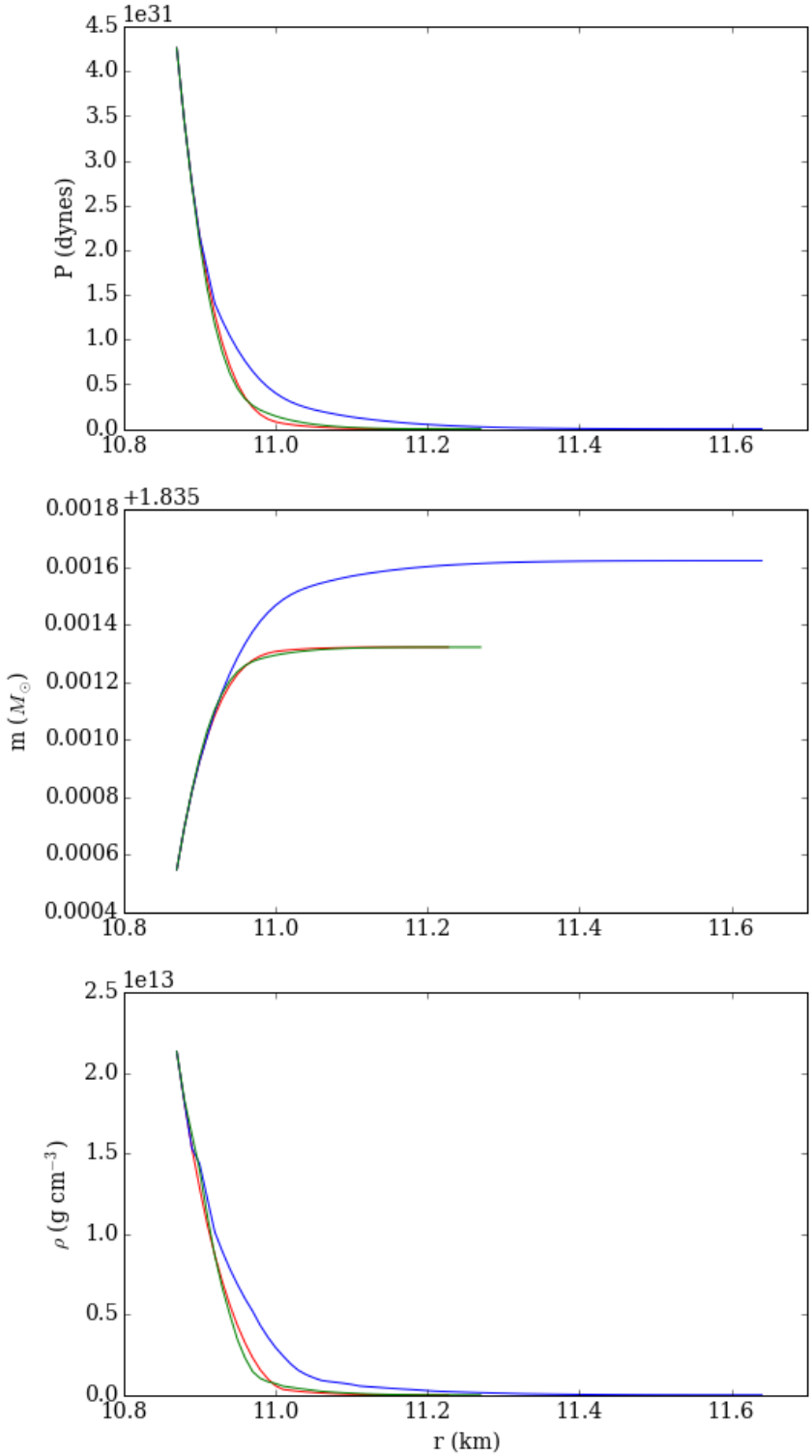

Figure 4.1.8: Same as figure 4.1.7, but for the crustal radii values only.

As an additional check on our stellar structure calculations, we also considered results shown in Haensel and Zdunik (1990a). Specifically, in Haensel and Zdunik (1990a) a plot of density and radius is provided and shown in figure 4.1.10. This figure shows the density profile of an accreted neutron star crust and a standard neutron star built out of cold catalysed matter, as described by the BPS model. This model was recreated by solving the FPS equation of state data using the TOV ODE solver detailed in this work. This enables a comparison of the accuracy of this model to be drawn and is shown in figure 4.1.9. It was possible to use the FPS data in place of the BPS data, as the FPS equation of state data is a modern improvement to the BPS equation of state data (Haensel and Potekhin, 2004b). The results from this calculation, along with figure 3 from Haensel and Zdunik (1990a) is shown in figure 4.1.10. Although the equation of state data is slightly different in the two models, the shape of the two graphs correspond well with each other. In both models, the accreted neutron star crust is slightly larger than that of the cold catalysed matter crust. The most substantial difference in the two models is the radius of the neutron stars produced, where the neutron star from this model is 1km smaller.

To sum up, using the accreted crust information from Ushomirsky et al. (2000) and Haensel and Zdunik (1990a) to make a comparison with the model produced by solving the TOV and Newtonian equations of state in this work, suggests solving for the accreted crust in the Newtonian approximation on a relativistic neutron star core, is a suitable assumption to make.

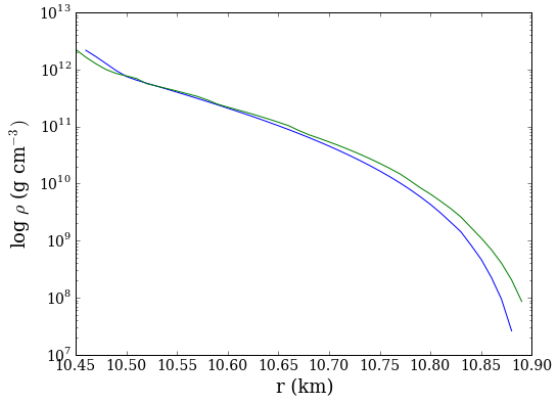

Figure 4.1.9: A plot of how the density varies with radius for a cold catalysed FPS equation of state neutron star crust (blue line) and an accreted crust (green line). In both cases the mass of the neutron star is $M = 1.4\mathrm{M}_{\odot}$.

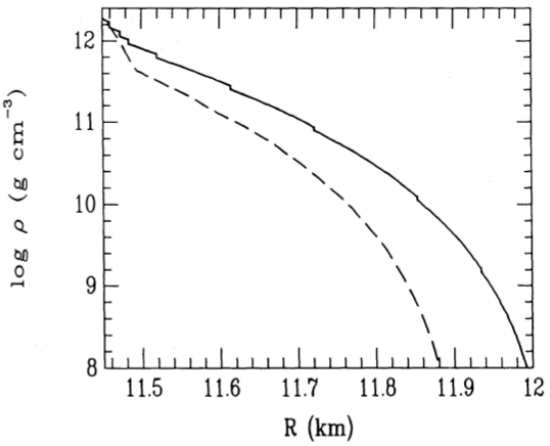

Figure 4.1.10: The density profile of an accreted neutron star crust (solid line) and a cold catalysed crust described by the BPS equation of state model (dashed line), for a neutron star with mass $M = 1.4\mathrm{M}_{\odot}$. This image is figure 3 in Haensel and Zdunik (1990a).

4.2 Density dependent variables

The hydrostatic structure equations given in section 4.1 are used to build a neutron star with an SLy core, solved in relativistic gravity using the TOV equations, with an accreted crust which is solved in Newtonian gravity.

In an accreted neutron star crust, many of the physical parameters are a function of position. When moving from the crust towards the centre of the star, the pressure and density monotonically increase. As the radius decreases, neutrons start dripping out of nuclei. Electron capture and pycnonuclear reactions occur at different densities giving rise to changes in composition. Haensel and Zdunik (1990a) have researched the evolution of matter in an accreting neutron star crust and produced tabulated values detailing how the composition changes with density. This table also includes the amount of heat deposited into the crust from nuclear reactions as well as the mass fraction of free neutrons X_n. Table 4.2.1 shows these values along with an additional column containing the radial values corresponding to the listed densities. These radial values were computed by solving for a neutron star with a TOV core (constructed from the SLy equation of state data) with an accreted Newtonian crust using hydrostatic equations as detailed in section 4.1. From the values listed in table 4.2.1 the density dependent variables of the crust are computed as a function of position.

$P_{\max}$ (dyn cm^{-2})	$\rho_{\max}$ (g cm^{-3})	r (km)	Z	A	μ_{e} (MeV)	X_{n}
7.24e+26	1.49e+09	11.599	26	56	0.00	0.01
9.57e+27	1.11e+10	11.498	24	56	0.00	0.01
1.15e+29	7.85e+10	11.335	22	56	0.00	0.01
4.75e+29	2.50e+11	11.210	20	56	0.00	0.01
1.36e+30	6.11e+11	11.098	18	56	0.00	0.05
1.98e+30	9.08e+11	11.058	16	52	0.07	0.09
2.25e+30	1.13e+12	11.044	14	46	0.18	0.10
2.64e+30	1.46e+12	11.029	12	40	0.29	0.47
2.77e+30	1.77e+12	11.023	20	68	0.39	0.05
3.22e+30	2.13e+12	11.013	18	62	0.45	0.05
3.82e+30	2.63e+12	11.001	16	56	0.50	0.06
4.70e+30	3.34e+12	10.986	14	50	0.55	0.07
6.04e+30	4.38e+12	10.969	12	44	0.61	0.28
7.23e+30	5.66e+12	10.956	18	66	0.70	0.02
9.24e+30	7.04e+12	10.941	16	60	0.73	0.02
1.23e+31	8.98e+12	10.925	14	54	0.76	0.03
1.60e+31	1.13e+13	10.913	12	48	0.79	0.11
1.61e+31	1.14e+13	10.912	24	96	0.79	0.01
1.82e+31	1.25e+13	10.903	22	88	0.80	0.00

Table 4.2.1: Table of the composition of an accreted neutron star crust listed according to the maximum density $\rho_{\max}$ and pressure $P_{\max}$. These values were taken from Haensel and Zdunik (1990a), except for the values in the radial column.

The values of proton number Z, mass number A, electron chemical potential $\mu_{\rm e}$ and the mass fraction of free neutrons $X_{\rm n}$ listed in table 4.2.1 are given for the corresponding maximum density, pressure and radius at which the nuclides are present. Initially, a function was created in python to output the mass number A, proton number Z and mass fraction of free neutrons $X_{\rm n}$ for any density value. This was important as the nuclear composition varies with density in discrete steps which corresponds to different electron capture layers. These composition parameters are plotted as a function of density using the python function which determines these values for any given density (using the tabulated data), and then checked against the tabulated values directly from Haensel and Zdunik (1990a) in figure 4.2.2.

From the density dependent parameters Z, A and $X_{\rm n}$ the density dependent variables can be computed. Initially the baryon number density is written as

$$n_{\rm b} = \frac{\rho}{m_{\rm b}}, \tag{4.2.1}$$

where $m_{\rm b}$ is the baryon mass. From this, the electron number density $n_{\rm e}$ is determined as

$$n_{\rm e} = n_{\rm b}\frac{Z}{A}\left(1 - X_{\rm n}\right). \tag{4.2.2}$$

The ion number density $n_{\rm ion}$ is calculated by dividing the electron number density by the proton number as

$$n_{\rm ion} = \frac{n_{\rm e}}{Z}. \tag{4.2.3}$$

A general expression for the Fermi momentum (Yakovlev and Urpin, 1980) is written as

$$p_{\rm F} = \hbar\left(3\pi^2 n_{\rm e}\right)^{\frac{1}{3}}. \tag{4.2.4}$$

The electron chemical potential is then calculated from the relativistic mass-energy equivalence principle as

$$\mu_{\rm e} = \left(m_{\rm e}^2 c^4 + p_{\rm F}^2 c^2\right)^{\frac{1}{2}}, \tag{4.2.5}$$

where $m_{\rm e}$ is the electron rest mass and c is the speed of light.

The effective electron mass $m_{\rm e}^*$ is equal to the electron chemical potential divided by c^{-2} and written as

$$m_{\rm e}^* = \left(m_{\rm e}^2 + \frac{p_{\rm F}^2}{c^2}\right)^{\frac{1}{2}}. \tag{4.2.6}$$

An expression for the Fermi velocity is derived from the non-relativistic expression for

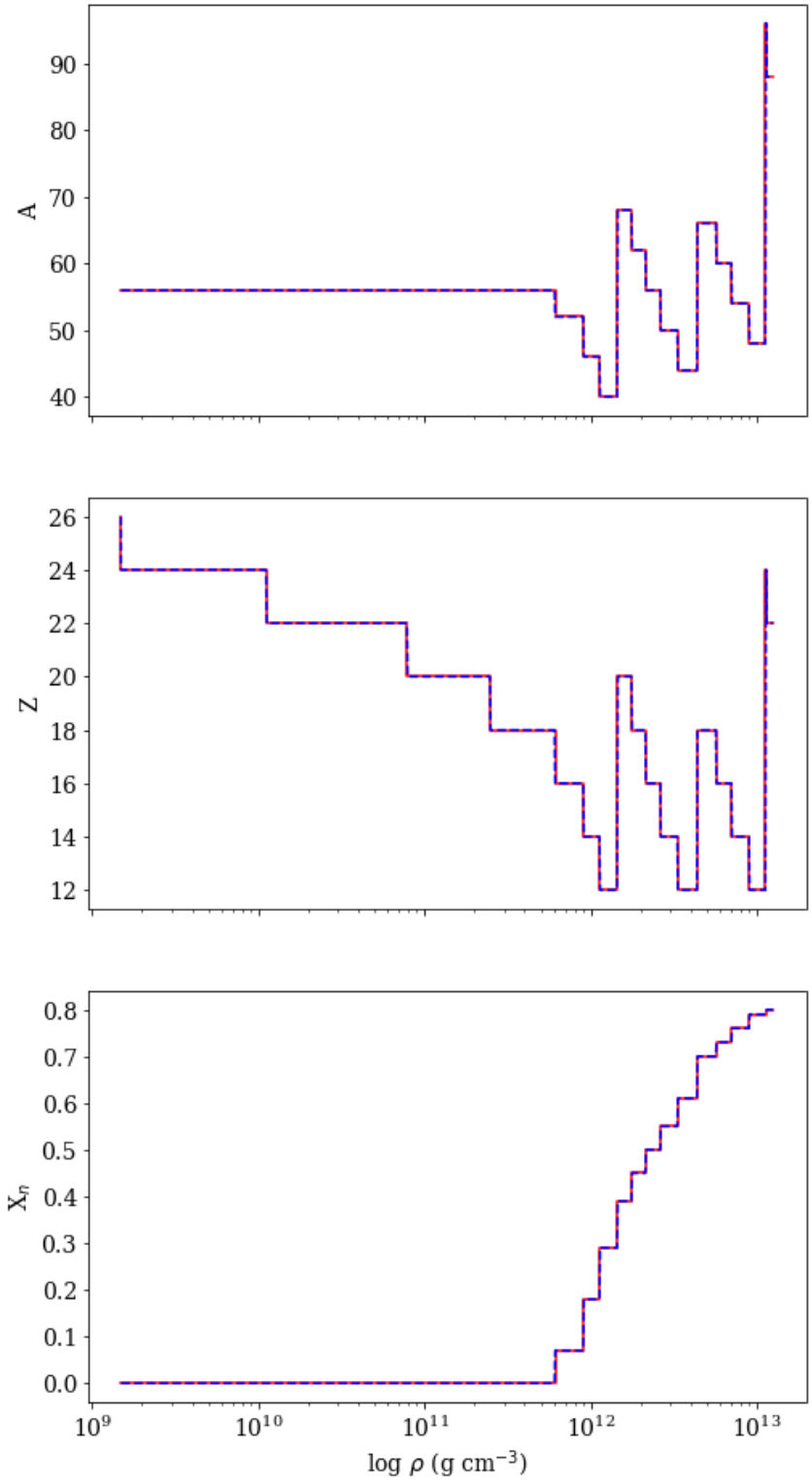

Figure 4.2.2: This figure shows how the mass number A, proton number Z and mass fraction of free neutrons X_n varies with density in an accreted neutron star crust. The red values are taken directly from 4.2.1 and the values shown in blue were obtained by a function written in python which extracts A, Z and X_n from the data set for any given density value that is within the data range. The two curves in each plot should agree exactly.

Fermi energy $E_{\rm F} = \gamma m_0 c^2$ where $\gamma = \left(1 - \frac{v_{\rm F}^2}{c^2}\right)^{-\frac{1}{2}}$ as

$$v_{\rm F} = \left[c^2\left(1 - \left(\frac{E_{\rm F}}{m_0 c^2}\right)^{-2}\right)\right]^{\frac{1}{2}}. \tag{4.2.7}$$

These accreted crust density dependent variables are plotted as a function of radius and shown in figures 4.2.3 and 4.2.4.

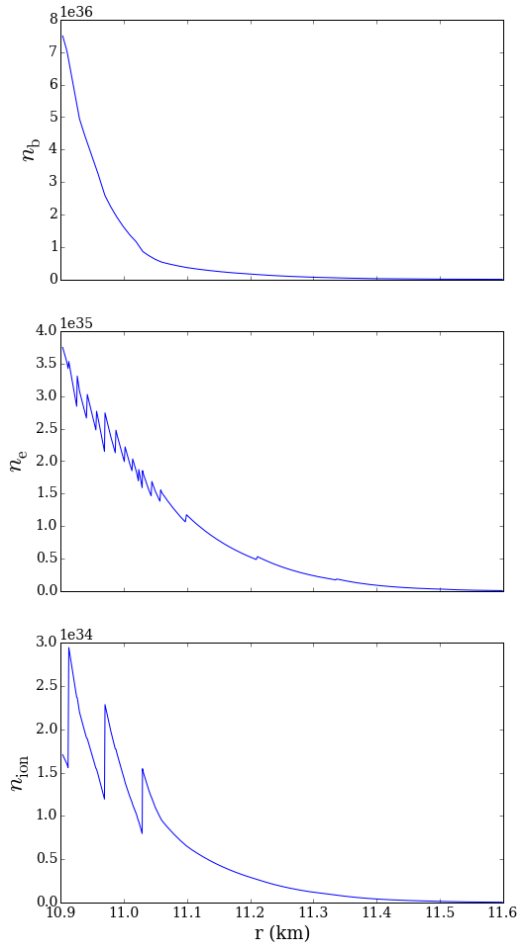

Figure 4.2.3: A plot to show how the density dependent parameters $n_{\rm b}$, $n_{\rm e}$ and $n_{\rm ion}$ vary as a function of radius inside the neutron star crust. All variables are given in cgs units.

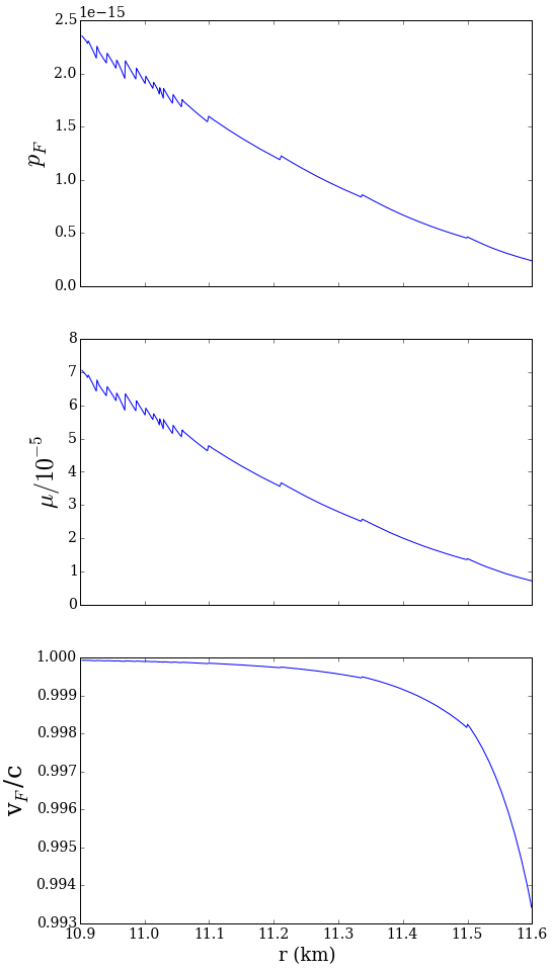

Figure 4.2.4: A plot to show how the density dependent parameters $p_{\rm F}$, μ and $v_{\rm F}$ vary as a function of radius inside the neutron star crust. All variables are given in cgs units.

The density dependent variables of an accreted neutron star crust can now be used to calculate the thermal conductivity. The thermal conductivity used in this chapter follows the formalism used in chapter 3 which is written as

$$K(\rho, T) = \frac{\pi^2 k_{\rm B}^2 n_{\rm e}(\rho) T}{3 m_{\rm e}^*(\rho)} \tau(\rho, T), \tag{4.2.8}$$

where $k_{\rm B}$ is the Boltzmann constant, $n_{\rm e}$ is electron number density and $m_{\rm e}^*$ is the elec-

tron effective mass (Yakovlev and Urpin, 1980). τ is the relaxation time. The thermal conductivity in the crust is governed by electron-phonon scattering $\nu_{\rm ep}$ and electron-impurity $\nu_{\rm eQ}$ scattering (Brown and Cumming, 2009), where the total scattering frequency is $\nu = \nu_{\rm ep} + \nu_{\rm eQ}$. Electron-phonon scattering is written as

$$\nu_{\rm ep} = \frac{13 e^2 k_{\rm B} T}{\hbar^2 c}, \tag{4.2.9}$$

where e is the charge of an electron and $\hbar$ is the reduced Planck constant. Electron-impurity scattering is written as

$$\nu_{\rm eQ} = \frac{4\pi Q_{\rm imp}(\rho) e^4 n_{\rm ion}(\rho)}{p_{\rm F}^2 v_{\rm F}} \Lambda_{\rm imp}, \tag{4.2.10}$$

where

$$Q_{\rm imp}(\rho) \equiv n_{\rm ion}^{-1(\rho)} \sum_i n_i (Z_i - \langle Z \rangle)^2, \tag{4.2.11}$$

is the impurity parameter, $\Lambda_{\rm imp} \sim 1$ is the coulomb logarithm, $n_{\rm ion} = \frac{n_{\rm e}}{Z}$ is the ion number density, p_F the Fermi momentum and $v_{\rm F}$ the Fermi velocity.

The thermal conductivity shown in equation (4.2.8) can be rewritten by collecting density dependent and temperature dependent terms as

$$K(\rho, T) = f_K(\rho) T \frac{1}{C_{\rm ep} T + \nu_{\rm eQ}}, \tag{4.2.12}$$

where

$$\begin{aligned} f_K(\rho) &= \frac{\pi^2 k_{\rm B}^2 n_{\rm e}}{3 m_{\rm e}^*}, \\ C_{\rm ep} &= \frac{13 e^2 k_{\rm B}}{\hbar^2 c}. \end{aligned} \tag{4.2.13}$$

The variables f_k, $\nu_{\rm eQ}$ and $K(T)$ can be computed as a function of radius if the temperature is known, using the tabulated values from Haensel and Zdunik (1990a) directly, ensuring the discrete nature of the density jumps, caused by sharp composition changes in the electron capture layers, is retained. Alternatively these functions can be computed as smoothly varying functions of radius by interpolating between the different density values contained with the tabulated data set. This results in a slight loss of physical information about the crust. For accuracy, we will use the variable values as calculated directly by Haensel and Zdunik (1990a), retaining the discrete density jumps, for calculations in our model.

4.3 Background Thermal Profile

The background thermal profile of a spherically symmetric accreted neutron star crust of varying density is modelled from the heat equation. Following the treatment given in chapter 3 and accounting for the density dependent variables, the heat flux for a spherically symmetric neutron star crust is written as

$$\boldsymbol{F} = -K\boldsymbol{\nabla}T, \tag{4.3.1}$$

where K is the scalar thermal conductivity. Following the treatment of Ushomirsky et al. (2000), the divergence of the flux can be written as

$$\boldsymbol{\nabla}\cdot\boldsymbol{F} = \dot{Q}, \tag{4.3.2}$$

where the net rate of change of heat per unit time $\dot{Q}$ is written as

$$\dot{Q} = \rho(\epsilon_{\rm nuc} - \epsilon_{\nu}), \tag{4.3.3}$$

where $\rho\epsilon_{\rm nuc}$ is nuclear heating and $\rho\epsilon_{\nu}$ is neutrino cooling.

An expression for the second order derivative of temperature with respect to radius is obtained by combining equations (4.3.1) and (4.3) and rearranging to give

$$\frac{d^2T}{dr^2} = -\frac{1}{K(\rho,T)}\frac{dK(\rho,T)}{dr}\frac{dT}{dr} - \frac{2}{r}\frac{dT}{dr} - \frac{\dot{Q}}{K(\rho,T)}. \tag{4.3.4}$$

Using equation (4.2.12) the differential equation shown in (4.3.4) can be written as

$$\frac{d^2T}{dr^2} = \frac{f'_{\rm K}}{f_{\rm K}}\frac{dT}{dr} + \frac{\nu_{\rm eQ}}{\nu}\frac{1}{T}\left(\frac{dT}{dr}\right)^2 - \frac{\nu'_{\rm eQ}}{\nu}\frac{dT}{dr} - 2\frac{dT}{dr} - \frac{\dot{Q}}{K}, \tag{4.3.5}$$

where the prime denotes a derivative w.r.t. r.

Alternatively, a thermal profile of the accreted crust can be constructed by solving a pair of coupled first order differential equations. An expression for the temperature derivative with respect to radius can be determined from equation 4.3.1, by exploiting the spherically symmetry to consider only the radial components as

$$\frac{dT}{dr} = -\frac{F_{\rm r}}{K}. \tag{4.3.6}$$

From equation (4.3), the derivative of the flux with respect to radius is

$$\frac{dF_{\rm r}}{dr} = -\frac{2}{r}F_{\rm r} + \dot{Q}. \tag{4.3.7}$$

This results in two simpler appearing equations without the requirement to find the derivatives of some of the density dependent variables.

Initially it was unclear which would be the best method to employ. In the previous chapter, when calculating the thermal profile of the neutron star crust, the first method shown here, of solving a second order differential equation, was employed. It was thought that this method would be sufficient to use for a star with a realistic equation of state. Upon further investigation, due to the discrete nature of the density dependent functions, this may not be the best method, as the derivatives of these functions don't converge. To overcome this, interpolation techniques can be used to smooth out the capture layers, although this method would lead to a loss of information of some of the underlying physics in the crust. Solving a pair of coupled first order differential equations negates the requirement to differentiate the density dependent variables. This enables a temperature profile of the neutron star crust of varying density to be constructed numerically without convergence issues, or the loss of physical information through the use of interpolation. The work contained within this chapter will use the coupled first order differential equations (4.3.6) and (4.3.7) to construct a background model of the temperature distribution within the accreted neutron star crust. The next step is to solve these equations numerically to build a temperature profile of an accreted neutron star crust for a realistic equation of state, using a small radial step size to ensure the sharp steps in density are resolved.

4.3.1 Heat Source

The net rate of change of heat per unit time is given as

$$\dot{Q} = \rho(\epsilon_{\rm nuc} - \epsilon_\nu), \tag{4.3.8}$$

where $\rho\epsilon_{\rm nuc}$ is the heat source term arising from the heat deposited in the crust by nuclear reactions and $\rho\epsilon_\nu$ is the heat sink term arising from neutrino bremsstrahlung radiation.

Through accretion, mass is transferred to the neutron star surface. This matter then undergoes compression as more accreted material falls on top. This compression causes the accreted to matter to then undergo density changes. As the material moves deeper into the crust, electron capture reactions begin to occur. These reactions take place at constant pressure and deposit heat into the crust (Haensel and Zdunik, 1990b). The heat deposited in MeV per nucleon at different densities is shown in table 4.2.1.

In table 4.2.1 the quantity of heat deposited in the crust is given at a specific density for a given composition. In reality, the heat is deposited in capture layers with a finite volume

than spans over a range of densities. To determine how the heat is deposited over the whole capture layer, a choice has to be made on the best way to treat the heat deposition based on the tabulated values. Ushomirsky et al. (2000) integrate the electron capture rates over each capture layer. As the work contained within this chapter is solving for the static heat equation, employing this method is unnecessary at this stage. Brown (1999) distributes the heat deposited per baryon $\epsilon_{\rm nuc} = 1$MeV over the region where pycnonuclear reactions occur. This approach of smearing the heat deposited over a large region of the crust is less accurate than is desired for this work. We instead decided to smear the heat deposited in each capture layer, over the relevant layer of fixed composition. Setting the capture layer outer boundary as the radius corresponding to the density where the heat is deposited and smearing down to the inner boundary, i.e the next density at which heat is deposited in the crust. It is worth noting that Ushomirsky et al. (2000) insert an addition ad hoc capture layer into the bottom of crust to extend the Haensel and Zdunik (1990a) crustal equation of state data to larger densities, and study the quadrupole moment induced by this layer as a function of its position. It is unclear how much heat would be deposited into this additional capture, so we have decided not to include this in our work.

The heat deposited in each electron capture layer per unit volume per unit time $\dot{Q}$, is a function of accretion rate. An approximate way of writing down the heat released in each capture layer is by smearing the heat deposited over whole shells as

$$\rho\epsilon_{\rm nuc} = \frac{\dot{M}\epsilon_{\rm nuc}}{\frac{4}{3}\pi m_{\rm b}(r^3_{\rm outer} - r^3_{\rm inner})}, \tag{4.3.9}$$

where $\dot{M}$ is the accretion rate, $\epsilon_{\rm nuc}$ is the heat deposited per nucleon by the relevant nuclear reaction, $m_{\rm b}$ is the mass of a baryon and $r_{\rm outer}$ and $r_{\rm inner}$ are the outer and inner radii of each layer of fixed composition respectively.

The neutrino cooling employed in this section is the same as that used in the 3 and is written as

$$\rho\epsilon_{\nu} = 3.229 \times 10^{17}\rho_{12}T_9^6\frac{Z^2}{A}X_A{\rm ergs}^{-1}{\rm cm}^{-3}, \tag{4.3.10}$$

where $X_{\rm A} = 1 - X_{\rm n}$ is the mass fraction contained within nuclei.

4.3.2 Boundary Conditions

The outer boundary is set to the interface where the crust meets the accreted material. Following the method used in chapter 3, and the boundary conditions given by Ushomirsky et al. (2000), the outer boundary temperature is set as a function of accretion rate and the steady burning temperature of the hydrogen/helium layer on the

surface of the star as

$$T_{\rm OB} = 5.3 \times 10^8 {\rm K} \left(\frac{\dot{m}}{\dot{m}_{\rm Edd}} \right)^{\frac{2}{7}}, \tag{4.3.11}$$

where $\dot{m}$ is the local accretion rate per unit time, and $\dot{m}_{\rm Edd}$ is the Eddington accretion rate. We do not allow $\dot{m}$ to vary from point to point, but will relax this restriction in chapter 5. The outer boundary radius and density is set as

$$r_{\rm OB} = 11.599 {\rm km}, \tag{4.3.12}$$

$$\rho_{\rm OB} = 1.49 \times 10^9 {\rm g\ cm^{-3}}. \tag{4.3.13}$$

To determine the inner boundary condition for a neutron star with a normal core, the core is assumed to be a perfect conductor. By making this assumption, all the flux that is conducted into the core is radiated out as neutrinos. The modified Urca formula is then used to set the flux value at the crust/core interface. The core luminosity, and consequently the flux is a function of temperature, enabling the inner boundary value of temperature to also be determined. From the energy conservation formula the flux at the inner boundary can be written as

$$F_{\rm IB} = -\frac{L_{\rm core}}{4\pi R_{\rm IB}^2}, \tag{4.3.14}$$

where the luminosity of the core due to the modified Urca formula is

$$L_{\rm core} = 5.3 \times 10^{39} {\rm erg\ s^{-1}} \left(\frac{M}{M_\odot} \right) \left(\frac{\rho_{\rm nuc}}{\rho} \right)^{\frac{1}{3}} T_9^8 \exp\left(-\frac{\Delta}{k_B T} \right). \tag{4.3.15}$$

The inner boundary condition is satisfied when the numerically computed flux is equal to the value of the flux shown in equation (4.3.14). It is worth noting the luminosity of the core shown here is for a constant density neutron star. This is the formula employed by Ushomirsky et al. (2000) and by us, in this work, to enable a comparison of the background model results to be made between the two models.

For a normal core $\Delta = 0$. For a superfluid core we assume $\Delta \gg k_{\rm B} T$ such that $L_{\rm core}$ is essentially zero. This condition is implemented by setting the flux at the inner boundary as

$$F_{\rm IB} = 0, \tag{4.3.16}$$

as superfluidity suppresses the core neutrino emissions (Ushomirsky et al., 2000).

The inner boundary radius and density is set as

$$r_{\rm IB} = 10.903{\rm km}, \tag{4.3.17}$$

$$\rho_{\rm IB} = 1.25 \times 10^{13}{\rm g\ cm^{-3}}. \tag{4.3.18}$$

4.4 Numerical Methods

The numerical methods employed to obtain solutions for the background flux and temperature distributions in the crust, are similar to those used in 3. To build a background thermal profile of an accreted neutron star crust, the two coupled first order differential equations (4.3.6) and (4.3.7) are solved using the shooting method. The ODEs are boundary valued problems with the boundary conditions as shown in equations (4.3.11) and (4.3.14). This boundary valued problem can be reduced to an initial value problem using the shooting method.

In the case of the work here, the value of the flux at the outer boundary is determined by shooting trajectories until the predefined inner flux boundary condition (equation (4.3.14) is satisfied. The python built in function scipy.optimize.brentq is then used to find the root value of the shooting function. This root value is then set as the flux outer boundary value $F_{\rm OB}$.

With the two outer boundary values of each of the coupled ODEs known, the python integration function scipy.integrate.odeint was then used to solve the two coupled first order differential equations by integrating over the radius of crust r from the crust outer boundary to the crust/core interface.

4.4.1 Non-dimensionalisation

The coupled differential equations (4.3.6) and (4.3.7) are solved using numerical integration. To ensure the calculations are as accurate as possible, the differential equations are non-dimensionalised. Three typical values are chosen for T, r and K, which are used to construct a typical value for the flux. The equations are then non-dimensionalised by dividing through by these typical values as

$$\hat{T} = \frac{T}{T_{\rm typ}}, \tag{4.4.1}$$

$$\hat{r} = \frac{r}{R_{\rm typ}}, \tag{4.4.2}$$

$$\hat{K} = \frac{K}{K_{\rm typ}}, \tag{4.4.3}$$

where '$\hat{}$' indicates the non-dimensionalised quantity, and values for $R_{\rm typ}$, $K_{\rm typ}$ and $T_{\rm typ}$ were chosen in section 3.2.1 as $R_{\rm typ} = 1 \times 10^6$ km, $K = 2.5 \times 10^{19}$ erg s^{-1} K^{-1} and $T_{\rm typ} = 2.13 \times 10^9$ K.

From equation 4.3.1 a value for $F_{\rm typ}$ can be chosen as

$$F_{\rm typ} = \frac{K_{\rm typ} T_{\rm typ}}{R_{\rm typ}}, \tag{4.4.4}$$

where a value of $F_{\rm typ}$ is determined to be =5.33×10^{22} erg s^{-1}.

Using the relations shown in equation (4.4.1), the differential equations dT/dr and dF/dr shown in equations (4.3.6) and (4.3.7) respectively, can be written in dimensionless form as

$$\frac{d\hat{T}}{d\hat{r}} = -\frac{\hat{F}}{K} K_{\rm typ}, \tag{4.4.5}$$

$$\frac{d\hat{F}}{d\hat{r}} = -2\frac{\hat{F}}{\hat{r}} + \dot{Q}\frac{R_{\rm typ}}{F_{\rm typ}}. \tag{4.4.6}$$

The boundary conditions in dimensionless form are then

$$\hat{T}_{\rm OB} = 2.87 \times 10^{-6} \dot{M}^{\frac{2}{7}}, \tag{4.4.7}$$

and for a neutron star with a normal core

$$\hat{F}_{\rm IB} = -\frac{L_{\rm core} K_{\rm typ} T_{\rm typ}}{4\pi \hat{R}_{\rm IB}^2}. \tag{4.4.8}$$

These dimensionless equations (4.4.5, 4.4.6) will be solved via numerical integration by employing the shooting method, to build the thermal profile of an accreted neutron star crust of varying density.

4.5 Background Model Results

A thermal profile of an accreted neutron star crust of variable density was produced. The two coupled first order differential equations (4.3.6) and (4.3.7) were solved numerically to provide solutions of both the flux and temperature of the crust for both a normal and superfluid core for the boundary conditions detailed in section 4.3.2.

The temperature distributions in the crust for a normal and superfluid core are shown in figures 4.5.1 and 4.5.2, respectively, for different accretion rates. For the neutron star with

a normal core, the temperature is at a maximum at the outer boundary and decreases with decreasing radius. Conversely in the case of a superfluid core, the temperature is at a maximum at the crust/core interface. This corresponds to the suppression of neutrino emission in the core, resulting in heat losses via thermal conduction at the outer boundary and neutrino bremsstrahlung emissions in the crust only. These plots both show a faster accretion rate gives rise to a hotter crust. This is expected as the nuclear heating rate of the crust is directly proportional to the accretion rate. We find for a superfluid core $T \approx 1 \times 10^9$ K, inputting this value into the exponential term in equation 4.3.15 gives $\exp\left(-\frac{\Delta}{k_B T}\right) \approx 10^{-6}$, for $\Delta = 1$ MeV. This confirms setting $F_{\mathrm{IB}} = 0$ for a superfluid core is accurate to a good approximation.

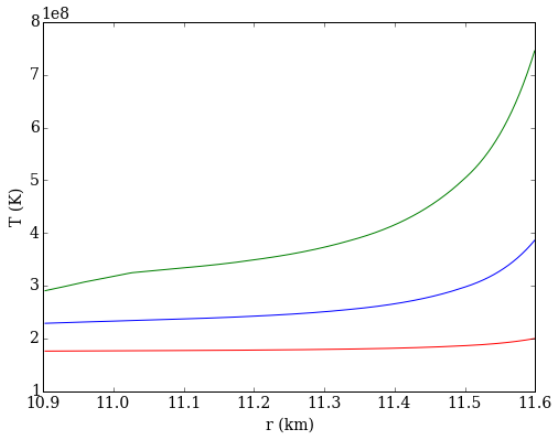

Figure 4.5.1: A plot to show how the temperature varies as a function of radius in an accreted neutron star crust for a normal core with different accretion rates and $Q_{\mathrm{imp}} = 1$. The red line represents $\dot{M} = 1 \times 10^{-10} M_\odot$ yr^{-1}, the blue line $\dot{M} = 1 \times 10^{-9} M_\odot$ yr^{-1}, and the green line $\dot{M} = 1 \times 10^{-8} M_\odot$ yr^{-1}.

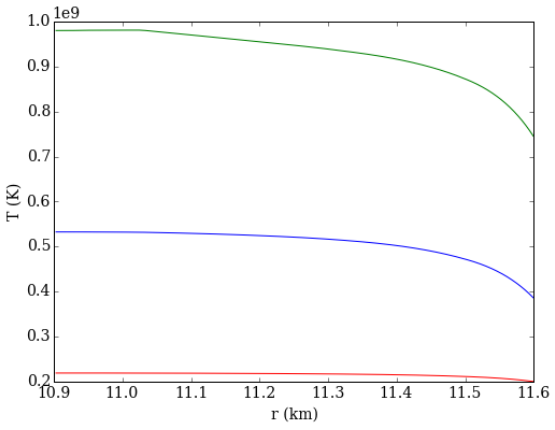

Figure 4.5.2: A plot to show how the temperature varies as a function of radius in an accreted neutron star crust for a superfluid core with different accretion rates and $Q_{\mathrm{imp}} = 1$. The red line represents $\dot{M} = 1 \times 10^{-10} M_\odot$ yr^{-1}, the blue line $\dot{M} = 1 \times 10^{-9} M_\odot$ yr^{-1}, and the green line $\dot{M} = 1 \times 10^{-8} M_\odot$ yr^{-1}.

A plot of how the flux varies with radius in the crust is shown for a normal core in figure 4.5.3 and a superfluid core in figure 4.5.4. In both figures, features can be seen at small radii, closer to the neutron star core. The majority of the heat deposited into the crust via nuclear heating, occurs at these smaller radii. At $r < 11$km, large step like features appear in the flux in both the normal and superfluid core. These steps correspond to where the pycnonuclear reactions occur in the crust. In the case of the superfluid core, the gradient of the flux fluctuates between positive and negative values. Local minima occur at radial points on the crust corresponding to where the pycnonuclear reactions occur. As neutrino emissions from the core is suppressed, the deposited heat is conducted outwards from the point of origin through the crust, resulting in these trough like features. For higher accretion rates, more heat is deposited into the crust, resulting in an increase in the magnitude of these local minima. In the case of the normal core, heat is able to pass from the crust into the core, resulting in a net flow of flux into the core.

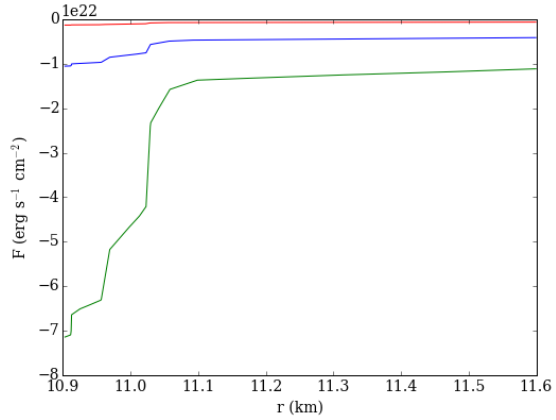

Figure 4.5.3: A plot of how the flux varies with radius in an accreted neutron star crust with a normal core for different accretion rates. The red line represents $\dot{M} = 1 \times 10^{-10} M_{\odot}$ yr^{-1}, the blue line $\dot{M} = 1 \times 10^{-9} M_{\odot}$ yr^{-1}, and the green line $\dot{M} = 1 \times 10^{-8} M_{\odot}$ yr^{-1}.

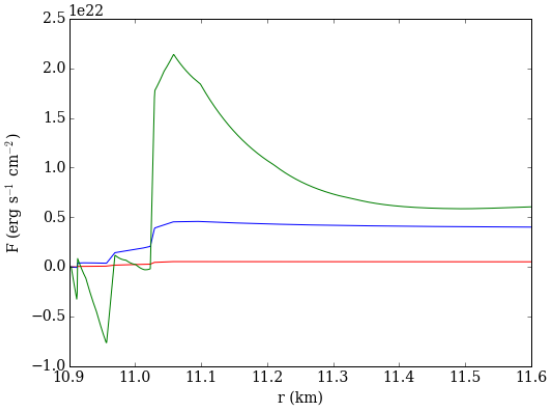

Figure 4.5.4: A plot of how the flux varies with radius in an accreted neutron star crust with a superfluid core for different accretion rates. The red line represents $\dot{M} = 1 \times 10^{-10} M_{\odot}$ yr^{-1}, the blue line $\dot{M} = 1 \times 10^{-9} M_{\odot}$ yr^{-1}, and the green line $\dot{M} = 1 \times 10^{-8} M_{\odot}$ yr^{-1}.

The net heat deposited into the crust per unit time is shown in figures 4.5.5 and 4.5.6 for a normal and superfluid core respectively. The step-like nature of the plot arises from the density dependent nuclear reactions depositing heat in the electron capture layers combined with neutrino cooling and thermal conduction, radiating the heat out of the crust.

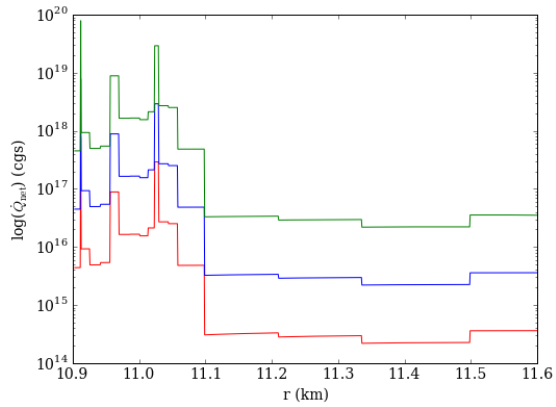

Figure 4.5.5: A graph to show the net heat deposited per unit time in an accreted neutron star crust for a normal core with different accretion rates and $Q_{\rm imp} = 1$. The red line represents $\dot{M} = 1 \times 10^{-10} M_{\odot}$ yr^{-1}, the blue line $\dot{M} = 1 \times 10^{-9} M_{\odot}$ yr^{-1}, and the green line $\dot{M} = 1 \times 10^{-8} M_{\odot}$ yr^{-1}.

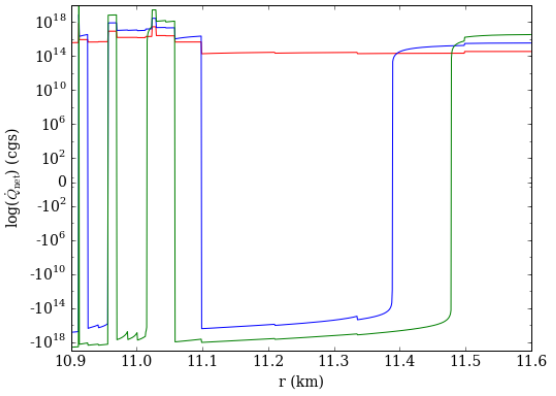

Figure 4.5.6: A graph to show the net heat deposited per unit time in an accreted neutron star crust with a superfluid core for different accretion rates and $Q_{\rm imp} = 1$. The red line represents $\dot{M} = 1 \times 10^{-10} M_{\odot}$ yr^{-1}, the blue line $\dot{M} = 1 \times 10^{-9} M_{\odot}$ yr^{-1}, and the green line $\dot{M} = 1 \times 10^{-8} M_{\odot}$ yr^{-1}.

Figure 4.5.7 shows how the thermal conductivity varies with radius inside the crust. This plot shows step-like features, which correspond to the sharp composition changes in crust, arising from the density dependent electron capture reactions and pycnonuclear reactions. More sharp features can be seen at lower radius values corresponding to the region where most of the heat from nuclear reactions is deposited into the crust.

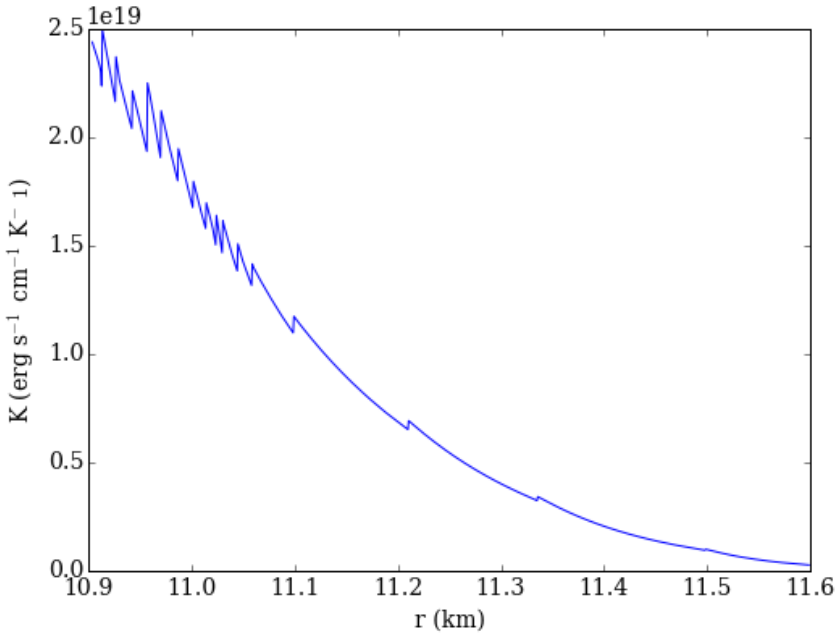

Figure 4.5.7: A graph to show how the thermal conductivity varies as a function of radius in an accreted neutron star crust for $Q_{\rm imp} = 1$ and $\dot{M} = 1 \times 10^{-9} M_{\odot}$.

The thermal conductivity is dependent on electron-phonon $\nu_{\rm ep}$ and electron-impurity $\nu_{\rm eQ}$ scattering. Each of these scattering frequencies is plotted as a function of radius for three different accretion rates and an impurity parameter $Q_{\rm imp} = 1$ in figure 4.5.8 for a normal core star and 4.5.9 for a superfluid core star. Electron-phonon scattering is temperature dependent, whereas electron-impurity scattering is a function of both position and impurity parameter, but independent of temperature. At high temperatures ($T \sim 10^8$ K) and low impurity parameter, electron-phonon scattering dominates. Stepwise features can be seen at low radii in the $\nu_{\rm eQ}$ plot, again this arises from the sharp composition changes that occur in the accreted neutron star crust.

4.5.1 Comparison with results in the literature

To investigate the accuracy of the results produced within this work, they were compared to the results of Ushomirsky et al. (2000) and Brown (1999) who considered similar, but non-identical models.

As described in section 4.1.2, the model created by Ushomirsky et al. (2000) consists of a Newtonian crust 1.1 km thick, with a mass of $0.06 M_{\odot}$, whereas our model has a Newtonian crust 1.45 km thick with a mass of $0.09 M_{\odot}$. The background temperature, flux and $\rho\epsilon$ for a normal core are plotted as a function of pressure, and shown in figure 4.5.10, to enable a comparison to be drawn with the results produced by Ushomirsky et al. (2000) which are shown in figure 4.5.11. In figure 4.5.10 the temperature decreases when moving from the outer boundary of the crust towards the core. Whereas in the Ushomirsky

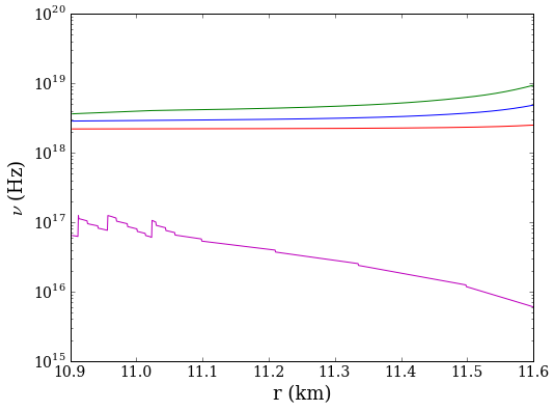

Figure 4.5.8: A graph to show the how electron-impurity (shown as the magenta curve), electron-phonon scattering vary as a function of radius in an accreted neutron star crust with a normal core for $Q_{\rm imp} = 1$. The red line represents $\nu_{\rm ep}$ for $\dot{M} = 1 \times 10^{-10} M_{\odot}$ yr^{-1}, the blue line $\nu_{\rm ep}$ for $\dot{M} = 1 \times 10^{-9} M_{\odot}$ yr^{-1}, and the green line $\nu_{\rm ep}$ for $\dot{M} = 1 \times 10^{-8} M_{\odot}$ yr^{-1}.

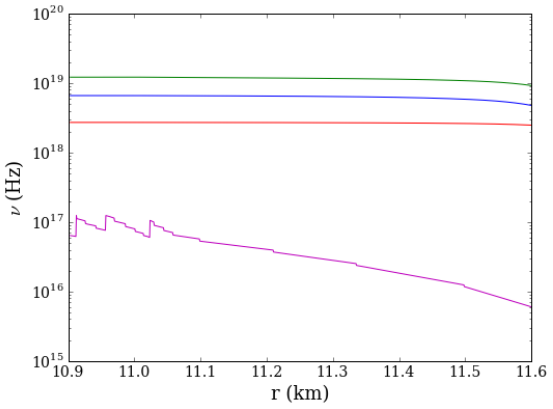

Figure 4.5.9: A graph to show the how electron-impurity (shown as the magenta curve) electron-phonon scattering vary as a function of radius in an accreted neutron star crust with a superfluid core for $Q_{\rm imp} = 1$. The red line represents $\nu_{\rm ep}$ for $\dot{M} = 1 \times 10^{-10} M_{\odot}$ yr^{-1}, the blue line $\nu_{\rm ep}$ for $\dot{M} = 1 \times 10^{-9} M_{\odot}$ yr^{-1}, and the green line $\nu_{\rm ep}$ for $\dot{M} = 1 \times 10^{-8} M_{\odot}$ yr^{-1}.

et al. (2000) results, the temperature increases with increasing pressure until $P \sim 10^{30}$ erg cm^{-3} when the temperature begins to decrease. The flux results of each model appear fairly similar. One notable difference is the flux at the outer boundary in figure 4.5.10 is negative and Ushomirsky et al. (2000) have a positive outer boundary flux value. Both cases show a steep decline in the flux at $P \sim 10^{30}$ erg cm^{-3}, with step-like features appearing in the plots at higher pressures, corresponding to the region where most of the heat is deposited into the crust from nuclear reactions. The plots of $\rho\epsilon$ are quite different in the two models, particularly in the case $\rho\epsilon_{\rm nuc}$. The difference in how $\rho\epsilon_{\rm nuc}$ varies with pressure may arise from a difference in treatment of how heat is deposited into the capture layers. In our model, the heat is smeared over an entire shell of constant A, and Z, whereas Ushomirsky et al. (2000) inject the heat over the narrow capture layers. How the neutrino cooling varies with pressure in the two models is quite similar, except the magnitude of $\rho\epsilon_{\nu}$ is approximately one order of magnitude larger at higher pressures in the Ushomirsky et al. (2000) model, when compared to our work. This is due to the slightly higher temperatures obtained by Ushomirsky et al. (2000), and the very steep temperature dependence of the neutrino cooling rate ($\nu_{\rm e} \propto T^6$).

The results for an accreted neutron star crust with a superfluid core are shown in figure 4.5.12 alongside the results calculated by Ushomirsky et al. (2000) as shown in figure 4.5.13. When the pressure exceeds $P \sim 10^{30}$ erg cm^{-3} the temperature model from this work appears to plateau, whilst the (Ushomirsky et al., 2000) temperature profile begins to decrease. The flux profile from each model differs quite significantly. Our model produces a positive flux, whereas the flux calculated by Ushomirsky et al. (2000) is positive at the outer boundary and starts to rapidly decrease at $P \sim 10^{30}$ erg cm^{-3}.

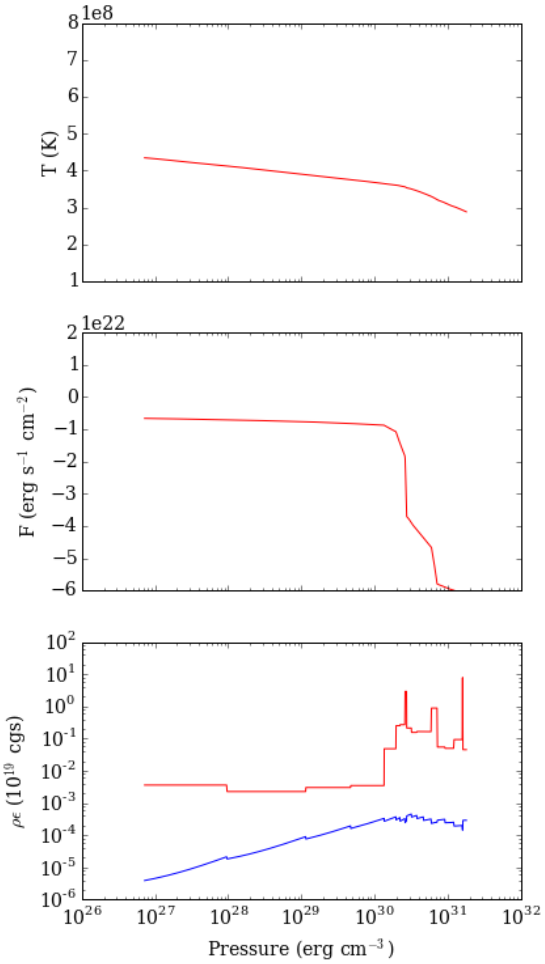

Figure 4.5.10: Temperature, flux, the heat deposited into the crust by nuclear reactions (red line) and the neutrino cooling (blue line) distribution in an accreted neutron star crust with a normal core for an accretion rate of $\dot{M} = 0.5\dot{M}_{\rm Edd}$ and $Q_{\rm imp} = 100$.

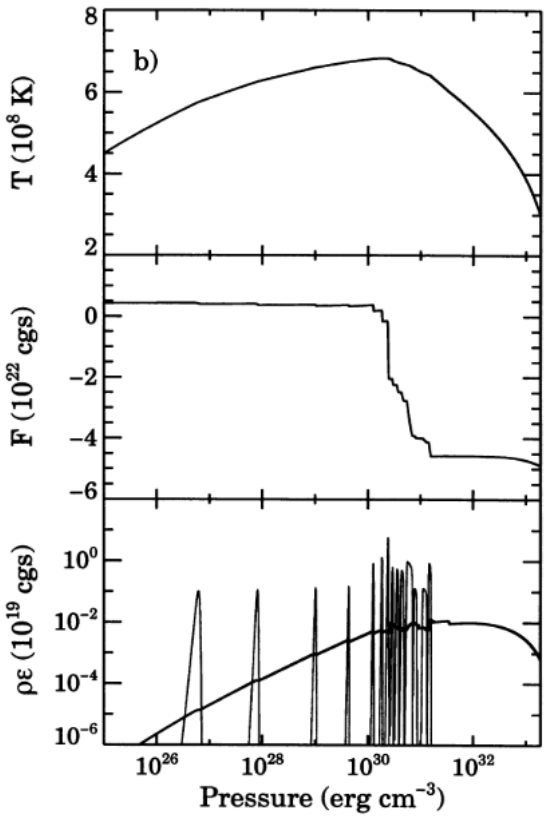

Figure 4.5.11: Thermal structure of model an accreted neutron star crust with a normal fluid core for an accretion rate of $0.5\dot{M}_{\rm Edd}$. The top panel shows the temperature of the crust. The middle panel shows the heat flux F_r in the crust (F_r , 0 means the heat is flowing toward the core). The bottom panel shows the local energy release $\rho\epsilon_{\rm nuc}$ (in erg cm^{-3} s^{-1}) due to reactions in the crust (sharp spikes) and the local rate of neutrino cooling $\rho\epsilon_\nu$ (also in erg cm^{-3} s^{-1}) (Ushomirsky et al., 2000).

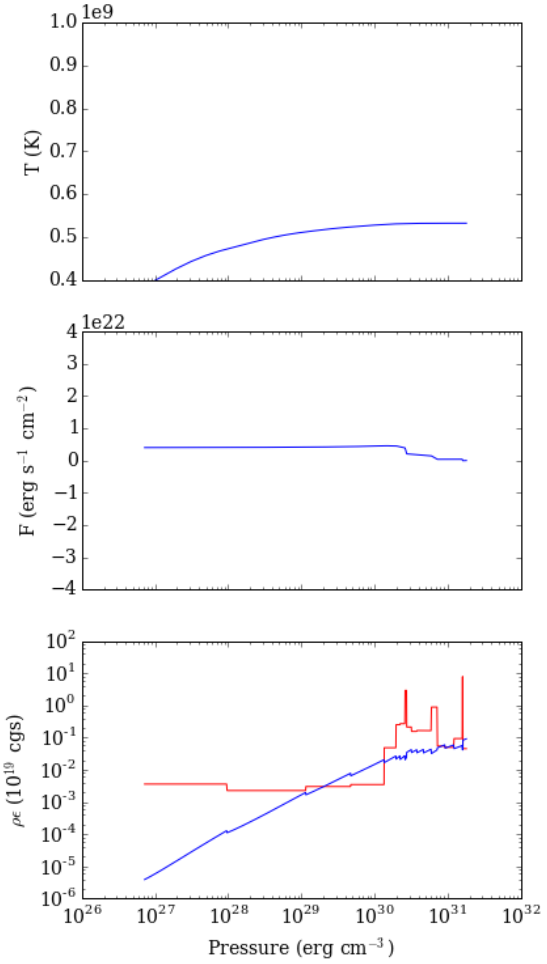

Figure 4.5.12: Temperature, flux, the heat deposited into the crust by nuclear reactions (red line) and the neutrino cooling (blue line) distribution in an accreted neutron star crust with a superfluid core for an accretion rate of $\dot{M} = 0.5\dot{M}_{\rm Edd}$ and $Q_{\rm imp} = 100$.

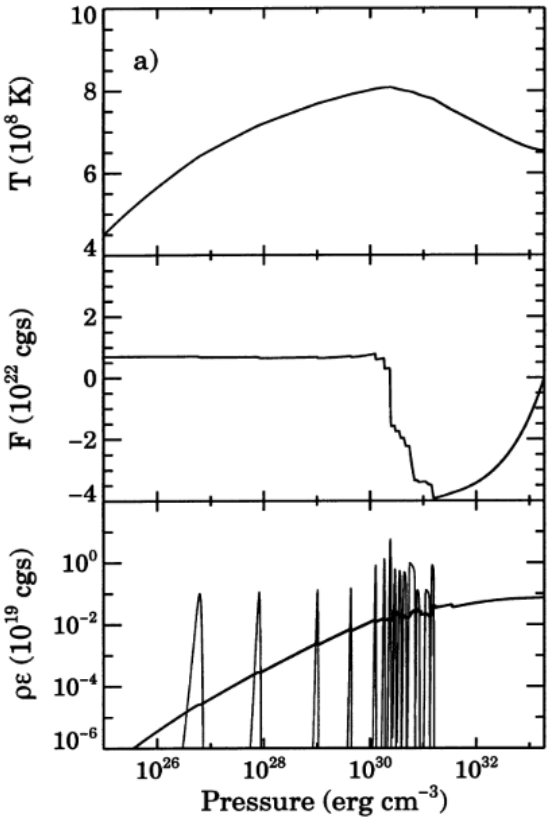

Figure 4.5.13: Same as figure 4.5.10, but for a superfluid core.

The way the heat is deposited into the crust via nuclear reactions is quite different in the two models, as was the case in the normal core neutron star results. The neutrino cooling, however, appears to be in good agreement.

A further comparison can be made between the work produced here, as shown in figure 4.5.14, and that of Brown (1999) shown in figure 4.5.15. The results produced by our model have been rescaled as a function of log(p/MeV fm^{-3}), where 1 MeV fm$^{-3} = 1.6 \times 10^{33}$ dyn cm^{-2}.

Brown (1999) constructed a neutron star in relativistic gravity only, whereas the work contained within this chapter has a Newtonian crust on a relativistic core. These different approaches will lead to discrepancies in the results from the two models. Both models use the same data from Haensel and Zdunik (1990a) as shown in table 4.2.1. Brown (1999) deposits the heat from nuclear reactions into the crust by smoothing the heat per baryon (1 MeV) over a pressure interval $\Delta p = 3.4 \times 10^{-2}$ MeV fm$^{-3} - 8.7 \times 10^{-4}$ MeV fm^{-3}, whereas we resolve the heat deposited into each shell of constant A and Z. The inner boundary conditions of each model are also different. Brown (1999) integrates from the centre of the star to the star's surface. In our model we only integrate over the crust setting the outer and inner boundaries to the top of the crust and the crust/core interface respectively. Brown (1999) presents results for two cases: electron-phonon scattering regime dominates thermal transport in the crust and for when electron-ion scattering dominates. In our work, we set $Q_{\rm imp} = 0$ to ensure electron-phonon scattering is the dominant regime, and $Q_{\rm imp} = 100$ for when electron-ion scattering dominates. It is unclear from the literature what value of $Q_{\rm imp}$ is used by Brown (1999) for the electron-ion scattering regime.

The temperature distribution for a superfluid core is shown in the top graph of figure 4.5.14 and the corresponding result from Brown (1999) is shown in the top panel of 4.5.15. Both models produce a positive temperature gradient, where the temperature at the outer boundary is at a minimum. When electron-phonon scattering dominates, a hotter crust is produced.

For a normal core neutron star (bottom plot of figure 4.5.14), the temperature decreases when moving from the top of the crust towards the core, for both scattering regimes. The electron-ion scattering regime results in a hotter crust when compared to when the electron-phonon scattering dominates. The corresponding plot from Brown (1999), shown in the bottom of graph of figure 4.5.15, shows a similar trend for the temperature distribution when electron-phonon scattering dominates. In the case when electron-ion scattering dominates Brown (1999) obtains a positive temperature gradient. This general trend corresponds well with that shown in the bottom graph of figure 4.5.14. The temperature distribution in figure 4.5.15 spans a broader pressure range than the tem-

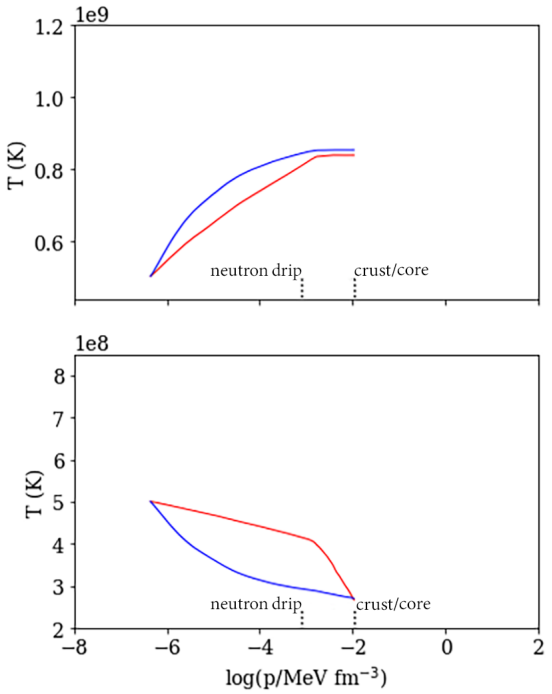

Figure 4.5.14: The background temperature profile of an accreted neutron star crust, for an accretion rate of $\dot{M} = \dot{M}_{\rm Edd}$, where the outer boundary temperature was set as $T_{\rm OB} = 5 \times 10^8$K. The top graph is for a neutron star with a superfluid core, and the bottom plot for a normal core. In both cases, the red line indicates when the conductivity is dominated by electron-ion scattering, and the blue line for when electron-phonon scattering dominates.

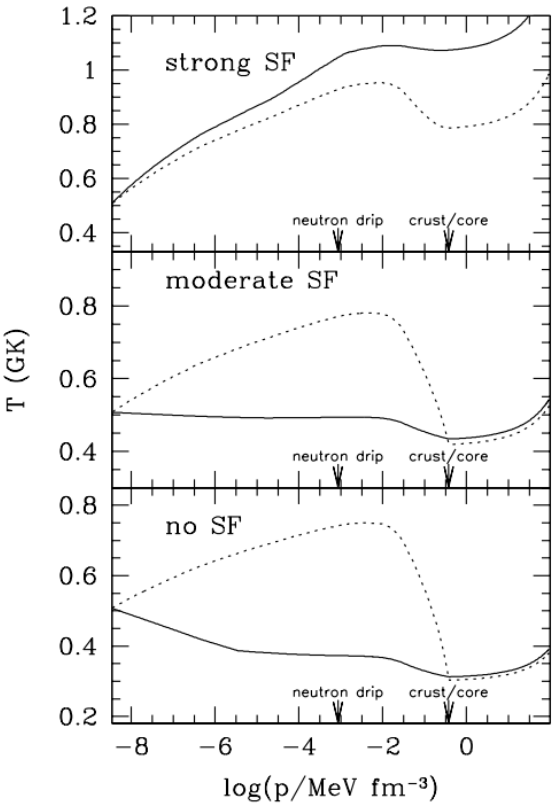

Figure 4.5.15: Temperature distribution of an accreted neutron star for a star with a strong superfluid core (top graph), moderate superfluid core (middle graph) and a normal core (bottom graph). Two cases are compared, with the conductivity dominated either by electron-phonon scattering (solid lines) or by electron-ion scattering (dotted lines). This is Figure 4 of Brown (1999).

perature distribution produced in this work (figure 4.5.14). This difference arises from the choice of computational domain employed.

We see that our results agree in rough form with those of Ushomirsky et al. (2000) and Brown (1999). The main difference lies in the shape of the plot of T verses r in Ushomirsky et al. (2000), and in the plot of T verses r in Brown (1999) for the normal core, electron-ion dominated thermal conductivity. These differences may be due to differences in where exactly the nuclear heating is deposited. In any case, we now proceed to carry out numerical tests of our results, to check their internal consistency.

4.5.2 Numerical testing

4.5.2.1 Inner Boundary Value

The simplest test that can be performed is that of the inner boundary condition. For a normal core, the core is assumed to be a perfect conductor, where all of the heat that is conducted into the core is radiated out via neutrinos. This assumption relates the heat flux to the luminosity of the core as

$$L(F) = -F_{\rm inner} 4\pi R_{\rm inner}^2. \tag{4.5.1}$$

Using the modified Urca formula (Shapiro and Teukolsky, 1983), the core luminosity can also be written as a function of temperature as

$$L(T) = 5.3 \times 10^{39}\ {\rm erg\ s^{-1}} \left(\frac{M}{M_\odot}\right) \left(\frac{\rho_{\rm nuc}}{\rho}\right)^{1/3} T_9^8 \exp\left(-\frac{\Delta}{k_{\rm B}T}\right). \tag{4.5.2}$$

A self-consistency check of the numerical integration can then be conducted by equating equations (4.5.1) and (4.5.2) as

$$L(F) = L(T). \tag{4.5.3}$$

The inner boundary values of F and T, obtained by numerically solving equations (4.3.7) and (4.3.6) respectively, are then input into equations (4.5.1) and (4.5.2) and checked for self consistency using equation (4.5.3). The results from this test are presented in table 4.5.16. The fractional error between the two luminosity values for each accretion rate is of order $10^{-5} - 10^{-6}$. This shows the numerical integration is performing to an excellent degree of accuracy.

$\dot{M}$ ($M_\odot$ yr^{-1})	L(F) (erg s^{-1} cm^{-2})	L(T) (erg s^{-1} cm^{-2})	Fractional Error
1×10^{-10}	-1.939078×10^{34}	-1.93909×10^{34}	7.71×10^{-6}
1×10^{-9}	-1.574406×10^{35}	-1.574403×10^{35}	1.70×10^{-6}
1×10^{-8}	-1.067480×10^{35}	-1.067458×10^{35}	2.12×10^{-5}

Table 4.5.16: Table to show the core luminosity as calculated as a function of flux and compared with the parameter as calculated as a function of temperature using the values computed via the shooting function. The final column shows the error arising from these two different methods of calculation for a normal core.

4.5.2.2 Energy Conservation

Following the formalism used in 3.3.1.2, an energy conservation test is conducted. The energy radiated away by neutrino bremsstrahlung emission E_ν (equation 3.3.5), is summed with the energy conducted into the core and out of the surface of the crust $E_{\mathrm{K(core)}}$ and $E_{\mathrm{K(crust)}}$, as evaluated at the relevant radial point using equation (3.3.6), to give the total energy E_{total}. E_{total} is then equated to the total energy deposited into the crust $\epsilon_{\mathrm{total}}$ (as shown in equation (3.3.8)). The energy conservation test is passed when the equation

$$E_{\mathrm{total}} = E_{\mathrm{K(crust)}} - E_{\mathrm{K(core)}} + E_\nu, \tag{4.5.4}$$

is satisfied. A summary of the energy conservation test results are shown in 4.5.17 for a normal and 4.5.18 for a superfluid core.

$\dot{M}$ ($M_\odot$ yr^{-1})	E_{total} (erg s^{-1} cm^{-3})	$\epsilon_{\mathrm{total}}$ (erg s^{-1} cm^{-3})	Fractional Error
1×10^{-10}	8.80516×10^{33}	8.80452×10^{33}	7.34×10^{-5}
1×10^{-9}	8.80518×10^{34}	8.80452×10^{34}	7.51×10^{-5}
1×10^{-8}	8.80519×10^{35}	8.80452×10^{35}	7.62×10^{-5}

Table 4.5.17: A summary of the error in the ratio of net heat input vs the net heat output for three different accretion rates for a normal core.

$\dot{M}$ ($M_\odot$ yr^{-1})	E_{total} (erg s^{-1} cm^{-3})	$\epsilon_{\mathrm{total}}$ (erg s^{-1} cm^{-3})	Fractional Error
1×10^{-10}	8.80508×10^{33}	8.80452×10^{33}	6.3×10^{-5}
1×10^{-9}	8.80337×10^{34}	8.80452×10^{34}	1.3×10^{-4}
1×10^{-8}	8.79809×10^{35}	8.80452×10^{35}	7.2×10^{-4}

Table 4.5.18: A summary of the error in the ratio of net heat input vs the net heat output for three different accretion rates for a superfluid core.

The results presented in table 4.5.17 shows the energy conservation test for a normal core has a fractional error of order 10^{-5}, and a superfluid core (table 4.5.18) has a fractional error of order $10^{-4} - 10^{-5}$. The error in both cases is sufficiently small to determine that energy has been conserved.

4.5.2.3 Convergence Testing

Convergence tests were performed for both the temperature and flux values as calculated by the ODE solver. The methods employed follow those outlined in 3.3.1.1.

In 3.3.1.1, the accuracy parameter of the built-in python function scipy.integrate.odeint was varied as the controlled error parameter. In this section, the number of steps in the numerical integration has been varied instead. Each resolution was defined by number of radial steps N of which the integration was calculated over for each case. $\delta^n_{\text{low}} = \frac{N}{4}$, $\delta^n_{\text{medium}} = \frac{N}{2}$ and $\delta^n_{\text{low}} = N$. The results from this convergence test are shown in table 4.5.19.

$\dot{M}$ ($\text{M}_\odot\ \text{yr}^{-1}$)	n_{flux}	$n_{\text{temperature}}$
1×10^{-10}	1.00437	1.00220
1×10^{-9}	1.00437	1.00216
1×10^{-8}	1.00437	1.00218

Table 4.5.19: Table of results of the converge test for both the flux and temperature values computed by numerical integration.

4.5.2.4 Finite Differencing

To check the accuracy of the ODE solver a finite difference test was performed. The methodology used here is similar to that detailed in section 3.3.1.3, except in this instance the finite difference stencils used are for first order differential equations and is written as

$$f'(x) = \frac{f(x + \frac{1}{2}h) - f(x - \frac{1}{2}h)}{h}. \tag{4.5.5}$$

The outer and inner boundaries require modified stencils to ensure each value of h selected is consecutive and corresponds to a decreasing value of r. The stencils for the finite difference boundary values are

$$\begin{aligned} f'(x)_{\text{OB}} &= \frac{f(x+h) - f(x)}{h}, \\ f'(x)_{\text{IB}} &= \frac{f(x) - f(x-h)}{h}. \end{aligned} \tag{4.5.6}$$

A comparison of $\frac{dF}{dr}$ between the values calculated by finite differencing and those directly from equation (4.3.7) using the results of the integration, is shown in figure 4.5.20. The fractional error of these plots is shown in figure 4.5.21.

A comparison of the finite difference values of $\frac{dT}{dr}$ with the values calculated directly from equation (4.3.6) is shown in figure 4.5.22. The fractional error of these plots is

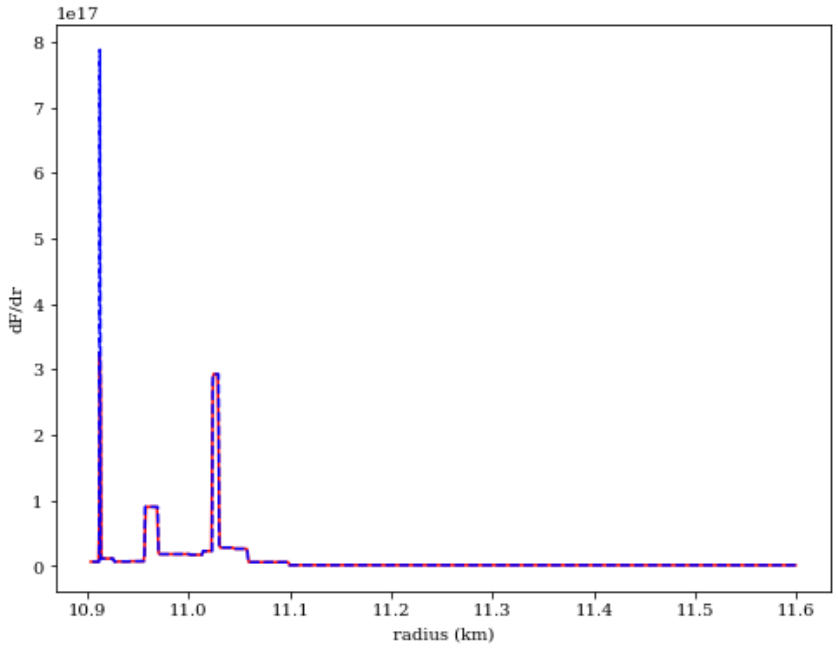

Figure 4.5.20: A plot of dF/dr calculated by finite differencing (red line) and from equation (4.3.7) (blue dashed line).

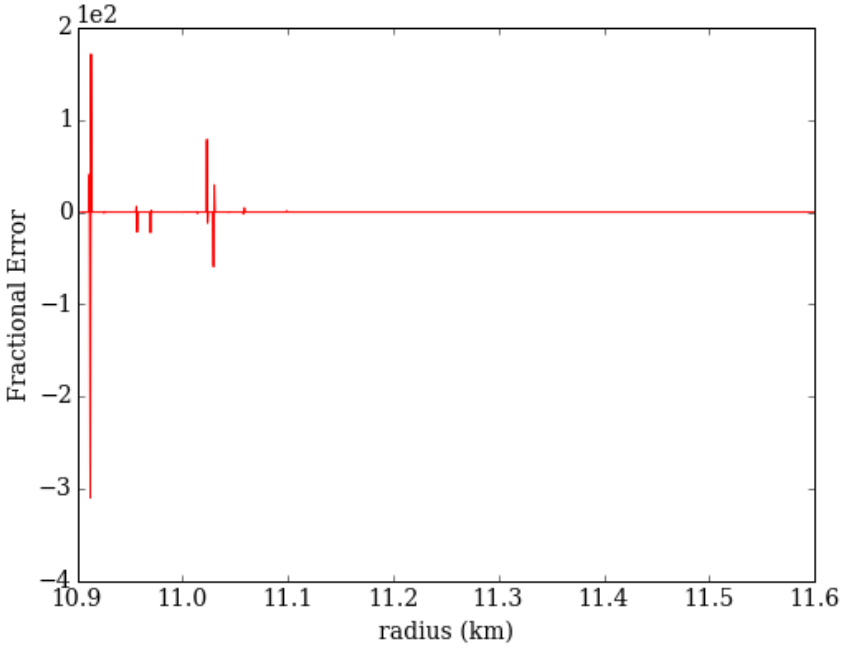

Figure 4.5.21: The fractional difference between the finite difference and ODE results shown in figure 4.5.20 for dF/dr.

shown in figure 4.5.23.

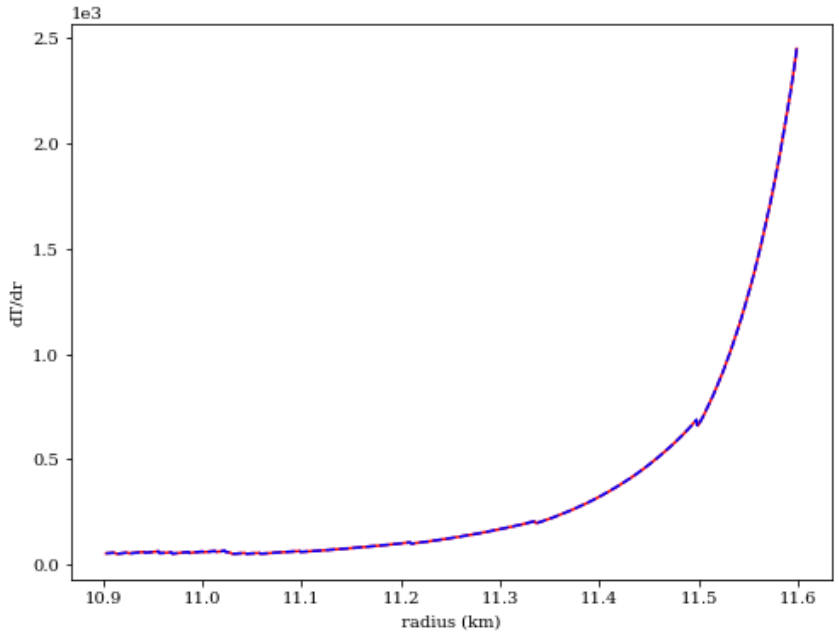

Figure 4.5.22: A plot of dT/dr calculated by finite differencing (red line) and from equation (4.3.6) (blue dashed line).

In figures 4.5.20 and 4.5.22, the plots appear to match up well. Taking a closer look at the fractional difference of each of these plots in figures 4.5.21 and 4.5.23, sharp spikes can be seen. This arises from the step-wise nature of the sharp composition changes that occur in the crust. The fractional error for $\frac{dF}{dr}$ is of order 10^2. This error is quite large, but only occurs at very limited ranges in r. For large ranges in r, the finite difference test is passed satisfactorily. The fractional error arising from $\frac{dT}{dr}$ is of order 10^{-4}. This is sufficiently small to satisfy the finite difference test for this equation has passed satisfactorily.

The finite difference test results for a superfluid core are passed to the same degree of accuracy as the normal core.

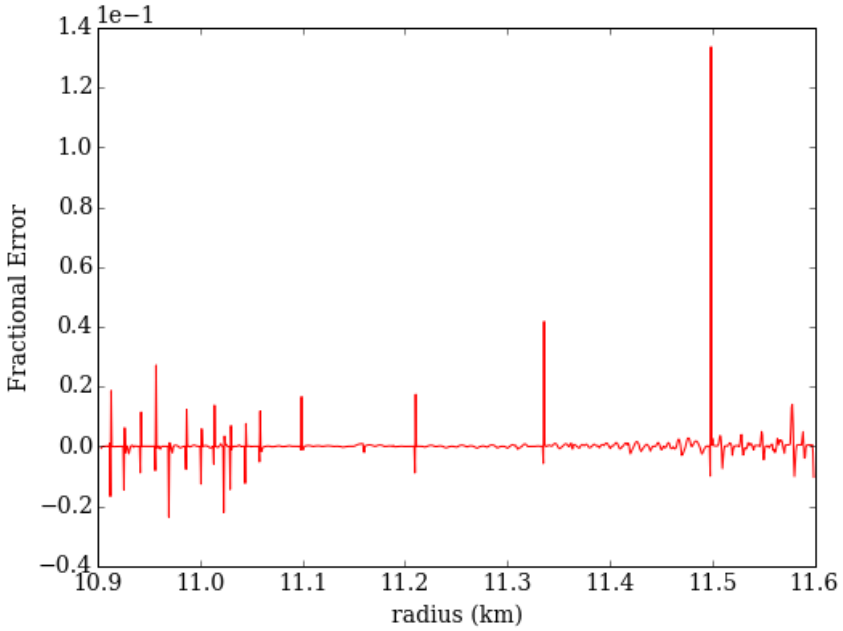

Figure 4.5.23: The fractional difference between the finite difference and ODE results shown in figure 4.5.22 for dT/dr.

4.6 Perturbed Thermal Profile

In this section, a magnetic field will be inserted into the neutron star crust to induce a temperature perturbation. The methodology used will be identical to that in chapter 3 except with a realistic crust of varying density. The scalar thermal conductivity is replaced with the tensor quantity κ, to accommodate for the anisotropy induced by the magnetic field.

The perturbed flux can be written in spherical harmonics as

$$\delta \boldsymbol{F} = \sum_{lm} U_{lm} \hat{\boldsymbol{r}} Y_{lm} + V_{lm} \boldsymbol{\nabla} Y_{lm}. \tag{4.6.1}$$

From 3.5.2 the perturbed flux is shown to be written as a function of thermal conductivity, temperature and the source term, which contains the magnetic field component as

$$\delta \boldsymbol{F} = -\kappa_0 \left[\boldsymbol{\nabla} \delta T + \tilde{\omega}_B \tau (\boldsymbol{B} \times \boldsymbol{\nabla} T) \right] - \delta \kappa_{\parallel} \boldsymbol{\nabla} T, \tag{4.6.2}$$

where $\delta \kappa_{\parallel}$ shown in equation (4.2.12) can be written as the derivative of thermal conductivity with respect to temperature multiplied by the perturbed temperature as

$$\delta \kappa_{\parallel} = \frac{d\kappa_0}{dT} \delta T = \frac{f_{\mathrm{k}} \delta T}{\nu} \frac{\nu_{\mathrm{eQ}}}{\nu^2}. \tag{4.6.3}$$

The divergence of the perturbed flux gives the perturbed net rate of change of heat per unit time as

$$\boldsymbol{\nabla} \cdot \delta \boldsymbol{F} = \delta \dot{Q} = \frac{d\dot{Q}}{dT} \delta T_{lm} Y_{lm}. \tag{4.6.4}$$

We assume there isn't a perturbation in the nuclear heating, only in neutrino cooling as shown in equation (3.5.18). The divergence of the perturbed flux (4.6.4) can be written as

$$\nabla \cdot \delta \boldsymbol{F} = -\rho \delta \epsilon_{\nu} = -6 C_{\epsilon} T^5 \delta T_{lm} Y_{lm}, \tag{4.6.5}$$

where $\rho \delta \epsilon_{\mathrm{nuc}} = 0$ and $C_{\epsilon} = 3.229 \times 10^{-37} \rho_{12} \frac{Z^2}{A} X_{\mathrm{A}} \mathrm{erg\ s^{-1}\ cm^{-3}}$.

From equation (4.6.1), the divergence of the flux can also be written in spherical harmonics as

$$\boldsymbol{\nabla} \cdot \delta \boldsymbol{F} = \sum_{lm} \frac{dU_{lm}}{dr} Y_{lm} + \frac{2}{r} U_{lm} Y_{lm} - \frac{l(l+1)}{r^2} V_{lm} Y_{lm}. \tag{4.6.6}$$

One of the coupled first order differential equations is derived by combining equations

(4.6.5) and (4.6.6) and rearranging to give

$$\frac{dU_{lm}}{dr} = -\frac{2}{r}U_{lm} + \frac{l(l+1)}{r^2}V_{lm} - 6C_\epsilon T^5 \delta T_{lm}. \tag{4.6.7}$$

The second coupled first order differential equation is obtained by equating equations (4.6.1) with (4.6.2), along with the expression for the toroidal magnetic field $\boldsymbol{B}_{\rm tor} = -\boldsymbol{r} \times \boldsymbol{\nabla}\Psi$ Pons and Geppert (2007), expanding and simplifying to give

$$\delta \boldsymbol{F} = -\frac{d\kappa_0}{dT}\frac{dT}{dr}\delta T_{lm}\hat{\boldsymbol{r}}Y_{lm} - \kappa_0\left[\frac{d\delta T_{lm}}{dr}\hat{\boldsymbol{r}}Y_{lm} + \left(\delta T_{lm} - \tilde{\omega}_B\tau\Psi_{lm}r\frac{dT}{dr}\right)\boldsymbol{\nabla}_\perp Y_{lm}\right]. \tag{4.6.8}$$

Using equations (4.6.1) and (4.6.8) an expression for the first order temperature derivative with respect to radius is written as

$$\frac{d\delta T_{lm}}{dr} = -\frac{1}{\kappa_0}\left(\frac{d\kappa_0}{dT}\frac{dT}{dr}\delta T_{lm} + U_{lm}\right), \tag{4.6.9}$$

and an expression for V_{lm} is obtained as

$$V_{lm} = \kappa_0\left(\tilde{\omega}_B\tau\Psi_{lm}r\frac{dT}{dr} - \delta T_{lm}\right). \tag{4.6.10}$$

A thermal profile of an accreted neutron star crust that is perturbed by the presence of a toroidal magnetic field is built by solving the coupled first order differential equations (4.6.7) and (4.6.9), with V_{lm} given by equation (4.6.10).

4.6.1 Perturbed Boundary Conditions

For both a normal and superfluid core star, the perturbed boundary conditions follow the same treatment as those used in 3.5.3 as

$$\delta T_{OB} = \delta T_{IB} = 0. \tag{4.6.11}$$

4.6.2 Magnetisation Parameter

An initial estimate of the influence the magnetisation parameter may have on the temperature distribution can be obtained by using the results from the spherically symmetric background model along with the equation for the magnetisation parameter

$$\omega_{\rm B}\tau = \frac{eB}{m_e^* c}\tau. \tag{4.6.12}$$

Figure 4.6.1 shows how the magnetisation parameter varies with radius for $B = 1 \times 10^9$G.

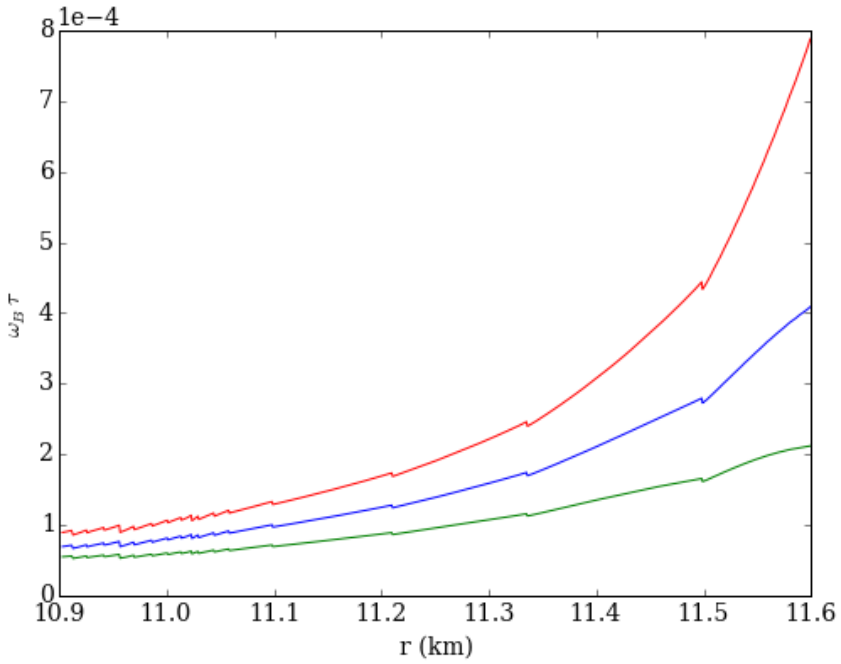

Figure 4.6.1: A graph to show how the magnetisation parameter varies with radius in a star with a normal core for a magnetic field $B = 1 \times 10^9$G, $Q_{\rm imp} = 1$ and three different accretion rates. The red line represents $\dot{M} = 1 \times 10^{-10} M_\odot$ yr^{-1}, the blue line $\dot{M} = 1 \times 10^{-9} M_\odot$ yr^{-1}, and the green line $\dot{M} = 1 \times 10^{-8} M_\odot$ yr^{-1}.

A comparison of figure 4.6.1 can be made with figure 3.5.1 from the constant density model. Both show a magnetisation parameter of order 10^{-4} for $B = 1 \times 10^9$ G. In figure 4.6.1 step-like features can be seen, which arise from the composition changes at different densities. In the constant density model $\omega_{\rm B}\tau$ decreases with increasing radii due to τ being inversely proportional to temperature. In this model with a realistic equation of state $\omega_{\rm B}\tau$ increases with increasing radii. These differences in the magnetisation parameter gradient is predominantly governed by the density dependence of τ.

4.7 Numerical Methods

The numerical methods employed to solve the first order coupled ODEs (4.6.7) and (4.6.9) are identical as those outlined in section 4.4. The shooting method is used to determine the outer boundary value of U_{lm}. The coupled differential equations are numerically integrated as a function of radius.

4.7.1 Non-dimensionalisation

To enable the numerical integration to solve the differential equations as accurately as possible, it is best to non-dimensionalise the equations. Using the definitions given in

equations (4.4.1) along with the additional relation

$$\hat{U} = \frac{U_{lm}}{F_{\rm typ}}, \tag{4.7.1}$$

the differential equations shown in (4.6.7) and (4.6.9) can be written in dimensionless form as

$$\frac{d\hat{U}}{d\hat{r}} = -\frac{2}{\hat{r}}\hat{U} + \frac{l(l+1)}{\hat{r}^2}\frac{V_{lm}}{F_{\rm typ}R_{\rm typ}} - 6C_{\rm e}T^5\delta T\frac{R_{\rm typ}}{F_{\rm typ}}, \tag{4.7.2}$$

$$\frac{d\delta\hat{T}}{d\hat{r}} = -\frac{1}{\kappa_0}\left(\frac{d\kappa_0}{d\hat{T}}\frac{d\hat{T}}{d\hat{r}}\delta\hat{T} + \hat{U}_{lm}K_{\rm typ}\right). \tag{4.7.3}$$

Equations (4.7.2) and (4.7.3) were solved using the shooting method in Python where the perturbed temperature at the outer and inner boundaries is set as $\delta T_{\rm OB} = \delta T_{\rm IB} = 0$, for both a normal and superfluid core.

4.8 Perturbed Model Results

The coupled ODEs describing how the heat flux and temperature vary in an accreted neutron star crust as shown in equations (4.6.7) and (4.6.9) respectively, were solved using the dimensionless forms of the equations as shown in (4.7.2) and (4.7.3), using the numerical techniques outlined in section 4.4. The results of this calculation are presented in this section.

The source term, from the last term in equation (4.6.8) is shown as a function of radius for both a normal and superfluid core, shown in figures 4.8.1 and 4.8.2 respectively, for three different accretion rates. At lower radii, spikes appear in the curves of both plots. These features arise from heat being deposited into the crust via pycnonuclear reactions. These spikes become more prominent with increasing accretion rates. The relation of the source term with temperature is complicated. An understanding of which scattering regime dominates in the crust for each accretion rate can be obtained from figures 4.5.8 for a normal core and 4.5.9 for a superfluid core. These figures show electron-phonon scattering as the dominant regime, due to the high crustal temperatures. Looking at equation (4.6.10), the source term scales as

$$T\frac{dT}{dr}(\nu_{\rm ep}(T) + \nu_{\rm eQ}(Q_{\rm imp}))^{-2}. \tag{4.8.1}$$

When electron-phonon scattering dominates, this can be approximated to $\sim \frac{1}{T}\frac{dT}{dr}$, which makes it difficult to predict how the source term scales with accretion rate for both a normal and superfluid core star.

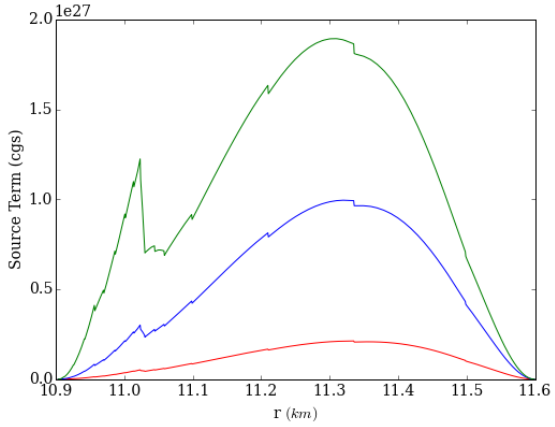

Figure 4.8.1: A graph to show how the source term in equation (4.6.8) varies with radius for a normal core, $B = 1 \times 10^{12}$G, $Q_{\rm imp} = 1$ and three different accretion rates. The red line represents $\dot{M} = 1 \times 10^{-10} M_{\odot}$ yr^{-1}, the blue line $\dot{M} = 1 \times 10^{-9} M_{\odot}$ yr^{-1}, and the green line $\dot{M} = 1 \times 10^{-8} M_{\odot}$ yr^{-1}.

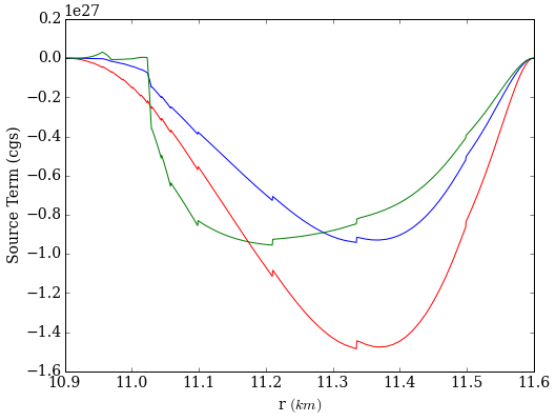

Figure 4.8.2: A graph to show how the source term in equation (4.6.8) varies with radius for a superfluid core, $B = 1 \times 10^{12}$G, $Q_{\rm imp} = 1$ and three different accretion rates. The red line represents $\dot{M} = 1 \times 10^{-10} M_{\odot}$ yr^{-1}, the blue line $\dot{M} = 1 \times 10^{-9} M_{\odot}$ yr^{-1}, and the green line $\dot{M} = 1 \times 10^{-8} M_{\odot}$ yr^{-1}.

The source term was also plotted as a function of impurity parameter, at the mid-point of the crust, for both a normal and superfluid core for three different accretion rates, the results are shown in figures 4.8.3 and 4.8.4 respectively. In both cases, the magnitude of the source term is at a maximum when the impurity parameter is small $Q_{\rm imp} \sim 1$, and decreases as the $Q_{\rm imp}$ increases. This pattern arises as the relaxation time τ becomes smaller as the crust becomes more impure. Again, it is difficult to predict the scaling with accretion rate due to the complex relationship of the source term with temperature.

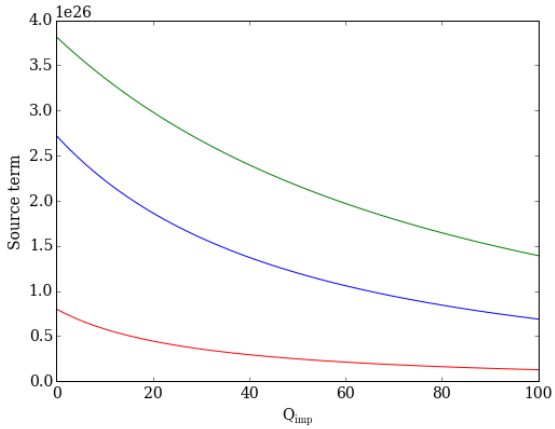

Figure 4.8.3: A graph to show how the source term in equation (4.6.8) varies with $Q_{\rm imp}$ at the mid point of the crust for a normal core, $B = 1 \times 10^{12}$G and three different accretion rates. The red line represents $\dot{M} = 1 \times 10^{-10} M_{\odot}$ yr^{-1}, the blue line $\dot{M} = 1 \times 10^{-9} M_{\odot}$ yr^{-1}, and the green line $\dot{M} = 1 \times 10^{-8} M_{\odot}$ yr^{-1}.

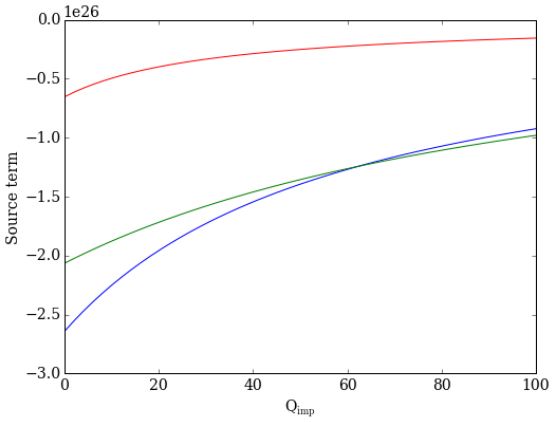

Figure 4.8.4: A graph to show how the source term in equation (4.6.8) varies with $Q_{\rm imp}$ at the mid point of the crust for a superfluid core, $B = 1 \times 10^{12}$G and three different accretion rates. The red line represents $\dot{M} = 1 \times 10^{-10} M_{\odot}$ yr^{-1}, the blue line $\dot{M} = 1 \times 10^{-9} M_{\odot}$ yr^{-1}, and the green line $\dot{M} = 1 \times 10^{-8} M_{\odot}$ yr^{-1}.

The perturbed temperature as a function of radius is shown in figure 4.8.5 for a normal

core and figure 4.8.6 for a superfluid core. For both a normal and superfluid core star, the temperature perturbation shows a clear peak at lower radii values. In the normal core star the magnitude of δT increases with higher accretion rates, whereas in the superfluid core case δT decreases with higher accretion rates. The perturbed temperature does not inherit noticeable jumps from the source term, as integrating over the source terms smooths the gradient.

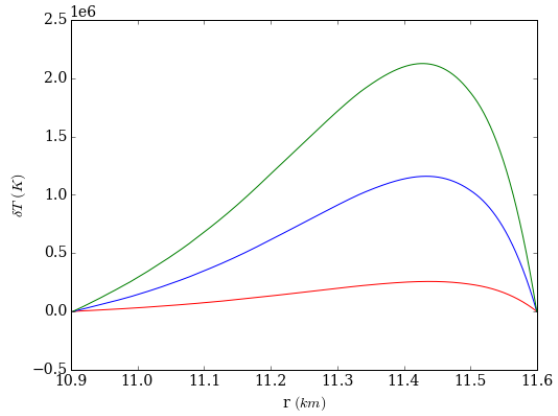

Figure 4.8.5: The perturbed temperature distribution, generated by the presence of a magnetic field of $B = 1 \times 10^{12}$G, with a normal core and $Q_{\rm imp} = 1$. The red line represents $\dot{M} = 1 \times 10^{-10} M_\odot$ yr^{-1}, the blue line $\dot{M} = 1 \times 10^{-9} M_\odot$ yr^{-1}, and the green line $\dot{M} = 1 \times 10^{-8} M_\odot$ yr^{-1}.

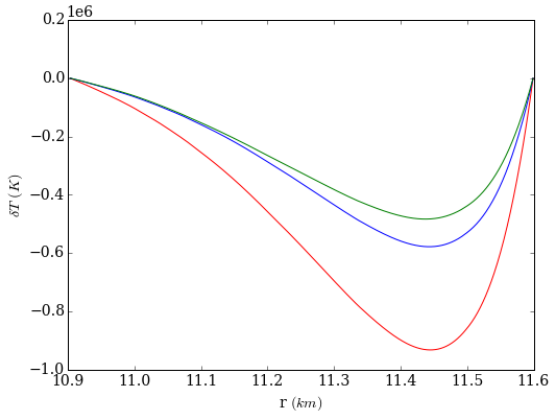

Figure 4.8.6: The perturbed temperature distribution, generated by the presence of a magnetic field of $B = 1 \times 10^{12}$G, with a superfluid core and $Q_{\rm imp} = 1$. The red line represents $\dot{M} = 1 \times 10^{-10} M_\odot$ yr^{-1}, the blue line $\dot{M} = 1 \times 10^{-9} M_\odot$ yr^{-1}, and the green line $\dot{M} = 1 \times 10^{-8} M_\odot$ yr^{-1}.

The perturbed radial flux U_{lm} as a function of radius is shown in figure 4.8.7 for a normal fluid core and figure 4.8.8 for a superfluid core. The magnitude of the perturbed flux is at a maximum at the inner boundary for both a normal and superfluid core star.

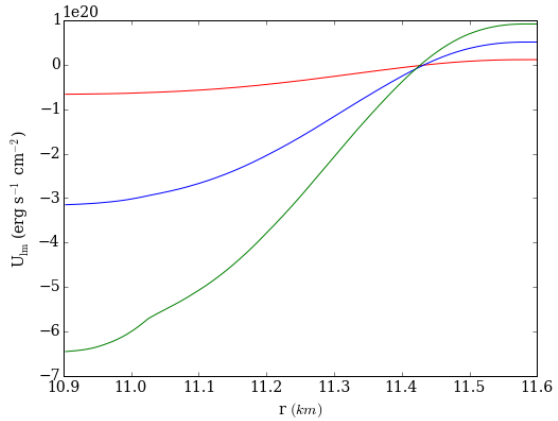

Figure 4.8.7: This figure shows how the heat flux in an accreted, magnetically perturbed neutron star crust varies as a function of radius for a normal core, $B = 1 \times 10^{12}$G and $Q_{\rm imp} = 1$. The red line represents $\dot{M} = 1 \times 10^{-10} M_\odot$ yr^{-1}, the blue line $\dot{M} = 1 \times 10^{-9} M_\odot$ yr^{-1}, and the green line $\dot{M} = 1 \times 10^{-8} M_\odot$ yr^{-1}.

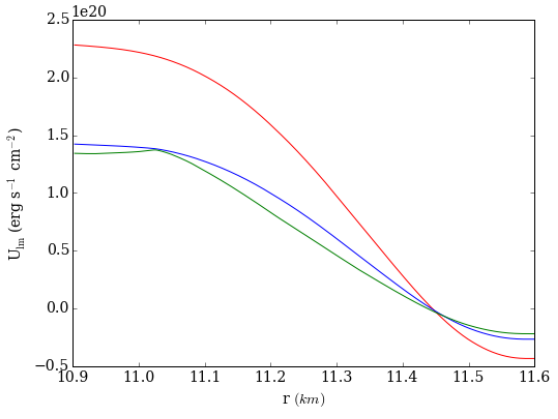

Figure 4.8.8: This figure shows how the heat flux in an accreted, magnetically perturbed neutron star crust varies as a function of radius for a superfluid core, $B = 1 \times 10^{12}$G and $Q_{\rm imp} = 1$. The red line represents $\dot{M} = 1 \times 10^{-10} M_\odot$ yr^{-1}, the blue line $\dot{M} = 1 \times 10^{-9} M_\odot$ yr^{-1}, and the green line $\dot{M} = 1 \times 10^{-8} M_\odot$ yr^{-1}.

A corresponding plot of $\delta T/T$ is shown in figures 4.8.9 and 4.8.10 for a normal and superfluid core respectively. Figure 4.8.9 shows a larger temperature perturbation ratio for higher accretion rates for a normal core star, and a smaller $\delta T/T$ for higher accretion rates for a superfluid core star. In both core cases the perturbed temperature ratio is of order $\sim 10^{-3}$, which corresponds to approximately $\delta T/T \sim 0.1\%$ for $B = 10^{12}$ G.

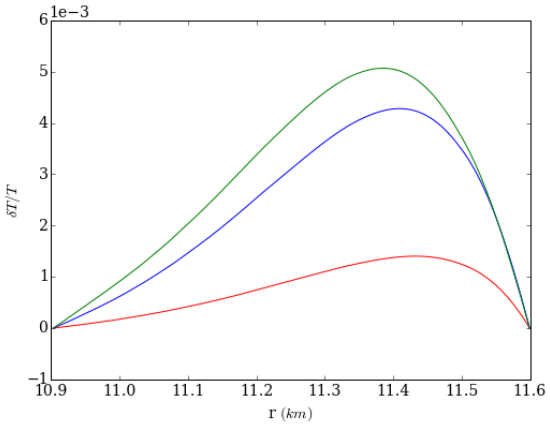

Figure 4.8.9: The magnitude of the temperature perturbation induced by the presence of a magnetic field of strength $B = 1 \times 10^{12}$G, with a normal core and $Q_{\rm imp} = 1$. The red line represents $\dot{M} = 1 \times 10^{-10} M_\odot$ yr^{-1}, the blue line $\dot{M} = 1 \times 10^{-9} M_\odot$ yr^{-1}, and the green line $\dot{M} = 1 \times 10^{-8} M_\odot$ yr^{-1}.

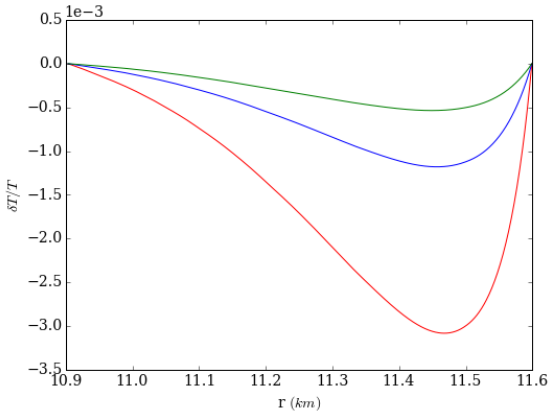

Figure 4.8.10: The magnitude of the temperature perturbation induced by the presence of a magnetic field of strength $B = 1 \times 10^{12}$G, with a superfluid core and $Q_{\rm imp} = 1$. The red line represents $\dot{M} = 1 \times 10^{-10} M_\odot$ yr^{-1}, the blue line $\dot{M} = 1 \times 10^{-9} M_\odot$ yr^{-1}, and the green line $\dot{M} = 1 \times 10^{-8} M_\odot$ yr^{-1}.

The corresponding plots of perturbed temperature as a function of density is shown for a normal and superfluid in figures 4.8.11 and 4.8.12 respectively. The perturbation ratio is also shown as a function of density in figures 4.8.13 for a normal core and 4.8.14 for a superfluid core.

The thermal conductivity and magnetisation parameter are both sensitive to the purity of the composition of the crust. The perturbed temperature ratio $\delta T/T$ was calculated for different impurity parameters, to investigate the influence the composition of the crust has on this ratio. The accretion rate was set to $\dot{M} = 1 \times 10^{-9} M_\odot$ yr^{-1}, and a magnetic field of $B = 1 \times 10^{12}$G, to generate a plot of $\delta T/T$ for different impurity parameters and is shown for a normal core in figure 4.8.15 and superfluid core in figure 4.8.16.

In both the normal and superfluid core plots, the smaller impurity parameters $Q_{\rm imp} \leq 10$ have little influence on the temperature perturbation ratio. This is because electron-phonon scattering is the dominant regime. When the impurity parameter is large $Q_{\rm imp} < 10$, we see for both a normal and superfluid core star, a larger impurity parameter generates a a larger $\delta T/T$. This may be because the value of τ decreases as $\nu_{\rm eQ}$ increases, resulting in a lower thermal conductivity, impeding the flow of heat through in the crust.

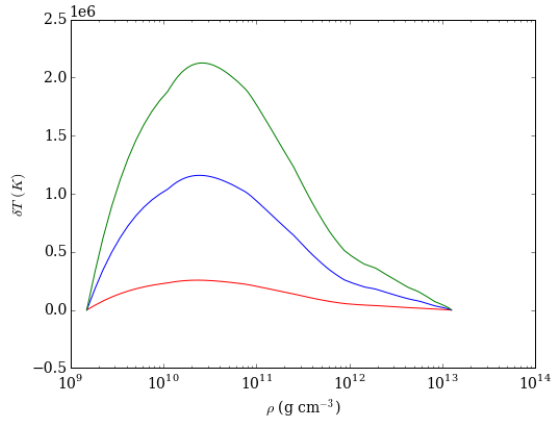

Figure 4.8.11: The perturbed temperature distribution, generated by the presence of a magnetic field of $B = 1 \times 10^{12}$G, with a normal core and $Q_{\rm imp} = 1$ as a function of ρ. The red line represents $\dot{M} = 1 \times 10^{-10} M_\odot$ yr^{-1}, the blue line $\dot{M} = 1 \times 10^{-9} M_\odot$ yr^{-1}, and the green line $\dot{M} = 1 \times 10^{-8} M_\odot$ yr^{-1}.

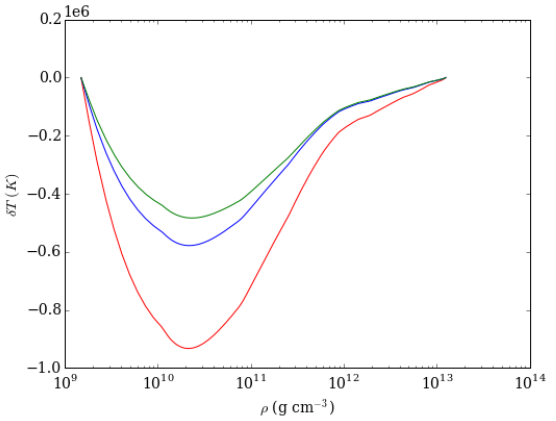

Figure 4.8.12: The perturbed temperature distribution, generated by the presence of a magnetic field of $B = 1 \times 10^{12}$G, with a superfluid core and $Q_{\rm imp} = 1$ as a function of ρ. The red line represents $\dot{M} = 1 \times 10^{-10} M_\odot$ yr^{-1}, the blue line $\dot{M} = 1 \times 10^{-9} M_\odot$ yr^{-1}, and the green line $\dot{M} = 1 \times 10^{-8} M_\odot$ yr^{-1}.

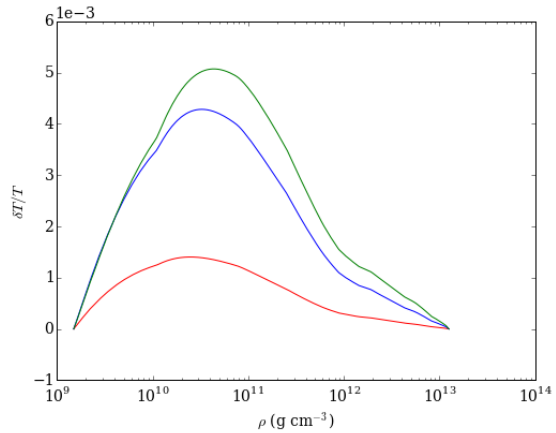

Figure 4.8.13: The magnitude of the temperature perturbation induced by the presence of a magnetic field of strength $B = 1 \times 10^{12}$G, with a normal core and $Q_{\rm imp} = 1$ as a function of ρ. The red line represents $\dot{M} = 1 \times 10^{-10} M_\odot$ yr^{-1}, the blue line $\dot{M} = 1 \times 10^{-9} M_\odot$ yr^{-1}, and the green line $\dot{M} = 1 \times 10^{-8} M_\odot$ yr^{-1}.

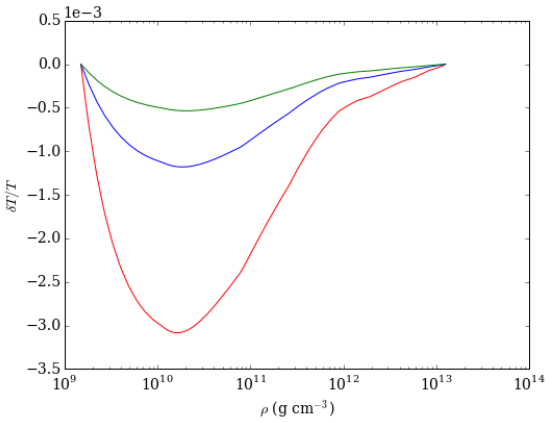

Figure 4.8.14: The magnitude of the temperature perturbation induced by the presence of a magnetic field of strength $B = 1 \times 10^{12}$G, with a superfluid core and $Q_{\rm imp} = 1$ as a function of ρ. The red line represents $\dot{M} = 1 \times 10^{-10} M_\odot$ yr^{-1}, the blue line $\dot{M} = 1 \times 10^{-9} M_\odot$ yr^{-1}, and the green line $\dot{M} = 1 \times 10^{-8} M_\odot$ yr^{-1}.

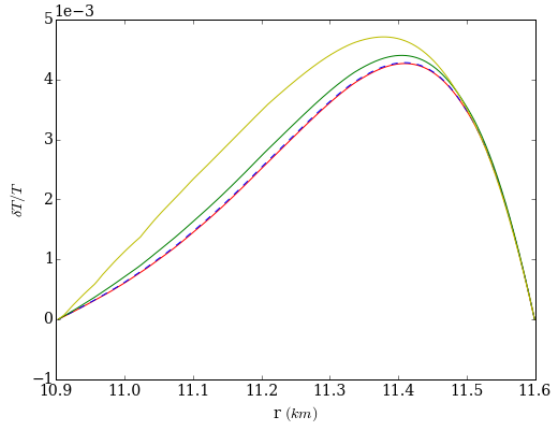

Figure 4.8.15: A graph to show how the magnitude of the temperature perturbation varies with impurity parameter as a function of radius for a normal core. The accretion rate was set to $\dot{M} = 1 \times 10^{-9} M_{\odot}$ yr^{-1}, a magnetic field of $B = 1 \times 10^{12}$G. The red line represents $Q_{\rm imp} = 0.1$, the blue dashed line $Q_{\rm imp} = 1$, the green line $Q_{\rm imp} = 10$ and yellow line $Q_{\rm imp} = 100$.

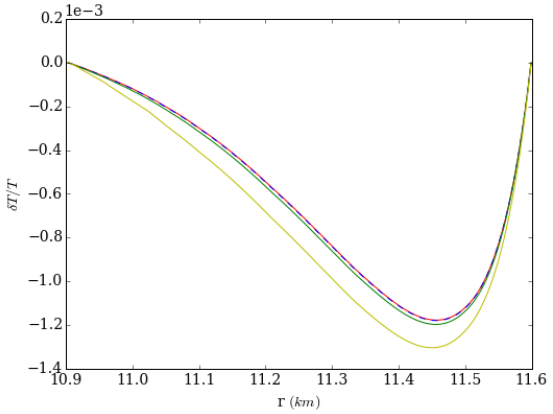

Figure 4.8.16: A graph to show how the magnitude of the temperature perturbation varies with impurity parameter as a function of radius for a superfluid core. The accretion rate was set to $\dot{M} = 1 \times 10^{-9} M_{\odot}$ yr^{-1}, a magnetic field of $B = 1 \times 10^{12}$G. The red line represents $Q_{\rm imp} = 0.1$, the blue dashed line $Q_{\rm imp} = 1$, the green line $Q_{\rm imp} = 10$ and yellow line $Q_{\rm imp} = 100$.

4.8.1 Numerical Testing

4.8.1.1 Convergence Testing

The results from the perturbed neutron star crust numerical calculations were tested for convergence using the same methods as those shown in section 4.5.2.2. The results of this test are shown in table 4.8.17.

$\dot{M}$ ($M_{\odot}$ yr^{-1})	$n_{\rm flux}$	$n_{\rm temperature}$
1×10^{-10}	1.00437	1.00220
1×10^{-9}	1.00437	1.00216
1×10^{-8}	1.00437	1.00218

Table 4.8.17: Summary of the converge test values obtained for both the perturbed temperature and flux for each accretion rate.

Table 4.8.17 shows the value for n for both the flux and temperature convergence test is positive for each accretion rate. This confirms the numerical calculations are convergent.

4.8.1.2 Finite Differencing

The accuracy of the ODE solver was tested using finite difference methods, as outlined in section 4.5.2.4. dU_{lm}/dr was calculated by finite differencing and the results compared to those obtained by using equation (4.6.7) directly. A comparison of these results is

shown in 4.8.18. The fractional error of this comparison is shown in figure 4.8.19.

The values of dU_{lm}/dr calculated using the two different techniques appear to agree well as shown in figure 4.8.18. Upon closer inspection, using the fractional error plot shown in 4.8.19, spikes appear showing deviations from the agreement of the two results. The larger spikes occur at points in the crust where step-wise features are seen in figure 4.8.18. These spikes lead to a fractional error of order 10^{-2}. This error is acceptable as it only this large over small ranges in r. Away from the spikes the error is of order 10^{-4}, which is within a suitable accuracy required of these calculations.

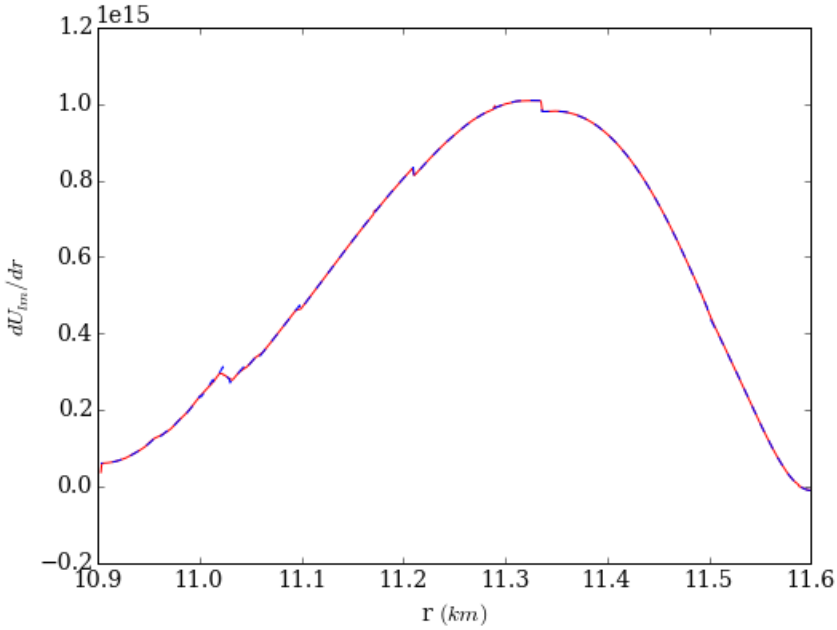

Figure 4.8.18: A comparison of dU_{lm}/dr as calculated by finite differencing (red line) and directly from equation (4.6.7) (blue line) for an accretion rate of $\dot{M} = 1\times10^{-9} M_{\odot}$ yr^{-1}, with a normal core and $B = 1\times10^{12}$ G.

A finite difference test was also conducted for $d\delta T/dr$. Figure 4.8.20 shows a comparison of values for $d\delta T/dr$ as calculated by finite differencing and equation 4.6.9. These two methods of calculation appear to correspond well. To investigate the validity of the results further, the fractional error of these values was calculated and is shown in figure 4.8.21. Similarly to the dU_{lm}/dr case, spikes are present and correspond to the step-wise features that occur in $d\delta T/dr$. These spikes are of order 10^{-2}, which is suitably low for the accuracy required of these calculations. The finite difference test was passed for both cases.

The finite difference tests were also conducted for a star with a superfluid core, and were found to have the same order of accuracy as the normal core finite difference test results presented here.

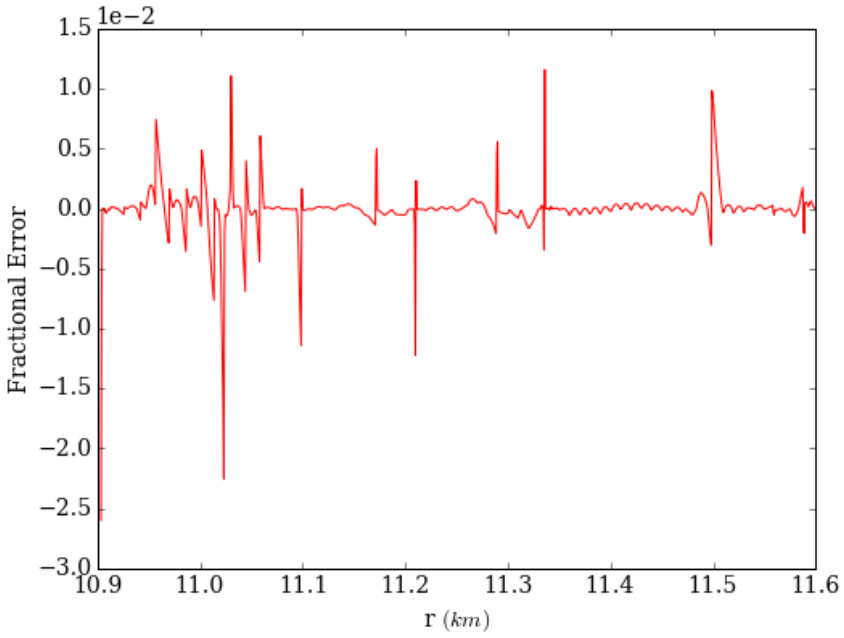

Figure 4.8.19: The fractional error between the two plots shown in figure 4.8.18.

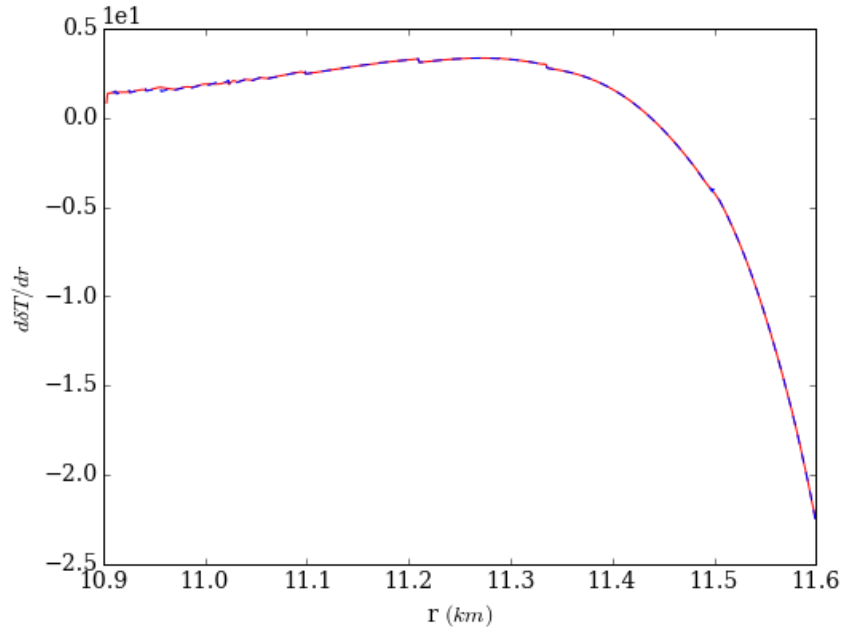

Figure 4.8.20: A comparison of $d\delta T/dr$ as calculated by finite differencing (red line) and directly from equation (4.6.7) (blue line) for an accretion rate of $\dot{M} = 1\times10^{-9} M_{\odot}$ yr^{-1}, with a normal core and $B = 1\times10^{12}$ G.

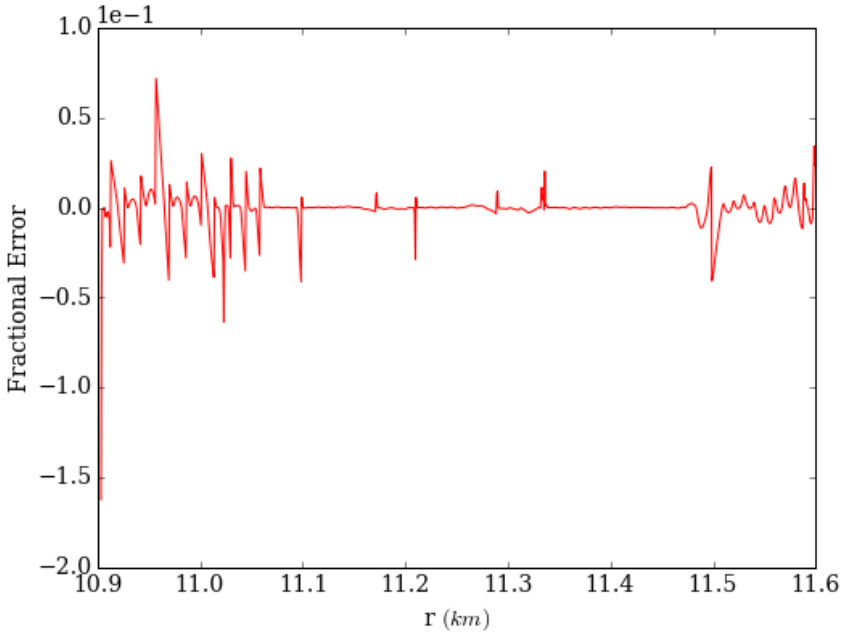

Figure 4.8.21: The fractional error between the two plots shown in figure 4.8.19.

4.9 Shallow crustal heating

In recent years, studies of cooling X-ray transiently accreting neutron stars have shown that cooling curves cannot be reproduced without the presence of a shallow heating source in the crust. At low densities $\rho \approx 10^8 - 10^{10}$g cm^{-3} an additional heat source of $\sim 1-10$ MeV is required (Deibel et al., 2015), (Waterhouse et al., 2016), (Parikh et al., 2017). To investigate the effects of shallow crustal heating on our model we input 6 MeV into the density range 10^9-10^{10} g cm^{-3}. From our crustal equation of state data (as shown in table 4.2.1) 2 MeV was input at regions of uniform volume between two density transitions for $r = 11.599$km, 11.498km, and 11.335km. Lower densities were not included as our data set does extend to densities below 10^9g cm^{-3}. The results with shallow heating included in our model are presented below, alongside the results produced in the absence of shallow heating to enable the reader to easily draw comparisons between the two data sets.

4.9.1 Background thermal profile with shallow crustal heating

The results presented in this subsection have been obtained by solving our background model for a spherically symmetric accreted neutron star crust for three different accretion rates $\dot{M} = 1 \times 10^{-10} M_\odot$ yr^{-1}, $\dot{M} = 1 \times 10^{-9} M_\odot$ yr^{-1}, and $\dot{M} = 1 \times 10^{-8} M_\odot$ yr^{-1} and for an impurity parameter $Q_{\rm imp} = 1$.

The background temperature profile of the crust in the presence of shallow heating is shown in figure 4.9.2, and without in figure 4.9.1 for a normal core star. There is a significant difference in the shape of the curve for the two models. In the case where shallow heating is present, we see an increase in temperature from the outer boundary when moving inwards through the crust to towards the core, peaking where shallow heating occurs. Higher accretion rates produce a hotter crust, which corresponds to more heat deposited into the crust via accretion. Overall, the background temperature is slightly hotter (less than one order of magnitude) when shallow heating is present.

The background flux in the absence of shallow heating is shown in figure 4.9.3 and in the presence of shallow heating in figure 4.9.4 for a normal core star. The curves in the shallow heating case has much steeper gradients throughout the crust. When shallow heating isn't present, we see the flux plateaus at higher radii then steeply decreases at low radii where pycnonuclear reactions begin to occur in the crust. The presence of shallow heating increases the background flux by less than one order of magnitude.

The background temperature results for a superfluid core star are shown in the presence of shallow heating and without shallow heating in figures 4.9.6 and 4.9.5 respectively. For accretion rate $\dot{M} = 1 \times 10^{-8} M_\odot$ yr^{-1}, a peak can clearly be seen at higher radii where

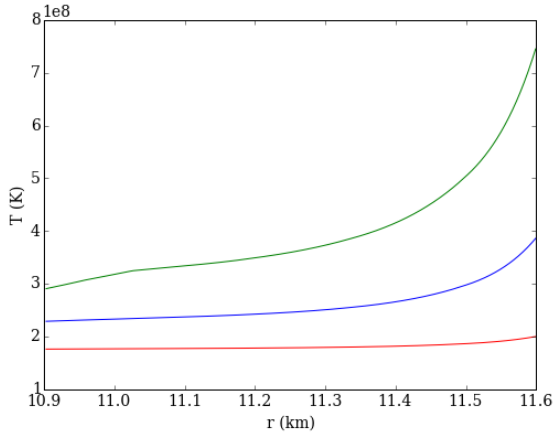

Figure 4.9.1: This figure shows how the temperature in an accreted neutron star crust varies as a function of radius for a normal core, $B = 1 \times 10^{12}$G and $Q_{\rm imp} = 1$. The red line represents $\dot{M} = 1 \times 10^{-10} M_\odot$ yr^{-1}, the blue line $\dot{M} = 1 \times 10^{-9} M_\odot$ yr^{-1}, and the green line $\dot{M} = 1 \times 10^{-8} M_\odot$ yr^{-1}.

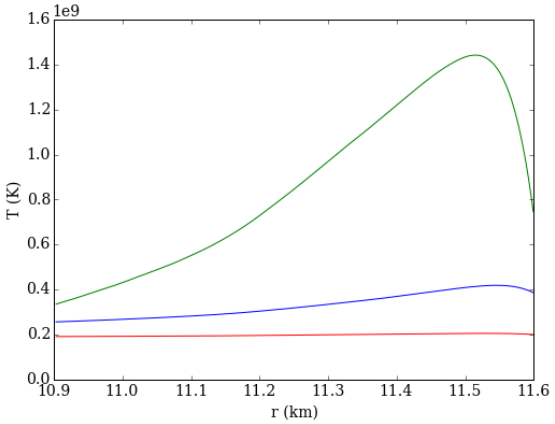

Figure 4.9.2: This figure shows how the temperature in an accreted neutron star crust varies as a function of radius for a normal core in the presence of crustal shallow heating, $B = 1 \times 10^{12}$G and $Q_{\rm imp} = 1$. The red line represents $\dot{M} = 1 \times 10^{-10} M_\odot$ yr^{-1}, the blue line $\dot{M} = 1 \times 10^{-9} M_\odot$ yr^{-1}, and the green line $\dot{M} = 1 \times 10^{-8} M_\odot$ yr^{-1}.

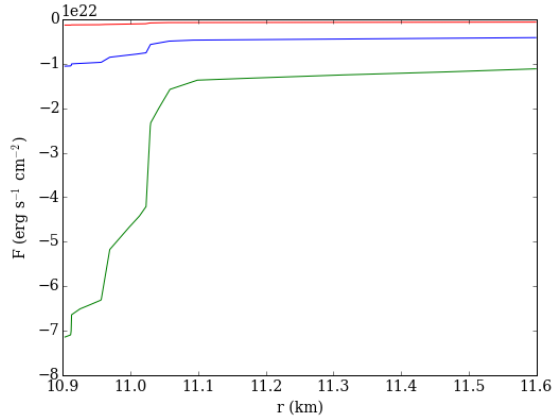

Figure 4.9.3: This figure shows how the heat flux in an accreted neutron star crust varies as a function of radius for a normal core, $B = 1 \times 10^{12}$G and $Q_{\rm imp} = 1$. The red line represents $\dot{M} = 1 \times 10^{-10} M_\odot$ yr^{-1}, the blue line $\dot{M} = 1 \times 10^{-9} M_\odot$ yr^{-1}, and the green line $\dot{M} = 1 \times 10^{-8} M_\odot$ yr^{-1}.

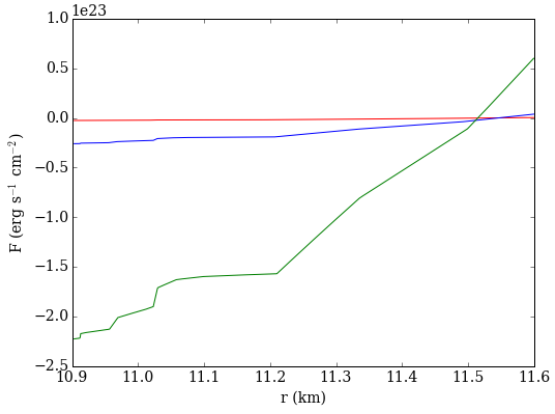

Figure 4.9.4: This figure shows how the heat flux in an accreted neutron star crust varies as a function of radius for a normal core in the presence of crustal shallow heating, $B = 1 \times 10^{12}$G and $Q_{\rm imp} = 1$. The red line represents $\dot{M} = 1 \times 10^{-10} M_\odot$ yr^{-1}, the blue line $\dot{M} = 1 \times 10^{-9} M_\odot$ yr^{-1}, and the green line $\dot{M} = 1 \times 10^{-8} M_\odot$ yr^{-1}.

shallow heating occurs in figure 4.9.6. For lower accretion rates, the presence of shallow heating has less influence on the background temperature and the results are similar to those when shallow heating is not present. A star with a superfluid core restricts the flow of flux to the core, causing the temperature to build up in the crust. Only at significantly high accretion rates $\dot{M} \geq 1 \times 10^{-8} M_{\odot}$ yr^{-1}, do we see the effects of shallow heating. The presence of shallow heating in the crust for a superfluid core produces a slightly hotter crust than when shallow heating isn't present.

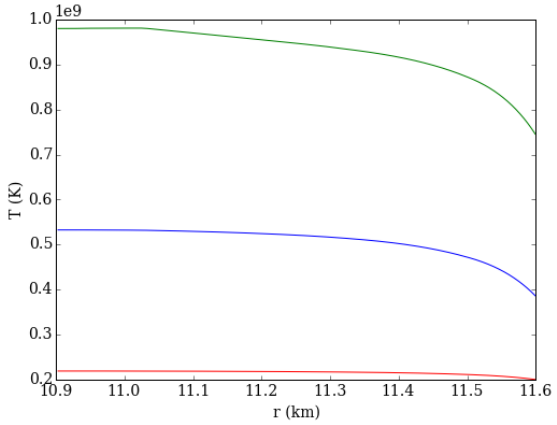

Figure 4.9.5: This figure shows how the temperature in an accreted neutron star crust varies as a function of radius for a superfluid core, $B = 1 \times 10^{12}$G and $Q_{\rm imp} = 1$. The red line represents $\dot{M} = 1 \times 10^{-10} M_{\odot}$ yr^{-1}, the blue line $\dot{M} = 1 \times 10^{-9} M_{\odot}$ yr^{-1}, and the green line $\dot{M} = 1 \times 10^{-8} M_{\odot}$ yr^{-1}.

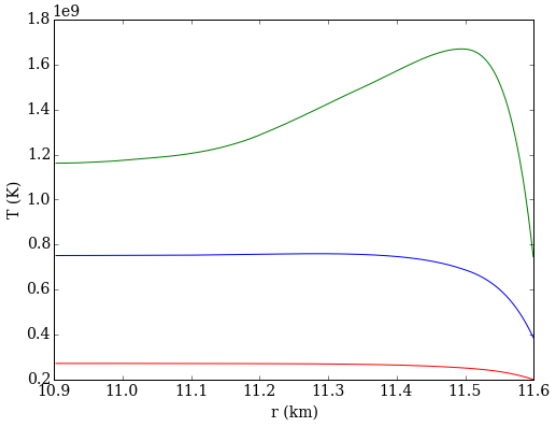

Figure 4.9.6: This figure shows how the temperature in an accreted neutron star crust varies as a function of radius for a superfluid core in the presence of crustal shallow heating, $B = 1 \times 10^{12}$G and $Q_{\rm imp} = 1$. The red line represents $\dot{M} = 1 \times 10^{-10} M_{\odot}$ yr^{-1}, the blue line $\dot{M} = 1 \times 10^{-9} M_{\odot}$ yr^{-1}, and the green line $\dot{M} = 1 \times 10^{-8} M_{\odot}$ yr^{-1}.

The background flux for a superfluid core with and without shallow heating is shown in figures 4.9.8 and 4.9.7 respectively. When shallow heating is present the flux is an order of magnitude larger than without. The distribution of flux in the crust differs quite significantly to the case without shallow crustal heating. The flux has a broader more negative curve when shallow heating is present, compared to a more consistently positive flux until the region of the crust where the pycnonuclear reactions begin to occur at lower radii.

4.9.2 Perturbed thermal profile with shallow crustal heating

The perturbed temperature in the presence of shallow heating for a normal core star is shown in figure 4.9.10 and without shallow heating in figure 4.9.9. The magnitude of δT is approximately 4 times larger in the presence of shallow heating when compared to the case without shallow crustal heating.

The perturbed flux for a normal core is shown with and without shallow heating in figures 4.9.12 and 4.9.11 respectively. In the presence of shallow heating U_{lm} is an order of

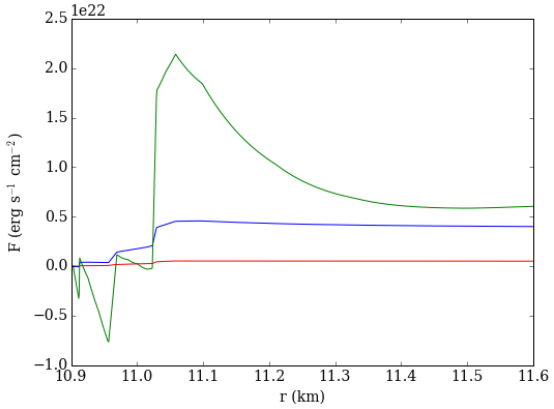

Figure 4.9.7: This figure shows how the heat flux in an accreted neutron star crust varies as a function of radius for a superfluid core, $B = 1 \times 10^{12}$G and $Q_{\rm imp} = 1$. The red line represents $\dot{M} = 1 \times 10^{-10} M_\odot$ yr^{-1}, the blue line $\dot{M} = 1 \times 10^{-9} M_\odot$ yr^{-1}, and the green line $\dot{M} = 1 \times 10^{-8} M_\odot$ yr^{-1}.

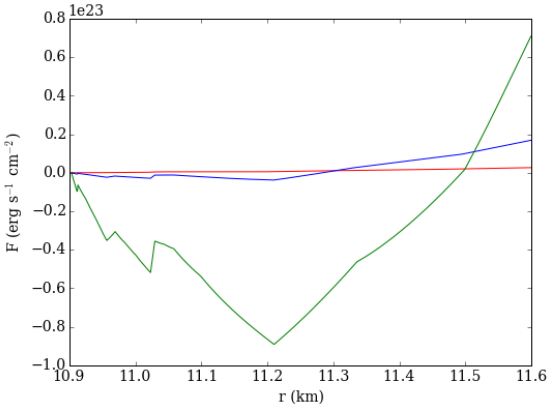

Figure 4.9.8: This figure shows how the heat flux in an accreted neutron star crust varies as a function of radius for a superfluid core in the presence of crustal shallow heating, $B = 1 \times 10^{12}$G and $Q_{\rm imp} = 1$. The red line represents $\dot{M} = 1 \times 10^{-10} M_\odot$ yr^{-1}, the blue line $\dot{M} = 1 \times 10^{-9} M_\odot$ yr^{-1}, and the green line $\dot{M} = 1 \times 10^{-8} M_\odot$ yr^{-1}.

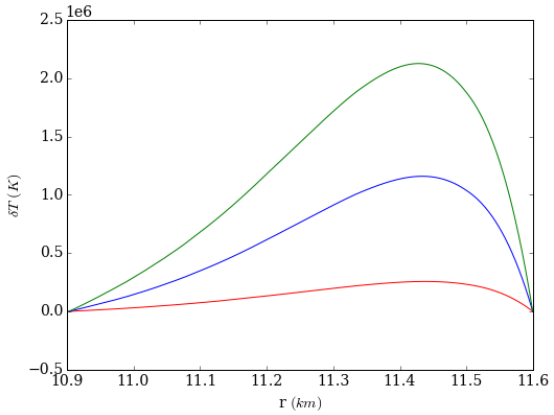

Figure 4.9.9: This figure shows how the perturbed temperature in an accreted, magnetically perturbed neutron star crust varies as a function of radius for a normal core, $B = 1 \times 10^{12}$G and $Q_{\rm imp} = 1$. The red line represents $\dot{M} = 1 \times 10^{-10} M_\odot$ yr^{-1}, the blue line $\dot{M} = 1 \times 10^{-9} M_\odot$ yr^{-1}, and the green line $\dot{M} = 1 \times 10^{-8} M_\odot$ yr^{-1}.

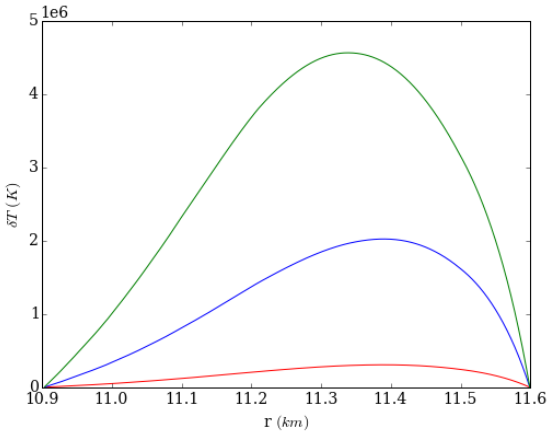

Figure 4.9.10: This figure shows how the perturbed temperature in an accreted, magnetically perturbed neutron star crust varies as a function of radius for a normal core in the presence of crustal shallow heating, $B = 1 \times 10^{12}$G and $Q_{\rm imp} = 1$. The red line represents $\dot{M} = 1 \times 10^{-10} M_\odot$ yr^{-1}, the blue line $\dot{M} = 1 \times 10^{-9} M_\odot$ yr^{-1}, and the green line $\dot{M} = 1 \times 10^{-8} M_\odot$ yr^{-1}.

magnitude larger than the case without shallow heating. Overall the flux distribution in the accreted crust is similar in both cases, with a positive flux spanning a broader range of radii when shallow heating is present.

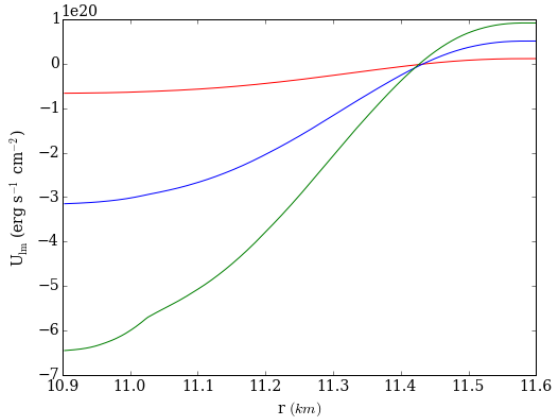

Figure 4.9.11: This figure shows how the perturbed heat flux in an accreted, magnetically perturbed neutron star crust varies as a function of radius for a normal core, $B = 1 \times 10^{12}$G and $Q_{\rm imp} = 1$. The red line represents $\dot{M} = 1 \times 10^{-10} M_{\odot}$ yr^{-1}, the blue line $\dot{M} = 1 \times 10^{-9} M_{\odot}$ yr^{-1}, and the green line $\dot{M} = 1 \times 10^{-8} M_{\odot}$ yr^{-1}.

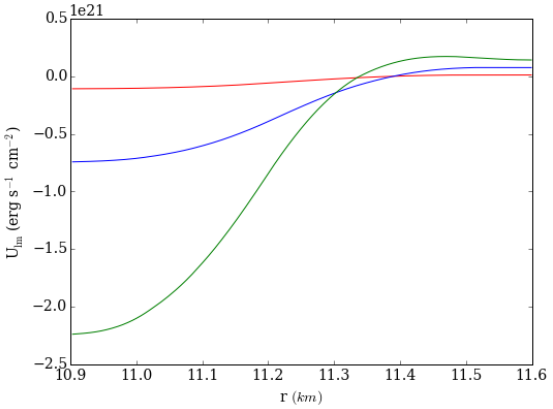

Figure 4.9.12: This figure shows how the perturbed heat flux in an accreted, magnetically perturbed neutron star crust varies as a function of radius for a normal core in the presence of crustal shallow heating, $B = 1 \times 10^{12}$G and $Q_{\rm imp} = 1$. The red line represents $\dot{M} = 1 \times 10^{-10} M_{\odot}$ yr^{-1}, the blue line $\dot{M} = 1 \times 10^{-9} M_{\odot}$ yr^{-1}, and the green line $\dot{M} = 1 \times 10^{-8} M_{\odot}$ yr^{-1}.

The most interesting result can be seen in the graphs of $\delta T/T$ for a normal core star, shown in figures 4.9.13 without shallow heating and 4.9.14 with shallow heating. When shallow heating is present, accretion rate $\dot{M} = 1 \times 10^{-9} M_{\odot}$ yr^{-1} produces a larger temperature perturbation than $\dot{M} = 1 \times 10^{-8} M_{\odot}$ yr^{-1}, it is unclear as to why shallow heating produces such a high $\delta T/T$ for accretion rate $\dot{M} = 1 \times 10^{-9} M_{\odot}$ yr^{-1} and not the other accretion rates. The overall temperature perturbation ratio produced when shallow heating is included in our model, is approximately twice as large as when this heating mechanism is excluded.

The perturbed temperature for a superfluid core star is shown without shallow heating in figure 4.9.15 and with shallow heating in figure 4.9.16. In the presence of shallow heating, the magnitude of δT is comparable for the lower accretion rates ($\dot{M} \leq 1 \times 10^{-9} M_{\odot}$ yr^{-1}). The highest accretion rate $\dot{M} = 1 \times 10^{-8} M_{\odot}$ yr^{-1}, produces the largest magnitude of δT with a a broader curve that peaks at smaller radii when compared to the lower accretion rates. The temperature perturbation is of the same order of magnitude for both cases.

For the superfluid core star, the perturbed flux with shallow crustal heating is shown in figure 4.9.18, and without crustal heating in figure 4.9.17. The perturbed flux curves when shallow heating is present are quite different to those in the absence of shallow heating. Small peaks in U_{lm} can be seen at lower radii for the higher accretion rates

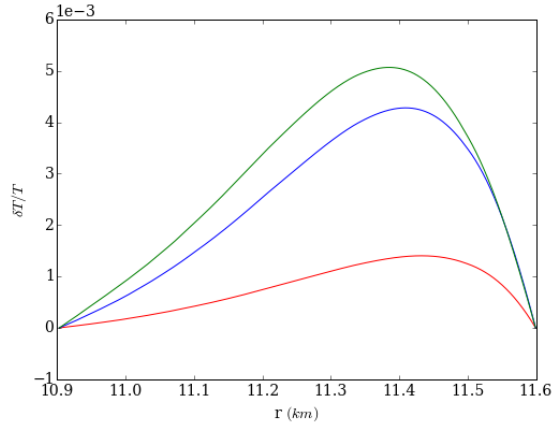

Figure 4.9.13: This figure shows how $\delta T/T$ in an accreted, magnetically perturbed neutron star crust varies as a function of radius for a normal core, $B = 1\times10^{12}$G and $Q_{\rm imp} = 1$. The red line represents $\dot{M} = 1 \times 10^{-10} M_\odot$ yr^{-1}, the blue line $\dot{M} = 1 \times 10^{-9} M_\odot$ yr^{-1}, and the green line $\dot{M} = 1 \times 10^{-8} M_\odot$ yr^{-1}.

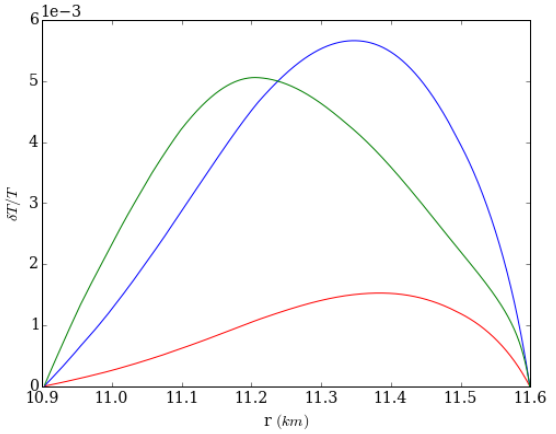

Figure 4.9.14: This figure shows how $\delta T/T$ in an accreted, magnetically perturbed neutron star crust varies as a function of radius for a normal core in the presence of crustal shallow heating, $B = 1 \times 10^{12}$G and $Q_{\rm imp} = 1$. The red line represents $\dot{M} = 1 \times 10^{-10} M_\odot$ yr^{-1}, the blue line $\dot{M} = 1 \times 10^{-9} M_\odot$ yr^{-1}, and the green line $\dot{M} = 1 \times 10^{-8} M_\odot$ yr^{-1}.

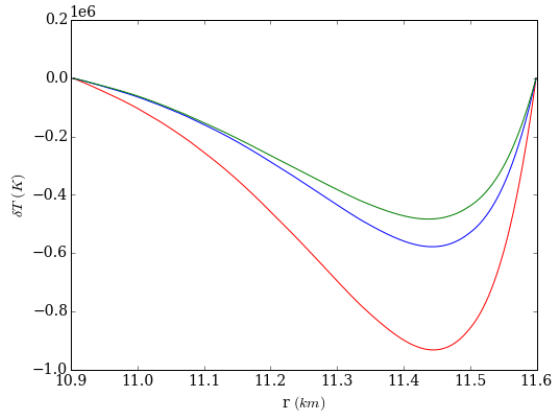

Figure 4.9.15: This figure shows how the perturbed temperature in an accreted, magnetically perturbed neutron star crust varies as a function of radius for a superfluid core, $B = 1 \times 10^{12}$G and $Q_{\rm imp} = 1$. The red line represents $\dot{M} = 1\times10^{-10} M_\odot$ yr^{-1}, the blue line $\dot{M} = 1 \times 10^{-9} M_\odot$ yr^{-1}, and the green line $\dot{M} = 1 \times 10^{-8} M_\odot$ yr^{-1}.

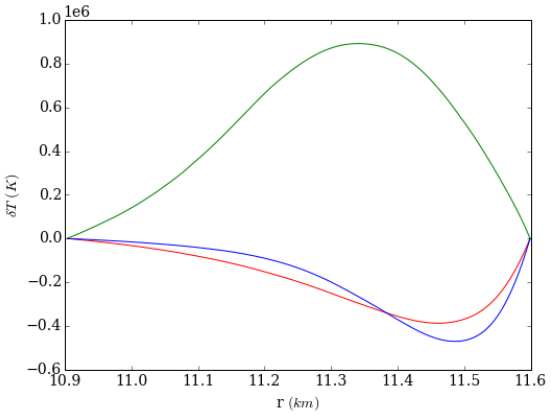

Figure 4.9.16: This figure shows how the perturbed temperature in an accreted, magnetically perturbed neutron star crust varies as a function of radius for a superfluid core in the presence of crustal shallow heating, $B = 1 \times 10^{12}$G and $Q_{\rm imp} = 1$. The red line represents $\dot{M} = 1 \times 10^{-10} M_\odot$ yr^{-1}, the blue line $\dot{M} = 1 \times 10^{-9} M_\odot$ yr^{-1}, and the green line $\dot{M} = 1 \times 10^{-8} M_\odot$ yr^{-1}.

$\dot{M} \geq 1 \times 10^{-9} M_{\odot}$ yr^{-1}, which aren't present when shallow heating isn't included.

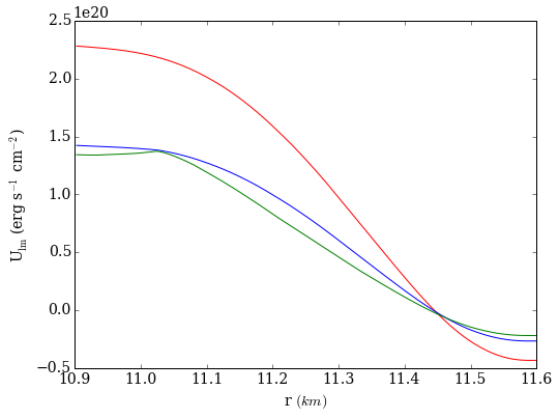

Figure 4.9.17: This figure shows how the perturbed flux in an accreted, magnetically perturbed neutron star crust varies as a function of radius for a superfluid core, $B = 1 \times 10^{12}$G and $Q_{\rm imp} = 1$. The red line represents $\dot{M} = 1 \times 10^{-10} M_{\odot}$ yr^{-1}, the blue line $\dot{M} = 1 \times 10^{-9} M_{\odot}$ yr^{-1}, and the green line $\dot{M} = 1 \times 10^{-8} M_{\odot}$ yr^{-1}.

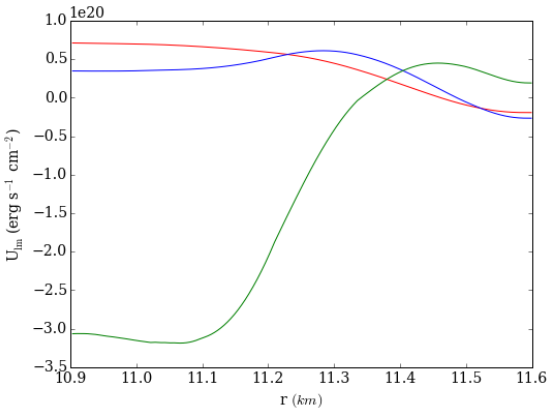

Figure 4.9.18: This figure shows how the perturbed flux in an accreted, magnetically perturbed neutron star crust varies as a function of radius for a superfluid core in the presence of crustal shallow heating, $B = 1 \times 10^{12}$G and $Q_{\rm imp} = 1$. The red line represents $\dot{M} = 1 \times 10^{-10} M_{\odot}$ yr^{-1}, the blue line $\dot{M} = 1 \times 10^{-9} M_{\odot}$ yr^{-1}, and the green line $\dot{M} = 1 \times 10^{-8} M_{\odot}$ yr^{-1}.

The ratio $\delta T/T$ for shallow crustal heating for a superfluid core star is shown in figure 4.9.20 and without in figure 4.9.19. The magnitude of $\delta T/T$ is approximately half the size when shallow crustal heating is present.

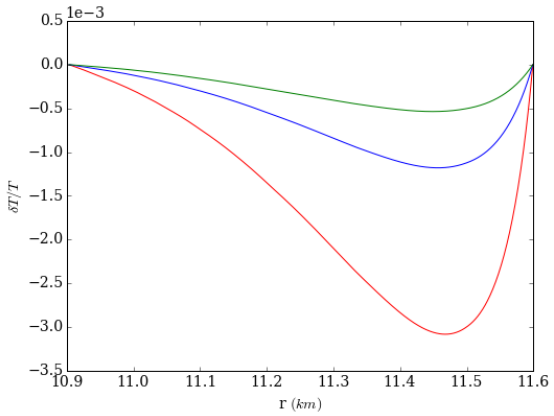

Figure 4.9.19: This figure shows how $\delta T/T$ in an accreted, magnetically perturbed neutron star crust varies as a function of radius for a superfluid core, $B = 1 \times 10^{12}$G and $Q_{\rm imp} = 1$. The red line represents $\dot{M} = 1 \times 10^{-10} M_\odot$ yr^{-1}, the blue line $\dot{M} = 1 \times 10^{-9} M_\odot$ yr^{-1}, and the green line $\dot{M} = 1 \times 10^{-8} M_\odot$ yr^{-1}.

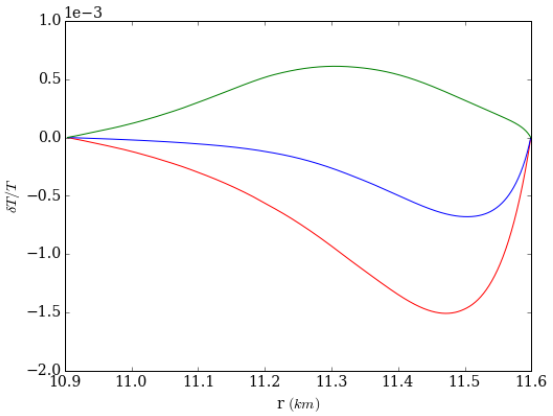

Figure 4.9.20: This figure shows how $\delta T/T$ in an accreted, magnetically perturbed neutron star crust varies as a function of radius for a superfluid core in the presence of crustal shallow heating, $B = 1 \times 10^{12}$G and $Q_{\rm imp} = 1$. The red line represents $\dot{M} = 1 \times 10^{-10} M_\odot$ yr^{-1}, the blue line $\dot{M} = 1 \times 10^{-9} M_\odot$ yr^{-1}, and the green line $\dot{M} = 1 \times 10^{-8} M_\odot$ yr^{-1}.

4.10 Summary and discussion

In chapter 3, a temperature perturbation ratio of $\delta T/T \sim 2 \times 10^{-6} \mathrm{B}_9$ was calculated for a constant density star with a normal fluid core giving rise to an ellipticity of $\epsilon \approx 2 \times 10^{-11} \mathrm{B}_9$ for $\dot{M} = 1 \times 10^{-9} M_\odot$ yr^{-1} and $Q_{\mathrm{imp}} = 1$.

In this chapter, the thermal profile of a realistic, spherically symmetric, accreted neutron star crust was constructed for both a normal and superfluid core. The crust was calculated from the Newtonian hydrostatic structure equations on a relativistic core which was computed using the TOV equations. Using accreted crust equation of state data from Haensel and Zdunik (1990a), density dependent variables were calculated as a function of position in the crust.

A background thermal profile was calculated from the heat equation in the steady state. Nuclear heating from accretion provided a heat source, and neutrino cooling a heat sink. This background model was then perturbed by the insertion of a toroidal magnetic field. The magnetic field influences how heat is transported around the crust, by interacting with electrons, the dominant heat carriers, resulting in a temperature perturbation.

From Ushomirsky et al. (2000), the ellipticity induced can be written as a function of $\delta T/T$ as

$$\epsilon \approx \frac{Q}{I} \approx 5 \times 10^{-6} \frac{\delta T}{T}, \tag{4.10.1}$$

where Q is the mass quadrupole moment and I is the moment of inertia. The value of $\delta T/T$ selected at $\rho = 1 \times 10^{12}$g cm^{-3}, as Ushomirsky et al. (2000) find that the higher density inner crust is the part that contributes most to the quadrupole moment. From figure 4.8.13, for a normal core star, we find

$$\frac{\delta T}{T} \approx 1 \times 10^{-3} \mathrm{B}_{12}, \tag{4.10.2}$$

and from figure 4.8.14, for a superfluid core star, as

$$\frac{\delta T}{T} \approx 2 \times 10^{-4} \mathrm{B}_{12}. \tag{4.10.3}$$

Combining these parametrised equations for the perturbed temperature ratio with equation 4.10.1 and rescaling for $B = 10^9$ G, we find in the case of a normal fluid core, the magnetic field induced an ellipticity

$$\epsilon \approx 5 \times 10^{-12} \mathrm{B}_9, \tag{4.10.4}$$

and for a superfluid core

$$\epsilon \approx 1 \times 10^{-12} \mathrm{B}_9 \tag{4.10.5}$$

for $\dot{M} = 1 \times 10^{-9} M_{\odot}$ yr^{-1}, $\rho = 10^{12}$g cm^{-3}, $Q_{\rm imp} = 1$ and $\rho = 10^{12}$ g cm^{-3}. These ellipticity values suggest a surprisingly large internal magnetic field would have to exist in accreting neutron stars for this model of mountain growth to viably exist. The ellipticity obtained from Ushomirsky et al. (2000), as shown in equation (4.10.1), is approximately independent of accretion rate. For simplicity, values of $\delta T/T$ the intermediate accretion rate ($\dot{M} = 1 \times 10^{-9} M_{\odot}$ yr^{-1}) were selected. The ellipticity scales linearly with the temperature perturbation ratio. Ushomirsky et al. (2000) show a temperature perturbation ratio of order $\sim 1\%$ is required to generate a mass quadrupole moment that is sufficiently large to produce gravitational wave energy losses that balance the spin-up torque from accretion. The parameter space was explored by varying the accretion rate and impurity parameter in the model. Higher accretion rates were found to induce a larger temperature perturbation ratio in the normal case, and a lower temperature perturbation ratio in the superfluid core case. From figures 4.8.15 and 4.8.16, a higher $Q_{\rm imp}$ representing an impure crust resulted in a higher magnitude $\delta T/T$ for both a normal and superfluid core star, as a higher value of $Q_{\rm imp}$ results in a smaller τ effectively reducing the thermal conductivity, impeding heat transport in the crust.

The effect of crustal shallow heating was also investigated with our model. The temperature perturbation ratio and ellipticity calculated by our model in the presence of shallow heating for a normal core star was found to be

$$\frac{\delta T}{T} = 2 \times 10^{-6} \mathrm{B}_9,$$
$$\epsilon \approx 1 \times 10^{-11} \mathrm{B}_9,$$

and for a superfluid core as

$$\frac{\delta T}{T} = 3.6 \times 10^{-8} \mathrm{B}_9,$$
$$\epsilon \approx 1.8 \times 10^{-13} \mathrm{B}_9.$$

Overall, in both the normal and superfluid core cases, the presence of the shallow crustal heating did not alter the magnitude of the temperature perturbation induced by the presence of the magnetic field.

In the literature, it has been shown that the magnetic field of a neutron star can induce ellipticities through the development of 'magnetic mountains'. These mountains differ from the work produced here, as a temperature asymmetry is not required. As a magnetic field is present in both cases, thermal and magnetic mountains, it would be interesting to compare the magnitude of ellipticities induced by each mechanism. Cutler (2002) showed for a normal core where the toroidal magnetic field $B_{\rm t} < 10^{15}$G, the

ellipticity generated for a 1.4 $M_\odot$ star and 10km radius was

$$\epsilon_{\rm B} = -1.6 \times 10^{-6} \left(\frac{< B_{\rm t}^2 >}{(10^{15}{\rm G})^2} \right), \tag{4.10.6}$$

and for a star with a superconducting core

$$\epsilon_{\rm B} = -1.6 \times 10^{-6} \left(\frac{< B_{\rm t} >}{10^{15}{\rm G}} \right), \tag{4.10.7}$$

where $< ... >$ is the volume averaged over the neutron star interior, and it was assumed the toroidal component of the magnetic field is stronger than the poloidal component. In more recent work, Lander (2013) found the ellipticity induced by magnetic mountains for a neutron star with a superconducting core to have an ellipticity a couple of orders of magnitude smaller than previous calculations as

$$\epsilon_{\rm B} = 3.1 \times 10^{-8} \left(\frac{< B_{\rm t} >}{10^{12}{\rm G}} \right) \left(\frac{< H_c >}{10^{15}{\rm G}} \right), \tag{4.10.8}$$

where H_c is the lower critical field for superconductivity. The ellipticity induced by thermal mountains, as calculated within this work, is a factor of a few smaller ($\sim 10^{-9} B_{12}$) than the calculations of Lander (2013). It is interesting that the two ellipticity-generating mechanisms produce rather similar results, despite their very different input physics.

The magnetic field of a neutron star decays ohmically on a timescale

$$\tau_{\rm Ohm} = \frac{4\pi\sigma L^2}{c^2}, \tag{4.10.9}$$

where σ is the electrical conductivity which is a function of the relaxation time as

$$\sigma = \frac{e^2 n_{\rm e} \tau(T, Q_{\rm imp})}{m_{\rm e}^*}, \tag{4.10.10}$$

and L is a characteristic length scale. The Ohmic timescale can be written in the parametrised form as (Pons and Geppert, 2018)

$$\tau_{\rm Ohm} = 4.4 \left(\frac{\sigma}{10^{24}{\rm s}^{-1}} \right) \left(\frac{L^2}{\rm km} \right) \ 10^6 \ {\rm years}. \tag{4.10.11}$$

The ohmic timescale is short compared to the lifetime of a LMXB. This indicates the magnetic field may have decayed away unless there a mechanism that continues to generate the field.

It would be interesting to build on this work by exploring other sources of temperature asymmetries that could arise within this model. Some examples of such sources of asymmetries may arise from non-spherical accretion, or the presence of temperature

asymmetries on the crustal surface i.e. pulsars. We explore the first of these possibilities in the next chapter.

CHAPTER 5

Temperature asymmetry on surface of an accreted neutron star crust

In this chapter, we will build on the work of chapter 4 by investigating other sources of where temperature perturbations may arise within our model. Looking at the key equations of the model, the flux

$$\boldsymbol{F} = -K\boldsymbol{\nabla}T, \tag{5.0.1}$$

and the divergence of the flux

$$\boldsymbol{\nabla}\cdot\boldsymbol{F} = \dot{Q} = \rho(\epsilon_{\rm nuc} - \epsilon_{\nu}), \tag{5.0.2}$$

possible sources of temperature perturbations could arise from the rate of change of heat per unit time $\dot{Q}$, as well as the perturbed temperature at the crustal boundaries, which were previously set to zero in chapters 3 and 4.

In this chapter, non-spherical accretion is introduced. This could incite a perturbation in the rate of change of heat per unit time, resulting in a perturbation in the $\rho\epsilon_{\rm nuc}$ component. Another possible temperature perturbation could arise from the dependence of neutrino cooling on the magnetic field. In this work, only neutrino bremsstrahlung cooling in the crust has been considered, as this is the dominant cooling mechanism. From the literature, Haensel et al. (1996) do not include the magnetic field in their Bremsstrahlung neutrino cooling calculations and Chamel and Haensel (2008) state the effect of the magnetic field on Bremsstrahlung neutrino cooling has not been calculated. For these reasons, any possible perturbation on $\rho\epsilon_{\nu}$ will not be considered further.

In this chapter, we investigate how a temperature asymmetry on the surface of the crust, arising from non-spherical accretion, influences the thermal profile of the star's crust.

Using the model from chapter 4, a temperature perturbation is induced by hand at the crustal outer boundary. The model is then solved numerically without a a magnetic field present, so the influence on the temperature distribution in the crust, arising solely from the boundary temperature perturbation, can be seen. Later, the model is solved with the perturbed outer boundary temperature in the presence of a magnetic field, to enable the cumulative effects of both of these perturbation mechanisms on the temperature distribution, in the accreted neutron star crust, to be seen.

5.1 Non-spherical accretion

A temperature asymmetry can arise in an accreted neutron star crust if accretion is non-spherical. For non-spherical accretion to occur, the accreted matter interacts with the external magnetic field, channelling the accreted matter onto the neutron star via the polar caps.

In chapter 4, the thermal profile of an accreted neutron star crust was calculated for spherical accretion. This model can be adjusted to include non-spherical accretion by introducing a non-zero-value for the perturbed outer boundary condition $\delta T_{\rm OB}$.

In chapters 3 and 4, the temperature at the outer boundary of the crust was set as a function of the local accretion rate, following the formalism used by Ushomirsky et al. (2000) as

$$T_{\rm OB} = T_{\rm burn}\left(\frac{\dot{m}}{\dot{m}_{\rm Edd}}\right)^{\frac{2}{7}}, \tag{5.1.1}$$

where $T_{\rm burn} = 5.3 \times 10^8$K is the thermally stable burning temperature of hydrogen and helium in the upper atmosphere for high accretion rates $\dot{M} > 10^{-8} M_\odot \ {\rm yr}^{-1}$ (Schatz et al., 1999). For weakly magnetised neutron stars ($B << 10^{11}$G) with lower accretion rates ($\dot{M} < 10^{-8} M_\odot \ {\rm yr}^{-1}$) the nuclear burning is thermally unstable, resulting in the production of energetic type I X-ray bursts. When accretion is non-spherical, the local accretion rate at the magnetic poles is usually high enough for stable hydrogen/helium burning to occur. The temperature sensitive helium burning governs the average nuclear mass of the ashes, which is dependent on the local accretion rate.

The external magnetic field may channel the flow of accreted matter, giving rise to a non-zero $\delta\dot{m}$. The perturbed outer boundary temperature can be written as a function

of the perturbed local accretion rate as

$$\delta T_{\rm OB} = \frac{2}{7} T_{\rm burn} \left(\frac{\dot{m}}{\dot{m}_{\rm Edd}} \right)^{-\frac{5}{7}} \frac{\delta \dot{m}}{\dot{m}_{\rm Edd}}. \tag{5.1.2}$$

The perturbed local accretion rate $\delta \dot{m}$ can be written as a function of a dimensionless free parameter α as

$$\delta \dot{m} = \alpha < \dot{m} >, \tag{5.1.3}$$

where $< \dot{m} >$ is the surfaced averaged accretion rate.

The expression for the perturbed outer boundary temperature shown in equation (5.1.2), will be employed as a modified boundary condition in the perturbed model outlined in chapter 4, for a realistic accreted neutron star crust.

Introducing spherical harmonics, we can write

$$\delta \dot{m} = {\rm Re} \sum_{lm} \alpha_{lm} \langle \dot{m} \rangle Y_{lm}. \tag{5.1.4}$$

Setting the indices as $l = m = 2$, for a quadrupole for gravitational wave production, equation (5.1.4) becomes

$$\delta \dot{m} = {\rm Re}[\alpha_{22} Y_{22} \langle \dot{m} \rangle]. \tag{5.1.5}$$

Using equations (5.1.1), (5.1.2) and (5.1.5), an expression for δT at the outer boundary can be written in spherical harmonics as

$$\delta T_{\rm OB} = \frac{2}{7} T_{\rm OB} {\rm Re}[\alpha_{22} Y_{22}]. \tag{5.1.6}$$

α_{22} and Y_{22} can be expressed as a function of phase factor for angle $\Delta\phi$ as

$$\begin{aligned} \alpha_{22} &= |\alpha_{22}| e^{-i2\Delta\phi}, \\ Y_{22}(\theta, \phi) &= Y_{22}(\theta, 0) e^{i2\phi}, \end{aligned} \tag{5.1.7}$$

combining these expressions with equation (5.1.6) and taking the real parts, the perturbed outer boundary temperature is then written as

$$\delta T_{\rm OB} = \frac{2}{7} T_{\rm OB} |\alpha_{22}| Y_{22}(\theta, 0) \cos[2(\phi - \Delta\phi)]. \tag{5.1.8}$$

From equation (5.1.8), $\Delta\phi$ represents the location of the hot-spot relative to the symmetry axis $\phi = 0$ of the internal toroidal magnetic field. For real positive α_{22}: $\Delta\phi = 0$ and for real negative α_{22}: $\Delta\phi = \frac{\pi}{2}$.

The perturbation ratio $\delta T/T$ scales linearly with α. Initially we set $\alpha = 0.01$ and $B = 0$ G.

Later we introduce an internal magnetic field $B \neq 0$ G, at which point the relative sizes of B and α will become important.

5.2 Thermal profile of an accreted neutron star crust in the presence of a magnetic field

The background thermal profile of an accreted neutron star crust is constructed in spherical symmetry for a realistic equation of state using the same formalism as in chapter 4. On this background model, a temperature perturbation was incited by two different methods: insertion of a magnetic field and non-spherical accretion.

In section 4.6, a magnetic field was inserted into the crust and two coupled first order differential equations, for the perturbed flux U_{lm} and temperature δT_{lm}, shown in equations (4.3.7) and (4.3.6) respectively, were solved for a magnetic field $B = 1 \times 10^{12}$ G and the boundary conditions $\delta T_{\rm OB} = \delta T_{\rm IB} = 0$. In the work presented here, we are building on this model by solving for an accreted neutron star crust that has existing temperature asymmetries present, which arise from non-spherical accretion. The existence of these temperature asymmetries is implemented into the model by introducing a non-zero $\delta T_{\rm OB}$. The coupled ODEs shown in equations (4.3.7) and (4.3.6) are solved for magnetic field strength $B = 0$G, for both a normal and superfluid core, using equation (5.1.6) with the outer boundary condition set as

$$\delta T_{\rm OB} = \frac{2}{7} T_{\rm OB} {\rm Re}[\alpha_{22} Y_{22}]. \tag{5.2.1}$$

The inner boundary condition for a normal core is set as

$$\delta T_{\rm IB} = 0, \tag{5.2.2}$$

and for a superfluid core

$$U_{lm} = 0. \tag{5.2.3}$$

The numerical methods used to solve equations (4.3.7) and (4.3.6) are the same as those detailed in sections 4.4 and 4.7.

5.3 Thermal profile results for non-spherical accretion

In this section, the results obtained for solving the coupled ODEs for temperature and flux, as shown in equations (4.3.7) and (4.3.6), for the boundary conditions shown in section 5.2 are presented for $B = 0$G in subsection 5.3.1, for both a normal and superfluid core and for both an internal field and a surface asymmetry in section 5.3.2.

5.3.1 Non-spherical accretion in the absence of a magnetic field

The results presented in this subsection are for the free parameters $\alpha = 0.01$ and $B = 0$G.

The perturbed temperature profile as a function of radius for $\alpha = 0.01$ is shown for a normal and superfluid core in figures 5.3.1 and 5.3.2 respectively. The perturbed temperature is at a maximum at the outer boundary, and a minimum at the inner boundary, for both a normal and superfluid core. This is a result of the inner boundary condition of $\delta T_{\rm IB} = 0$. Both stars produce identical temperature distributions, with a temperature perturbation of order 10^6K, with a larger δT for higher accretion rates.

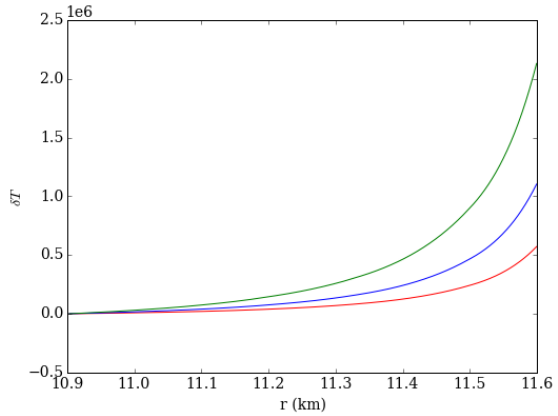

Figure 5.3.1: A plot of how the perturbed temperature varies with radius for $Q_{\rm imp} = 1$, $B = 0$G and $\alpha = 0.01$ for a normal core. The red line represents $\dot{M} = 1 \times 10^{-10} M_\odot$ yr^{-1}, the blue line $\dot{M} = 1 \times 10^{-9} M_\odot$ yr^{-1}, and the green line $\dot{M} = 1 \times 10^{-8} M_\odot$ yr^{-1}.

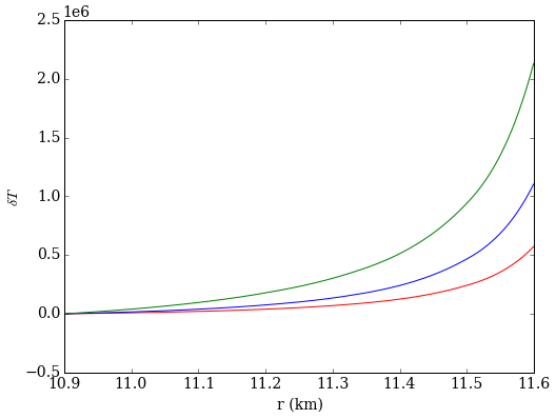

Figure 5.3.2: A plot of how the perturbed temperature varies with radius for $Q_{\rm imp} = 1$, $B = 0$G and $\alpha = 0.01$, for a superfluid core. The red line represents $\dot{M} = 1 \times 10^{-10} M_\odot$ yr^{-1}, the blue line $\dot{M} = 1 \times 10^{-9} M_\odot$ yr^{-1}, and the green line $\dot{M} = 1 \times 10^{-8} M_\odot$ yr^{-1}.

A plot of how the perturbed flux varies with radius in an accreted neutron star crust is shown for a normal and superfluid core in figures 5.3.3 and 5.3.4 respectively. For both a normal and superfluid core star the magnitude of the perturbed flux decreases almost linearly with radius when moving from the crust-core boundary towards the surface of the crust. The magnitude of the flux is the same for both a normal and superfluid core star.

The ratio $\delta T/T$ is shown as a function of radius in figures 5.3.5 and 5.3.6 for a normal and superfluid core respectively. For both stars, $\delta T/T$ decreases in magnitude when moving from the top of the crust towards the crust core boundary. The temperature perturbation in both the normal and superfluid core cases are of order $\delta T/T \sim 10^{-3}$. The results produced here show that the type of core a neutron star has does not significantly affect the thermal profile of an accreted crust when a significant temperature asymmetry exists on the surface of the crust. For a normal core star a higher accretion rate produces a larger $\delta T/T$. In the case of the superfluid core star, the relation between accretion

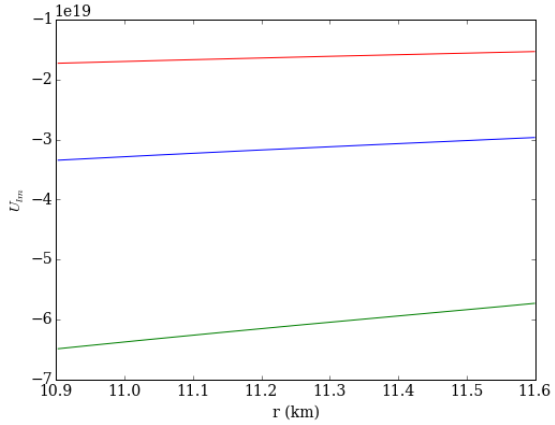

Figure 5.3.3: A plot of how the perturbed flux varies with radius for $Q_{\rm imp} = 1$, $B = 0$G and $\alpha = 0.01$, for a normal core. The red line represents $\dot{M} = 1 \times 10^{-10} M_{\odot}$ yr^{-1}, the blue line $\dot{M} = 1 \times 10^{-9} M_{\odot}$ yr^{-1}, and the green line $\dot{M} = 1 \times 10^{-8} M_{\odot}$ yr^{-1}.

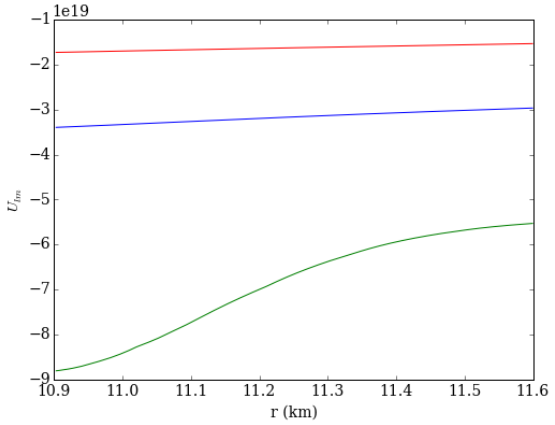

Figure 5.3.4: A plot of how the perturbed flux varies with radius for $Q_{\rm imp} = 1$, $B = 0$G and $\alpha = 0.01$, for a superfluid core. The red line represents $\dot{M} = 1 \times 10^{-10} M_{\odot}$ yr^{-1}, the blue line $\dot{M} = 1 \times 10^{-9} M_{\odot}$ yr^{-1}, and the green line $\dot{M} = 1 \times 10^{-8} M_{\odot}$ yr^{-1}.

rate and perturbation ratio is more complex. Accretion rates $\dot{M} = 1 \times 10^{-10} M_{\odot}$ yr^{-1} and $\dot{M} = 1 \times 10^{-8} M_{\odot}$ yr^{-1} produce a larger $\delta T/T$, when compared to accretion rate $\dot{M} = 1 \times 10^{-9} M_{\odot}$ yr^{-1}.

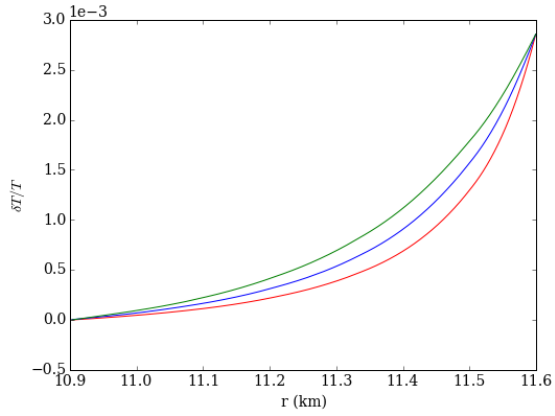

Figure 5.3.5: A plot of how the perturbed temperature ratio varies with radius for $Q_{\rm imp} = 1$, $B = 0$G and $\alpha = 0.01$, for a normal core. The red line represents $\dot{M} = 1 \times 10^{-10} M_{\odot}$ yr^{-1}, the blue line $\dot{M} = 1 \times 10^{-9} M_{\odot}$ yr^{-1}, and the green line $\dot{M} = 1 \times 10^{-8} M_{\odot}$ yr^{-1}.

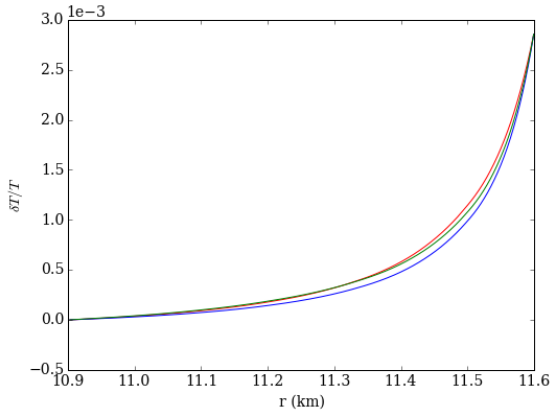

Figure 5.3.6: A plot of how the perturbed temperature ratio varies with radius for $Q_{\rm imp} = 1$, $B = 0$G and $\alpha = 0.01$, for a superfluid core. The red line represents $\dot{M} = 1 \times 10^{-10} M_{\odot}$ yr^{-1}, the blue line $\dot{M} = 1 \times 10^{-9} M_{\odot}$ yr^{-1}, and the green line $\dot{M} = 1 \times 10^{-8} M_{\odot}$ yr^{-1}.

The corresponding plots of perturbed temperature as a function of density is shown for a normal and superfluid in figures 5.3.7 and 5.3.8 respectively. The perturbed temperature gradients as a function of density, for the normal core and superfluid core stars, are identical stars. The perturbation ratio is also shown as a function of density in figures 5.3.9 for a normal core and 5.3.10 for a superfluid core.

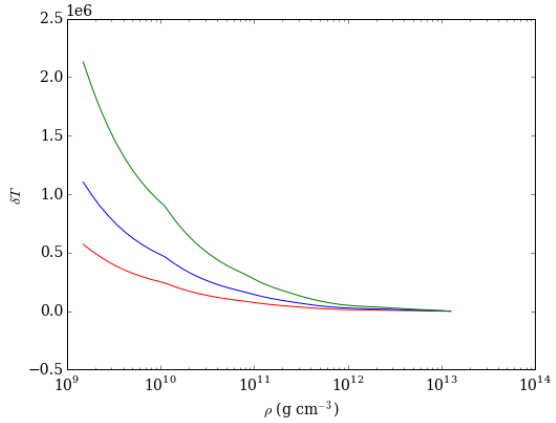

Figure 5.3.7: A plot of how the perturbed temperature varies with density for $Q_{\rm imp} = 1$, $B = 0$G and $\alpha = 0.01$, for a normal core. The red line represents $\dot{M} = 1 \times 10^{-10} M_\odot$ yr^{-1}, the blue line $\dot{M} = 1 \times 10^{-9} M_\odot$ yr^{-1}, and the green line $\dot{M} = 1 \times 10^{-8} M_\odot$ yr^{-1}.

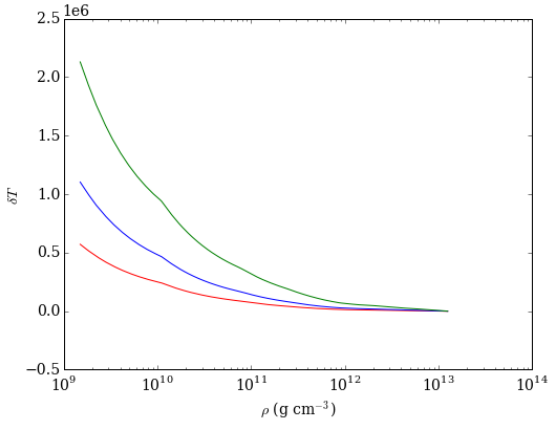

Figure 5.3.8: A plot of how the perturbed temperature varies with density for $Q_{\rm imp} = 1$, $B = 0$G and $\alpha = 0.01$, for a superfluid core. The red line represents $\dot{M} = 1 \times 10^{-10} M_\odot$ yr^{-1}, the blue line $\dot{M} = 1 \times 10^{-9} M_\odot$ yr^{-1}, and the green line $\dot{M} = 1 \times 10^{-8} M_\odot$ yr^{-1}.

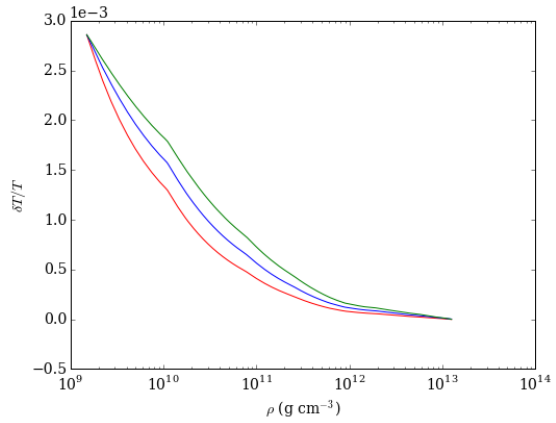

Figure 5.3.9: A plot of how the perturbed temperature ratio varies with density for $Q_{\rm imp} = 1$, $B = 0$G and $\alpha = 0.01$, for a normal core. The red line represents $\dot{M} = 1 \times 10^{-10} M_\odot$ yr^{-1}, the blue line $\dot{M} = 1 \times 10^{-9} M_\odot$ yr^{-1}, and the green line $\dot{M} = 1 \times 10^{-8} M_\odot$ yr^{-1}.

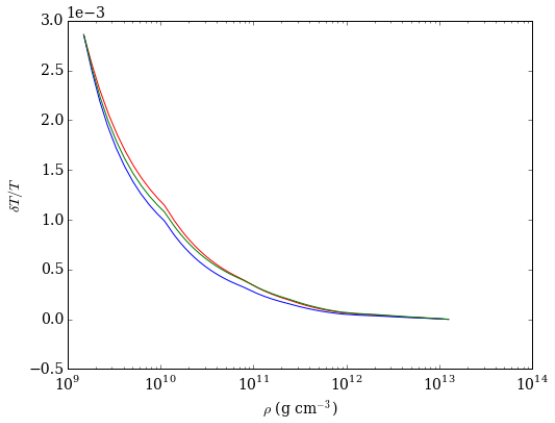

Figure 5.3.10: A plot of how the perturbed temperature ratio varies with density for $Q_{\rm imp} = 1$, $B = 0$G and $\alpha = 0.01$, for a superfluid core. The red line represents $\dot{M} = 1 \times 10^{-10} M_\odot$ yr^{-1}, the blue line $\dot{M} = 1 \times 10^{-9} M_\odot$ yr^{-1}, and the green line $\dot{M} = 1 \times 10^{-8} M_\odot$ yr^{-1}.

5.3.2 Combining the two temperature perturbation mechanisms

In this original work, two methods are used to invoke a temperature perturbation in the accreted crust of a neutron star: the presence of an internal magnetic field, and non-spherical accretion.

To gain an insight into how the temperature perturbation ratio scales with α and the internal magnetic field B, a scaling formula was constructed from the values of $\delta T/T$. For consistency, the value of $\delta T/T$ was selected at $\rho = 1 \times 10^{12}$ g cm^{-3} as Ushomirsky et al. (2000) find that the higher density inner crust is the part that contributes most to the quadrupole moment, and for an accretion rate of $\dot{M} = 1 \times 10^{-9}$ M$_\odot$ yr^{-1}. For a normal core star, ellipticity scales with α as

$$\epsilon \approx 5 \times 10^{-9}\alpha, \tag{5.3.1}$$

and for a superfluid core as

$$\epsilon \approx 3 \times 10^{-8}\alpha, \tag{5.3.2}$$

where $\alpha = 1$. Using these ellipticity values, the relation between α and B can be found, such that the two quadrupole generating mechanisms are equally effective, by combining these formulae with the magnetic field scaling equations shown in 4.10.2 and 4.10.3. As the temperature perturbation scales linearly with both α and B, the internal magnetic field can be written as a function of α for a normal star as

$$B = 1 \times 10^{12}\alpha, \tag{5.3.3}$$

and for a superfluid core star as

$$B = 3 \times 10^{13}\alpha. \tag{5.3.4}$$

To gain an insight into the influence each perturbation mechanism has on the model, a phase-space plot of magnetic field against α was calculated for $\delta T/T$ at $\rho = 1 \times 10^{12}$g cm^{-3} for an accretion rate of $\dot{M} = 1 \times 10^{-9} M_\odot$ yr^{-1}, this is shown in figure 5.3.11 for a normal core and 5.3.12 for a superfluid core. For strong magnetic fields B$> 10^{12}$G, and small values for $\alpha < 0.1$, the magnetic field begins to become the dominant quadrupole generating mechanism. From figures 5.3.11 and 5.3.12, it can be seen for $\alpha \sim 0.01$ is approximately as effective as $B = 10^{11}$G (normal core) and $B = 10^{12}$G (superfluid core) at generating a temperature asymmetry in the accreted crust.

An investigation into the effects of $B \neq 0$ and $\alpha \neq 0$ was conducted on δT and $\delta T/T$ for both a normal and superfluid core. Although the results produced here are guaranteed to be a simple linear sum of the separate results, it is still interesting to see what the plots

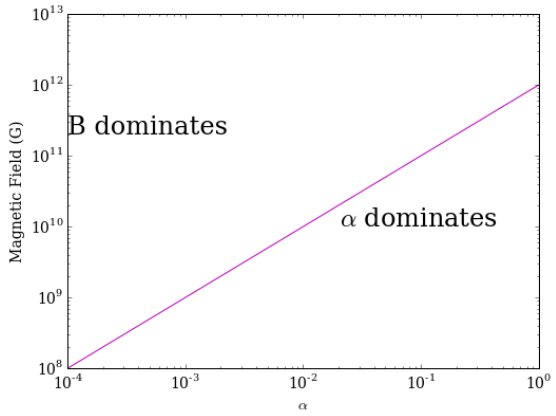

Figure 5.3.11: A phase space plot of magnetic field and the free parameter α for a normal core, to demonstrate which perturbation mechanism dominates for different values of B and α.

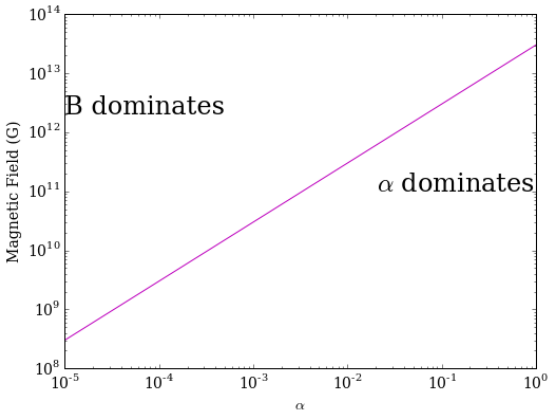

Figure 5.3.12: A phase space plot of magnetic field and the free parameter α for a superfluid core, to demonstrate which perturbation mechanism dominates for different values of B and α.

look like. In each star core case, the value of the free parameter α was set as $\alpha = 0.01$, and the value of B was determined using equations 5.3.3 and 5.3.4, to ensure contributions from both perturbation mechanisms were invoked. For a normal core the internal magnetic field was set as $B = 6.5 \times 10^{11}$ and for a superfluid core as $B = 5.2 \times 10^{12}$. The perturbed temperature and $\delta T/T$ was then computed for both stars for $Q_{\rm imp} = 1$ and accretion rates $\dot{M} = 1 \times 10^{-10} M_\odot$ yr^{-1}, $\dot{M} = 1 \times 10^{-9} M_\odot$ yr^{-1} and $\dot{M} = 1 \times 10^{-8} M_\odot$ yr^{-1}. The results for a normal core are presented in figures 5.3.13 and 5.3.14, and a superfluid core in 5.3.15 and 5.3.16.

For a normal core star, a comparison can be drawn between the results for δT and $\delta T/T$ when both the magnetic field and non-spherical accretion perturbation generating mechanisms are present with the perturbation induced by the only the internal magnetic field as shown in figures 4.8.5 and 4.8.9 respectively, as well as the perturbation induced when only non-spherical accretion is present, as shown in figures 5.3.1 and 5.3.2 respectively. In each temperature perturbation mechanism case, the magnitude of δT is of the same order of $\sim 10^6$ K and $\delta T/T \sim 10^{-3}$. The shape of the curves produced when both perturbation mechanisms are present differ from the independent mechanism cases, showing how the temperature profile of the accreted crust changes due to the temperature perturbation mechanism.

In the superfluid core case, the shape of the curve for δT (shown in figure 5.3.15) is quite different in shape to that produced when only the non-spherical accretion perturbation mechanism is present as shown in figure 5.3.2, where contributions from both perturbation mechanisms can be seen. The magnitude of δT produced is the same for all three perturbation mechanism cases of $\sim 10^6$ K. For $\delta T/T$ shape of the curve produced when both perturbation mechanisms are present (shown in figure 5.3.16) is similar to the δT curve and quite different to the cases when only the internal magnetic field is the per-

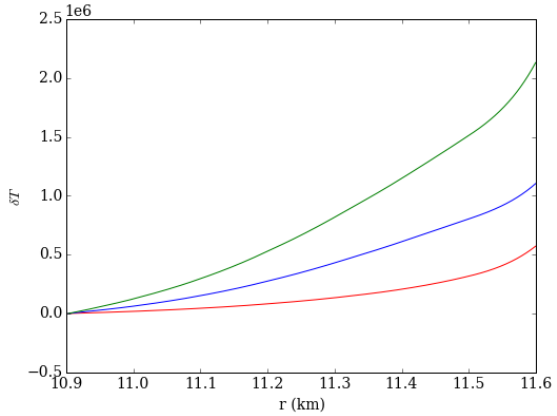

Figure 5.3.13: A plot of how δT varies with radius for $\alpha = 0.01$, $B = 6.5 \times 10^{11}$ G, $Q_{\rm imp} = 1$ for a normal core star. The red line represents $\dot{M} = 1 \times 10^{-10} M_\odot$ yr^{-1}, the blue line $\dot{M} = 1 \times 10^{-9} M_\odot$ yr^{-1}, and the green line $\dot{M} = 1 \times 10^{-8} M_\odot$ yr^{-1}.

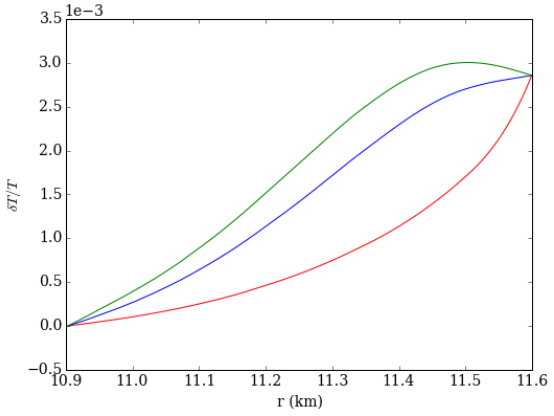

Figure 5.3.14: A plot of how $\delta T/T$ varies with radius for $\alpha = 0.01$, $B = 6.5 \times 10^{11}$ G, $Q_{\rm imp} = 1$ for a normal core star. The red line represents $\dot{M} = 1 \times 10^{-10} M_\odot$ yr^{-1}, the blue line $\dot{M} = 1 \times 10^{-9} M_\odot$ yr^{-1}, and the green line $\dot{M} = 1 \times 10^{-8} M_\odot$ yr^{-1}.

turbation mechanism as shown in figure 4.8.10 and the case where only non-spherical accretion is present as shown in figure 5.3.6. The magnitude of $\delta T/T$ produce by all three perturbation mechanism cases is of the same order as $\sim 10^{-3}$.

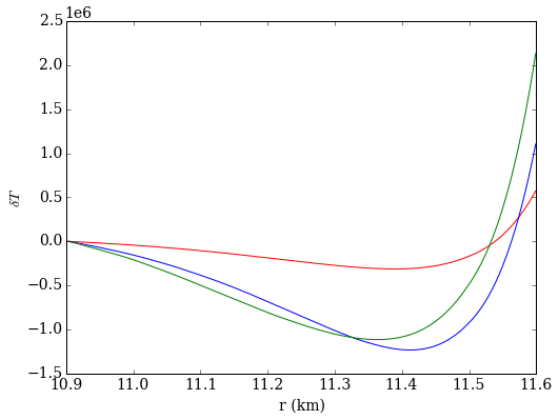

Figure 5.3.15: A plot of how δT varies with radius for $\alpha = 0.01$, $B = 5.2 \times 10^{12}$ G, $Q_{\rm imp} = 1$ for a superfluid core star. The red line represents $\dot{M} = 1 \times 10^{-10} M_\odot$ yr^{-1}, the blue line $\dot{M} = 1 \times 10^{-9} M_\odot$ yr^{-1}, and the green line $\dot{M} = 1 \times 10^{-8} M_\odot$ yr^{-1}.

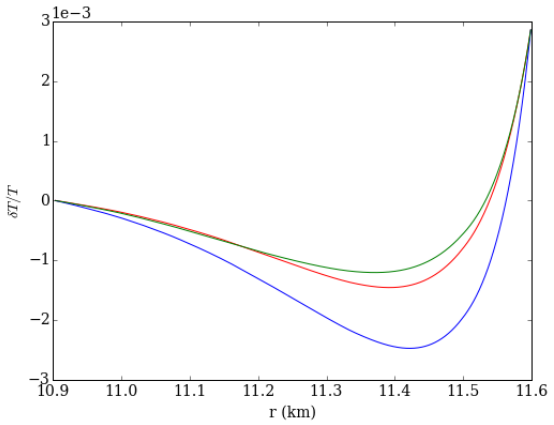

Figure 5.3.16: A plot of how $\delta T/T$ varies with radius for $\alpha = 0.01$, $B = 5.2 \times 10^{12}$ G, $Q_{\rm imp} = 1$ for a superfluid core star. The red line represents $\dot{M} = 1 \times 10^{-10} M_\odot$ yr^{-1}, the blue line $\dot{M} = 1 \times 10^{-9} M_\odot$ yr^{-1}, and the green line $\dot{M} = 1 \times 10^{-8} M_\odot$ yr^{-1}.

5.4 Summary

In this chapter, a temperature asymmetry was introduced onto the surface of the crust. One way in which this could happen is if accreted matter is channelled onto the neutron star surface via the magnetic field lines. This produces hot spots on the polar caps.

A spherically symmetric background thermal profile was modelled, for a realistic equa-

tion of state, using the same methods as detailed in section 4.3. From this, a temperature perturbation in the crust was incited, for instance as might be caused by non-spherical accretion. The temperature perturbation was modelled using the same methods outlined in section 4.6 with no internal magnetic field. Non-spherical accretion was introduced into this model by adjusting the perturbed outer boundary temperature to be a function of the perturbed local accretion rate $\delta\dot{m} = \alpha\langle\dot{m}\rangle$. The temperature perturbation for this model was calculated by solving for two different neutron stars: one with a normal core and one with a superfluid core.

The temperature perturbation ratio generated by non-spherical accretion for $\rho = 10^{12}$ g cm^{-3}, $\dot{M} = 1 \times 10^{-9}$ M$_\odot$ yr^{-1}, $Q_{\rm imp} = 1$ $B = 0$G, from figures 5.3.9 and 5.3.10 for a normal and superfluid core star respectively, was found to be

$$\left.\frac{\delta T}{T}\right|_{\rm normal} = 0.001\alpha,$$
$$\left.\frac{\delta T}{T}\right|_{\rm superfluid} = 0.006\alpha,$$

where $\alpha = 1$. This corresponds to an ellipticity generated for a normal core of

$$\epsilon \approx 5 \times 10^{-9}\alpha, \tag{5.4.1}$$

and for a superfluid core

$$\epsilon \approx 3 \times 10^{-8}\alpha. \tag{5.4.2}$$

The ellipticity produced by non-spherical accretion is a few orders of magnitude larger than that produced by the internal magnetic field field alone. Ushomirsky et al. (2000) show a temperature perturbation ratio of order $\sim 1\%$ is required to generate a mass quadrupole moment that is sufficiently large to produce gravitational wave energy losses that balance the spin-up torque from accretion. This suggests that if a neutron star is accreting in an asymmetric way, and is able to generate a temperature asymmetry of order unity, then a sufficiently large mountain may develop in the crust. This is unlikely as an asymmetry of this magnitude has not been observed in the surface flux.

CHAPTER 6

Thesis discussion and summary

Work by Bildsten (1998) and Ushomirsky et al. (2000) has shown that if temperature asymmetries exist in an accreted neutron star crust, then these stars are able to develop a time-varying mass quadrupole resulting in the production of gravitational waves. Bildsten (1998) calculated a mass quadrupole moment of $Q \approx 4.5 \times 10^{37} \mathrm{g\ cm}^2$ is sufficiently large to generate energy losses via gravitational wave radiation, that balances the spin-up torque from accretion. This physical process provides a possible explanation of the observed narrow spin frequencies of LMXBs.

Bildsten (1998) proposes a mass quadrupole moment of this magnitude may develop in an accreted crust via electron capture reactions if temperature asymmetries are present. Electron capture reactions are sensitive to both density and temperature. In hotter regions of the crust, electron capture occurs at lower densities, closer to the surface of the star, than cooler regions. An anisotropic temperature distribution gives rise to lateral density variations, resulting in the formation of mountains.

Ushomirsky et al. (2000) calculated the maximum crust quadrupole moment the crust could sustain before cracking as $Q \approx 10^{38}$ g cm^{-3}. This is approximately a factor of two larger than the mass quadrupole moment required, as calculated by Bildsten (1998). Ushomirsky et al. (2000) find a temperature perturbation ratio $\delta T/T \sim 1\%$ would generate a quadrupole moment of $Q \sim 2 \times 10^{-6} \frac{\delta T}{T}$ per capture layer. Approximating this

result over a several capture layers generates an ellipticity of

$$\epsilon \approx 5 \times 10^{-6} \frac{\delta T}{T}. \tag{6.0.1}$$

In this work, we calculated the temperature asymmetry induced by the presence of a magnetic field in an accreted neutron star crust. The presence of a magnetic field causes anisotropies in the thermal conductivity to form, which leads to the development of a temperature gradient in the crust.

In chapter 3, we constructed a toy model of an accreted crust of constant density. The background thermal profile of the crust was constructed by solving the heat equation for a static, spherically symmetric star. Heat was deposited into the crust via nuclear reactions from accreted material, and neutrino Bremsstrahlung emission generated heat losses from the crust. The total heat deposited into the crust was 1 MeV. Heat transport in the crust is mediated by electrons, more specifically electron-phonon and electron-impurity scattering processes governed the thermal conductivity. On this background model, a magnetic field was inserted, consequently taking the thermal conductivity from a scalar quantity to a tensor quantity, due to the electron interactions with the magnetic field. The temperature perturbation ratio induced in an accreted crust of constant density, by the presence of a magnetic field, was found to be

$$\frac{\delta T}{T} \approx 2 \times 10^{-6} \mathrm{B}_9, \tag{6.0.2}$$

corresponding to an ellipticity of

$$\epsilon \approx 1 \times 10^{-11} \mathrm{B}_9, \tag{6.0.3}$$

for $Q_{\mathrm{imp}} = 1$ and $\dot{M} = 1 \times 10^{-9}$ $\mathrm{M}_\odot$ yr^{-1}. We began with this simplified case, to provide an initial estimate of the temperature perturbation induced by a magnetic field, to determine if a more thorough examination is required. Although this value produced here is a few orders of magnitude smaller than the temperature perturbation required to produce a sufficiently large mountain, we felt it was still worth while investigating this temperature perturbation mechanism in more detail.

In chapter 4, we developed our toy model from chapter 3 to include a realistic equation of state. A star of varying density was constructed by solving the relativistic hydrostatic structure equations for the core, and Newtonian gravity for the crust. For the accreted crust, we used the equation of state data from Haensel and Zdunik (1990a). From this data, heat from nuclear reactions was deposited into shells of constant A and Z, with a total heat deposited of 1.33 MeV per nucleon. The heat equation was solved numerically for a background spherically symmetric neutron star for two cases: a star with a normal core and a star with a superfluid core. A magnetic field was then inserted into this back-

ground model to induce a temperature perturbation. From this model, at $\rho = 1 \times 10^{12}$, $Q_{\rm imp} = 1$ and $\dot{M} = 1 \times 10^{-9}$ M$_\odot$ yr^{-1}, a temperature perturbation ratio for a normal core star was found to be

$$\delta T/T \sim 1 \times 10^{-6} \mathrm{B}_9, \tag{6.0.4}$$

and for a superfluid core star as

$$\delta T/T \sim 2 \times 10^{-7} \mathrm{B}_9. \tag{6.0.5}$$

These temperature perturbation values correspond to inducing an ellipticity in the crust for a normal core star of

$$\epsilon \sim 5 \times 10^{-12} \mathrm{B}_9, \tag{6.0.6}$$

and for a superfluid core star as

$$\epsilon \sim 1 \times 10^{-12} \mathrm{B}_9 \tag{6.0.7}$$

The ellipticity calculated in this model, for a normal core star with a realistic equation of state, is an order of magnitude smaller than the value calculated in the toy model from chapter 3. This suggests the density dependent parameters play an important role in the thermal transport of an accreted neutron star crust. The accretion rate also plays an important role in our model as the temperature of the crust at the outer boundary is a function of accretion rate. For a normal core star we find a higher accretion rate produces a larger δT and $\delta T/T$ in the crust. In the case of a superfluid core star we find the opposite. A higher accretion rate gives rise to a δT and $\delta T/T$ of a smaller magnitude. This arises from the relationship of the source term with temperature which scales as $\sim \frac{1}{T}\frac{dT}{dr}$ when electron-phonon scattering dominates. This relation makes it difficult to predict how the source term, and ultimately δT and $\delta T/T$ scale with accretion rate in the accreted crust.

In chapter 4 we also investigated the effects shallow crustal heating has on the perturbed temperature. We found shallow heating did affect the perturbed temperature distribution in the accreted crust for both a normal and superfluid core. The temperature perturbation ratio and ellipticity calculated by our model in the presence of shallow heating for a normal core star was found to be

$$\begin{aligned} \frac{\delta T}{T} &= 2 \times 10^{-6} \mathrm{B}_9, \\ \epsilon &\approx 1 \times 10^{-11} \mathrm{B}_9, \end{aligned}$$

and for a superfluid core as

$$\frac{\delta T}{T} = 3.6 \times 10^{-8} \mathrm{B}_9,$$
$$\epsilon \approx 1.8 \times 10^{-13} \mathrm{B}_9.$$

The overall magnitude of $\delta T/T$ and consequently ϵ, was not altered by this mechanism. This result most likely arises because the magnitude of our source term is largest at densities higher than the region where shallow crustal heating occurs.

In chapter 5, we extended our model to include non-spherical accretion resulting in an existing temperature perturbation on the surface of the accreted crust. We considered this for two cases: as an isolated temperature asymmetry and along with the temperature asymmetry in the presence of an internal magnetic field. We introduced the free parameter α to perturb the local accretion rate. Positive real values of α correspond to a hot spot occurring at $\Delta\phi = 0$ and negative real values of α occurring at $\Delta\phi = \pi/2$, where $\Delta\phi$ is the location of the of the hot spot relative to the axis of symmetry $\phi = 0$. We find the temperature perturbation ratio induced in the absence of an internal magnetic field at $\rho = 1\times10^{12}$ g cm^{-3}, $Q_{\rm imp} = 1$, $\alpha = 1$ and accretion rate $\dot{M} = 1\times10^{-8}$ M$_\odot$ yr^{-1} produces for a normal core $\delta T/T \sim 1.5 \times 10^{-2}\alpha$ and for a superfluid core $\delta T/T \sim 2.6 \times 10^{-2}\alpha$. The corresponding ellipticity generated for a normal core is

$$\epsilon \sim 5 \times 10^{-9}\alpha, \tag{6.0.8}$$

and for a superfluid core as

$$\epsilon \sim 3 \times 10^{-8}\alpha. \tag{6.0.9}$$

The temperature perturbation ratios and ellipticities induced by non-spherical accretion for $\alpha = 1$ is are orders of magnitude larger than that generated by the internal magnetic field of $B = 1 \times 10^9$ G from chapter 4, although a temperature asymmetry existing on the surface of the crust of order unity is unlikely. As both the magnetic field induced perturbation and non-spherical accretion temperature perturbation scale linearly in both B and α, the relation of the dividing line between stars where the internal field-induced temperature asymmetry is comparable to the surface-induced temperature asymmetry can be written for a normal core star as

$$B = 1 \times 10^{12}\alpha, \tag{6.0.10}$$

and a superfluid core star

$$B = 3 \times 10^{13}\alpha. \tag{6.0.11}$$

In conclusion, we find it is unlikely for a LMXB to develop a temperature asymme-

try, induced by the internal magnetic field, that is sufficiently large to generate a mass quadrupole moment that produces energy losses via gravitational wave radiation to balance the spin-up torque from accretion. To generate the required mass quadrupole moment, a normal core neutron star would require an internal magnetic field of strength $B \sim 10^{13}$ G and a superfluid core star requires a magnetic field of $B \sim 5 \times 10^{13}$ G. If a neutron star is accreting in an asymmetric way, and is able to generate a temperature asymmetry of order $\sim 0.1 - 1$, then a sufficiently large mountain may develop in the crust.

Bibliography

Abbott et al. (2018a). Gw170817: Measurements of neutron star radii and equation of state. Phys. Rev. Lett. 121, 161101 (2018).

Abbott, B. et al. (2016a). Gw151226: Observation of gravitational waves from a 22-solar-mass binary black hole coalescence. Physical Review Letters, 116(24).

Abbott, B. et al. (2016b). Observation of gravitational waves from a binary black hole merger. Physical Review Letters, 116(6):1–16.

Abbott, B. et al. (2017a). A gravitational wave standard siren measurement of the hubble constant. Arxiv e-print, 1710.05835.

Abbott, B. et al. (2017b). Gw170104: Observation of a 50-solar-mass binary black hole coalescence at redshift 0.2. Physical Review Letters, 118(22).

Abbott, B. et al. (2017c). Gw170608: Observation and of a 19 solar mass binary and black hole and coalesence. The Astrophysical Journal Letters, 851(2).

Abbott, B. et al. (2017d). Gw170814: A three-detector observation of gravitational waves from a binary black hole coalescence. Physical Review Letters, 119(14).

Abbott, B. et al. (2017e). Gw170817: Observation of gravitational waves from a binary neutron star inspiral. Physical Review Letters, 119(16).

Abbott, B. P. et al. (2017f). Gravitational waves and gamma-rays from a binary neutron star merger: Gw170817 and grb 170817a. The Astrophysical Journal, 848(2):L13.

Abbott, B. P. et al. (2017g). Gravitational waves and gamma-rays from a binary neutron star merger: Gw170817 and grb 170817a. The Astrophysical Journal, 848(2):L13.

Abbott, B. P. et al. (2017h). Multi-messenger observations of a binary neutron star merger. The Astrophysical Journal, 848(2):L12.

Abbott, B. P. et al. (2018b). Gwtc-1: A gravitational-wave transient catalog of compact binary mergers observed by ligo and virgo during the first and second observing runs. Arxiv e-prints, 1811.12907.

Aguilera, D. N., Pons, J. A., and Miralles, J. A. (2008). 2d cooling of magnetized neutron stars. Astronomy and Astrophysics, 486(1):255–271.

Andersson, N. (1998). A new class of unstable modes of rotating relativistic stars. Astrophys.J., 502:708-713.

Andersson, N. (2003). Gravitational waves from instabilities in relativistic stars. Class. Quantum Grav., 20 R105–R144.

Andersson, N., Kokkotas, K. D., and Stergioulas, N. (1999). On the relevance of the r-mode instability for accreting neutron stars and white dwarfs. Astrophys.J., 516(307).

Bildsten, L. (1998). Gravitational radiation and rotation of accreting neutron stars. The Astrophysical Journal, 501(1):L89–L93.

Brown, E. (1999). Nuclear heating and melted layers and in the and inner crust and of an and accreting neutron and star. In THE ASTROPHYSICAL JOURNAL, 531 :988È1002, 2000 March 10 (2000. The American Astronomical Society. All rights reserved. Printed in U.S.A.

Brown, E. F. and Cumming, A. (2009). MAPPING CRUSTAL HEATING WITH THE COOLING LIGHT CURVES OF QUASI-PERSISTENT TRANSIENTS. The Astrophysical Journal, 698(2):1020–1032.

Chamel, N. and Haensel, P. (2008). Physics of neutron star crusts. Living Reviews in Relativity, 11(1).

Chandrasekhar, S. (1970). Solutions of two problems in the theory of gravitational radiation. In Physical Review Letters 24 611.

Cutler, C. (2002). Gravitational waves from neutron stars with large toroidal b fields. Physical Review D, 66(8).

Deibel, A., Cumming, A., Brown, E. F., and Page, D. (2015). A strong shallow heat source in the accreting neutron star maxi j0556-332. The Astrophysical Journal, 809(2):L31.

Duncan, R. C. and Thompson, C. (1992). Formation of very strongly magnetized neutron stars: Implications for gamma ray bursts. In The Astrophysical Journal, 392:L9-L13,1992 June 10 © 1992. The American Astronomical Society. All rights reserved. Printed in U.S.A.

Einstein, A. (1916). The foundation of the general theory of relativity. In Annalen de Physik 49, 6769.

Fornberg, B. (1988). Generation of finite and difference formulas and on arbitrarily and spaced grids. In Mathematics of computation volume 51.

Friedman, J. L. and Schutz, B. F. (1978). Secular instability of rotating newtonian stars. The Astrophysical Journal, 222:281.

Geppert, U., Küker, M., and Page, D. (2004). Temperature distribution in magnetized neutron star crusts. Astronomy & Astrophysics, 426(1):267–277.

Glampedakis, K. and Gualtieri, L. (2018). Gravitational waves from single neutron stars: an advanced detector era survey. Arxiv e-print, (1709.07049).

Gupta, S., Brown, E. F., Schatz, H., Möller, P., and Kratz, K.-L. (2007). Heating in the accreted neutron star ocean: Implications for superburst ignition. The Astrophysical Journal, 662(2).

Gupta, S., Kawano, T., and Möller, P. (2008). Neutron reactions in accreting neutron stars: A new pathway to efficient crust heating. Physical Review Letters, 101.

Haensel, P., Kaminker, A. D., and Yakovlev, D. G. (1996). Electron neutrino pair bremsstrahlung in a liquid phase of neutron star crusts. Astronomy and Astrophysics, 314:328–340.

Haensel, P. and Potekhin, A. (2004a). Analytical representations of equations of state of neutron star matter. http://www.ioffe.ru/astro/NSG/NSEOS/sly4.html.

Haensel, P. and Potekhin, A. Y. (2004b). Analytical representations of unified equations of state of neutron-star matter. Astron. Astrophys, 560(A48).

Haensel, P. and Zdunik, J. L. (1990a). Equation Of State And Structure Of The Crust Of An Accreting Neutron Star. Astronomy and Astrophysics, 229:117–122.

Haensel, P. and Zdunik, J. L. (1990b). Non-equilibrium Processes In The Crust Of An Accreting Neutron Star. Astronomy & Astrophysics, 227:431–436.

Hartle, J. B. (2003). Gravity An introduction to Einstein's general relativity.

Haskell, B., Jones, D. I., and Andersson, N. (2006). Mountains on neutron stars: accreted versus non-accreted crusts. Monthly Notices of the Royal Astronomical Society, 373(4):1423–1439.

Haskell, B., Samuelsson, L., Glampedakis, K., and Andersson, N. (2008). Modelling magnetically deformed neutron stars. Monthly Notices of the Royal Astronomical Society, 385(1):531–542.

Johnson-McDaniel, N. K. and Owen, B. J. (2013). Maximum elastic deformations of relativistic stars. Physical Review D, 88(4).

Jones, D. and Andersson, N. (2001). Gravitational waves from freely precessing neutron stars. Mon.Not.Roy.Astron.Soc., 331(203).

Kasen, D., Metzger, B., Barnes, J., Quataert, E., and Ramirez-Ruiz, E. (2017). Origin of the heavy elements in binary neutron-star mergers from a gravitational-wave event. Nature, 551(7678):80–84.

Landau, L. D., Lifshitz, E. M., Sykes, J. B., Reid, W. H., and Dill, E. H. (1986). Theory of elasticity: Vol. 7 of course of theoretical physics. Physics Today, 13(7):44–46.

Lander, S. K. (2013). The contrasting magnetic fields of superconducting pulsars and magnetars. Monthly Notices of the Royal Astronomical Society, 437(1):424–436.

Maier, T. (2005). Wavelet mie representations for solenoidal vector fields with applications to ionospheric geomagnetic data. SIAM Journal on Applied Mathematics, 65(1888-1912).

Martynov, D. V. et al. (2016). Sensitivity of the advanced ligo detectors at the beginning of gravitational wave astronomy. Physical Review D, 93(11).

Meadors, G., Goetz, E., Riles, K., Creighton, T., and Robinet, F. (2017). Searches for continuous gravitational waves from scorpius x-1 and xte j1751-305 in ligo's sixth science run. Physical Review D, 95(4):1–12.

Melatos, A. and Payne, D. J. B. (2005). Gravitational radiation from an accreting millisecond pulsar with a magnetically confined mountain. The Astrophysical Journal, 623:1044 –1050.

Misner, C. W., Thorne, K. S., and Wheeler, J. (1973). gravitation_misner_thorne_wheeler.pdf.

Oppenheimer, J. and Volkoff, G. (1939). On massive neutron cores. Physical Review, 55(374).

Page, D., Geppert, U., and Küker, M. (2007). Cooling of neutron stars with strong toroidal magnetic fields. Isolated Neutron Stars: From The Surface To The Interior, pages 403–412.

Page, D. and Reddy, S. (2013). Forecasting neutron star temperatures: Predictability and variability. Physical Review Letters, 111(24).

Papaloizou, J. and Pringle, J. E. (1978). Gravitational radiation and the stability of rotating stars. In 1978MNRAS.184..501P.

Parikh, A. S., Homan, J., Wijnands, R., Ootes, L., Page, D., Altamirano, D., Degenaar, N., Brown, E. F., Cackett, E., Cumming, A., Deibel, A., Fridriksson, J. K., Lin, D., Linares, M., and Miller, J. M. (2017). Different accretion heating of the neutron star crust during multiple outbursts in MAXI j0556−332. The Astrophysical Journal, 851(2):L28.

Patruno, A., Haskell, B., and Andersson, N. (2017). The spin distribution of fast-spinning neutron stars in low-mass x-ray binaries: Evidence for two subpopulations. The Astrophysical Journal, 850(1).

Paul D. Lasky (2015). Gravitational Waves from Neutron Stars: A Review. PASA, 32:34.

Payne, D. J. B. and Melatos, A. (2004). Burial of the polar magnetic field of an accreting neutron star – i. self-consistent analytic and numerical equilibria. Monthly Notices of the Royal Astronomical Society, 351(2):569–584.

Pons, J. A. and Geppert, U. (2007). Magnetic field dissipation in neutron star crusts: from magnetars to isolated neutron stars. Astron.Astrophys., 470(303).

Pons, J. A. and Geppert, U. (2018). Magnetic field dissipation in neutron star crusts and from magnetars to isolated neutron stars. In Astronomy & Astrophysics manuscript no. mspons ©c ESO 2018 October.

Pons, J. A., Vigano, D., and Rea, N. (2013). A highly resistive layer within the crust of x-ray pulsars limits their spin periods. Nature Physics, 9(431-434).

Price, S., Link, B., Epstein, R. I., and Li, H. (2012). Thermoresistive instability in magnetar crusts. Monthly Notices of the Royal Astronomical Society, 420(2):949–956.

Riles, K. (2017). Recent searches for continuous gravitational waves. Modern Physics, A.

Sathyaprakash, B. S. and Schutz, B. F. (2009). Physics, astrophysics and cosmology with gravitational waves. Living Reviews in Relativity, 12(1):2.

Saulson, P. (1994). Fundamentals of Interferometric Gravitational Wave Detectors. WorldScientific Publishing Co. Pte. Ltd.

Schatz, H., Bildsten, L., Cumming, A., and Wiescher, M. (1999). The rapid proton process ashes from stable nuclear burning on an accreting neutron star. The Astrophysical Journal, 524(2):1014–1029.

Schatz, H., Gupta, S., Möller, P., Beard, M., Brown, E. F., Deibel, A. T., Gasques, L. R., Hix, W. R., Keek, L., Lau, R., Steiner, A. W., and Wiescher, M. (2014). Strong neutrino cooling by cycles of electron capture and − decay in neutron star crusts. Nature, 505.

Shapiro, S. L. and Teukolsky, S. A. (1983). Black Holes, White Dwarfs, and Neutron Stars. Wiley-Verlag.

Ushomirsky, G., Cutler, C., and Bildsten, L. (2000). Deformations of accreting neutron star crusts and gravitational wave emission. Monthly Notices of the Royal Astronomical Society, 319(3):902.

Vigelius, M. and Melatos, A. (2009). Resistive relaxation of a magnetically confined mountain on an accreting neutron star. Monthly Notices of the Royal Astronomical Society, 395(4):1985–1998.

Wagoner, R. V. (1984). Gravitational radiation from accreting neutron stars. In The Astrophysical Journal.

Waterhouse, A. C., Degenaar, N., Wijnands, R., Brown, E. F., Miller, J. M., Altamirano, D., and Linares, M. (2016). Constraining the properties of neutron star crusts with the transient low-mass x-ray binary aql x-1. Monthly Notices of the Royal Astronomical Society, 456(4):4001–4014.

White, N. E. and Zhang, W. (1997). Millisecond x-ray pulsars in low-mass x-ray binaries. The Astrophysical Journal, 490(1).

Yakovlev and Urpin (1980). Thermogalvanomagnetic effects in white dwarfs and neutron stars. Soviet Astronomy, 24:425.